Vibrational energy dissipation mechanisms in granular dampers

Furkan Terzioglu

A thesis submitted in partial fulfilment of the requirements for the degree of

Doctor of Philosophy

The University of Sheffield

Faculty of Engineering

Department of Mechanical Engineering

April 2023

i

Acknowledgements

First of all, and foremost, I would like to thank my supervisors, Dr. Jem Rongong and Dr. Charles Lord, for their great ideas that have guided me to find my path to the end, invaluable support and patience throughout the production of this thesis. I would also like to express my appreciation to the Dynamic Research Group of the University of Sheffield, a special thanks to Mathew J. Hall for his helps when setting-up my laboratory setups.

I am grateful to the Turkish Ministry of National Education for the scholarship provided during my thesis. This work would not have been possible without this financial support.

Finally, I would like to express my gratitude to my loving and supportive wife Ayse Betul whose love and guidance are with me in wherever I pursue, and to my parents and brothers. Without their invaluable understanding and encouragements, it would have been impossible to complete this thesis.

Abstract

Granular damping has been found to be a robust solution for attenuating noise and vibration in difficult operating conditions such as space and aviation applications. However, despite its huge potential, it has never been the first design option for enhancing the damping of structures in practical applications. The primary reason of this is that the energy dissipation behaviour of a granular damper exhibits amplitude and frequency dependent non-linearity. The work presented here investigates the link between the non-linear granular energy dissipation and dynamic motional behaviour of particles considering a broad range of excitation amplitude and frequency. The optimum operating conditions of granular dampers are obtained. The most significant factors which control the optimum conditions are determined to provide reliable guidance for the efficient design of granular dampers. As an extension to the relationship developed between the granular motional phase and energy dissipation, the influence of particle shape is systematically studied using a large collection of non-spherical particle shapes.

List of Contents

List of Symbols

$E_{\text{dissipated}}$	Total energy dissipated over a time frame, [J]
$\tilde{E}_{\text{dissipated}}$	Total energy dissipated over a vibration cycle, [J]
E_{max}	Maximum kinetic energy in a vibration cycle, [J]
ψ_{granular}	Specific damping capacity, [-]
Γ	Non-dimensional acceleration amplitude, [-]
g	Gravitational acceleration, [m/s^2]
η_{loss}	Loss factor, [-]
m_{particle}	Mass of a spherical particle, [kg]
R_{particle}	Radius of a spherical particle, [m]
$\mathbf{r}_{\text{particle}}$	Centre of mass position vector of a spherical particle, [m]
$\boldsymbol{\omega}_{\text{particle}}$	Angular velocity vector of a spherical particle, [rad/s]
$\mathbf{A}_{\text{surface}}, \mathbf{B}_{\text{surface}}, \mathbf{C}_{\text{surface}}$	Vertex position vectors of a surface defined by three points, [m]

$\mathbf{n}_{\mathrm{PP}}$	Normal unit vector of a sphere-sphere contact, [-]
$\mathbf{t}_{\mathrm{PP}}$	Tangential unit vector of a sphere-sphere contact, [-]
δ_{PP}	Deformation in a sphere-sphere contact, [m]
$\mathbf{v}_{\mathrm{PP}}$	Relative velocity vector of a sphere-sphere contact, [m/s]
$a_{\mathrm{surface}}, b_{\mathrm{surface}}, c_{\mathrm{surface}}, d_{\mathrm{surface}}$	Coefficients of a surface equation, [-]
$\mathbf{n}_{\mathrm{surface}}$	Normal vector (not unit) of a surface, [m]
δ_{PS}	Deformation in a sphere-surface contact, [m]
d_{closest}	Closest distance between a sphere centre and surface, [m]
$\mathbf{n}_{\mathrm{PS}}$	Normal unit vector of a sphere-surface contact, [-]
$\mathbf{t}_{\mathrm{PS}}$	Tangential unit vector of a sphere-surface contact, [-]
$\mathbf{v}_{\mathrm{PS}}$	Relative velocity vector of a sphere-surface contact, [m/s]
N_{sphere}	Number of spherical particles employed, [-]
$\mathbf{F}_{\mathrm{resultant}}$	Resultant force imposed by a particle, [N]
I_{particle}	Mass moment of inertia of a particle, [kgm^2]
$\omega_{\mathrm{particle}}$	Angular velocity of a particle, [rad/s]
N_{PP}	Number of particle-particle contact, [-]
N_{PS}	Number of particle-surface contact, [-]
$\mathbf{M}_{\mathrm{resultant}}$	Resultant moment imposed by a particle, [Nm]

t	Time, [s]
Δt	Time step, [s]
ρ_{particle}	Density of a particle, [kg/m^3]
G_{particle}	Shear modulus of a particle, [Pa]
E_{particle}	Elastic modulus of a particle, [Pa]
v_{particle}	Poisson's ratio of a particle, [-]
S_f	Safety factor, [-]
$\mathbf{r}_{\text{MS}}$	Centre of mass position vector of a multi-sphere particle, [m]
$\boldsymbol{\omega}_{\text{MS}}$	Angular velocity vector of a multi-sphere particle, [rad/s]
$m_{\text{sub-sphere}}$	Mass of a sub-sphere, [kg]
m_{MS}	Mass of a multi-sphere particle, [kg]
$R_{\text{sub-sphere}}$	Radius of a sub-sphere, [m]
N_{MS}	Number of sub-spheres, [-]
$\mathbf{r}_{\text{sub-sphere}}$	Centre of mass position vector of a sub-sphere, [m]
$\mathbf{F}_{\text{MS}}$	Resultant force imposed by a multi-sphere particle, [N]
$\mathbf{F}_{\text{PP}}$	Force due to sphere-sphere interactions, [N]
$\mathbf{F}_{\text{PS}}$	Force due to sphere-surface interactions, [N]

$\mathbf{M}_{\text{resultant}}$	Resultant moment imposed by a multi-sphere particle, [Nm]
a_{spheroid}, b_{spheroid}	Principal dimensions of a spheroid, [m]
$d_{\text{sub-sphere}}$	Distance between centres of two sub-spheres, [m]
A	Area of a particle, [m^2]
P	Perimeter of a particle, [m]
a_{toroid}, b_{toroid}	Principal dimensions of a circular toroid, [m]
$\Delta\varphi_{\text{sub-sphere}}$	Angle between sub-sphere centres, [rad]
$\varphi_{\text{sub-sphere}}$	Angular position of a sub-sphere, [rad]
$d_{\text{intersecting}}$	Intersecting distance between two sub-spheres, [m]
$\mathbf{F}_{\text{contact}}$	Contact force between two bodies, [N]
$\mathbf{n}_{\text{contact}}$	Normal unit vector of a contact, [-]
$\mathbf{t}_{\text{contact}}$	Tangential unit vector of a contact, [-]
δ_{contact}	Contact deformation, [m]
σ_{contact}	Normal contact pressure, [Pa]
a_{contact}	Contact area, [m^2]
R_{eq}	Equivalent radius, [m]
E_{eq}	Equivalent elastic modulus, [Pa]
m_{eq}	Equivalent mass, [kg]

G_{eq}	Equivalent shear modulus, [Pa]
$\gamma_{contact}$	Coefficient that establishes sticking-slipping stage, [-]
$k_{contact}$	Stiffness of a contact, [kg/m]
$c_{contact}$	Viscous damping coefficient of a contact, [kg/s]
$e_{contact}$	Coefficient of restitution of an impact, [-]
σ_{yield}	Yield strength of a particle, [Pa]
v_{yield}	Yield velocity of a particle, [m/s]
v_{impact}	Impact velocity, [m/s]
$\zeta_{contact}$	Viscous damping ratio of a contact, [-]
$V_{particle}$	Volume of a particle, [m^3]
$V_{enclosure}$	Volume of an enclosure, [m^3]
υ	Volume fill ratio of an enclosure by particles, [-]
L	Length of a cylindrical enclosure, [m]
u	Motion of an enclosure, [m]
ω	Excitation frequency of an enclosure, [rad/s]
$N_{contact}$	Total number of contacts that a particle generates, [-]
$\Delta E_{dissipated}$	Energy dissipated at each time step, [J]
v_{rel}	Relative velocity between particles in contact, [m/s]

η_{granular}	Granular damping efficiency, [-]
$\tilde{E}_{\text{dissipated}}{}^{\text{max}}$	Maximum energy dissipatable over a vibration cycle, [J]
$h_{\text{clearance}}$	Clearance in an enclosure, [m]
z_{path}	Depth profile of a selected path on a rough surface, [m]
L_{path}	Length of a selected path on a rough surface, [m]
v_{impact}	Impact velocity, [m/s]
T	Time period, [s]
$P_{\text{dissipated}}$	Dissipated power, [W]
a	Acceleration signal, [m/s^2]
f	Force signal, [N]
V	Complex velocity, [m/s]
F	Complex force, [N]
j	Imaginary number, [-]
$\varphi_{\mathbf{V}}$	Phase angle of complex velocity, [rad]
$\varphi_{\mathbf{F}}$	Phase angle of complex force, [rad]
$m_{\text{enclosure}}$	Enclosure mass, [kg]
Ψ	Sphericity parameter, [-]
S_{particle}	Surface area of a particle, [m^2]

α_{spheroid} Aspect ratio of a spheroid, [-]

r_{spheroid} Radius of an equivalent sphere for a spheroid, [m]

h_{toroid} Hole ratio of a circular toroid, [-]

r_{toroid} Radius of an equivalent sphere for a circular toroid, [m]

Declaration

I, the author, confirm that this thesis is my own work. I am aware of the University's Guidance on the Use of Unfair Means (www.sheffield.ac.uk/ssid/unfair-means). This work has not previously been presented for an award at this, or any other, university.

1 Introduction

1.1 Role of Vibration Damping

Mechanical vibrations are often regarded as undesirable motions in machineries, mechanical systems and structural elements because prolonged vibration at a resonance frequency can be highly destructive. Therefore, vibrational concerns have been a unignorable part of all engineering designs for centuries.

In order to control and avoid excessive vibrations in structures, the introduction of 'damping' is necessary. It is a substantial property for structures which results in transforming the vibrational energy in a system into the form of heat, sound and wear, depending on the type of damping method by generating a resistance force against the velocity of system. The relative ratio of the amount of this converted (or dissipated) energy to a structural dissipation need (or a maximum achievable level) determines the effectiveness of damping.

If inherent damping is not sufficient to reduce vibration amplitudes to desired levels, as it is the case in most of engineering structures, an additional damping design is implemented. Whereas active or semi-active damping techniques have been developed for special applications, passive damping methods preserve their popularity. Because they are generally cost-effective, require relatively low maintenance, can be used as retro-fit implementations and can work in broad environmental and dynamic conditions.

The importance and fundamentals of mechanical vibrations had been first addressed in a comprehensive way when Rayleigh published his monumental work "The Theory of Sound" in 1894 [1]. Up to date, many passive damping applications have been presented in literature. These involve friction dampers, viscoelastic material patches, tuneable liquid and mass dampers [2,3], but are not limited to those mentioned. However, all damping methods have their own limitations, and, therefore, the type of damper design depends on many factors such as operating temperature, number of targeted vibrational modes and excitation condition. For example; despite their effectiveness in a variety of applications, viscoelastic material applications suffer from several major drawbacks: their damping and stiffness properties significantly change with frequency and temperature, they are not suitable under both cryogenic and extremely high temperatures, and over time they lose their effectiveness, frequently requiring maintenance [4,5].

1.2 Granular Damping

The 'particle damper' is an alternative damping application where relatively small (typically spherical) particles are placed inside one or more cavities created at appropriate positions within a vibrating structure (a non-obstructive design) or attached to those locations using enclosures as shown in Figure 1.1. As damping particles construct a granular medium, the 'granular damper' term is also used to indicate this damping design.

One of the earliest granular fill suggestions for vibration damping purposes is mentioned in [6]. It has been suggested that if thickness of a granular medium is arranged according to wavelengths of resonances high structural damping would be achieved at resonance frequencies owing to particle material damping. The validity of this viewpoint has been tested and verified for very low vibration amplitudes at which particles have small relative motions without slipping with respect to each other and enclosure as a result of tension and compression within the particles [7].

However, as vibration amplitudes become larger, particles can lose contacts with their neighbours over parts of the vibration cycle. When this happens, impact and sliding interactions occur with neighbouring particles and with the enclosure inner surface. Therefore, friction and contact stiffness become affecting vibrational energy dissipation. This thesis is primarily interested in medium to large vibration amplitudes where these particle relative motions are observed.
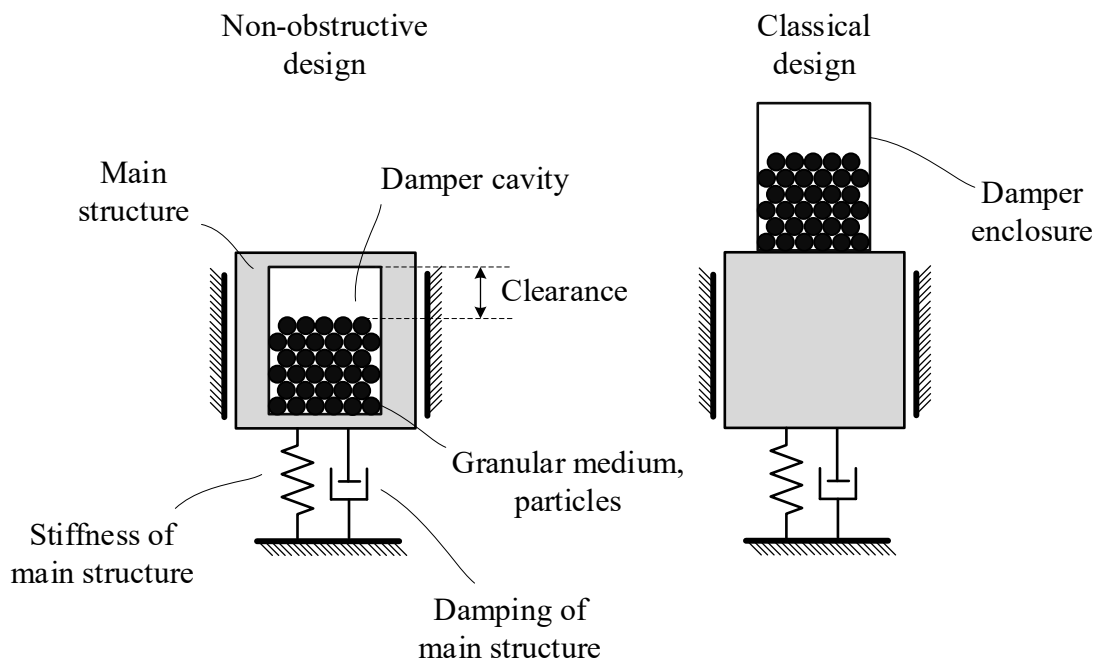
Figure 1.1: Granular damper designs implemented in a single-degree-of-freedom (SDOF) system.

Granular dampers normally consist of high-modulus, low-loss metallic particles as they dissipate the vibrational kinetic energy by friction and impact. Thus, they have a great potential for resulting in an efficient reduction in noise and vibration under severe environmental conditions. They do not need to operate at a tuned frequency as they can provide damping for a broad frequency range. They do not notably affect the host structure stiffness. They can operate for a long time requiring relatively low maintenance unlike friction dampers – need to provide appropriate fastener tightness to maintain their operations. As a result of these advantages and their potential in the continuously developing aviation

3

and space technologies, the applications and investigations of granular dampers have notably accelerated in recent years as can be seen in Figure 1.2.
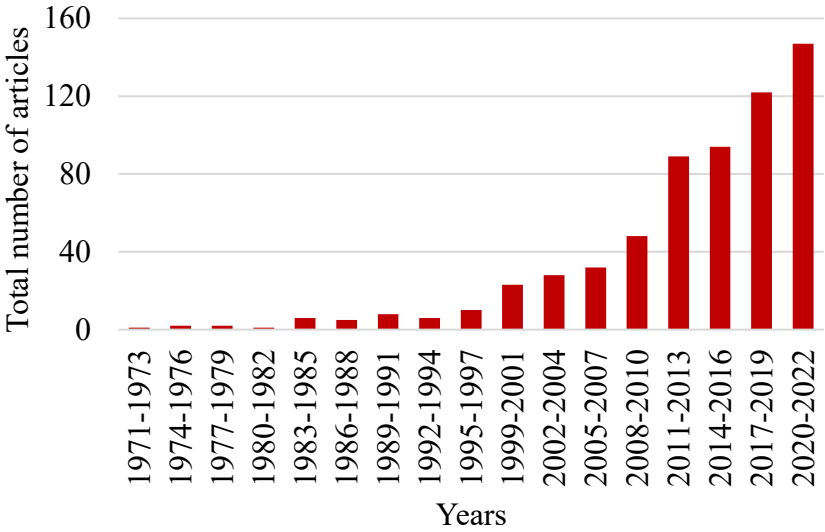
Figure 1.2: Number of published works per three years related with "granular damper/damping" or "particle damper/damping" – sourced from Scopus.

Despite their many advantages, granular dampers have not reached their potential in the field of noise and vibration control applications. Because granular energy dissipation is highly non-linear (amplitude and frequency dependent). The predictions shown in literature to obtain optimum granular damper design are inconsistent with each other. In addition, there is still a debate on how the dissipative performance of granular dampers is affected by design properties such as particle size, particle material, particle shape, particle number, particle packing and void gap (clearance). Thus, these sometimes cause the false impression that granular dampers are unpredictable in practical applications.

1.3 Thesis Aim and Objectives

This thesis focuses on the determination of fundamental granular energy dissipation mechanisms that drive the non-linear behaviour and control dissipation effectiveness in granular dampers. As a result, it aims to address the inconsistent nature of observations and conclusions presented in literature and lead to the real potential of granular dampers.

The study conducted in this thesis can be divided into two main paths as they are hinted in the Research Motivation (Section 2.7) following a broad literature review on granular dampers presented in Chapter 2.

The first one is to outline and conduct a relationship between the motional pattern of damping particles (granular phase) and their overall non-linear energy dissipation characteristic. Granular phase maps are used to show the variation of granular phases depending on vibration amplitude and frequency. The primary work here is to produce phase maps and compute corresponding dissipated energies for a broad range of excitation conditions using computer models. Based on these results, the physical particle motion insights in each motional phase are investigated in detail along with granular energy dissipation effectiveness potential of each phase. As a result, it aims to generalise the conducted relationship which would provide a great design guidance for effective granular damper operations and a valuable understanding on the effect of changes in excitation conditions on granular energy dissipation effectiveness. The findings are tested by controlled experimental studies for a wide range of excitation conditions to show the validity of relationship in real environmental conditions. As briefly, the first objective of this thesis can be summarised as:

Research Objective I.   To understand the behaviour and efficiency of the principal motional mechanisms that govern granular energy dissipation.

Secondly, most scientific granular damping studies have been conducted using spherical particles. However, particles (even hard ones with high durability) can deviate from being perfect spheres in practical applications because of plastic deformation and wear arising from excessive impact and friction interactions during vibrations. Moreover, particle shapes may be deliberately selected as non-spherical for cost and practical reasons [8,9]. Hence, the

recent granular damping literature has began accelerating upon this relatively new research field [10–12]. Still, the literature on this topic is quite insufficient, and a systematic investigation of non-spherical damping particles is desperately needed.

The second objective can therefore be written as:

Research Objective II.   To investigate the effect of particle shape on the granular energy dissipation behaviour in different motional phases and further extend the understanding of the relationship between the granular motional behaviour and energy dissipation.

It should be noted that two different sets of particles are determined for the latter objective to comply with the systematic investigation target. First, varying deviation level from a perfect sphere is considered by changing its sphericity. This is achieved by employing a range of oblate and prolate spheroids at different aspect ratios by altering principal dimensions of these particle shapes. The second set is determined to obtain the effect of varying hollow level in a damping particle. This is studied by employing a range of circular toroids at varying ratio of hole diameter to diameter of circular cross-section.

2   Granular Damping: State of the Art

2.1   Overview

This literature review has been conducted to investigate the opportunities and challenges associated with the efficient design of granular dampers for vibrational energy dissipation. Effort has been focused on work carried out to determine and understand the fundamental factors which affect non-linear granular energy dissipation behaviour.

A brief historical development of granular damping phenomena is presented in Section 2.2, including a review of its existing engineering applications for noise and vibration control to compare the advantages of granular damping with other technologies. An overview of the methods that have been used to determine the dissipated energy achieved by granular dampers is presented in Section 2.3. The main characteristic behaviours of granular energy dissipation are discussed in Section 2.4. Following this, an emerging area of research, the relationship between the motional behaviour of granular medium and granular energy dissipation effectiveness, is reviewed in Section 2.5. The effects of different damper design properties on granular energy dissipation behaviour are then shown in Section 2.6.

2.2   Development of Granular Energy Dissipation Approach

2.2.1   Impact dampers (single configuration)

An 'impact damper', which is the origin of granular dampers, typically consists of a single auxiliary mass (impactor) that can move between the end walls of a cavity inside a vibrating

7

system as depicted in Figure 2.1. Vibrational energy is dissipated via inelastic impacts between the impactor and the walls of the cavity while momentum transfer at each impact maintains the operation of damper.
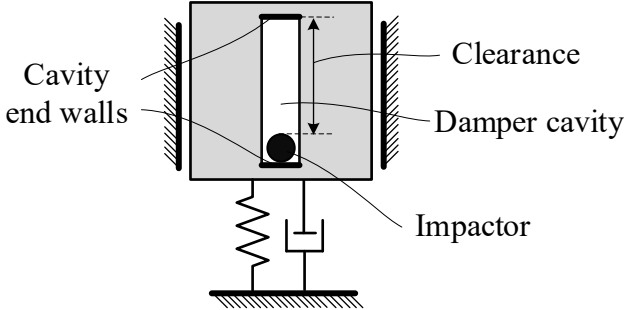
Figure 2.1: Impact damper in a SDOF system.

Despite the simple design of impact dampers, they can efficiently suppress structural vibrations [13–15]. As the impactor is typically made of metal materials, the energy dissipation effectiveness is relatively insensitive to environmental conditions when compared to the traditional vibration damping techniques [14,16]. For example, it has been shown that an impact damper design can control harmonic lateral shaft vibrations of rocket engine turbopumps in a cryogenic environment [17].

Impact dampers show significantly non-linear characteristics. They result in linear decaying in the amplitude of a system undergoing free vibrations [14] and strong amplitude-dependent damping performance in a harmonically forced vibrating system [17]. It should be noted that such behaviours do not occur in linearly damped vibrating systems [3,18].

Exact and approximate analytical solutions of the impactor motion are based on several assumptions due to the non-linearity of impact dampers [13,16,19]. These solutions and corresponding experimental studies have shown that an optimum damper is obtained if two equally spaced impacts occur in each vibration cycle in which the impactor and the walls have opposite motions (out of phase) at each impact [13,14,19]. Although this optimum condition can be met under harmonic excitation, it may not be possible if the vibrations are

non-stationary or random [20]. It has been noted that impact dampers produce low damping effect in structures if this motional condition is not provided [17].

There are several parameters that can affect the performance of impact dampers as well as the optimum motional condition. The 'mass ratio', defined as the ratio of impactor mass to main structure mass, monotonically increases the effect of damping in structures [13], and this increasing trend slows down at higher mass ratios [14]. The damper clearance is the main parameter that controls the optimum motional condition as the impactor needs to travel this distance twice in each vibration cycle for the optimum case [13,14,16]. Therefore, the optimum clearance is adjusted according to vibration displacement amplitude exposed [14]. Impact dampers can be successfully used for controlling resonant vibrations which require tuning the damper to a specific frequency similar to well-known tuned mass dampers. As impact dampers dissipate energy through inelastic impacts, the coefficient of restitution (COR, see Section 5.5.2 for more details) influences damper effectiveness [13,16,21].

Several attempts have also been made to reduce vibrations of multi-degrees-of-freedom (MDOF) structures by employing impact dampers [22–24]. These studies have concluded that properly designed impact dampers can provide efficient damping for several vibration modes of MDOF systems.

A major problem with an impact damper is intensive impacts occurred in each vibration cycle. These impacts produce high level of impulsive forces, applied to both the impactor and the walls, which may yield distortions (significant plastic deformations) on the surfaces, and so that can considerably decrease the damper effectiveness. They also generate sequential loud noises. To solve this, several studies reinforce the cavity walls with a softer material [21,24], but this can reduce the effectiveness as it alters COR and contact stiffness. Another major concern of impact dampers is that their performance strongly depends on

both mechanical properties of the impactor and enclosure (stiffness, yield strength and COR) and operating parameters (vibration amplitude and frequency). It should be also noted that impact dampers are not suitable for broadband frequency applications.

2.2.2 Multi-unit impact dampers

To reduce the negative effects of intense impacts, the 'multi-unit impact damper' configuration which involves multiple impactors and damper cavities has been developed as shown in Figure 2.2.
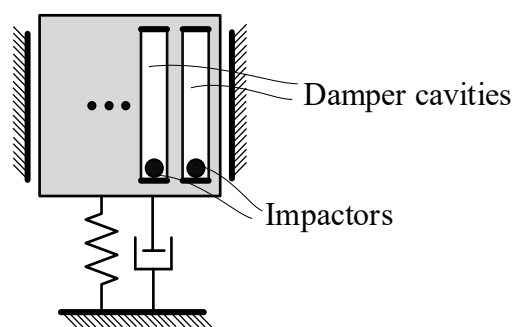
Figure 2.2: Multi-unit impact damper in a SDOF system.

It has been found that a multi-unit impact damper can provide a damping level as much as an equivalent impact damper (with the same damper mass), generating less noise [25,26].

Nevertheless, many of the unfavourable issues in impact dampers are also valid for multi-unit impact dampers such as strong dependency to loading conditions. It may also not be feasible to create multiple voids in a structure to place many impactors. However, as the published literature on multi-unit impact dampers is limited and this type of impact damper design can demonstrate a rich dynamic behaviour, it is thought that this field appears to have a potential for future investigations.

2.2.3 Bean-bag impact dampers

A 'bean-bag impact damper' comprises a resilient bag filled with relatively small particles as illustrated in Figure 2.3. It can be realised that bean-bag impact dampers are the most similar form of impact damper to granular dampers in terms of physical construction (see

Figure 1.1). In fact, it has been claimed that a granular damper is a novel derivative of bean-bag damper impact dampers [27].
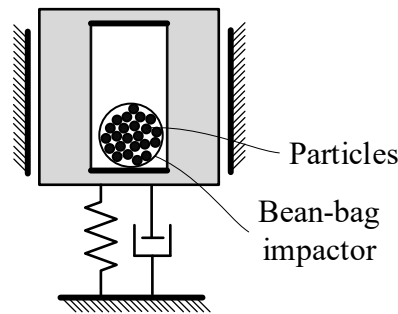
Figure 2.3: Bean-bag impact damper in a SDOF system.

Apart from reducing noise levels and excessive impact forces, bean-bag impact dampers have also been shown to be useful in attenuating vibrations for broadband frequency excitations and non-stationary vibrations [20,28]. The effectiveness of bean-bag impact dampers has been associated with the flexibility level of bean-bag impactor as it reduces the pressure of impacts and helps to distribute impact forces to particles [27].

As a result of the extraordinary physical model of bean-bag dampers, damping (or vibration reduction level) estimations are mainly based on empirical approaches [28] or threshold predictions using approximated models [27]. Also, the damper performance is highly dependent on the bag material, bag shape and bag tightness [28], which complicate the design of these dampers.

2.2.4 Granular dampers: advantages and practical applications

In order to reduce both the sensitivity of impact dampers to single impactor material properties and the adverse effects of intense impacts, a design has been developed: granular dampers [29] – where the impactor of impact dampers is replaced by many small particles as previously shown in Figure 1.1. The scientific journey of granular dampers accelerated when Panossian [4] successfully employed such dampers to reduce high-frequency

vibrations in the liquid oxygen inlet tee of a space shuttle engine. Panossian also identified the advantages of granular dampers [4,30]. For clarity, these are listed below:

- They are applied to structures in a non-obstructive way so changes in host structure stiffness and inertial properties are low.

- The effectiveness of granular dampers is relatively insensitive to working conditions and operating durations, so that they do not need extensive maintenance work.

- Granular dampers can efficiently operate under harsh environmental conditions (e.g., oily, extremely hot or cold) where viscoelastic materials, isolators and tuned mass or liquid dampers would generally fail to work.

- De-tuning problems generally encountered in tuned mass dampers or impact dampers do not significantly affect the performance of granular dampers as they can be designed to provide effective broadband energy dissipation.

- Granular dampers relatively produce less noise levels and less-intensive impacts (smaller impact forces) than any version of impact damper.

Granular dampers are deployed in a variety of industrial fields to reduce structural vibrations [31,32]. This involves the following specific applications: antenna boom [33], turbomachinery part [34], circuit board [35,36], automotive oil pan [37,38], gear transmission system [39,40], tennis racket [41], additively manufactured machine part [42], mechanical system exposing chatter vibrations [43], buildings [44], exterior panels of a launch vehicle [45] and automotive steering wheel [46], but not limited with these. Granular dampers are not only used for vibration attenuation, but in contrast to impact dampers, they can also provide noise reduction in structures. A study has shown that existing noise of a desktop banknote processing machine can be decreased to a suitable level for an office

environment by placing particles at appropriate points [47]. It has been found that granular dampers would considerably attenuate sound pressure levels inside an enclosed cavity against both acoustical [45] and mechanical [48] excitations. Many of these different engineering applications have been extensively reviewed elsewhere [30,46]. Some of granular damper designs are illustrated in Figure 2.4 to show the simple applicability of such dampers in a variety of structures.
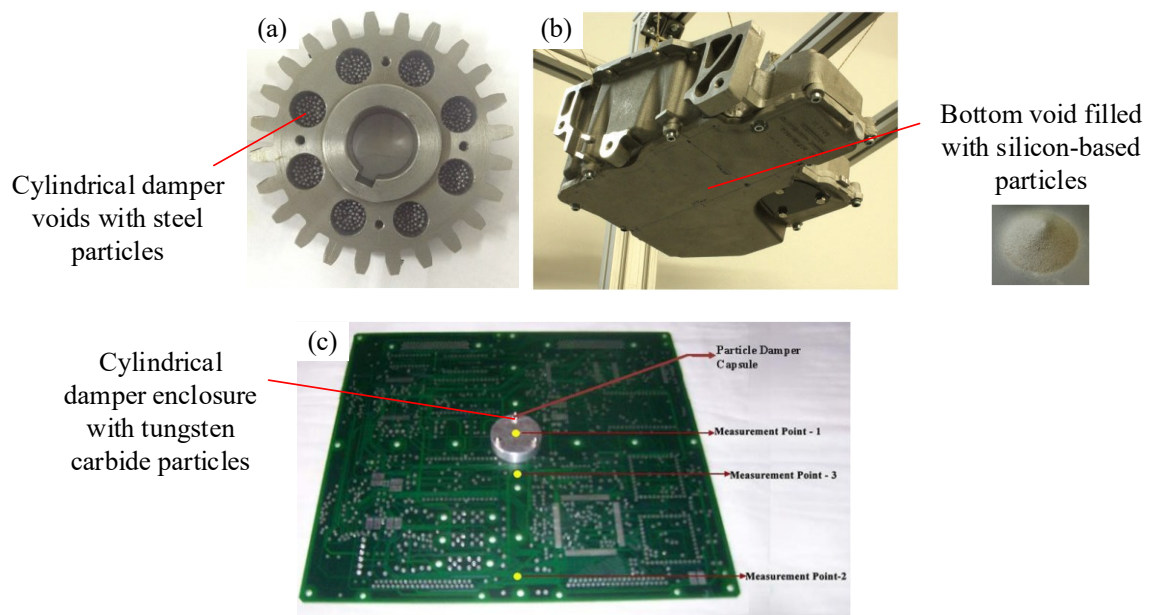
Figure 2.4: Some of the interesting granular damper practical applications: (a) gear [40], (b) automotive oil pan [37] and (c) circuit board [36].

One application area of granular dampers that has received a particular attention from researchers and engineers involves the honeycomb structures generally used in space and aircraft parts for stiffer and lightweight design. As honeycomb structures naturally have voids and also suffer from low-damping capability, granular dampers are directly integrated into these voids to enhance their damping capability [38,49,50]. Although it was considered that the employed particles would highly increase the total mass of a honeycomb structure, it was found that changes in the natural frequencies stay within a moderate range [49]. This is because particles do not behave as a lumped mass. Also, it has been shown that the

honeycomb structures enriched with particles are very robust to solve vibro-acoustic problems [38].

As it is not possible to construct a general design procedure for all these applications due to the complex nature of granular dampers [51], they remain a rich research area for vibration damping and noise attenuation applications. Addressing to the effectiveness and robustness of granular dampers for wide temperature range and harsh environments, it is thought that these dampers will particularly be the main damping method in space and aviation industries. Apart from the shown classical implementations, different granular damper integration models may be another future path of these dampers – such as the thrust granular damping system in which damping particles are placed in an enclosure to absorb vibrations through a piston movement inside damper [52], tuned particle mass damper [44,53,54] and improved granular damping by optimising particle movements [55–57] It is believed that active and semi-active control of particle movements will also be an exciting research field amongst researchers to enhance the performance of granular dampers – e.g., applying controllable pressure to granular medium for more energy dissipation than the use of loose particles [12,58].

2.3 Granular Damping Evaluation Methods

2.3.1 Experimental approaches

Most publications on granular damping involves an experimental investigation because theoretical modelling techniques for granular dampers do not adequately address the complexity of particle movements in the damper enclosure. The purposes of experimental granular damper investigations have been summarised as [31]:

- Determine granular energy dissipation behaviour to develop and improve theoretical models.

- Validate results obtained from models.

- Enhance the existing understanding of granular energy dissipation.

- Verify the findings from sensitivity analyses, and, therefore ensure efficient application in structures.

As a result, different experimental approaches have been used to measure the level of granular damping achieved. For the free vibration analysis of structures enhanced with a granular damper, the dissipated energy for each cycle is determined from the decay in amplitude of successive oscillations at the natural frequency [5,59]. For forced vibration, the traditional vibration analyses are used for both discrete and continuous systems such as direct measurement of amplitude reduction in the time domain [44,60,61], construction of the frequency response function (FRF) to obtain either a damping parameter or peak amplitude reduction at particular frequencies [8,50,62] and vibration power input methods to detect the reduction in the required power to keep the damped system in steady-state [27,63].

All these methods, however, require a host structure which means that measurement findings become specific to the investigated structure. Because of this, the main physical insights of granular dampers can be overlooked. Therefore, the most common experimental method used for characterising granular dampers is Yang's structure-independent dissipated energy measuring approach [64,65]. As it enables investigations that focus on the physics behind the granular damping phenomena, many scholars have used this experimental methodology [66–70].

2.3.2 Theoretical modelling

There is a need for reliable and cost-effective models to design granular dampers that are suitable for specific structures. Since granular dampers show non-linear characteristics and the damping particles often follow complex trajectories when vibrated, no inclusive exact

analytical approach has been proposed. Instead, several approximated analytical methods and numerical tools have been developed to simulate granular dampers.

One theoretical modelling approach is to represent a granular damper as an equivalent single impact damper for which various exact and approximate solutions already exist [44,61,71]. It has been reported that this type of modelling provides reasonably accurate estimations [61]. This modelling type does not enable particle-level investigations (individual particle motions and local dissipations in contacts) in granular dampers which is very important to simulate the real physical behaviours of granular dampers.

A similar approach models all particles as a single compacted mass, and assumes completely plastic collective collision between this collection of particles and the two end walls of damper enclosure [29]. In this way, dissipated energy is estimated for collisions under steady-state harmonic vibrations. This approximate analytical model is improved in another work by implementing variable inelasticity level in these collective collisions based on empirical data [72]. However, as can be understood, such a modelling approach is limited to the case where the granular medium collides with the two end walls during each vibration cycle. This method also does not consider the particle-level relative motions and dissipations, and it has been demonstrated that it is not applicable for the use of small damping particles [73]. However, as this method offers simple and fast solution without considering individual particle movements, the author of the thesis believes that such theoretical models would be enlarged, and a general theoretical approach based on this method can be developed by providing a particular solution for each different motional pattern of granular medium.

Another approximate analytical method is to model a granular damper as a viscous medium utilising the multi-phase flow theory where the particles are assumed as gas particles with

low Reynold's number [74,75]. Although this approach ensures low computational complexity and has good correlation with experimental results for specific excitation conditions [74,75], a particle-level investigation is again not possible and effectively working parameter range of this method is scarce as there are a number of assumptions. However, as this type of analytical modelling would be a valuable tool to estimate the damping level achieved by a granular damper, it is also believed by the author that this method can be further improved by future researches to design granular dampers.

Few attempts have been carried out to characterise non-linear granular dampers as viscous dampers by using curve-fitting tools on experimental results [8,70,76], and some authors have implemented such models into the Finite Element Method (FEM) to allow low-cost dynamic analysis of structures with granular dampers [62,70]. It should be noted that such a modelling approach is specific to the damper tested in experiments.

In addition, several dissipated energy estimation methods have been proposed in literature for granular dampers. These methods mainly investigate the predictions of continuous engineering structures enriched with granular dampers by utilising modal kinetic energy approach [55], modal strain and kinetic energies [34], maximal energy dissipation by individual damping mechanisms [27]. Recently, authors has started to develop analytical formulas to estimate dissipated energy for some specific motional patterns of damping particles [77–82] – showing a great potential for future developments in granular damper designs.

As briefly discussed above, there is no inclusive theoretical approach that accurately represents the dynamic behaviour of a granular medium [83]. Therefore, numerical methods are typically used to simulate granular medium for comprehensive and reliable simulations [84]. The molecular dynamic simulation method, where each particle of granular medium is

considered, is the most widely used approach for this task. There are two different methods: the event-driven [83] and the Discrete Element Method (DEM) [85]. The event-driven method is very useful when the number of inter-particle impacts is low and the typical duration of a contact is significantly shorter than the mean time between successive impacts of a particle since the algorithm is stimulated by impact events [83].

On the other hand, DEM is an inclusive numerical tool which provides numerous advantages such as applying a wide range of contact models at particle-level and can operate reliably with either hard or soft particle types as irrespective of contact durations. As a result, it has been found that DEM simulations of granular dampers show remarkable compatibility with the experimental results [86–88].

In addition to these numerical methods, for more complex engineering applications, some coupled simulation methods with DEM have recently been employing for granular damper designs such as DEM-the multi body dynamics [39] and DEM-FEM [89] where the total force and moment generated by damping particles are transferred to FEM from DEM to calculate structural response and the motional information at the damper location obtained from the structural response is transferred to DEM from FEM at each solution time step. It should be noted that this type of methods generally requires a large computational effort.

2.4 Dissipative Characteristics of Granular Dampers

2.4.1 Fundamental granular energy dissipation sources

Granular energy dissipation can be described considering two main operations:

i) the input vibrational kinetic energy is transmitted to the particles through momentum exchanges as the particles and the vibrated damper enclosure interact,

ii) this energy is dissipated through interactions between particles and between the particles and the enclosure.

For clarity, the energy dissipated by a granular damper can be formulated as:

$$E_{\text{dissipated}} = \left(E_{\text{dissipated}}\right)_{\text{PS}} + \left(E_{\text{dissipated}}\right)_{\text{PP}} + \left(E_{\text{dissipated}}\right)_{\text{other sources}} \tag{2.1}$$

where $(E_{\text{dissipated}})_{\text{PS}}$ stands for the total energy dissipated by all the contacts between the particles and the enclosure walls and $(E_{\text{dissipated}})_{\text{PP}}$ represents the total energy dissipated by the inter-particle interactions.

The interactions between the particles and the enclosure walls are the way in which the energy flows from the host structure (as the enclosure is rigidly connected to the host structure) to the granular medium. They are essential for the operation of granular energy dissipation as they provide energy transmission to the granular medium [90]. It has been demonstrated in a recent study that inter-particle interactions are responsible for the most of the energy dissipated by granular dampers [59], i.e., $(E_{\text{dissipated}})_{\text{PP}} > (E_{\text{dissipated}})_{\text{PS}}$.

Energy dissipation in both interaction types (i.e., the particle-enclosure surface and the inter-particle) mostly results from friction and inelastic impact. Therefore, supposing that there is no other energy dissipation source such as air viscosity, Equation (2.1) can be re-written explicitly showing the frictional and impact dissipation components:

$$E_{\text{dissipated}} \approx \underbrace{\left(E_{\text{dissipated}}\right)_{\text{PS}}^{\text{friction}} + \left(E_{\text{dissipated}}\right)_{\text{PP}}^{\text{friction}}}_{\left(E_{\text{dissipated}}\right)^{\text{friction}}} + \underbrace{\left(E_{\text{dissipated}}\right)_{\text{PS}}^{\text{impact}} + \left(E_{\text{dissipated}}\right)_{\text{PP}}^{\text{impact}}}_{\left(E_{\text{dissipated}}\right)^{\text{impact}}} \tag{2.2}$$

Even though some theoretical studies have neglected one of these sources (friction) [72,91], it has been shown that the existence of both sources is substantially important for realistic modelling as granular dampers clearly exhibit the characteristics of both frictional and impact losses [27,92]. The role of these dissipation sources changes depending on vibrational conditions and contact properties [5,67,90]. It has been noted elsewhere [30] that exploring

the insights of these two dissipation sources in both micro-scale (particle-level) and macro-scale (damper-level) has an importance for accurate granular damper models.

Typically, the dominant dissipation source (especially for particles with high elastic modulus) is friction for granular dampers [8,55]. It has been claimed that friction remains dominant as long as the vibration acceleration amplitudes are smaller than $400g$ where g is the gravitational acceleration [5] while its importance can differ depending on the vibration amplitude [67]. There is a consensus among the authors that higher volume fill ratio leads more energy dissipation through frictional interactions within the granular medium [5,88,93]. The importance of frictional dissipation becomes very high when the particle size is small [90]. It subsequently decreases with increasing particle size, since larger particles result in raising impact forces [90].

In the view of all studies that have been considered above, it can be realised that the trade-off between the mentioned granular energy dissipation sources is a subject of very few studies. In fact, most of the existing literature on this topic has dealt with only free transient vibrations. As a result, these granular dissipation sources are neither well understood nor completely explored. Thus, it is believed that further attention to identify any relationship between the importance of dissipation sources and the energy dissipation behaviour of granular medium would contribute the existing granular damper literature and help to improve granular damper designs.

2.4.2   Granular damping in free vibration

In the literature, free vibration analysis is one of the methods used to explore granular energy dissipation and to measure the effectiveness of granular dampers. It is typically carried out by giving an initial perturbation to a structure (such as a beam) as shown in Figure 2.5.

As can be seen in Figure 2.6, while the vibrations decay exponentially in the case without particles due to the existence of viscous damping in the host structure, they reduce linearly when the granular damper is attached, particularly at high amplitude and then exponentially. The linear decay implies that the vibrational energy is dissipated within a finite time for high amplitudes [91,92], which is a great superiority of granular dampers when comparing with the other traditional viscous-based type dampers.
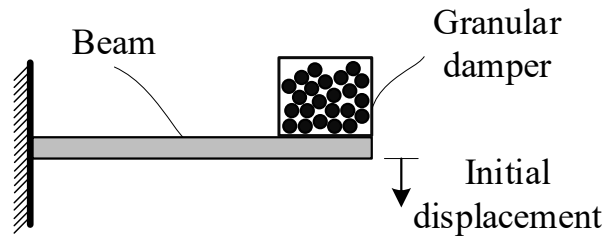
Figure 2.5: A beam with a granular damper on the tip subjected to free vibration due to initial displacement.
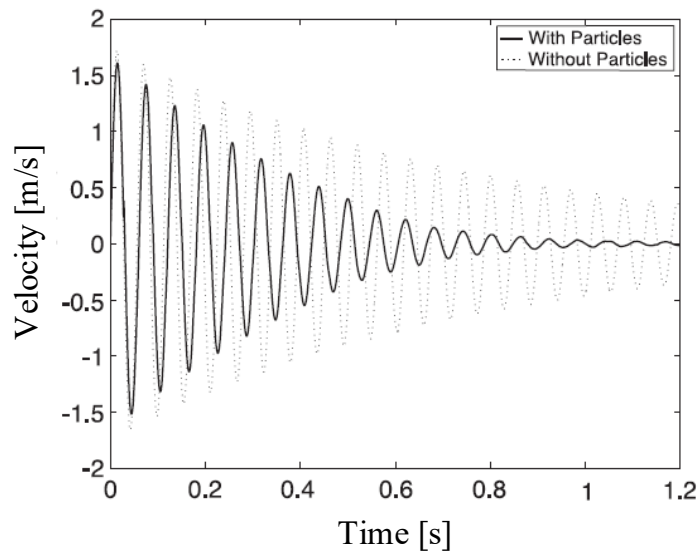
Figure 2.6: Typical behaviour of a granular damper on a beam in free vibration time response [5].

In order to show the amplitude-dependent nonlinear behaviour of granular dampers and measure the damper effectiveness, the 'specific damping capacity' is generally employed for free vibration analyses:

$$\psi_{\text{granular}} = \tilde{E}_{\text{dissipated}} / E_{\text{max}} \tag{2.3}$$

where $\tilde{E}_{\text{dissipated}}$ is the energy dissipated over one vibration cycle which can be estimated using the velocity amplitudes of subsequent peaks in the vibration signal; and E_{max} is the maximum kinetic energy of system that can be calculated using the initial velocity at the start of each cycle and the total mass (i.e., mass of particles and effective mass of host structure). The specific damping capacity of the same study demonstrated in Figure 2.6 is given in Figure 2.7 where the non-dimensional amplitude is typically used in literature to represent the vibration amplitude in granular damping results and defined as:

$$\Gamma = \text{Vibration acceleration amplitude} / \text{Gravitational acceleration} \qquad (2.4)$$
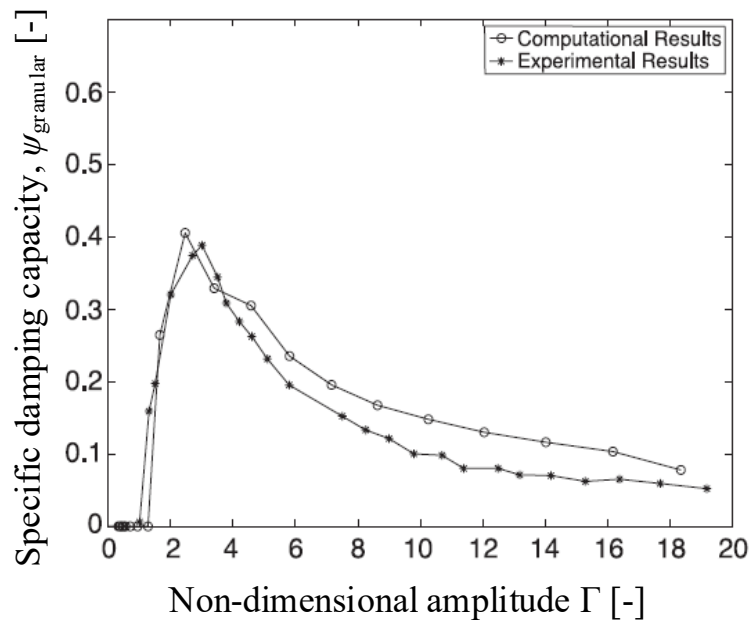
Figure 2.7: Typical amplitude-dependent damping characteristic of granular dampers under free vibration [5].

As it can be seen in Figure 2.7, granular dampers exhibit an unambiguous vibration amplitude dependency, which means that they are highly non-linear [5,59,72,74]. It can be seen in Figure 2.7 that there are three different granular damping regions in free vibration that depend on amplitude:

i. Damping is rather low at the beginning of the free transient vibration (note that the vibration amplitude decreases as the time increases), and while Γ decreases damping increases up to a maximal point at a particular amplitude, $\Gamma = \Gamma_{peak,\ free\ vibration}$.

ii. Damping suddenly drops between $\Gamma = \Gamma_{peak,\ free\ vibration}$ and $\Gamma \approx 1$.

iii. For $\Gamma < 1$, the damping is negligible.

It has been noticed that these different dissipative regimes are somewhat related with the change in the dynamic motional pattern of damping particles at different amplitudes of free vibration [5,94].

2.4.3 Granular damping in forced vibration

As there is at least one external excitation source for most of the vibrational problems, it is generally more useful to investigate the behaviour of granular dampers in forced vibration. As shown in Figure 2.8, forced vibration of granular dampers can be investigated in a structure by considering generally a single natural mode of structure for simplicity or as free of structure (as also discussed in Section 2.3).
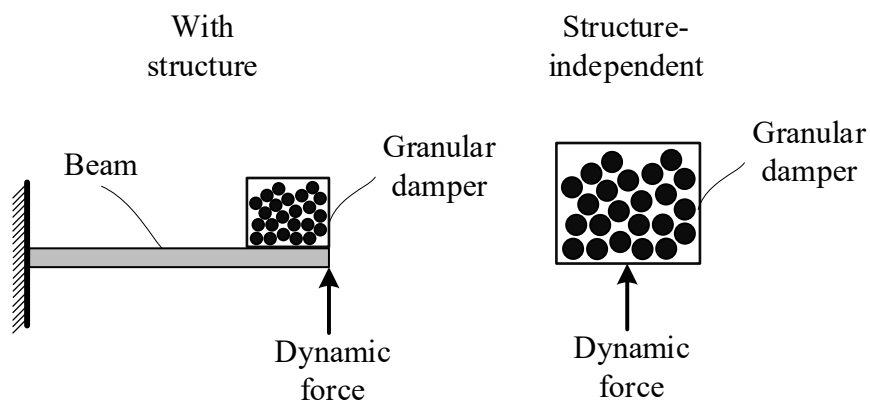
Figure 2.8: Typical granular damper investigation types under a dynamic forcing.

Granular dampers can exhibit vibration damping and noise attenuation for a wide range of excitation frequency [61,71,95]. However, it does not mean that granular dampers are

completely insensitive to frequency. In fact, this can be clearly seen in the results of a study presented Figure 2.9. Here, the loss factor η_{loss} is computed as:

$$\eta_{loss} = \tilde{E}_{dissipated} / 2\pi E_{max} \tag{2.5}$$

where the authors have measured the energy dissipated over a cycle ($\tilde{E}_{dissipated}$) and the maximum kinetic energy stored in a cycle (E_{max}) from the experiments on a structure-independent damper configuration [70]. As shown in Figure 2.9, the granular damping level is maximised at a particular frequency, and becomes relatively insensitive to frequency at high frequencies.
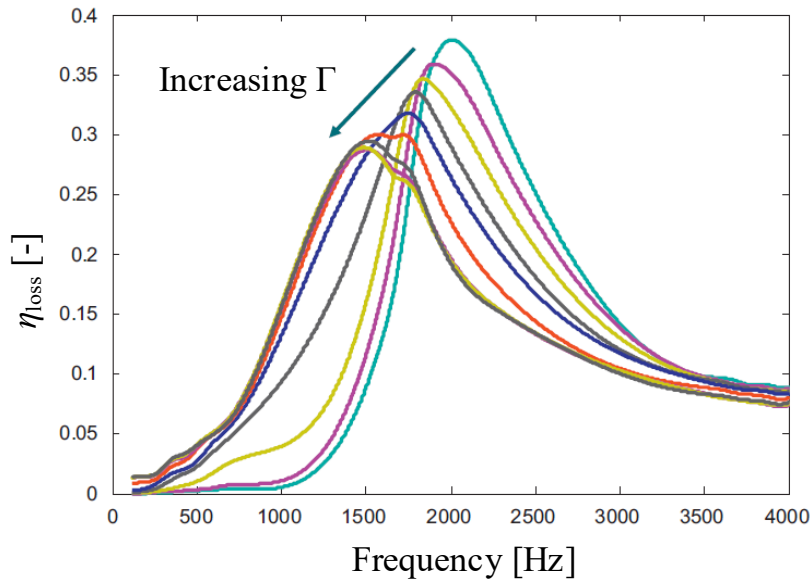
Figure 2.9: Typical granular damping under harmonic excitation [70].

As can be observed from Figure 2.9, granular dampers produce amplitude-dependent non-linear characteristic in forced vibration as in the free vibration case. This high non-linearity can also be seen in Figure 2.10 where a granular damper attached to a SDOF structure is investigated.
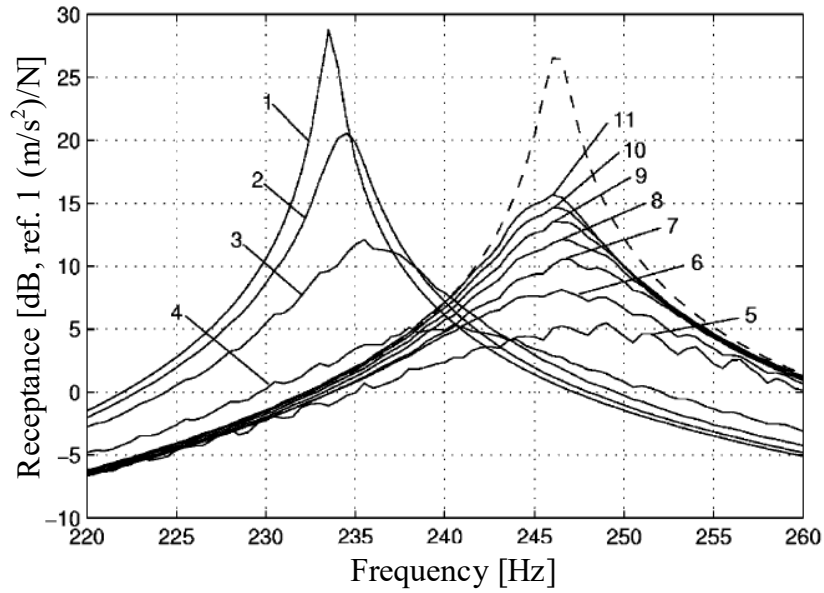
Figure 2.10: Typical FRFs around a natural mode of a structure enriched with a granular damper [8]: dash line is for the original structure response, no. 1 ($\Gamma = 0.1$) to no. 11 ($\Gamma = 40$) indicates increasing amplitude.

As shown in this plot and explained in the reference study [8], granular dampers decrease the system natural frequency at low vibration amplitudes as they behave as solid mass attached to the structure. As the amplitude increases, the particles start to move (activation), and, accordingly the damping level provided to the structure significantly improves. With further increase in the amplitude, the damping level begins to decrease and the natural frequency gradually converges to the frequency of the system with no particles.

2.5   Dynamic Motional Behaviours of Granular Medium

2.5.1   An overview on principal granular motions

When a granular medium is subjected to vibration, the particles can follow various trajectories, change position, lose contacts, and create new contacts. These operations are the main particle behaviours that result in energy dissipation in a granular medium. Therefore, it is essential to understand the principles of granular motion [9,32].

If the granular medium is exposed to periodic vibrations (particularly harmonic excitation), the particles generally exhibit similar motional behaviours cycle-to-cycle. As a result, all

particles together generate an approximately-periodic motional behaviour [96] – referred as a 'granular motional phase'. The exhibited granular motional phase changes depending on the vibration amplitude and frequency [97,98]. Many granular motional phases have been observed and named under different vibrational conditions in the literature. In fact, there are still some studies which explore novel granular phases [99]. It should be noted that not all discovered phases are observed in every study as the occurrence of granular phases also depends on the configurations of particles and enclosure [69].

If the granular medium motion is linked with the granular energy dissipation, 5 different principal granular motional phases can be identified. They are explicitly described below – for comprehensive visual guidance for motional behaviours see the simulation printouts and the representative motion sketches presented in Chapter 6.

Solid-like phase:

For small vibration amplitudes, i.e., $\Gamma < \Gamma_{fluidisation}$ where typically $\Gamma_{fluidisation} \approx 1$ (equal to gravitational acceleration) and can change depending on frequency, the 'solid-like' (sometimes called as 'glass-like') phase is observed. In this phase, there is principally no relative motion between the enclosure and the granular medium which resembles a solid mass attached to the bottom surface of the enclosure throughout the vibration cycle. Because, the dynamic forces that are generated are not sufficiently large to overcome the sum of inter-particle static forces (e.g., friction) and gravitational loads under such low-amplitude vibrations. Note that there are various studies to determine $\Gamma_{fluidisation}$ [9,100–102] as it indicates the threshold of particle activation in the granular medium.

Fluidisation-based phases:

When the vibration amplitude exceeds the critical activation threshold, i.e., $\Gamma > \Gamma_{fluidisation}$, and there is a sufficient clearance between the upper layer of particles and the enclosure top,

the particles partially overcome the force which bonds them together in the solid-like phase, and the granular medium produces the fluidisation-based phases. While the definition of granular 'fluidisation' motion can be different in the literature, it is described here as: the particles have relative motions with respect to each other within a vibration cycle, but they preserve their overall position and existing contacts at the end of each cycle. The particular type of fluidisation-based phase varies depending on the fraction of fluidisation motion initiated into the granular medium. There have been different fluidisation-based phases named in the literature [44,100,103–105].

Convection-based phases:

If the particles exchange their overall positions and generate new contacts while breaking up their previous contacts at each cycle apart from their relative motions, the motion is called as the granular 'convection'. When the convective particles dominate the granular medium over the fluidised particles (at amplitudes larger than a threshold amplitude, i.e., $\Gamma > \Gamma_{convection}$), the granular motional phase turns into a convection-based phase [101,102,106]. As the convective particles travel through the granular medium, the particular type of convection-based phase is typically identified depending on the dominating particle motional pattern [69,103,107,108]. Two of them are demonstrated in Figure 2.11. The granular 'Leidenfrost effect' phase indicates that a relatively dense packed particle cluster is entirely lifted off from the enclosure bottom and supported by a small number of fast-moving particles that impacts with the enclosure bottom at each vibration cycle [108]. Even though the number of particle layers in the cluster can vary during vibrations, it approximately maintains its average height inside the enclosure [69]. Note that this phase is analogous to its original definition in thermodynamics, in which a water droplet over a plate is elevated on its own vaporized layer if the plate temperature is sufficiently high [109]. As shown in

Figure 2.11, the convection rolls phase is defined by upward and downward motions of more mobilised small particle clusters.

Leidenfrost effect

Convection rolls
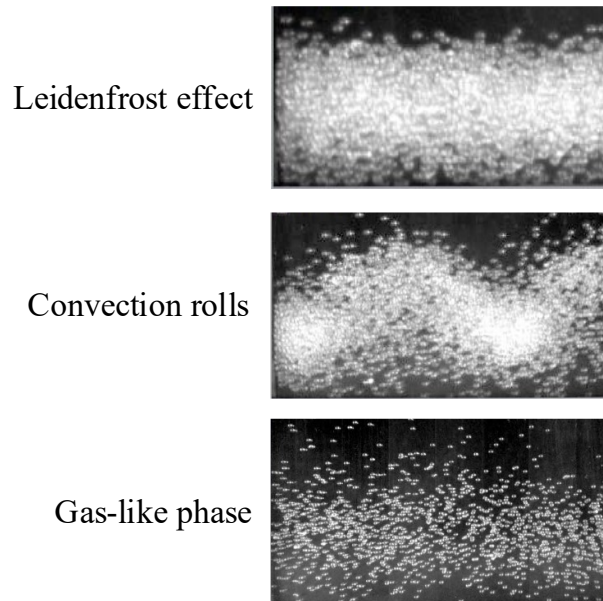
Gas-like phase

Figure 2.11: Examples of granular motional phases [103].

Gas-like phase:

When the majority of particles entirely break up any static forces applied and float inside the enclosure without generating contacts, the granular motional behaviour is named as the granular 'gas-like' phase. This phase is demonstrated in Figure 2.11. In this phase, the particles can rarely impact with each other and the enclosure walls. This granular phase is observed at larger amplitudes than an amplitude i.e., $\Gamma > \Gamma_{gas-like}$.

Bouncing bed phase:

As can be realised, the solid-like phase, the fluidisation-based phases, the convection-based phases and the gas-like phase can be considered as the equivalent granular analogy of solid-fluid-convection-gas phase process path in thermodynamics. As a distinctive granular motional behaviour from these phases, the 'bouncing bed' (sometimes called as 'collect-and-collide') phase can be observed in the granular medium if the vibration displacement amplitude is sufficiently large. In this phase, the granular medium forms a compact structure

and collectively collides with the both enclosure end walls during a vibration cycle [89,110–112]. As in single particle case (i.e., impact dampers), the collective collisions periodically occur between the granular medium and the enclosure. It should be noted that whilst the other onset boundary amplitudes, $\Gamma_{\text{fluidisation}}$, $\Gamma_{\text{convection}}$ and $\Gamma_{\text{gas-like}}$ are generally determined by observations of granular medium, the onset amplitude of bouncing bed phase, $\Gamma_{\text{bouncing bed}}$ can be analytically calculated by considering the travel time of the granular medium between the enclosure ends [91].

Some other special formations can also occur in the granular medium such as the 'undulations' where the standing wave patterns are observed perpendicular to the enclosure side walls [69]. However, as these formations are encountered for very particular sets of physical properties (e.g., granular packing, enclosure geometry and excitation conditions) [98,103,106,113–115], no detailed review has been carried out on these formations in this thesis.

2.5.2   Mapping of granular phases, and effect of gravity

As the observed granular motional phase depends on vibration amplitude and frequency, a map which shows the variation of motional phases as a function of vibrational condition is a useful tool in granular-related studies [89,99,103]. General variation of the classified motional phases is sketched in Figure 2.12. Here, the vertical and the horizontal cases means that the gravity direction is parallel and perpendicular to the vibration direction, respectively. The approximate onset amplitudes are also identified in these sketches to show the relations between the thresholds.

As demonstrated in Figure 2.12, the number of observed motional phases changes depending on the existence of gravity. The granular medium produces only two phases in case of no

gravity applied, while it can exhibit all the mentioned principal phases under the effect of gravity.

Although the principal motional behaviours are commonly observed in the vertical and horizontal cases, there are some motional differences because of the difference in the gravity-to-vibration directional orientation. The type of fluidisation-based and convection-based phases may differ, as the trajectories of particles are affected by the gravity-to-vibration directional orientation. The other main difference between these two orientation cases is the onset amplitudes. For example, at between 3 Hz and 15 Hz, it has been found that $1 < \Gamma_{\text{fluidisation}} < 1.2$ for the vertical case whereas $0.8 < \Gamma_{\text{fluidisation}} < 0.9$ for the horizontal case [116].

No gravity case

Bouncing-bed phase

$\Gamma_{\text{bouncing bed}}$

Gas-like phase

Γ [-]

Frequency [Hz]

Vertical (or Horizontal) case

Bouncing-bed phase

Gas-like phase

$\Gamma_{\text{gas-like}}$

$\Gamma_{\text{bouncing bed}}$

Convection-based phases

Γ [-]

$\Gamma_{\text{convection}}$

Fluidisation-based phases

Solid-like phase

$\Gamma_{\text{fluidisation}}$

Frequency [Hz]
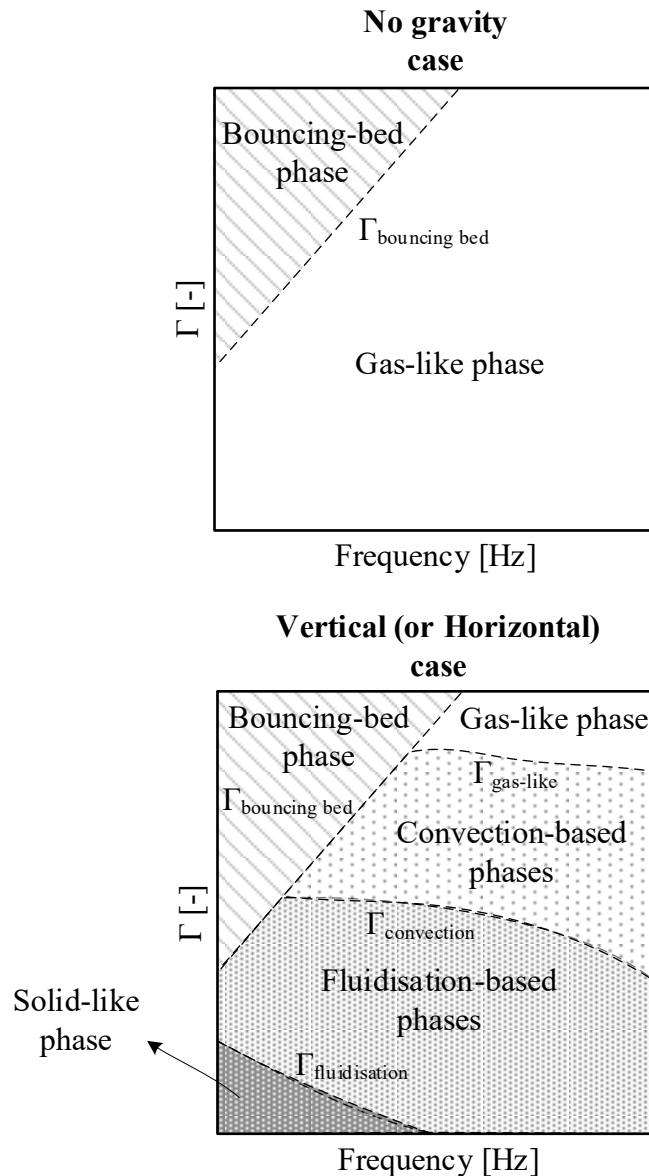
Figure 2.12: General views of phase maps.

2.5.3 Influence of granular phase on granular damping

The collective dynamic motional behaviour of particles (granular phase) is a major factor that affects granular energy` dissipation. Although the effects of granular motional behaviours have been roughly noticed in prior studies [29], it has recently been understood that the operating motional phase is the most important criteria when optimising a granular damper [32,69,117]. Motional phases are mainly stimulated by the excitation condition (amplitude and frequency) which is significantly associated with non-linear granular damping characteristics. As a result, more recent literature has begun focusing on

determining the efficient and inefficient granular phases to improve granular energy dissipation in structures.

As the particles follow nearly the exact trajectory of enclosure without any relative motion in the solid-like phase, granular energy dissipation in this phase has been found insignificant [8,55,69,112,118]. The gas-like phase exhibits no notable granular energy dissipation as the particles float randomly inside the enclosure and rarely produce dissipative contacts with each other in this phase [57,77,91,110].

It has been reported that the highest effectiveness of granular energy dissipation can be accomplished at the transition region between the solid-like phase and a fully convective phase [9,12,56,58,119,120]. These studies have explained the reason of this observation by stating that the particles slip more intensively (larger friction force and larger relative velocity between the particles) in this transition region.

On the other hand, some works have claimed that the Leidenfrost effect phase is the optimum motional behaviour [54,69,99,112,118,121,122], whilst the buoyancy convection has been also found as the optimal operating granular phase in a study [111]. Some other studies have indicated that the granular energy dissipation effectiveness is maximised at the onset of the bouncing bed phase [5,57,72,73,77,89,91,92,110]. As a result, it has been noticed that there is still no absolute agreement on the optimum motional phase of a granular medium. This can lead to inefficient designs of granular damping.

2.6 Primary Damper Parameters Affecting Energy Dissipation

2.6.1 Review approach

A large volume of the granular damper literature has focused on investigating the effects of damper design properties on energy dissipation by conducting a series of numerical or/and experimental analyses [67,95,120]. However, because of the significant non-linearities,

studies have often reached very different conclusions. Also, as the most of studies have not considered the motional behaviour of granular medium while performing these analyses, the results can be specific to a particular operating motional condition. Hence, damper parameters that may have an effect on granular energy dissipation behaviour are reviewed in this section along with the motional analogy (where possible) to clarify these effects and detect any lack of understanding in literature.

2.6.2   Particle mass – in terms of material density

It has been found that even if a small mass of particles is used, significant damping levels can be obtained from granular dampers – e.g., 6% of the host structure mass can produce $\psi_{granular}$ = 50% [72]. This shows that granular dampers can offer a mass-efficient damping application for structures.

A number of works has studied the effect of total particle mass on granular damping [45,123]. It should be noted that although some have changed total particle volume to alter particle mass [124], the studies, which have changed particle density, are considered here in order to present solely the effect of particle mass without changing the damper clearance.

It has been shown that higher particle density indicates more attenuation in vibration amplitudes of a structure [61,86,94,120]. However, this positive effect slows down as the mass ratio of the particles to the host structure ($\mu_{granular}$) increases. Some studies [72,73] indeed have reported that it is proportional with the particle mass ratio by the factor of $\mu_{granular}$ / $(1 + \mu_{granular})^2$. Also, if the particle mass ratio is increased much, the structure mode that needs to be controlled shifts to lower frequencies as effective modal mass grows [60].

2.6.3   Dissipative and elastic properties of individual contacts

Even though the coefficient of restitution (COR) and the coefficient of friction (COF) are known as the contact properties directly related with granular energy dissipation, the

influence of these properties has been found to be limited [39,59,66,67,125]. Nevertheless, several studies have investigated the effects of relatively major changes in COR and COF on granular dissipative behaviours for some particular conditions [94,95].

A work has reported that higher COR ensures efficient granular energy dissipation for a wider range of excitation levels [120]. Another study has found that COR values smaller than 0.9 lead to increase the contribution of impact dissipation source in overall energy dissipation [67]. It should be also noted that increasing COR induces a reduction in overall energy dissipation in the gas-like phase as the most of dissipated energy arises from inelastic impacts in this phase [125].

Although the majority of findings suggests that changes in COF do not notably affect energy dissipation [94,95], it has been claimed by others that high COF values may be detrimental for large clearances [59,120].

The effects of elastic modulus have generally been found very small on granular energy dissipation [38,120]. Softer particles (lower elastic modulus) which have high material damping can exhibit efficient granular energy dissipation at high frequencies and low vibration amplitudes [62,76,126]. However, it should be noted that the dissipation performance of granular dampers utilising such materials is not better for $\Gamma > \Gamma_{\text{fluidisation}}$ [73]. As a result, even though the implementations of low-modulus, high-loss particles reduce impact noises and increases damping at low vibration amplitudes, traditional high-modulus, low-loss (hard) particle materials are more suitable for both larger vibration amplitudes and harsh environmental conditions. Nevertheless; for vibration amplitudes $\Gamma \ll \Gamma_{\text{fluidisation}}$, in which the granular medium demonstrates the solid-like phase, soft particle materials (e.g., viscoelastic) enhance granular damping as overall energy dissipation would only arise from particle material in this phase [6,7,66,76,119,126–131]. This also shows that granular

dampers can be efficiently utilised even in the solid-like phase where the granular damper actually does not operate.

Despite all these studies, the effects of COR, COF and elasticity on granular energy dissipation change depending on the operating granular motional phase. Thus, it is believed that they need granular motional phase-specific analyses to clarify.

2.6.4 Particle size and total number of particles

If the mass of particles is a design criterion (which is the case in most of engineering applications), particle size and total number of particles are dependent variables. For instance; when the particle size of a granular damper is increased, the total number of particles decreases accordingly to provide the same total design mass. Also, in the controlled studies which explore the effect of particle size (or number of particles), it is important to keep total mass of particles as the same to eliminate the effects of other damper parameters.

For very low numbers of particles, granular energy dissipation can slightly decrease as the particles may not touch to each other and float freely [73,86,124] However, it has been noticed that the number of particles (sometime expressed as particle size) does not affect granular energy dissipation if there are a few particle layers in the damper enclosure [35,125].

Even though it is rare for the effect of particle size (or number of particles), there are also some contradictive conclusions amongst researchers as each conducted study has been interested in a particular excitation condition which generates a specific motional phase in the granular medium. For example, one study has suggested that larger particles can be more successful in suppressing low vibration amplitudes (possibly the solid-like phase) [123]. On the other hand, it has generally been agreed in the literature that smaller particles (or larger number of particles) generally ensure both less sensitivity of damper designs to damper

parameters [60,72,73,120,125] and extending the effective working excitation range of granular dampers [124].

2.6.5 Damper enclosure geometry

Damper enclosure geometry can affect the relative ratio of static and dynamic pressures (by changing the particle bed depth) and the clearance (by changing the packing properties of particles). The enclosure geometry also affects the directions of particles after enclosure-particle impacts. As they can affect the motional conditions of particles, the importance of enclosure geometry should be considered along with the dynamic motional phase of particles. As there are only very few framework studies that investigate the geometric properties of the enclosure [70,132], there is no clear conclusion and this field still needs more comprehensive works considering the operating motional phase of particles.

Nevertheless, although rectangular shaped and any other type of damper enclosures have been used in several previous studies, cylindrical shaped enclosures are most commonly employed for the granular dampers vibrated axially. It is because cylindrical enclosures can exhibit better performance rather than rectangular ones by means of reduction in vibration amplitudes at the same vibrational conditions [95]. This is probably resulted from which the boundaries of cylindrical enclosures can have more particle contacts owing to the lack of sharp corners.

2.6.6 Volume fill ratio – in terms of damper enclosure size

Volume fill ratio is defined as the ratio of the total volume of all the particles to the internal volume of the enclosure. This can be simply arranged by changing the enclosure volume to keep the mass of particles and the number of particles the same. As this is directly related with the clearance distance in a granular medium, it is one of the most important damper design parameters which affect the granular motional phase, and therefore the granular energy dissipation.

36

However, as the most of studies on volume fill ratio have not considered the operating motional phase of granular dampers, there is no consensus on the effect of volume fill ratio on granular energy dissipation. For example, while increasing clearance (or decreasing volume fill ratio) has been found to improve the effectiveness of granular dampers in several studies [72,73,92,93,123] there are others which show that clearance has an optimum value in terms of dissipation effectiveness [29,91,94,120,124]. All these different outcomes can be related to the fact that change in clearance can alter the observed motional phase even if the excitation remains the same [103].

2.6.7 Particle shape

Conventional hard (high elastic modulus) spherical particles used in granular dampers ensure efficient working under severe environmental conditions for a long period of time. However, over time their shape may deviate from a perfect sphere because of plastic deformation and material loss. Manufacturing tolerances can also result in non-spherical particles. In addition, non-spherical particles may be deliberately employed for either cost reasons or to address practical design limitations such as particle packing in small voids. Furthermore, it has been determined in experimental studies that particle shape can change the effective mechanical properties of a granular medium (e.g., effective elastic modulus or stiffness against compression, effective elastic-plastic force-deformation behaviour, effective yielding stress, porosity in granular medium) [133–135]. This showed that particle shape can affect granular energy dissipation.

In one of the pioneering studies on granular damping with non-spherical particles, the effect of triangular, square and hexagonal particles was examined using two-dimensional DEM simulations, and it was claimed that non-spherical particles do not affect granular energy dissipation [11]. However, it should be noted that it has only considered the vibrational conditions at which the granular medium never touches the top of enclosure. Another study

has investigated the granular dissipative behaviours of non-spherical particles using three-dimensional DEM simulations under no gravity [10]. The particles investigated had unusual geometric shapes formed side-by-side fixing spheres at their surfaces (no overlapping between fixed spheres). They have concluded that whilst the particle shape does not notably matter in the bouncing bed phase, perfect spherical particles provide higher levels of granular energy dissipation than non-spherical ones in the gas-like phase. In another study which experimentally investigates active controllability of optimum granular motional activities to accomplish higher damping for structures, more realistic non-spherical particle shapes (cylindrical and cubic) have been studied [12,58]. It has been reported that cylindrical and cubic particles exhibit higher effectiveness over perfect spheres.

Together the findings of these studies confirm that there is a valuable research field about the non-spherical particle usage in granular dampers, and therefore the interest has been fast growing. However, the literature focused on non-spherical particles is still very scarce, and much uncertainty and questionable results are noticed in the literature. In addition, the literature has generally ignored the fact that the effect of particle shape can change depending on the operating motional phase of granular dampers. Thus, these issues need to be addressed by systematic studies supported by experimental observations.

2.7 Research Questions

An overview of granular damping literature has been presented in this chapter. As a result, the gaps in the current knowledge have been determined and the key research questions that lead to the aims of this thesis have been identified.

The problems and uncertainties related to the efficient design of granular damper and their cost-effective theoretical modelling are associated with the non-linearity in dissipating vibrational energy. This non-linear granular energy dissipation is found to be a result of the

existence of various dynamic motional patterns (granular phases) that the granular medium displays depending on the amplitude and frequency of the excitation. This suggests that there is a relationship between the energy dissipation and the operating motional phase for these dampers. However, there is no agreement on the most efficient granular phase in the literature as each piece of work has indicated a different optimum condition. Therefore, the following research question is identified.

I. What are the fundamental motional phases and mechanisms that drive efficient energy dissipation in granular dampers?

The other problem is to determine the main damper parameters that control the occurrence of a particular granular motional phase, and thus the effectiveness of granular energy dissipation. The effects of some of these parameters have already been discussed in the literature.

It has been found that the material density, COR, COF and number of particles have a minor effect whereas enclosure shape, volume fill ratio and particle shape are significant.

The effect of volume fill ratio can be obtained by investigating a sensitivity analysis of the phase map to the volume fill ratio as in the reference study [103].

While some works have been done on the effect of enclosure shape, it has generally been limited to changes in the volume fill ratio or particle bed depth as these represent the most common modifications to damper designs. There is little work on unusually shaped enclosures (for example, with non-parallel walls), and it is therefore not known whether similar motional phases are observed. Because of this, this subject would be a significant but slightly less related piece of work itself, and it is kept outside the scope of this thesis.

The particle shape may have an influence on the motional phase as it affects the inertia of each particle and the way in which they interact with each other. Thus, as a different feature

from other damper parameters, the particle shape can have a significant role to change the motional phase-dependent dissipative characteristics of granular dampers. However, it has been noticed in the review that there is limited work on the effect of particle shape. In addition, discussions with one author of the reference work [8] have revealed that the particles used in shot blasting (slightly spheroidal rather perfectly spherical) provided better dissipative performance than perfect spheres. As a result, the research questions shown below are identified.

II. Why does the particle shape have an effect on the dissipative performance?

III. In what way does the particle shape affect the operating motional phase of granular dampers?

3 Fundamentals of Discrete Element Method

3.1 Overview

Numerical methods can enable the solution of engineering problems without performing physical experiments. They can be used to optimise engineering designs by analysing the effects of design parameters without physical limitations. However, the most suitable numerical approach should be carefully selected for the investigated problem.

When studying the dynamics of a granular medium, numerical studies add considerable value because it would be very difficult to obtain, via experimental means, information such as the motion trajectories and interaction forces relating to individual particles. Sensitivity studies relating to parameters such as gravity loading and the coefficients of friction and restitution are also much more conveniently achieved using numerical simulation.

The literature review has shown that it is feasible to use the Discrete Element Method (DEM) for the granular damper simulations of this thesis. Unlike a continuum approach where the entire medium is represented using constitutive equations, with DEM the medium is represented by many individual bodies which can move relative to each other. DEM is a numerical computation scheme which explicitly calculates both positions and rotations of each body. Determination of three-dimensional motions is based on integrating the equations of motions of each body at short discretised time steps which they constitute a full-time

simulation history. In this way, DEM is able to accommodate any desired force-deformation behaviours right down to contact interactions between individual particles.

The fundamental theory behind the DEM computational scheme is briefly described in this chapter assuming that the granular medium is constructed using perfect spheres. Although a three-dimensional DEM algorithm was developed in the MATLAB environment to implement the theory presented in this chapter, Altair EDEM commercial three-dimensional DEM software [136] was used throughout the thesis because of its calculation speed and graphical interface advantages.

3.2 An Introduction to DEM

The fundamental principles of DEM were introduced by Cundall and Strack [137]. It has since been found applications in a variety of fields such as granular flow analysis, powder and rock mechanics, crowd dynamics, pharmaceuticals and grain storage and transport [135,138–140]. DEM is particularly attractive in granular damping studies because of its capability to control and observe contact parameters at micro-scale and their effects on the energy dissipation achieved [67]. Hence, DEM has been extensively adapted for granular damper applications and designs [67,68,86,87,141–145].

There are two different DEM approaches depending on whether contacts are assumed hard or soft.[138]. In the hard contact approach, impacts take place instantly and particles are not allowed to deform. Particle motions are obtained by solving the impulse-momentum relations for each impacting pair of particles. On the other hand, the soft-particle approach assumes that deformations take place according to a contact model (often defined using spring, viscous damping and Coulomb friction elements) that can represent the physical force-deformation relation of the contact. Particle motions are determined by integrating the Newton-Euler equations of motions for short but finite time steps. The ability to define a

variety of contact conditions has made the soft contact approach in DEM the preferred route for most researchers.

3.3   Contact Kinematics

Before applying any physical law, the kinematic basics of an interaction between bodies should be known. Here, considering perfect spherical geometry that the original work is based on [137], particle-particle and particle-arbitrary geometrical surface (enclosure wall) contacts are evaluated. In Figure 3.1, these contact types are illustrated along with the required vectorial and scalar quantities.
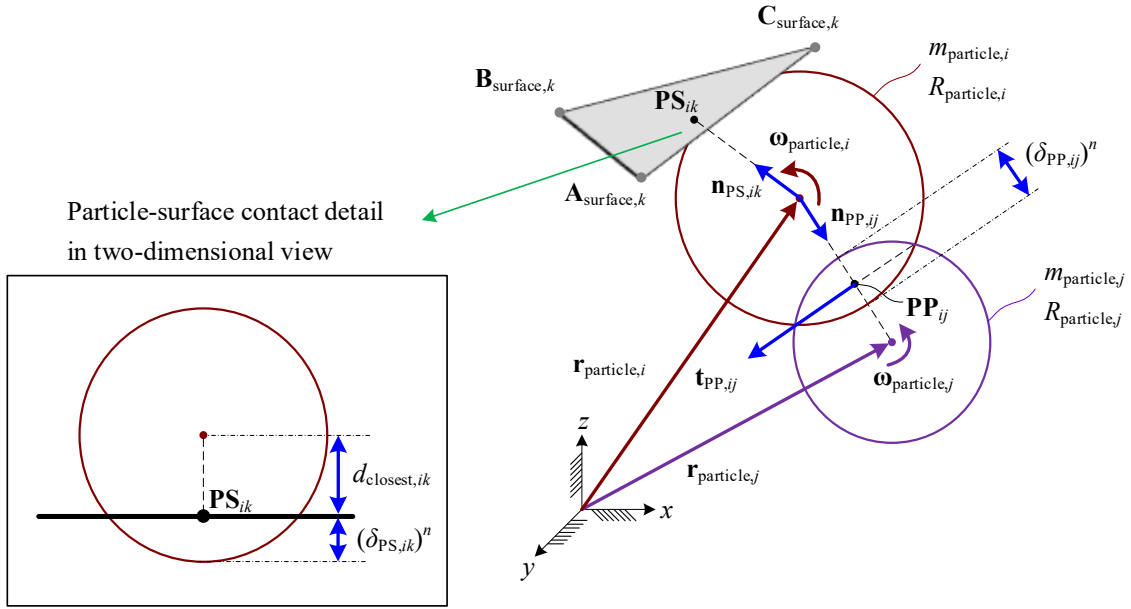
Figure 3.1: Representation of particle-particle and particle-surface contacts.

In this figure, the main particle, the contacting particle and the contacting arbitrary surface are indexed by i, j and k, respectively. The mass, radius, centre of mass position vector with respect to the global xyz cartesian coordinate system whose unit vectors are described by $\mathbf{i}$, $\mathbf{j}$ and $\mathbf{k}$, and angular velocity of the particles are respectively depicted by m_{particle}, R_{particle}, $\mathbf{r}_{\text{particle}}$ and $\boldsymbol{\omega}_{\text{particle}}$. The arbitrary surface is defined by the known three points which belong to the surface: $\mathbf{A}_{\text{surface}}$, $\mathbf{B}_{\text{surface}}$, and $\mathbf{C}_{\text{surface}}$. The time is shown by t, and note that all quantities

are the functions of time except the global coordinate system unit vectors, particle mass and particle radius.

First, the particle-particle contact is considered. The normal unit vector of particle-particle contact, $\mathbf{n}_{\text{PP},ij}$, is obtained from the centre of the main particle to the particle-particle contact point, $\mathbf{PP}_{ij}$.

$$\mathbf{n}_{\text{PP},ij} = \frac{\mathbf{r}_{\text{particle},j} - \mathbf{r}_{\text{particle},i}}{\left| \mathbf{r}_{\text{particle},j} - \mathbf{r}_{\text{particle},i} \right|} \tag{3.1}$$

The deformation along this direction (i.e., normal direction) or the normal overlap, $(\delta_{\text{PP},ij})^n$ is determined as given below.

$$\left(\delta_{\text{PP},ij} \right)^n = R_{\text{particle},i} + R_{\text{particle},j} - \left| \mathbf{r}_{\text{particle},j} - \mathbf{r}_{\text{particle},i} \right| \tag{3.2}$$

The relative velocity between the particles in contact, $\mathbf{v}_{\text{PP},ij}$, can be found as:

$$\mathbf{v}_{\text{PP},ij} = \mathbf{v}_{\text{PP},i} - \mathbf{v}_{\text{PP},j} \tag{3.3}$$

where $\mathbf{v}_{\text{PP},i}$ and $\mathbf{v}_{\text{PP},j}$ are the velocities of the corresponding particle surfaces at the contact point:

$$\mathbf{v}_{\text{PP},i} = \dot{\mathbf{r}}_{\text{particle},i} + \boldsymbol{\omega}_{\text{particle},i} \times \left(R_{\text{particle},i} - \frac{\left(\delta_{\text{PP},ij} \right)^n}{2} \right) \mathbf{n}_{\text{PP},ij} \tag{3.4}$$

$$\mathbf{v}_{\text{PP},j} = \dot{\mathbf{r}}_{\text{particle},j} + \boldsymbol{\omega}_{\text{particle},j} \times \left(-R_{\text{particle},j} + \frac{\left(\delta_{\text{PP},ij} \right)^n}{2} \right) \mathbf{n}_{\text{PP},ij} \tag{3.5}$$

where the superscript dot, '˙' indicates time derivative and '×' shows vectorial product. As they are needed separately in DEM, the normal and tangential components of the relative velocity can be subtracted from the relative velocity (Equation 3.3) as:

$$\left(\mathbf{v}_{\mathrm{PP},ij}\right)^{n} = \mathbf{n}_{\mathrm{PP},ij} \frac{d\left(\delta_{\mathrm{PP},ij}\right)^{n}}{dt} = \mathbf{n}_{\mathrm{PP},ij}\left(\mathbf{n}_{\mathrm{PP},ij} \cdot \mathbf{v}_{\mathrm{PP},ij}\right) \tag{3.6}$$

$$\left(\mathbf{v}_{\mathrm{PP},ij}\right)^{t} = \mathbf{t}_{\mathrm{PP},ij} \frac{d\left(\delta_{\mathrm{PP},ij}\right)^{t}}{dt} = \mathbf{v}_{\mathrm{PP},ij} - \left(\mathbf{v}_{\mathrm{PP},ij}\right)^{n} \tag{3.7}$$

where $(\delta_{\mathrm{PP},ij})^{t}$ is the tangential deformation or the tangential overlap. The tangential unit vector of particle-particle contact is now known by the following simple relation.

$$\mathbf{t}_{\mathrm{PP},ij} = \frac{\left(\mathbf{v}_{\mathrm{PP},ij}\right)^{t}}{\left|\left(\mathbf{v}_{\mathrm{PP},ij}\right)^{t}\right|} \tag{3.8}$$

Integrating the tangential relative velocity from the time of contact initiation, t_0, to the time point investigated, the tangential deformation is obtained.

$$\left(\delta_{\mathrm{PP},ij}\right)^{t} = \int_{t_0}^{t} \left|\left(\mathbf{v}_{\mathrm{PP},ij}\right)^{t}\right| dt \tag{3.9}$$

In DEM simulations, geometries other than particles are used to create desired boundary conditions. In order to model them, geometries are generally divided into small surfaces such as $\mathbf{A}_{\mathrm{surface},k}\mathbf{B}_{\mathrm{surface},k}\mathbf{C}_{\mathrm{surface},k}$ triangle in Figure 3.1 [85,136,146]. In this way, the contact kinematics between a particle and an arbitrary geometry surface can be evaluated by generating classical plane equations for each geometry segment.

For the given three points (a geometry segment) in Figure 3.1, the well-known plane equation can be constructed as:

$$f_{\mathrm{surface},k} = a_{\mathrm{surface},k}x + b_{\mathrm{surface},k}y + c_{\mathrm{surface},k}z - d_{\mathrm{surface},k} = 0 \tag{3.10}$$

where the coefficients, $a_{\mathrm{surface},k}$, $b_{\mathrm{surface},k}$ and $c_{\mathrm{surface},k}$, are the corresponding components of the surface normal, $\mathbf{n}_{\mathrm{surface},k}$, determined by:

$$\mathbf{n}_{\text{surface},k} = \left(\mathbf{B}_{\text{surface},k} - \mathbf{A}_{\text{surface},k} \right) \times \left(\mathbf{C}_{\text{surface},k} - \mathbf{A}_{\text{surface},k} \right) \tag{3.11}$$

Note that $\mathbf{n}_{\text{surface},k}$ is not a unit vector. As Equation (3.10) is valid through the surface of geometry segment, $d_{\text{surface},k}$ can be simply determined using one of the known points on this segment.

The deformation along the normal direction for particle-surface contact, $(\delta_{\text{PS},ij})^n$ is computed as:

$$\left(\delta_{\text{PS},ik} \right)^n = R_{\text{particle},i} - d_{\text{closest},ik} \tag{3.12}$$

where the closest distance between the main particle centre and the surface, $d_{\text{closest},ik}$ is obtained by:

$$d_{\text{closest},ik} = \frac{\left| \mathbf{r}_{\text{particle},i} \cdot \mathbf{n}_{\text{surface},k} + d_{\text{surface},k} \right|}{\left| \mathbf{n}_{\text{surface},k} \right|} \tag{3.13}$$

where the dot, ' $\cdot$ ' denotes scalar product. As the closest point on the surface to the main particle is $\mathbf{PS}_{ik}$, the normal unit vector of particle-surface contact, $\mathbf{n}_{\text{PS},ik}$, is defined as:

$$\mathbf{n}_{\text{PS},ik} = \frac{\mathbf{PS}_{ik} - \mathbf{r}_{\text{particle},i}}{d_{\text{closest},ik}} \tag{3.14}$$

where:

$$\mathbf{PS}_{ik} = \mathbf{r}_{\text{particle},i} - \frac{\mathbf{r}_{\text{particle},i} \cdot \mathbf{n}_{\text{surface},k} + d_{\text{surface},k}}{\left| \mathbf{n}_{\text{surface},k} \right|} \cdot \mathbf{n}_{\text{surface},k} \tag{3.15}$$

The other kinematic relations for particle-surface contact can be obtained re-arranging the equations presented for particle-particle interaction employing the same analogy. The relative velocity between the particle and the surface in contact, $\mathbf{v}_{\text{PS},ik}$, is determined by:

$$\mathbf{v}_{\text{PS},ik} = \mathbf{v}_{\text{PP},i} - \mathbf{v}_{\text{PS},k} \qquad (3.16)$$

where $\mathbf{v}_{\text{PP},i}$ is known from Equation (3.4) and the surface velocity, $\mathbf{v}_{\text{PS},k}$ is determined by the pre-definitions from the initial conditions in a DEM simulation. The normal and tangential components of relative velocity can be respectively found as:

$$\left(\mathbf{v}_{\text{PS},ik} \right)^n = \mathbf{n}_{\text{PS},ik} \frac{d\left(\delta_{\text{PS},ik} \right)^n}{dt} = \mathbf{n}_{\text{PS},ik} \left(\mathbf{n}_{\text{PS},ik} \cdot \mathbf{v}_{\text{PS},ik} \right) \qquad (3.17)$$

$$\left(\mathbf{v}_{\text{PS},ik} \right)^t = \mathbf{t}_{\text{PS},ik} \frac{d\left(\delta_{\text{PS},ik} \right)^t}{dt} = \mathbf{v}_{\text{PS},ik} - \left(\mathbf{v}_{\text{PS},ik} \right)^n \qquad (3.18)$$

where $(\delta_{\text{PS},ik})^t$ is the tangential deformation between the particle and the surface.

$$\left(\delta_{\text{PS},ik} \right)^t = \int_{t_0}^{t} \left| \left(\mathbf{v}_{\text{PS},ik} \right)^t \right| dt \qquad (3.19)$$

The tangential unit vector of particle-surface contact is determined as:

$$\mathbf{t}_{\text{PS},ik} = \frac{\left(\mathbf{v}_{\text{PS},ik} \right)^t}{\left| \left(\mathbf{v}_{\text{PS},ik} \right)^t \right|} \qquad (3.20)$$

3.4   Contact Detection

In order to apply any related calculations, contacts created either by two particles or between a particle and an enclosure wall should be established at each time step in DEM. However, contact detection results in a significant computational load for DEM simulations and is the most demanding part of the whole DEM computational procedure. Thus, an improvement in this step can provide noticeable reduction in computational times [5,147,148].

In DEM algorithms, a contact is typically established by checking the distance between two distinct bodies. Considering two spherical particles given in Figure 3.1, it can be said that if

the distance between the centres of particles is shorter than the sum of their radii this is a contact. The described condition is expressed as in the following relation.

$$\left| \mathbf{r}_{\text{particle},i} - \mathbf{r}_{\text{particle},j} \right| \leq R_{\text{particle},i} + R_{\text{particle},j} \tag{3.21}$$

For particle-surface contact detection, the relation becomes:

$$\left| \mathbf{r}_{\text{Particle},i} - \mathbf{PS}_{ik} \right| \leq R_{\text{particle},i} \tag{3.22}$$

Since checking each particle with one another particle or enclosure surface in this way requires very high computational efforts, an efficient but simple idea called 'box (sometimes called cell) algorithm' has been typically employed in DEM simulations [5,136,143]. As illustrated in Figure 3.2, the simulation environment, which is generally wider than outer enclosure geometry, is broken into a series of boxes (or cells). Instead of checking each pair in the simulation environment, the cells that intersect with the processed particle are marked as 'active searching area' (sometimes called as 'active cells'). The other employed bodies which intersect with these active cells are checked whether they shows a contact with the processed particle or not according to Equations (3.21) and (3.22) whilst those which are not positioned in the active cells are not checked and assigned directly as non-contact pair. In this way, the computational complexity which is $O(N_{\text{sphere}}{}^2)$ without the cell algorithm is reduced to $O(N_{\text{sphere}})$ at the best case and $O(N_{\text{sphere}}\log(N_{\text{sphere}}))$ at the worst case where N_{sphere} is the total number of spherical particles used in a DEM simulation [147].
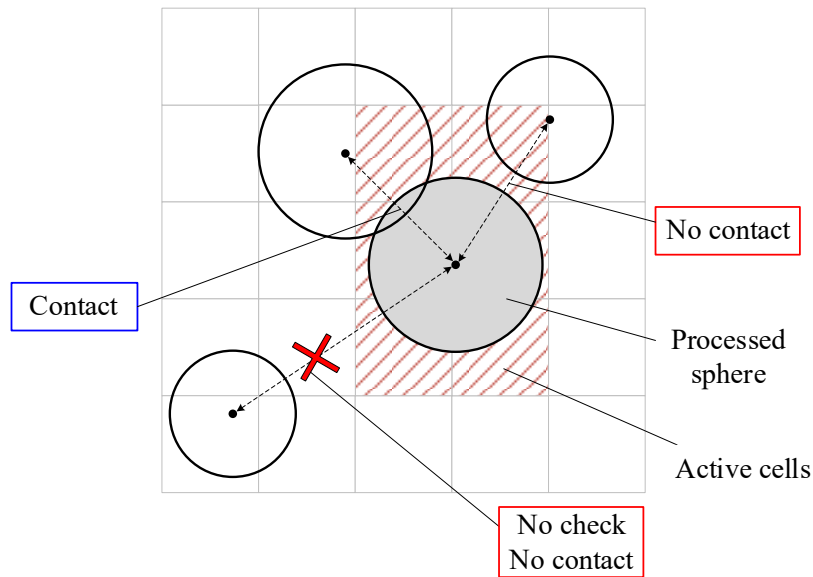
Figure 3.2: A sketch of cell algorithm approach at a particular time step.

In this algorithm, the cell grid size affects the computational time as illustrated in Figure 3.3. It is suggested to use at least 1.5 times of the smallest particle radius as the cell size to adequately detect contacts [5,148]. For DEM simulations of this thesis, 2.5 times of particle radius was generally used as the cell size.
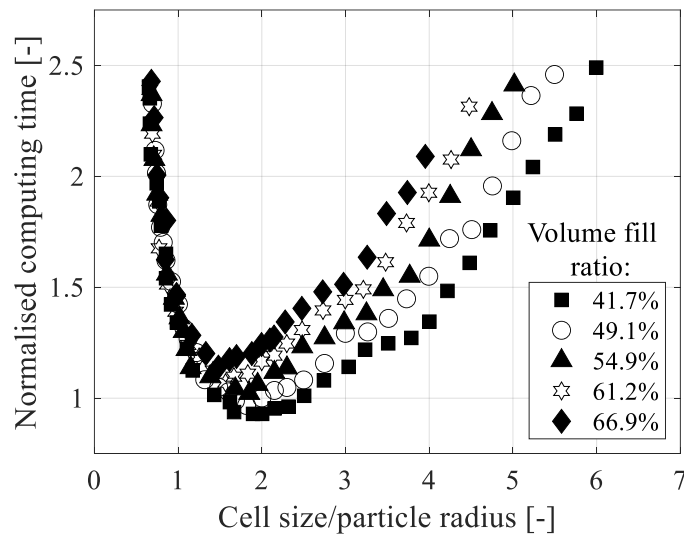
Figure 3.3: Computational effect of cell size [148].

3.5   Governing Equations of Particle Motion

As the motion of an enclosure surface is typically known by the initial definitions in a DEM model, only particle motions need to be evaluated. Therefore, the Newton- Euler equations

of motions which govern translational and rotational motions of a rigid body should be derived for each particle [149–151]:

$$\mathbf{F}_{\text{resultant},i} = m_{\text{particle},i} \ddot{\mathbf{r}}_{\text{particle},i} \tag{3.23}$$

$$
\begin{aligned}
M^{\bar{x}}{}_{\text{resultant},i} &= I^{\overline{xx}}{}_{\text{particle},i} \dot{\omega}^{\bar{x}}_{\text{particle},i} + \left(I^{\overline{zz}}{}_{\text{particle},i} - I^{\overline{yy}}{}_{\text{particle},i} \right) \omega^{\bar{y}}{}_{\text{particle},i} \omega^{\bar{z}}{}_{\text{particle},i} \\
M^{\bar{y}}{}_{\text{resultant},i} &= I^{\overline{yy}}{}_{\text{particle},i} \dot{\omega}^{\bar{y}}_{\text{particle},i} + \left(I^{\overline{xx}}{}_{\text{particle},i} - I^{\overline{zz}}{}_{\text{particle},i} \right) \omega^{\bar{x}}{}_{\text{particle},i} \omega^{\bar{z}}{}_{\text{particle},i} \\
M^{\bar{z}}{}_{\text{resultant},i} &= I^{\overline{zz}}{}_{\text{particle},i} \dot{\omega}^{\bar{z}}_{\text{particle},i} + \left(I^{\overline{yy}}{}_{\text{particle},i} - I^{\overline{xx}}{}_{\text{particle},i} \right) \omega^{\bar{x}}{}_{\text{particle},i} \omega^{\bar{y}}{}_{\text{particle},i}
\end{aligned}
\tag{3.24}
$$

where $I^{\overline{xx}}{}_{\text{particle},i}$, $I^{\overline{yy}}{}_{\text{particle},i}$ and $I^{\overline{zz}}{}_{\text{particle},i}$ are the mass moments of inertia with respect to the axes frame fixed at the centre of interested particle whose axes (i.e., $\overline{xyz}$) are principal axes of inertia; $\omega^{\bar{x}}{}_{\text{particle},i}$, $\omega^{\bar{y}}{}_{\text{particle},i}$ and $\omega^{\bar{z}}{}_{\text{particle},i}$ are the angular velocity vector components of particle with respect to the same axes frame.

Here, the resultant force imposed by the particle, $\mathbf{F}_{\text{resultant},i}$ can be obtained as:

$$\mathbf{F}_{\text{resultant},i}(t) = m_{\text{particle},i}\mathbf{g} + \sum_{j=1}^{N_{\text{PP},i}} \mathbf{F}_{\text{PP},ij} + \sum_{k=1}^{N_{\text{PS},i}} \mathbf{F}_{\text{PS},ik} \tag{3.25}$$

where $\mathbf{g}$ is the gravitational acceleration vector; $\mathbf{F}_{\text{PP},ij}$ and $\mathbf{F}_{\text{PS},ik}$ represent the interaction force vectors acting on the main particle generated by the contacting particles and the contacting enclosure surfaces, respectively; $N_{\text{PP},i}$ and $N_{\text{PS},i}$ are respectively the total number of particle and surface contacts that the main particle has.

The moment about the mass centre of particle due to the described forces, whose components are $M^{\bar{x}}{}_{\text{resultant},i}$, $M^{\bar{y}}{}_{\text{resultant},i}$ and $M^{\bar{z}}{}_{\text{resultant},i}$, can be found as:

$$\mathbf{M}_{\text{resultant},i} = \sum_{j=1}^{N_{\text{PP},i}} \left\{ \mathbf{d}_{\text{PP},ij} \times \mathbf{F}_{\text{PP},ij} \right\} + \sum_{k=1}^{N_{\text{PS},i}} \left\{ \mathbf{d}_{\text{PS},ik} \times \mathbf{F}_{\text{PS},ik} \right\} \tag{3.26}$$

where the corresponding moment arms are obtained by the following relations.

$$\mathbf{d}_{\text{PP},ij} = \left(R_{\text{rarticle},i} - \frac{\left(\delta_{\text{PP},ij} \right)^{n}}{2} \right) \mathbf{n}_{\text{PP},ij} \tag{3.27}$$

$$\mathbf{d}_{\text{PS},ik} = \left(R_{\text{rarticle},i} - \frac{\left(\delta_{\text{PS},ik} \right)^{n}}{2} \right) \mathbf{n}_{\text{PS},ik} \tag{3.28}$$

3.6   Time Integration

Equations (3.23) and (3.24) need to be solved to determine the motion of each particle in a DEM simulation. To integrate these second order ordinary differential equations, there are various numerical methods such as the Euler method (the simplest Runge-Kutta method), the Verlet integration methods. As Altair EDEM uses Euler method as the main solver and this solution method is computationally simple and fast, it was used for all numerical models in the thesis.

By integrating Equations (3.23) and (3.24) using Euler method, the updated translational and angular velocities and positions of main particle are obtained, respectively:

$$\begin{aligned}
\dot{\mathbf{r}}_{\text{particle},i} \left(t + \Delta t \right) &= \dot{\mathbf{r}}_{\text{particle},i} \left(t \right) + \ddot{\mathbf{r}}_{\text{particle},i} \left(t \right) \Delta t \\
\boldsymbol{\omega}_{\text{particle},i} \left(t + \Delta t \right) &= \boldsymbol{\omega}_{\text{particle},i} \left(t \right) + \dot{\boldsymbol{\omega}}_{\text{particle},i} \left(t \right) \Delta t
\end{aligned} \tag{3.29}$$

$$\begin{aligned}
\mathbf{r}_{\text{particle},i} \left(t + \Delta t \right) &= \mathbf{r}_{\text{particle},i} \left(t \right) + \dot{\mathbf{r}}_{\text{particle},i} \left(t \right) \Delta t \\
\boldsymbol{\theta}_{\text{particle},i} \left(t + \Delta t \right) &= \boldsymbol{\theta}_{\text{particle},i} \left(t \right) + \boldsymbol{\omega}_{\text{particle},i} \left(t \right) \Delta t
\end{aligned} \tag{3.30}$$

where Δt is the time step size defined as the duration between each iteration point in DEM. Note that the angular acceleration, velocity and position vectors given in Equations (3.29) and (3.30) are with respect to the global xyz cartesian coordinate system.

Since the accuracy of DEM approach depends on detecting contacts which occur within a very short duration and evaluating contact behaviours during such small amount of time, the time step size should be sufficiently small. Indeed, the Euler method needs a sufficiently

small-time step size for the stability of integration. Hence, it is known that the typical time step size in DEM approach is much smaller than the dynamic analyses of Computational Fluid Dynamics or FEM.

However, smaller time step size indicates more iterations and therefore longer computational times in DEM. To provide both accuracy (and stability) and acceptable computational effort, a criterion should be implemented to select time step size. This is generally done by calculating the wave travelling time along a particle diameter which is nothing but finding the natural frequency of the equivalent one-degree-of-freedom natural frequency of the smallest particle in DEM simulation [139]. To prevent propagating disturbances of a particle far from away, accurately capture particle deformations and reduce numerical integration errors, the Rayleigh time step approximation based on the Rayleigh surface wave propagation speed is employed to estimate a critical time step for DEM iterations [136,139,140].

$$\Delta t_{\text{Rayleigh}} \approx \frac{\pi R_{\text{particle,min}} \sqrt{\dfrac{\rho_{\text{particle}}}{G_{\text{particle}}}}}{0.1631 \nu_{\text{particle}} + 0.8766} \tag{3.31}$$

Here, ρ_{particle}, G_{particle}, ν_{particle} and $R_{\text{particle,min}}$ denote the particle density, shear modulus, Poisson's ratio and the minimum particle radius, respectively. As can be understood from this relation, the critical time step is only a function of particle properties. Hence, in order to speed-up DEM simulations researchers often preferred decreasing shear modulus supposing that a relatively small deviation in the shear modulus does not affect overall results considerably but significantly decrease the overall computational effort [140,152–155].

The actual simulation time step should be set a bit smaller than the critical time step estimation. Generally, it is suggested to use a safety factor, S_ρ for this as:

$$\Delta t = S_f \Delta t_{Rayleigh} \qquad (3.32)$$

It should be noted that the safety factor is typically between 0.1-0.4 [136,154].

3.7 Chapter Summary

As this thesis presents various particle simulation studies utilising DEM, the basic DEM theory has been briefly presented in this chapter considering perfect spheres. The DEM calculation scheme involves several distinct but inter-related steps to complete a solution for a granular medium related problem. Each step has unique properties that need to be determined as specific to the problem investigated. In order to easily follow the described DEM computation procedure, a flowchart is shown in Figure 3.4. It should be noted that no contact force-deformation model (will be discussed in Chapter 5) has been described in this chapter whilst the interaction forces are introduced for constructing the equations of motions.
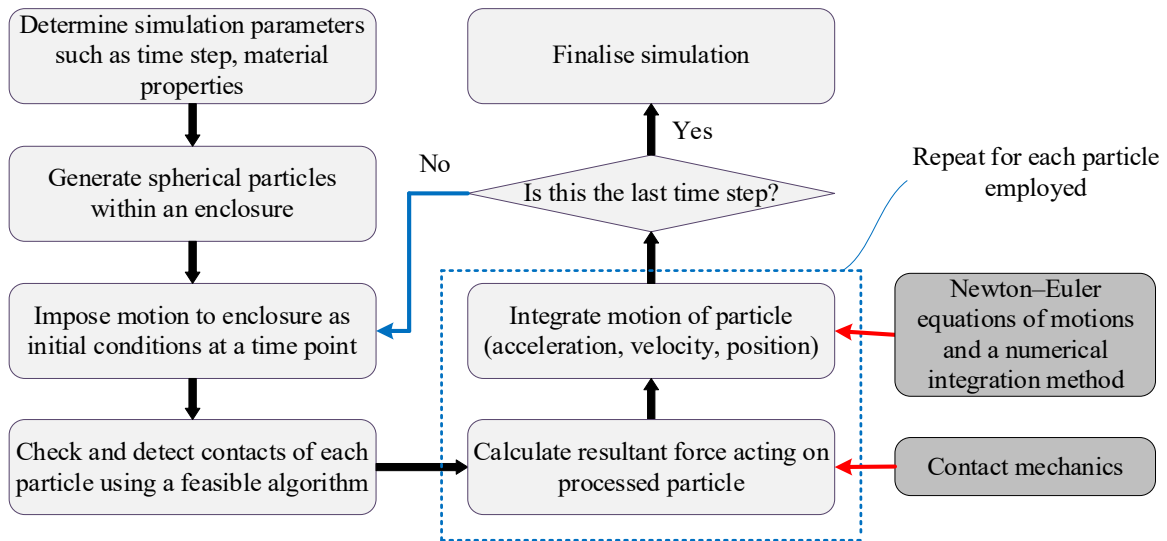
Figure 3.4: DEM simulation computation flowchart for spherical particles.

4 Non-Spherical Particle Generation in DEM

4.1 Overview

The most commonly used shapes in DEM are the perfect sphere (in three dimensions) and the disc (in two dimensions) based on the original work [137]. Nevertheless, the particle shapes encountered in practical applications of granular systems can be non-spherical and have a geometry which cannot be modelled by using an equivalent spherical particle shape [135,156].

One of the important properties which defines a particle in a granular medium is its geometric shape as it affects the inertial properties of individual particles and so, the dynamic behaviour of the whole granular medium. Therefore, non-spherical particles should be modelled in DEM simulation environment. Several algorithms have been recently developed to generate non-spherical particles employing geometric surface segments [85,146]. However, this is computationally complex, and has limited contact detection and contact modelling methods when compared to DEM with spherical particles. In addition to such drawbacks, the definition of some physical parameters in DEM (such as COR [135,157,158]) would be relatively problematic for the non-spherical particle shapes created using this approach as they need to be determined depending on contacting surface segments.

The multi-sphere approach, on the other hand, where two or more intersecting spherical particles are allowed to be rigidly joined together to form a non-spherical particle assembly,

is commonly used in DEM approaches. The major reason for this is that it has the advantage of spherical DEM computations which offer deeply researched and advanced contact models and contact detection methods. In addition, the multi-sphere approach allows the use of spherical properties as DEM inputs. The multi-sphere approach has been extensively tested and found reliable for representing non-spherical particles in DEM [159–161]. Thus, the multi-sphere approach has been widely used for granular medium based studies in the literature [10,133,134].

In the multi-sphere approach, the use of larger number of sub-spheres generally results in more precise shapes, however, it also causes significant increase in computational effort. Therefore, a balance between the computational efficiency and the accuracy of representative non-spherical shape should be provided.

In this chapter, the motion of non-spherical particles created using the multi-sphere approach is derived for DEM simulations by re-applying the same principles as in the previous chapter. The generation of the multi-sphere particle shapes investigated in this thesis (i.e., oblate spheroid, prolate spheroid and circular toroid) is discussed. A novel approach based on the multi-sphere method is proposed to generate circular toroid non-spherical particles for DEM simulations. The accuracy of generated non-spherical particles as a function of the number of sub-spheres used is also investigated by calculating the geometrical errors.

4.2 Motion of Non-Spherical Particles in DEM

The kinematics and contact detection for both sphere-sphere and sphere-enclosure surface contacts described by Equations (3.1)–(3.22) are also valid for the multi-sphere particles as the shape of sub-spheres is still a sphere. However, as the overall particle shape is no longer a perfect sphere, the governing equations of motions and the resultant forces and moments should be re-written.

A non-spherical particle shape indexed by l is illustrated in Figure 4.1 where $\mathbf{r}_{MS,l}$ and $\boldsymbol{\omega}_{MS,l}$ are the mass centre position vector and the angular velocity of the non-spherical particle.
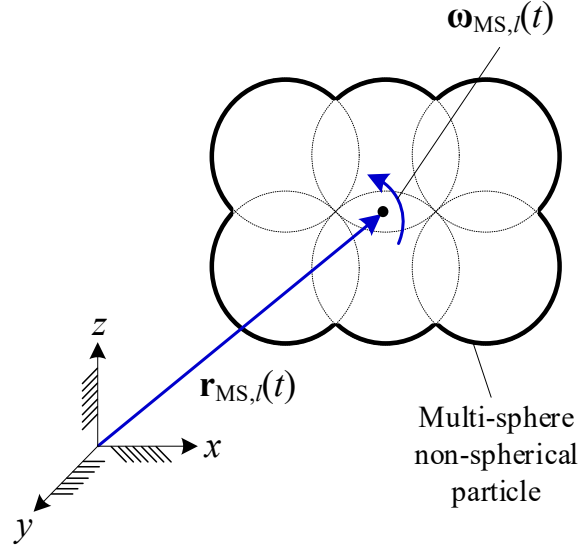
Figure 4.1: Arbitrary non-spherical particle shape composed of sub-spheres.

The particle mass is calculated by considering the sub-sphere particle properties (i.e., the density that can be determined by the mass, $(m_{\text{sub-sphere},i})_l$, and the radius, $(R_{\text{sub-sphere},i})_l$, of a sub-sphere i which forms the multi-sphere non-spherical particle), and the particle volume ($V_{MS,l}$) is found using the outer surface of non-spherical particle:

$$m_{MS,l} = \frac{\left(m_{\text{sub-sphere},i}\right)_l}{4\pi \left(R_{\text{sub-sphere},i}\right)_l^3 / 3} V_{MS,l} \tag{4.1}$$

The mass centre position of non-spherical particle is related with the used sub-spheres:

$$\mathbf{r}_{MS,l} = \frac{\sum_{i=1}^{N_{MS,l}} \left(m_{\text{sub-sphere},i}\right)_l \left(\mathbf{r}_{\text{sub-sphere},i}\right)_l}{\sum_{i=1}^{N_{MS,l}} \left(m_{\text{sub-sphere},i}\right)_l} \tag{4.2}$$

where $N_{MS,l}$ and $(\mathbf{r}_{\text{sub-sphere},i})_l$ respectively denote the number of sub-spheres and the position of the mass centre of sub-sphere i.

For the integration of translational motions, the governing equations (3.23) is re-arranged as:

$$\mathbf{F}_{\text{MS},l} = m_{\text{MS},l} \ddot{\mathbf{r}}_{\text{MS},l} \tag{4.3}$$

where $\mathbf{F}_{\text{MS},l}$ is the resultant force arising from all sub-spheres. It can be obtained by applying Equation (3.25) for each sub-sphere as:

$$\mathbf{F}_{\text{MS},l} = m_{\text{MS},l}\mathbf{g} + \sum_{i=1}^{N_{\text{MS},l}} \left\{ \sum_{j=1}^{(N_{\text{PP},i})_l} \left(\mathbf{F}_{\text{PP},ij}\right)_l + \sum_{k=1}^{(N_{\text{PS},i})_l} \left(\mathbf{F}_{\text{PS},ik}\right)_l \right\} \tag{4.4}$$

where $(N_{\text{PP},i})_l$ and $(N_{\text{PS},i})_l$ are respectively the numbers of total sphere-sphere contacts and total sphere-enclosure surface contacts that the sub-sphere i produces; $(\mathbf{F}_{\text{PP},ij})_l$ and $(\mathbf{F}_{\text{PS},ik})_l$ are the interaction force vectors acting on the sub-sphere i generated by the contacting sub-spheres and the contacting enclosure surfaces, respectively.

The governing equations of angular motions given in Equation (3.24) can be directly adopted for non-spherical particles by only substituting the angular velocities of non-spherical particle and calculating the mass moment of inertia terms for non-spherical particles as:

$$I^{\overline{xx}}{}_{\text{MS},l} = \int_{m_{\text{MS},l}} \left(\hat{x}\right)_l^2 dm$$

$$I^{\overline{yy}}{}_{\text{MS},l} = \int_{m_{\text{MS},l}} \left(\hat{y}\right)_l^2 dm \tag{4.5}$$

$$I^{\overline{zz}}{}_{\text{MS},l} = \int_{m_{\text{MS},l}} \left(\hat{z}\right)_l^2 dm$$

where $\left(\hat{x}\right)_l$, $\left(\hat{y}\right)_l$ and $\left(\hat{z}\right)_l$ are the corresponding distances of differential mass element dm to the non-spherical particle centre of mass. For the angular motion governing equations, the resultant moment about the non-spherical particle mass centre due to all forces acting on each individual sub-sphere is calculated by:

58

$$\mathbf{M}_{\text{MS},l} = \sum_{i=1}^{N_{\text{MS},l}} \left\{ \sum_{j=1}^{\left(N_{\text{PP},i}\right)_l} \left\{ \left(\mathbf{d}_{\text{PP},ij}\right)_l \times \left(\mathbf{F}_{\text{PP},ij}\right)_l \right\} + \sum_{k=1}^{\left(N_{\text{PS},i}\right)_l} \left\{ \left(\mathbf{d}_{\text{PS},ik}\right)_l \times \left(\mathbf{F}_{\text{PS},ik}\right)_l \right\} \right\} \tag{4.6}$$

where the corresponding moment distances are:

$$\left(\mathbf{d}_{\text{PP},ij}\right)_l = \left(\left(R_{\text{sub-sphere},i}\right)_l - \frac{\left(\delta_{\text{PP},ij}\right)^n_l}{2} \right) \left(\mathbf{n}_{\text{PP},ij}\right)_l + \left(\mathbf{r}_{\text{sub-sphere},i}\right)_l - \mathbf{r}_{\text{MS},l}$$

$$\left(\mathbf{d}_{\text{PS},ik}\right)_l = \left(\left(R_{\text{sub-sphere},i}\right)_l - \frac{\left(\delta_{\text{PS},ik}\right)^n_l}{2} \right) \left(\mathbf{n}_{\text{PS},ik}\right)_l + \left(\mathbf{r}_{\text{sub-sphere},i}\right)_l - \mathbf{r}_{\text{MS},l} \tag{4.7}$$

where $(\mathbf{n}_{\text{PP},ij})_l$ and $(\mathbf{n}_{\text{PS},ik})_l$ are respectively the normal unit vectors of sphere-sphere and sphere-enclosure surface contacts; $(\delta_{\text{PP},ij})^n_l$ and $(\delta_{\text{PP},ij})^n_l$ are the corresponding normal overlaps along these vectors.

The integration scheme is carried out as the same way presented in Equations (3.29) and (3.30). The time step obtained by the equation (3.31) is also valid in this case by using the smallest sub-sphere radius in the constructed particle.

4.3 Arbitrarily Shaped Non-Spherical Particles

In order to create complex non-spherical particle shapes using the multi-sphere approach, Altair EDEM [136] provides a simple but useful feature. In this thesis, this non-spherical particle generation algorithm is used to create oblate spheroid particles as no analytical solution has been found for this type of geometry.

The geometry of an oblate particle and a multi-sphere representation of it are shown in Figure 4.2. Here, a_{spheroid} and b_{spheroid} are the principal dimensions of the oblate spheroid particle. As $a_{\text{spheroid}} < b_{\text{spheroid}}$, the particle is flattened. Note that if $a_{\text{spheroid}} > b_{\text{spheroid}}$ was met, the spheroid particle would have an elongated shape which is a prolate spheroid.

A basic demonstration of how this algorithm works is presented in Figure 4.3. As a first step, a geometry mesh template of the non-spherical particle is introduced. A surrounding grid system comprising several squares (or cubic cells) is generated till the exterior boundary of the geometry. The cells located inside the particle shape and the cells that involves the shape boundaries are separated from each other as shown in Figure 4.3a. The distances from each inner cell centre to all boundary cell centres are calculated. For each inner cell, the shortest path of those distances is identified, and a sub-sphere whose radius equals the identified shortest distance is created at the centre of inner cell as demonstrated in Figure 4.3b. Note that similar algorithms based on the multi-sphere approach can be found elsewhere in literature [162].
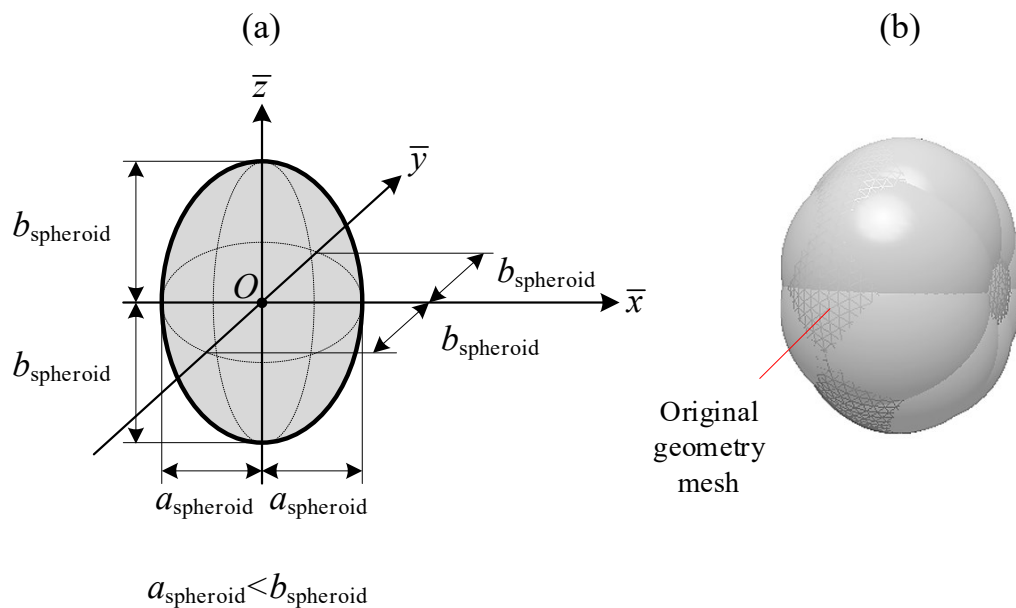

Figure 4.2: Axisymmetric oblate spheroid particle shape: (a) original smooth geometry, (b) multi-sphere model.
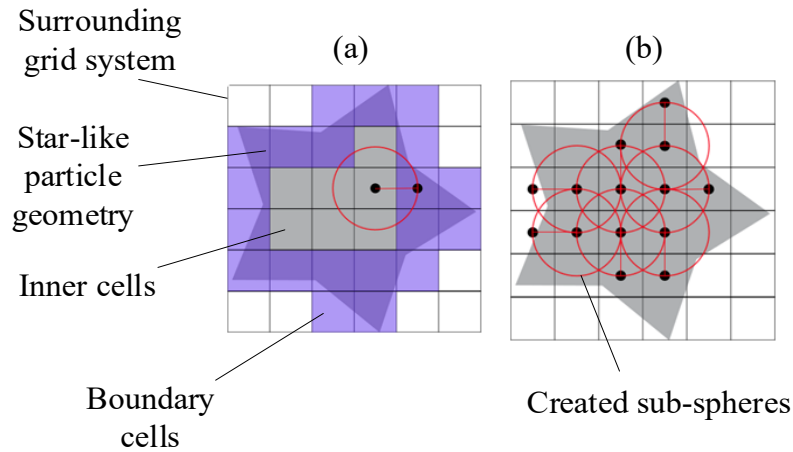
Figure 4.3: A schematic demonstration of geometric mesh-based algorithm: (a) inner and boundary cell generation, and (b) placed sub-spheres [136].

A rock shape example is illustrated in Figure 4.4 to show both the consistency level of this algorithm and the effect of the number of sub-spheres on the representative shape. As can be seen from this figure, the shape become more precise when the number of sub-spheres increases. However, it can also lead the employment of extremely small sub-spheres which results in a significant decrease of the iteration time step defined by Equation (3.31). Hence, the number of sub-spheres and their minimum radius should be restricted considering both the consistency of overall shape and the computational effort in this algorithm.

Number of spheres	835	363	69	22
Smallest particle radius [mm]	56	75	131	224
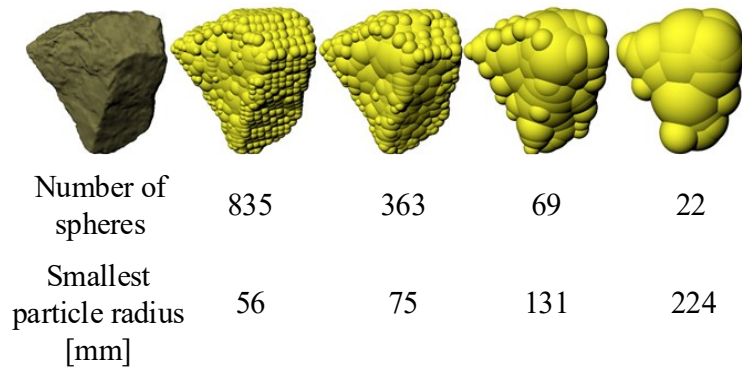
Figure 4.4: A three-dimensional rock shape generated by the multi-sphere approach employing the geometric-mesh based algorithm [136].

## 4.4   Analytical Approaches to Model Non-Spherical Particles

As illustrated in Figure 4.2b and Figure 4.4, the geometric mesh-based algorithm is not able to match the surface of non-spherical particles. To address this, analytical approaches have

been developed for some specific particle shapes. In this section, the analytical solutions are presented for two different particle shapes used in this thesis: prolate spheroid and circular toroid.

4.4.1 Prolate spheroid particle

An analytical solution for prolate spheroid particle generation in the DEM environment had been previously studied employing only four identical sub-spheres [163]. This approach has been improved and generalised for the use of an arbitrary number of sub-spheres by Markauskas et al. [164]. This analytical method is used in this thesis to create prolate non-spherical particles and is summarised below.

The geometry of an axisymmetric prolate spheroid particle shape and the multi-sphere model of this are shown in Figure 4.5a and Figure 4.5b.
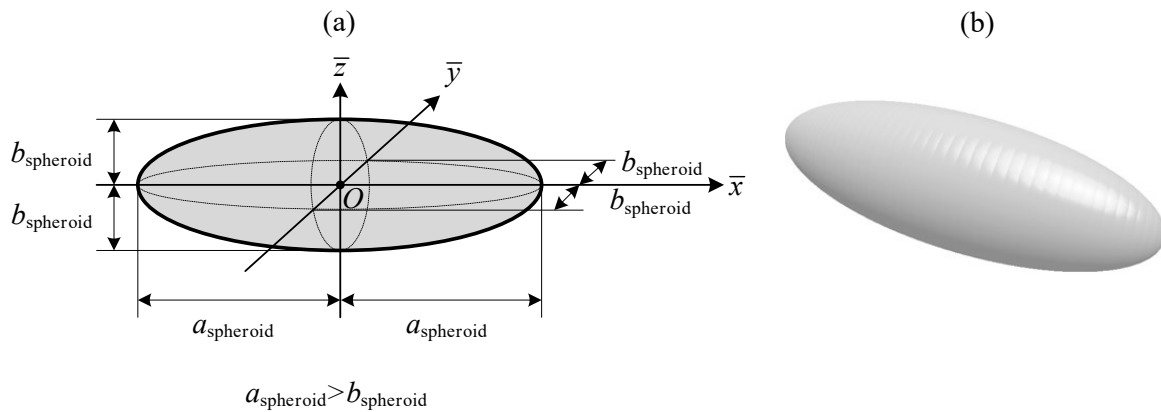

Figure 4.5: Axisymmetric prolate spheroid particle: (a) original smooth geometry, (b) multi-sphere model.

Note that the principal axes and dimensions are defined in the same way presented for the oblate spheroid in Figure 4.2. The geometric equation of the prolate spheroid surface can be written as:

$$f_{\text{spheroid}} = \left(\frac{\bar{x}}{a_{\text{spheroid}}} \right)^2 + \left(\frac{\bar{y}}{b_{\text{spheroid}}} \right)^2 + \left(\frac{\bar{z}}{b_{\text{spheroid}}} \right)^2 - 1 = 0 \tag{4.8}$$

Since the prolate spheroid particle is axisymmetric, it is more convenient to consider it in this way, as shown in Figure 4.6. Here, the sub-scripts 0, 1, …, i, …, n denote the individual sub-sphere. The total number of sub-spheres in the whole particle is $2n + 1$. All sub-sphere centres coincide with the $\bar{x}$ axis. The definitions of the notations used are listed below.

- $R_{\text{sub-sphere}}$ is the sub-sphere radius.

- $\bar{x}_{\text{sub-sphere}}$ is the $\bar{x}$ position of sub-sphere centre.

- $\bar{z}_{\text{spheroid}}$ is the $\bar{z}$ position of the spheroid particle surface that corresponds to $\bar{x}_{\text{sub-sphere},i}$ and it can be obtained from Equation (4.8).

- $\bar{z}_{\text{conjunction}}$ is the $\bar{z}$ position of each conjunction points of sub-spheres and it should be noticed that there are $n - 1$ conjunction points.

- $\ell^{(1)}_{\text{sub-sphere}}$ and $\ell^{(2)}_{\text{sub-sphere}}$ are the horizontal distances of right and left conjunction points to $\bar{z}_{\text{spheroid}}$ of sub-sphere centres, respectively.
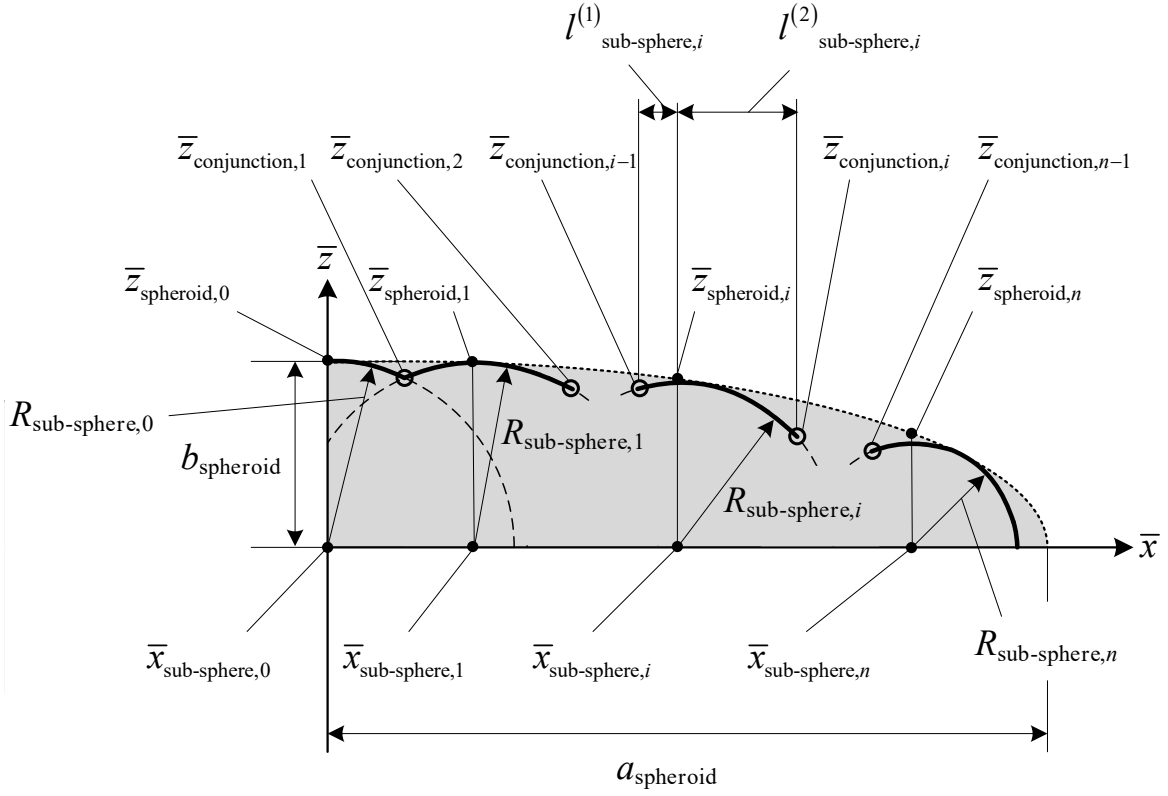
Figure 4.6: Two-dimensional half view of prolate spheroid particle shape with sub-spheres.

The inter sub-sphere segment is described as the distance between the centres of two neighbouring sub-spheres and calculated by the following relation.

$$d_{\text{sub-sphere},i} = \overline{x}_{\text{sub-sphere},i} - \overline{x}_{\text{sub-sphere},i-1} \tag{4.9}$$

Note that $d_{\text{sub-sphere},0}$ does not exist. Using the inverse approach, the position of each sub-sphere centre can be computed as:

$$\overline{x}_{\text{sub-sphere},i} = \sum_{j=1}^{i} d_{\text{sub-sphere},j} \tag{4.10}$$

As can be seen from Figure 4.6, the largest sub-sphere is positioned at $\overline{x}_{\text{sub-sphere},0} = 0$ and its radius $R_{\text{sub-sphere},0} = b_{\text{spheroid}}$. Also, $\overline{z}_{\text{spheroid},0} = b_{\text{spheroid}}$.

Each sub-sphere touches the original geometry surface. At the contact point, the surfaces of the particle and the sub-sphere have the same position and gradient. From these conditions, the radius is obtained as:

$$R_{\text{sub-sphere},i} = \sqrt{\frac{b_{\text{spheroid}}^2 \left(a_{\text{spheroid}}^2 - b_{\text{spheroid}}^2 - \overline{x}_{\text{sub-sphere},i}^2 \right)}{a_{\text{spheroid}}^2 - b_{\text{spheroid}}^2}} \qquad (4.11)$$

Ideally, sub-spheres fill the geometry along the major dimension of the spheroid so the final contact point occurs at:

$$\overline{x}_{\text{sub-sphere},n} = a_{\text{spheroid}} - R_{\text{sub-sphere},n} \qquad (4.12)$$

where the radius of this sub-sphere can be found substituting the position into the equation (4.11).

$$R_{\text{sub-sphere},n} = \frac{b_{\text{spheroid}}^2}{a_{\text{spheroid}}} \qquad (4.13)$$

In order to achieve this, the half of prolate spheroid major dimension should equal the sum of the inter segments and the radius of the smallest sub-sphere:

$$a_{\text{spheroid}} = \sum_{i=1}^{n} d_{\text{sub-sphere},i} + R_{\text{sub-sphere},n} \qquad (4.14)$$

If the spacing between sub-sphere centres is related to the relevant distance to the particle surface:

$$d_{\text{sub-sphere},i+2} = d_{\text{sub-sphere},i+1} \frac{\overline{z}_{\text{spheroid},i+1}}{\overline{z}_{\text{spheroid},i}} \qquad (4.15)$$

Therefore, there is only one unknown in Equation (4.14). For a given number of sub-spheres, the simultaneous iterative solution of Equation (4.14) along with Equations (4.8), (4.10) and

(4.15) provides the positions of each sub-sphere. Subsequently, the radius of each sub-sphere is obtained employing Equation (4.11).

To assess the accuracy of this approach, the area and the perimeter of the multi-sphere prolate particle (considering its two-dimensional cross-section shown in Figure 4.6) are computed and they are compared with the area and the perimeter of the quarter ellipse geometry.

The area of the multi-sphere particle is obtained as:

$$A_{\text{prolate,MS}} = A_{\text{sub-sphere},0} + \sum_{i=1}^{n-1} A_{\text{sub-sphere},i} + A_{\text{sub-sphere},n} \qquad (4.16)$$

where the area terms are:

$$
\begin{aligned}
A_{\text{sub-sphere},0} = {} & \frac{R_{\text{sub-sphere},0}^{2}}{2}\left(\frac{\pi}{2} - \tan^{-1}\left(\frac{\overline{z}_{\text{conjunction},1}}{d_{\text{sub-sphere},1} - \ell^{(1)}_{\text{sub-sphere},1}}\right)\right) \\
& + \frac{\overline{z}_{\text{conjunction},1}\left(d_{\text{sub-sphere},1} - \ell^{(1)}_{\text{sub-sphere},1}\right)}{2}
\end{aligned}
\qquad (4.17)
$$

$$
\begin{aligned}
A_{\text{sub-sphere},i} = {} & \frac{R_{\text{sub-sphere},i}^{2}}{2}\left(\pi - \tan^{-1}\left(\frac{\overline{z}_{\text{conjunction},i}}{\ell^{(1)}_{\text{sub-sphere},i}}\right) - \tan^{-1}\left(\frac{\overline{z}_{\text{conjunction},i+1}}{\ell^{(2)}_{\text{sub-sphere},i}}\right)\right) \\
& + \frac{1}{2}\left(\overline{z}_{\text{conjunction},i}\ell^{(1)}_{\text{sub-sphere},i} + \overline{z}_{\text{conjunction},i+1}\ell^{(2)}_{\text{sub-sphere},i}\right)
\end{aligned}
\qquad (4.18)
$$

$$
\begin{aligned}
A_{\text{sub-sphere},n} = {} & \frac{R_{\text{sub-sphere},n}^{2}}{2}\left(\pi - \tan^{-1}\left(\frac{\overline{z}_{\text{conjunction},n-1}}{d_{\text{sub-sphere},n} - \ell^{(2)}_{\text{sub-sphere},n-1}}\right)\right) \\
& + \frac{\overline{z}_{\text{conjunction},n-1}\left(d_{\text{sub-sphere},n} - \ell^{(2)}_{\text{sub-sphere},n-1}\right)}{2}
\end{aligned}
\qquad (4.19)
$$

The perimeter of the multi-sphere particle is similarly calculated as:

$$P_{\text{prolate,MS}} = P_{\text{sub-sphere},0} + \sum_{i=1}^{n-1} P_{\text{sub-sphere},i} + P_{\text{sub-sphere},n} \qquad (4.20)$$

where the perimeter terms are:

66

$$P_{\text{sub-sphere},0} = R_{\text{sub-sphere},0} \left(\frac{\pi}{2} - \tan^{-1} \left(\frac{\overline{z}_{\text{conjunction},1}}{d_{\text{sub-sphere},1} - \ell^{(1)}_{\text{sub-sphere},1}} \right) \right) \tag{4.21}$$

$$P_{\text{sub-sphere},i} = R_{\text{sub-sphere},i} \left(\pi - \tan^{-1} \left(\frac{\overline{z}_{\text{conjunction},i}}{\ell^{(1)}_{\text{sub-sphere},i}} \right) - \tan^{-1} \left(\frac{\overline{z}_{\text{conjunction},i+1}}{\ell^{(2)}_{\text{sub-sphere},i}} \right) \right) \tag{4.22}$$

$$P_{\text{sub-sphere},n} = R_{\text{sub-sphere},n} \left(\pi - \tan^{-1} \left(\frac{\overline{z}_{\text{conjunction},n-1}}{d_{\text{sub-sphere},n} - \ell^{(2)}_{\text{sub-sphere},n-1}} \right) \right) \tag{4.23}$$

The exact area and very close approximation for the perimeter of quarter ellipse geometry are determined by:

$$A_{\text{prolate,exact}} = \pi a_{\text{spheroid}} b_{\text{spheroid}} / 4 \tag{4.24}$$

$$P_{\text{prolate,exact}} \approx \pi \left\{ 3 \left(a_{\text{spheroid}} + b_{\text{spheroid}} \right) - \sqrt{ \left(3 a_{\text{spheroid}} + b_{\text{spheroid}} \right) \left(a_{\text{spheroid}} + 3 b_{\text{spheroid}} \right) } \right\} / 4 \tag{4.25}$$

The errors arising from the multi-sphere approximation are plotted depending on the number of sub-spheres for three different aspect ratios in Figure 4.7. The multi-sphere approach underestimates the area whereas it overestimates the perimeter as expected (see Figure 4.6). Increasing the number of sub-spheres reduces the error, but with diminishing gains when many sub-spheres are used. Higher aspect ratio particles require more sub-spheres to maintain accuracy.
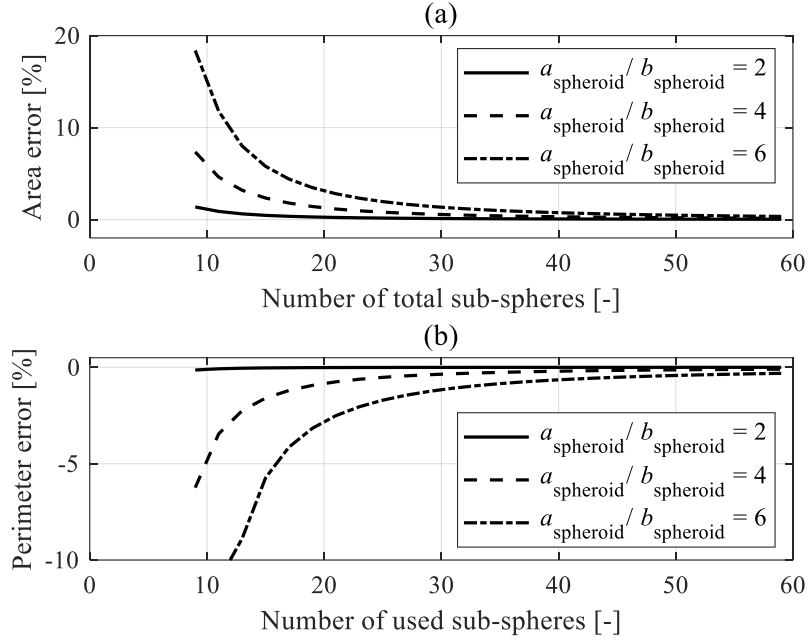
Figure 4.7: Geometric errors in the approximated multi-sphere prolate spheroid: (a) area and (b) perimeter.
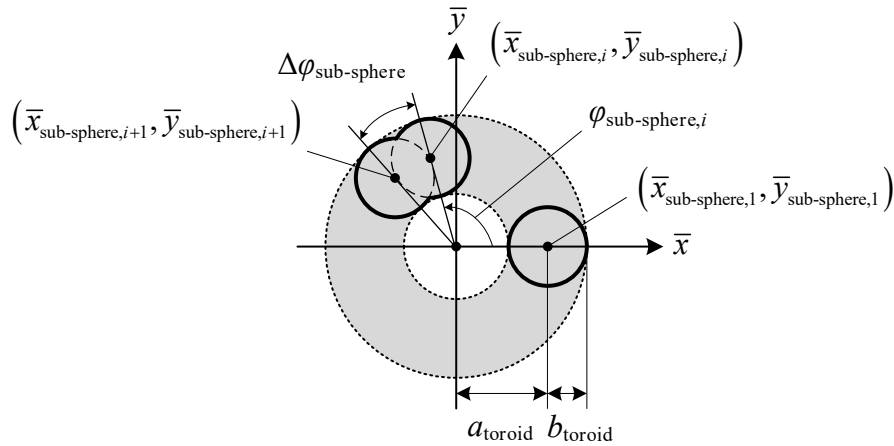
4.4.2 Circular toroid particle

Utilising a similar approach, an analytical method is developed here to generate circular toroidal particles for DEM simulations. A circular toroid is generated by sweeping a circle through a circle path which is perpendicular to the sweeping circle. Three-dimensional view of a circular toroid geometry with the principal dimensions and a circular toroid particle constructed with sub-spheres are illustrated in Figure 4.8. Note that a_{toroid} represents the radius of whole circular toroid shape whilst b_{toroid} is the radius of circular tube.

It is more convenient to consider the circular toroid on a two-dimensional plane to ensure geometric simplicity for evaluating the alignment of sub-spheres as the particle geometry is radially axisymmetric around the $\overline{z}$ axis as shown in Figure 4.9. In the analytical method presented here, it is considered that the centre of each sub-sphere coincides with the circular axis of toroid geometry which pass through the centre of circular tube cross-section (the $\overline{z}$ coordinate of each sub-sphere is 0) as can be seen in Figure 4.8b and Figure 4.9. The method

68

assumes that the circular toroid shape is filled by a number of identical overlapping sub-spheres which all touch the tube surface. This means that the radius of each sub-sphere equals to the radius of the tube.
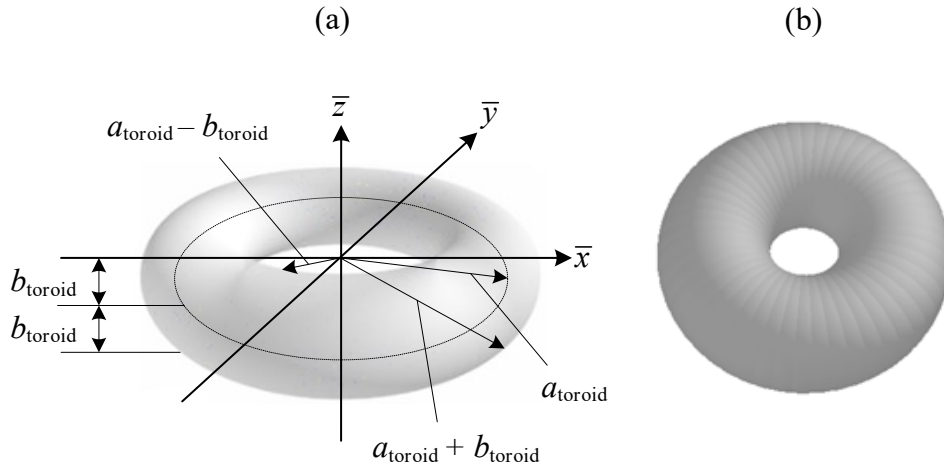
Figure 4.8: Circular toroid particle shape: (a) original smooth geometry and (b) multi-sphere model.

Figure 4.9: Circular toroid particle shape with sub-spheres on two-dimensional plane. The sub-script i indexes the sub-spheres, and it goes up to the total number used n. Note that the sub-spheres are aligned from $\left(\overline{x}_{\text{sub-sphere},1}, \overline{y}_{\text{sub-sphere},1}\right) = \left(a_{\text{toroid}}, 0\right)$ along the anti-clockwise direction.

The angle of between sub-sphere centres, $\Delta\varphi_{\text{sub-sphere}}$, determines the number used:

$$n = \frac{2\pi}{\Delta\varphi_{\text{sub-sphere}}} \qquad (4.26)$$

If $\Delta\varphi_{\text{sub-sphere}} \to 0$, n theoretically becomes infinite and this indicates the exact circular toroidal particle with the multi-sphere approach.

There is a limitation for the minimum number of sub-spheres that should be used. This condition can be defined assuming that each sub-sphere touches its neighbours. Thus, the following criteria must be met.

$$\Delta\varphi_{\text{sub-sphere}} < \frac{2b_{\text{toroid}}}{a_{\text{toroid}}} \qquad (4.27)$$

Satisfying this condition, a sufficient separation angle is provided, and the number of sub-spheres is determined. Afterwards, the centre positions of each sub-sphere can be determined by:

$$\begin{aligned}
\bar{x}_{\text{sub-sphere},i} &= a_{\text{toroid}} \cos\left(\varphi_{\text{sub-sphere},i}\right) \\
\bar{y}_{\text{sub-sphere},i} &= a_{\text{toroid}} \sin\left(\varphi_{\text{sub-sphere},i}\right)
\end{aligned} \qquad (4.28)$$

where $\varphi_{\text{sub-sphere},i}$ is found from the following relation.

$$\varphi_{\text{sub-sphere},i} = \Delta\varphi_{\text{sub-sphere}}\left(i-1\right) \qquad (4.29)$$

Similar to prolate spheroid particle case, the closeness of the approximated particle shape to the smooth geometry is investigated. The area and perimeter of multi-sphere toroid particle (considering two-dimensional cross section on $\overline{xy}$ plane – see Figure 4.9) should be obtained first. These calculations depend on the intersection distance between two adjacent sub-spheres. The intersecting distance between two sub-spheres shown in Figure 4.10 is obtained as below.

$$d_{\text{intersecting}} = 2a_{\text{toroid}} \sin\left(\Delta\varphi_{\text{sub-sphere}} / 2\right) \qquad (4.30)$$
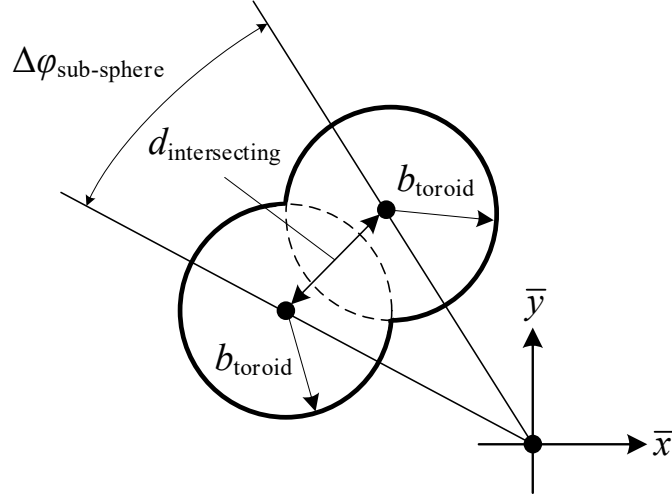
Figure 4.10: Two intersecting sub-spheres in a multi-sphere circular toroid particle.

Using the intersecting distance, the area can be computed by removing the overlapped areas from the total area of sub-spheres as:

$$
\begin{aligned}
A_{\text{toroid,MS}} &= n\pi b_{\text{toroid}}^{2} \\
&- 2n\left\{ \int_{d_{\text{intersecting}}/2}^{b_{\text{toroid}}} \sqrt{b_{\text{toroid}}^{2} - \bar{x}^{2}}\, d\bar{x} + \int_{d_{\text{intersecting}} - b_{\text{toroid}}}^{d_{\text{intersecting}}/2} \sqrt{b_{\text{toroid}}^{2} - \left(\bar{x} - d_{\text{intersecting}}\right)^{2}}\, d\bar{x} \right\} \quad (4.31) \\
&= n\left(\pi b_{\text{toroid}}^{2} - 2b_{\text{toroid}}^{2} \cos^{-1}\left(\frac{d_{\text{intersecting}}}{2b_{\text{toroid}}} \right) + d_{int}\sqrt{b_{\text{toroid}}^{2} - d_{\text{intersecting}}^{2}/4} \right)
\end{aligned}
$$

and the surface perimeter of this approximated particle can be similarly obtained by:

$$
\begin{aligned}
P_{\text{toroid,MS}} &= 2nb_{\text{toroid}}\left(\pi \right. \\
&\left. - 2\sin^{-1}\left(\frac{2\sqrt{\left(b_{\text{toroid}} - d_{\text{intersecting}}/2\right)\left(b_{\text{toroid}} + d_{\text{intersecting}}/2\right)}}{2b_{\text{toroid}}} \right) \right)
\end{aligned} \quad (4.32)
$$

The area and perimeter of the original smooth circular toroid geometry are known by:

$$
A_{\text{toroid,exact}} = 4\pi a_{\text{toroid}} b_{\text{toroid}} \quad (4.33)
$$

$$
P_{\text{toroid,exact}} = 4\pi a_{\text{toroid}} \quad (4.34)
$$

The errors in area and perimeter are shown in Figure 4.11 depending the number of sub-spheres for three different hole ratios. As can be seen, the accuracy is very similar to the prolate spheroid particle investigation. The approximated shape underestimates the actual area, and it overestimates the perimeter. The error decreases as the number of sub-spheres increases. However, the gain with the increase in the number of sub-spheres diminishes for large number of sub-spheres. Larger ratio of the hole length to the tube length requires more sub-spheres to maintain accuracy.
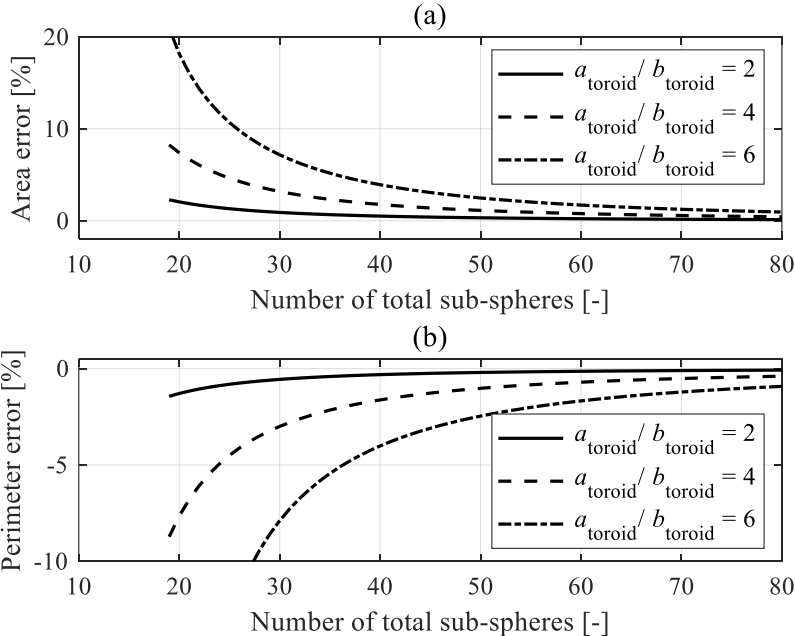
Figure 4.11: Geometric errors in the multi-sphere circular toroid particle: (a) area and (b) perimeter.

4.5   Chapter Summary and Conclusions

In this chapter, use of the multi-sphere approach has been shown for modelling non-spherical particles. The generation of oblate spheroid, prolate spheroid and circular toroid particles has been considered. The governing equations of motions shown for spherical particles in Chapter 3 have been re-arranged considering multi-sphere non-spherical particles. In order to show the DEM computation scheme with non-spherical particles, the updated version of Figure 3.4 flowchart is illustrated in Figure 4.12.

Geometric mesh-based algorithms (such as [162]), where a number of sub-spheres are employed to fill a provided particle geometry, are used to generate arbitrary shaped particles in DEM. One of these approaches was considered for the generation of oblate spheroid particles in this chapter. Additionally, two analytical methods (one from literature and one novel) have been presented to generate prolate spheroid and toroidal particles, respectively.

The ability of the analytical approaches to create accurate representations of prolate spheroid and toroidal particles has been investigated. It has been found that increasing number of sub-spheres provides a more accurate representation. However, this increases the computational effort of DEM solution and the improvement in shapes is not affected much after a number of sub-spheres. Therefore, a number of sub-spheres can be selected to conduct a balance between the computational effort and accuracy depending on the geometric error analyses.
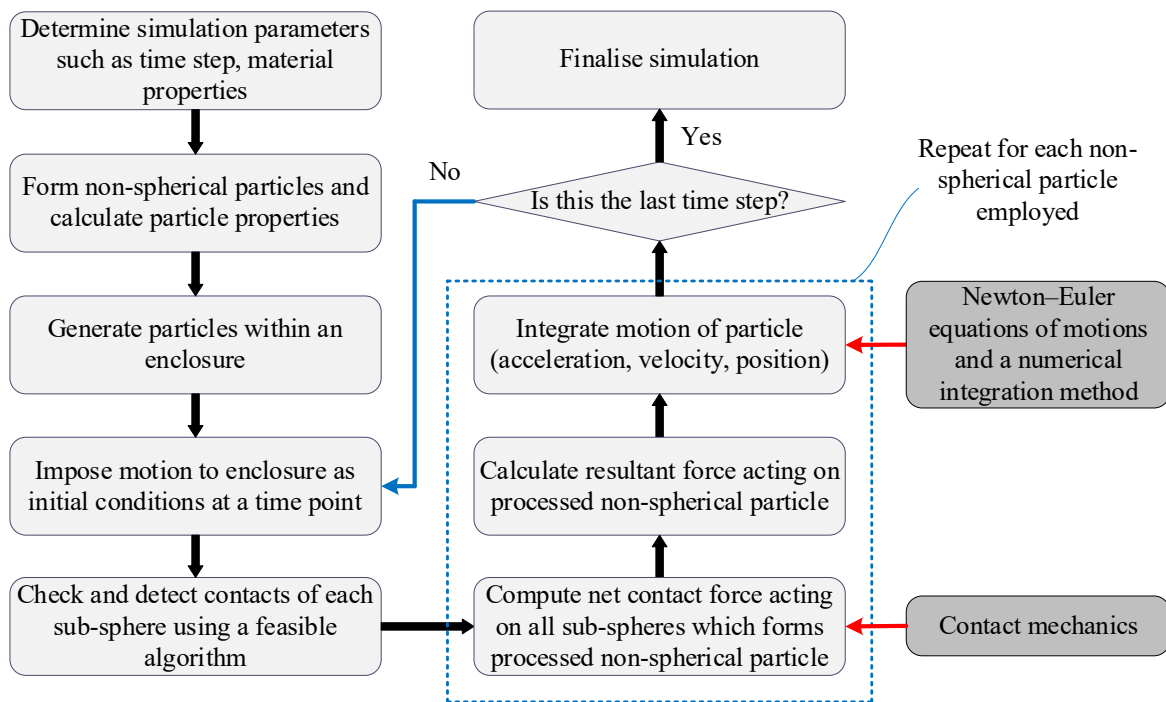
Figure 4.12: DEM simulation computation flowchart for non-spherical particles created via the multi-sphere approach.

5 Contact Force-Deformation Model for DEM Simulations

5.1 Overview

Forces acting on each particle and enclosure surface at a specific time step should be evaluated to obtain particle motions in DEM. For numerical granular damper investigations, these forces are typically modelled by computing the sum of gravitational and physical contact forces acting on each body involved. However, it should be noted that force models in DEM can also involve cohesive or adhesive forces, electrostatic forces, magnetic forces and fluid-based forces.

When two bodies (for example, particle-particle or particle-enclosure surface) are in contact, an amount of deformation is initiated on both bodies over the contact area which yield a mutual contact force acting on both bodies as opposite directions. In order to represent this behaviour in a numerical simulation, a force-deformation relation should be identified. As impacts in a granular medium tend to be oblique, it is more convenient to consider the force-deformation relation in two principal directions, i.e., normal and tangential. Thus, the contact force resulting from an interaction between two distinct bodies i and j, and acting on the body i can be written as:

$$\mathbf{F}_{\text{contact},ij} = -\left(F_{\text{contact},ij}\right)^n \mathbf{n}_{\text{contact},ij} - \left(F_{\text{contact},ij}\right)^t \mathbf{t}_{\text{contact},ij} \tag{5.1}$$

where $(F_{\text{contact},ij})^n$ is the normal contact force along the normal unit vector of contact $\mathbf{n}_{\text{contact},ij}$ and $(F_{\text{contact},ij})^t$ is the tangential contact force along the tangential unit vector of contact $\mathbf{t}_{\text{contact},ij}$. Note that the superscripts n and t represent normal and tangential directions, respectively.

Contact mechanic theories are addressed to determine the contact forces [165,166]. Utilising these theories for perfect spheres, a number of contact models has been developed and comprehensively tested in the literature [137,152,167–184].

This chapter briefly shows two contact theories (one for the normal direction and one for the tangential direction) that provide very good approximation for representing physical interactions of spheres. A computationally efficient dissipative force model is also presented here. Qualitative and quantitative analyses are conducted to show the validity and limitations of the used contact model.

5.2 Hertz Theory for Normal Contact

The Hertz elastic contact theory is widely employed to represent contacts along normal direction in DEM [5,7,57,111]. This non-linear model has been found to be very accurate and reliable while remaining computationally efficient [152,168]. Therefore, the Hertz contact model is used to represent normal contact behaviours of particle-particle and particle-enclosure interactions in DEM simulations.

Heinrich Hertz [185] originally developed the theory to represent physical normal contact problem of two non-conforming smooth elastic surfaces. This contact type is illustrated for two perfect spheres in Figure 5.1. Here, m_{particle} and R_{particle} are the mass and the radius of individual spheres; $(\delta_{\text{contact},ij})^n$ and $a_{\text{contact},ij}$ are the normal deformation (i.e. the normal overlap) and the radius of the circular contact area, respectively; $(F_{\text{contact},ij})^n$ and $(F_{\text{contact},ji})^n$

are the normal contact forces which are equal in magnitude and act on particles i and j, respectively.
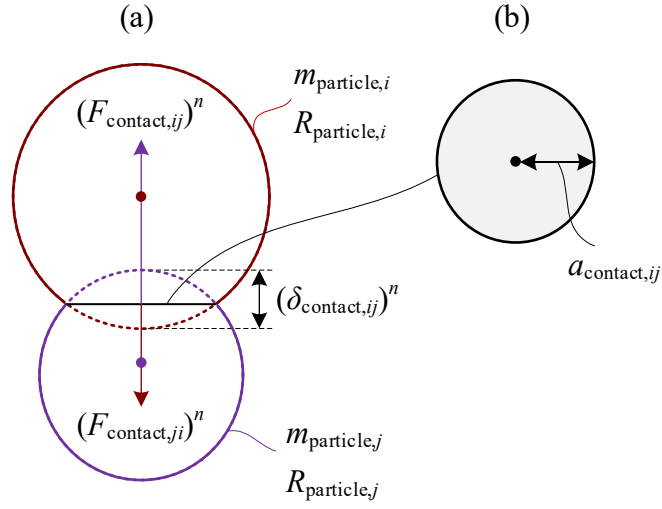
Figure 5.1: Normal contact of two interacting spheres: (a) deformed spheres and (b) circular contact area.

The Hertz theory assumes that:

i) the contacting surfaces are continuous and frictionless,

ii) the radius of circular contact area is much smaller than the radii of contacting surface curvatures,

iii) the deformations at any positions of contacting bodies rather than the contact area are negligible.

Under these assumptions, the Hertz theory approximates the pressure applied on the contact area as an elliptical distribution [165,166]:

$$\sigma_{\mathrm{contact},ij}(r;t) = \sigma_{\mathrm{contact},ij}(0;t)\sqrt{1 - \left(\frac{r}{a_{\mathrm{contact},ij}(t)}\right)^2} \tag{5.2}$$

where r depicts the radial position on the contact area ranging from 0 to $a_{\mathrm{contact},ij}$, t is the time, and $\sigma_{\mathrm{contact},ij}(0;t)$ shows the maximum pressure which occurs at the centre of contact area.

The relation between the contact area radius and the maximum pressure can be obtained considering the elasticity theory of an elastic surface subjected to a normal force [165].

$$a_{\text{contact},ij} = \sqrt{\left(\delta_{\text{contact},ij}\right)^n R_{\text{eq},ij}} \tag{5.3}$$

$$\sigma_{\text{contact},ij}(0;t) = \frac{2E_{\text{eq},ij}a_{\text{contact},ij}}{\pi R_{\text{eq},ij}} \tag{5.4}$$

Here, the equivalent radius and the equivalent elastic modulus can be obtained by:

$$R_{\text{eq},ij} = \left(\frac{1}{R_{\text{particle},i}} + \frac{1}{R_{\text{particle},j}}\right)^{-1} \tag{5.5}$$

$$E_{\text{eq},ij} = \left(\frac{\left(1 - \nu_{\text{particle},i}^2\right)}{E_{\text{particle},i}} + \frac{\left(1 - \nu_{\text{particle},j}^2\right)}{E_{\text{particle},j}}\right)^{-1} \tag{5.6}$$

where E_{particle} and ν_{particle} stand for the elastic modulus and the Poisson's ratio of individual spheres, respectively. Note that if one of the contacting bodies is a flat surface rather than a sphere (such as a segment of the enclosure mentioned in Chapter 3), it should be considered that the curvature of the relevant body would be zero.

In order to find out the normal elastic contact force depending on the normal deformation, the pressure given in Equation (5.2) is integrated over the whole contact area, and the relations provided by Equations (5.3) and (5.4) are substituted into this integral.

$$\left(F_{\text{contact},ij}\right)^n = \int_0^{a_{\text{contact},ij}} \sigma_{\text{contact},ij} 2\pi r dr = \frac{4}{3} E_{\text{eq},ij} \sqrt{R_{\text{eq},ij}} \left(\left(\delta_{\text{contact},ij}\right)^n\right)^{3/2} \tag{5.7}$$

For two impacting spheres with the normal impact velocity of $\left(\dot{\delta}_{\text{contact},ij}\right)^n(t=0)$, the maximum normal deformation that can occur is [165,166]:

$$\left(\delta_{\text{contact},ij}\right)^n \left(t = t_{\text{max,def}}\right) = \left(\frac{15 m_{\text{eq},ij} \left(\left(\dot{\delta}_{\text{contact},ij}\right)^n (t = 0)\right)^2}{16 E_{\text{eq},ij} \sqrt{R_{\text{eq},ij}}}\right)^{2/5} \tag{5.8}$$

where the equivalent mass is defined as:

$$m_{\text{eq},ij} = \left(\frac{1}{m_{\text{particle},i}} + \frac{1}{m_{\text{particle},i}}\right)^{-1} \tag{5.9}$$

and the time at which the maximum normal deformation is observed, $t_{\text{max,def}}$, is found by the following relation.

$$t_{\text{max,def}} = 1.435 \left(\frac{m_{\text{eq},ij}{}^2}{E_{\text{eq},ij}{}^2 R_{\text{eq},ij} \left(\left(\dot{\delta}_{\text{contact},ij}\right)^n (t = 0)\right)}\right)^{1/5} \tag{5.10}$$

It should be noted that the total contact time is twice that shown in Equation (5.10) for fully elastic contacts as a contact involves loading and unloading stages. Note that the estimated contact durations utilising the Hertz theory have been shown to give excellent agreement with experimental results [174,186].

As consistent with physical reality of impacts, the contact time is significantly small – especially for metallic-like hard materials which have high elastic modulus as can be realised from Equation (5.10). Therefore, impacts create large dynamic stresses on contacting bodies, and it may induce travelling dilatational waves. As a result, a great amount of impact energy can be observed at the positions of impacting bodies away from the contact area which conflicts with the Hertz theory. In order to avoid such unwanted phenomenon and sustain the validity of the Hertz theory, a limitation criteria is suggested which restricts the impact velocity according to the dilatational wave speed [165]:

$$\left(\mathrm{c}_{\mathrm{dilatational},i} \Big/ \left(\left(\dot{\delta}_{\mathrm{contact},ij} \right)^{n} \left(t = 0 \right) \right) \right)^{1/5} \gg 1 \tag{5.11}$$

where the dilatational wave speed on the sphere i is determined by:

$$\mathrm{c}_{\mathrm{dilatational},i} = \sqrt{E_{\mathrm{particle},i} \left(1 - \nu_{\mathrm{particle},i} \right) \Big/ \rho_{\mathrm{particle},i} \left(1 - \nu_{\mathrm{particle},i} - 2\nu_{\mathrm{particle},i}^{2} \right)} \tag{5.12}$$

where $\rho_{\mathrm{particle},i}$ is the density of the sphere material.

5.3 Mindlin-Deresiewicz Theory for Tangential Contact

The tangential contact force-deformation relationship is not independent from the normal direction. Thus, the normal contact behaviour should be adequately defined for an interaction before describing the tangential behaviour. In order to model such contact, the Mindlin-Deresiewicz (MD) approach has been developed assuming that the normal contact behaviour follows the Hertz theory [187].

The original MD theory considers not only elastic behaviour of a contact in the tangential direction but also involves frictional and plastic behaviour. Therefore, a hysteretic non-linear force-deformation behaviour occurs as simply shown in Figure 5.2. Since there is frictional surface interaction between contacting bodies in the tangential direction, the tangential force is limited with a friction-based force determined by the applied normal force. In fact, the existence of friction results in a separation in the tangential force-deformation behaviour: the sticking stage where the contacting bodies stick each other with a varying mutual tangential overlap and contact force up to the friction force limit and the slippage stage where the contacting bodies have relative motion with respect to each other in tangential direction with a constant tangential contact force which equals to the friction force limit.
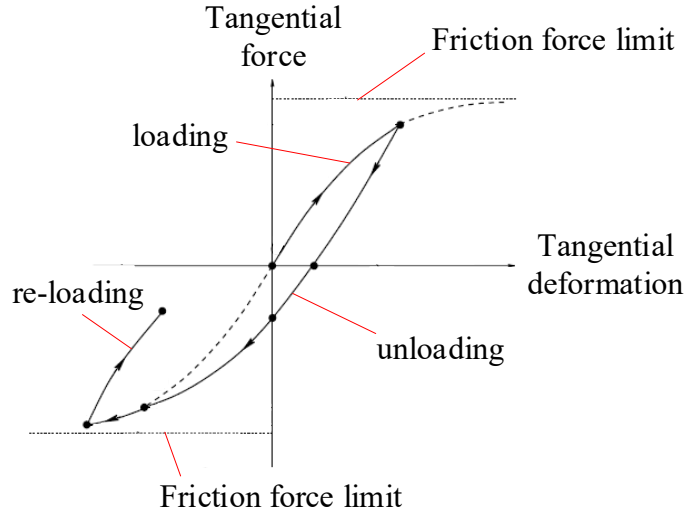
Figure 5.2: Tangential contact force-deformation relation of two contacting bodies under a constant normal force.

In case of constant normal force (similar to Figure 5.2), MD calculates the tangential contact force in the loading case incrementally [152] as shown below for a sphere-sphere contact:

$$\left(F_{\text{contact},ij}\right)^t(t) = \left(F_{\text{contact},ij}\right)^t(t-\Delta t) + \Bigg\{ 8G_{\text{eq},ij}\sqrt{R_{\text{eq},ij}\left(\delta_{\text{contact},ij}\right)^n(t)}$$

$$\sqrt{1 - \frac{16G_{\text{eq},ij}\sqrt{R_{\text{eq},ij}\left(\delta_{\text{contact},ij}\right)^n(t)}\left(\delta_{\text{contact},ij}\right)^t(t)}{3\mu_{\text{contact},ij}\left(F_{\text{contact},ij}\right)^n(t)}}$$

$$\left(\left(\delta_{\text{contact},ij}\right)^t(t) - \left(\delta_{\text{contact},ij}\right)^t(t-\Delta t)\right)\Bigg\}$$

(5.13)

where Δt is the time step; $(\delta_{\text{contact},ij})^t$ is the tangential deformation, $\mu_{\text{contact},ij}$ is the coefficient of friction, and $G_{\text{eq},ij}$ is the equivalent shear modulus determined by:

$$G_{\text{eq},ij} = \left(\frac{2-\nu_{\text{particle},i}}{G_{\text{particle},i}} + \frac{2-\nu_{\text{particle},j}}{G_{\text{particle},j}}\right)^{-1}$$

(5.14)

being G_{particle} the shear modulus of individual spheres. Note that the superscript t shows the tangential direction.

For the unloading and the re-loading cases demonstrated in Figure 5.2, Equation (5.13) slightly differs (see the reference [152] for more details), but the incremental calculation process, which needs the tangential force-deformation history, exists. This requires a large computational effort in DEM simulations when many contacts are present at each iteration time. As stated before, the demonstrated tangential force-deformation characteristic is only a limited version of MD which assumes a constant normal load. The generalised MD model considers varying normal load and varying tangential deformation which would cause even more complex and computationally more expensive solutions in DEM simulations.

By applying several subsequent simplification, various improved tangential contact force-deformation models have been proposed by Vu-Quoc et al. using particular loading cases [167,172,173,183]. However, the computational load of tangential contact force-deformation model for DEM simulations is still significant. Hence, by eliminating the inelastic part of MD (i.e., plastic deformation), Tsuji et al. analytically derived a simplified and computationally effective elastic tangential force-deformation relationship for DEM simulations [179]. In addition to the elastic tangential force, the Coulomb friction model is typically implemented into this simplified model to apply the frictional force limit. This simple model is shown in the following equation:

$$
\begin{aligned}
\left(F_{contact,ij} \right)^{t} = \left(1 - \gamma_{contact,ij} \right) 8 G_{eq,ij} \sqrt{ R_{eq,ij} \left(\delta_{contact,ij} \right)^{n} } \left(\delta_{contact,ij} \right)^{t} \\
+ \gamma_{contact,ij} \mu_{contact,ij} \left(F_{contact,ij} \right)^{n}
\end{aligned}
\tag{5.15}
$$

where the coefficient $\gamma_{contact,ij}$ establishes sticking-slipping stage as:

$$
\gamma_{contact,ij} = \begin{cases} 0 \ \ if \ \ \left| \left(F_{contact,ij} \right)^{t} \right| < \mu_{contact,ij} \left| \left(F_{contact,ij} \right)^{n} \right| \\ 1 \ \ if \ \ \left| \left(F_{contact,ij} \right)^{t} \right| > \mu_{contact,ij} \left| \left(F_{contact,ij} \right)^{n} \right| \end{cases}
\tag{5.16}
$$

It is apparent from Equation (5.15) that the elastic tangential force is linearly proportional to the tangential deformation whilst the force non-linearly depends on the normal overlap. Similar to the Hertz theory, the simplified MD model is often implemented and reliably used for DEM simulations in many different research fields [69,111,112,118,138,139].

## 5.4   Contact Force-Deformation Behaviours of Individual Contacts

To show the validity of the described contact models, a set of numerical investigations was carried out using a perfect sphere and the non-spherical particles introduced in Chapter 4. In these studies, the contact force-deformation behaviours on individual particles were examined. The numerical studies involved the theoretical evaluations from Section 5.2 and 5.3, DEM simulations implementing the described contact models and FEM analyses. As this section considers the contact behaviours of non-spherical particles, it also provides a validation of the non-spherical particles generated with the multi-sphere approach.

FEM is a well-known elasticity theory based numerical approach which discretises a continuous structure into many relatively small elements by meshing the original geometry. In this section, FEM models were used to show the validity of contact models providing the force-deformation relations of investigated contacts with smooth non-spherical particles. The fundamental properties (e.g., shape functions) and strain-stress formulations for some of the commonly used elements have been derived, validated and even catalogued for many years [188–190]. A typical three-dimensional 10-noded quadratic tetrahedral element (i.e., C3D10 in the used commercial FEM software library [191]) was used to both sufficiently discretise original particle geometries and accurately obtain strains and stresses within the elements. In order to adequately model contact areas between contacting bodies in FEM, the standard penalty formulation was utilised providing non-linear contact stiffness on contact fields [189]. It should be also noted that geometric non-linearities were taken into account in each FEM model.

First, the contact models were tested on perfect spheres. Since the presented contact models had been derived for perfectly spherical surfaces, the accuracy level of contact models should be high and, therefore, it is expected that the results from the FEM analyses are very similar to the DEM simulations or the theoretical investigations. This would show that the FEM model can reliably represent the contact behaviours between individual bodies. Afterwards, the contact models were examined on multi-sphere non-spherical particles, and the obtained results were compared with the smooth FEM models.

5.4.1   Spherical particle

The numerical models for sphere particle analysis are demonstrated in Figure 5.3. The material type for all bodies is stainless steel whose properties are shown in Table 5.1. It should be noted that the presented configurations and material properties were used for all particle investigations in Section 5.4.
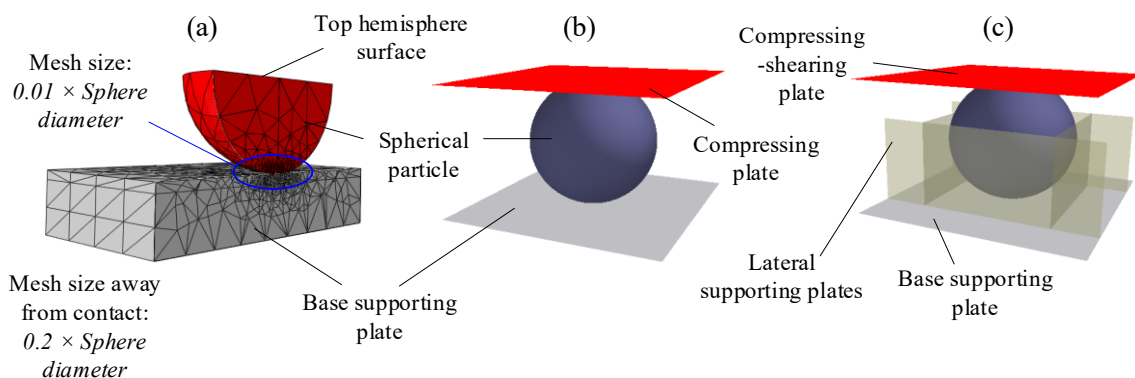
Figure 5.3: Numerical models for individual spherical particle-surface interaction investigation: (a) FEM, (b) DEM for normal contact, and (c) DEM for tangential contact.

The FEM model involved the half of the particle and a base supporting plate. The model is shown in Figure 5.3a as a cut view to demonstrate the mesh variation. Note that the compatibility of mesh was checked changing the typical mesh size and conducting re-analyses with those mesh customisations. The bottom plane of supporting plate was restricted to any translational motion to let the particle and the plate deform during contact. The investigation of normal contact was achieved imposing axial displacement to the top

surface of particle hemisphere. Although the surfaces were modelled as frictionless for the normal contact case to ensure the same assumptions as in the Hertz theory, a friction coefficient was implemented for the tangential contact investigation to assess the friction force limit. For the tangential contact analysis, a constant normal pressure was given to the hemisphere top surface to restrict slipping and, therefore, capture the sticking-slipping transition region. Then, the shear displacement was applied to the hemisphere top surface as perpendicular to the normal pressure.

Table 5.1: Material and contact properties for individual particle contact investigations.

Property	Value
Elastic modulus [GPa]	206
Poisson's ratio [-]	0.3
Density [kg/m^3]	7860
Friction coefficient for tangential interactions [-]	0.4

In the DEM models in Figure 5.3b and Figure 5.3c, the base supporting plate had the similar function as in the FEM model. Displacements for the normal and tangential investigations were imposed by the upper plates introduced in the DEM models (i.e., compressing and compressing-shearing plates) as initial motions or boundary conditions could be specified for geometric surfaces much easier than particles in DEM. Because of the same reason, four lateral supporting plates were employed in the tangential model to ensure that the required boundary conditions were met.

In Figure 5.4, the particle-surface and particle-particle contact force-deformation results are presented for 3 mm diameter spheres. Note that the DEM results mean that the results produced using the DEM model created in the commercial DEM software.

The normal and tangential displacement results are normalised dividing them by $2r_{sphere}$ where r_{sphere} is the particle radius. The normalised normal and tangential forces are obtained respectively by:

$$\text{Normalised normal contact force} = \frac{\text{Actual normal contact force}}{10^3\,E_{\text{material}}\pi r_{\text{sphere}}\delta^n{}_{\text{max}}}$$

$$\text{Normalised tangential contact force} = \frac{\text{Actual tangential contact force}}{10^3\,G_{\text{material}}\pi r_{\text{sphere}}\delta^t{}_{\text{max}}} \qquad (5.17)$$

where E_{material} is the elastic modulus of used material, G_{material} is the shear modulus that can be calculated using the elastic modulus and Poisson's ratio, $\delta^n{}_{\text{max}}$ is the maximum normal displacement applied in the test, and $\delta^n{}_{\text{max}}$ is the maximum tangential displacement applied in the test.
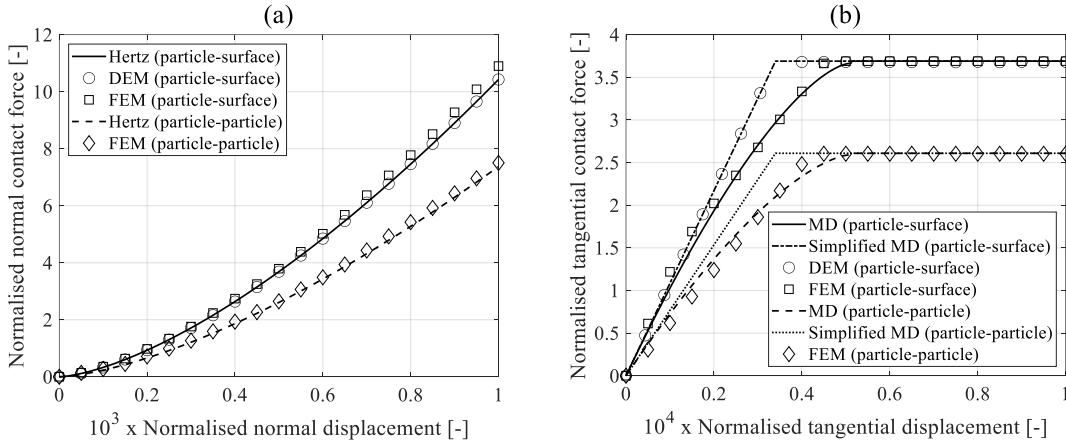
Figure 5.4: Individual contact force-deformation comparisons for a perfect sphere in (a) normal and (b) tangential directions.

For the normal direction, as shown in Figure 5.4a, the DEM particle-surface results exactly match with the Hertz as the DEM model uses this contact theory. Nearly perfect agreement is observed between the Hertz theory (or the DEM model) and the FEM model for both individual interaction types, i.e., particle-surface and particle-particle. It can be seen that the particle-particle contact induces smaller force than the particle-surface. However, they display similar force-deformation characteristics. Therefore, the particle-particle contact was not investigated for non-spherical particles for conciseness.

As illustrated in Figure 5.4b, the tangential DEM particle-surface results exactly follow the simplified MD theory as this theory is used by the DEM model. For the both particle-surface

and particle-particle contacts, the simplified MD theory slightly overestimates the exact MD theory during the sticking state, and the error increases around the sticking-slipping transition region until the friction force limit is initiated. Nevertheless, it can be said that the simplified MD is in a good agreement with the exact theory addressing its simplicity and huge computational advantage. In addition, it can be seen that the FEM model accurately follows the exact MD theory in the both interaction types.

5.4.2   Oblate spheroid particle

To assess the accuracy of the contact force-deformation behaviour for oblate spheroid particles created by the geometry mesh-based multi-sphere approach, DEM and FEM contact analyses were conducted. The investigated oblate particle shape is illustrated in Figure 5.5. The major principal dimension of the oblate particle was 3 mm while the minor principal dimension was 2.8 mm.
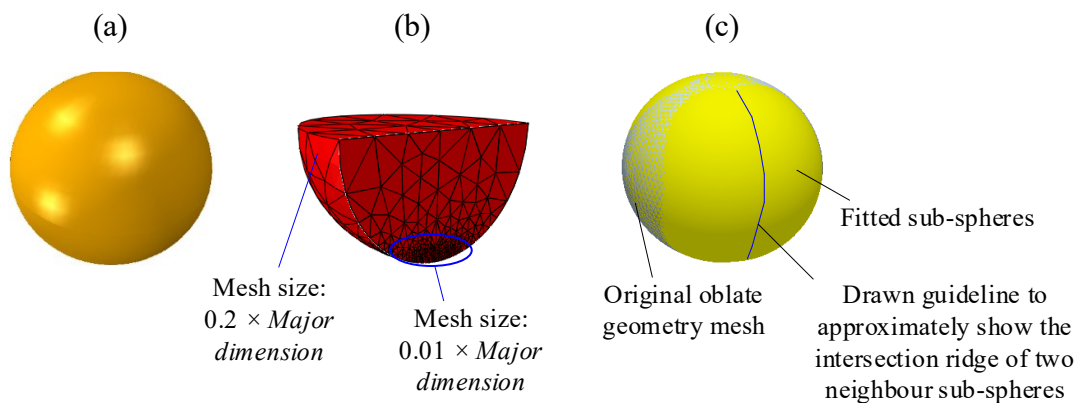
Figure 5.5: Oblate particle: (a) smooth geometry, (b) mesh of smooth geometry for FEM, and (c) multi-sphere shape for DEM with original smooth geometry mesh template.

The smooth particle geometry shown in Figure 5.5a was used for meshing process and, the meshed particle hemispheroid was obtained for the FEM investigation. The cut view of the model is demonstrated in Figure 5.5b. As shown in Figure 5.5c, the multi-sphere oblate particle does not perfectly replicate the original oblate geometry. There was about 3% error in the volume.

The investigations were conducted using the same testing configurations presented in Figure 5.3. Note that the minor dimension axis of oblate particle was the normal deformation direction. It should be noticed that only particle-surface interaction type was analysed as explained in the previous section. The normalisations made by Equation (5.17) and for displacements were similarly used for the oblate particle by replacing the sphere radius with the half of oblate minor dimension.

The contact force-deformation results are set out in Figure 5.6. Since the oblate particle was generated using the non-analytical multi-sphere algorithm (presented in Section 4.3), the alignment order of sub-spheres was not regular within the smooth oblate geometry. Therefore, a theoretical contact force-deformation relationship could not be obtained.
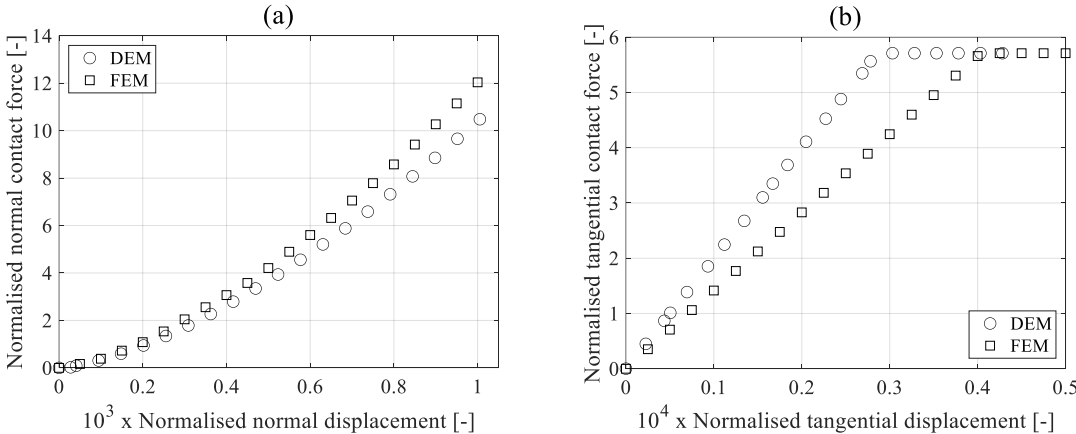
Figure 5.6: Individual contact force-deformation comparisons for an oblate spheroid in (a) normal and (b) tangential directions.

It can be said from Figure 5.6a that the multi-sphere oblate particle represents the smooth particle behaviour in normal contacts with small differences, and the error seems larger than the normal direction for the tangential direction as shown in Figure 5.6b. It should be noted that the considered contact configurations are specific and can rarely occur in a vibrated granular medium in which comprises many particles.

5.4.3 Prolate spheroid particle

One of the analytical multi-sphere non-spherical particles considered for granular dampers in this thesis is the prolate spheroid. The contact force-deformation relationship of this particle is investigated here. The particle shape is illustrated in Figure 5.7. The major principal dimension of prolate spheroid was 12 mm, and the minor dimension was 6 mm.
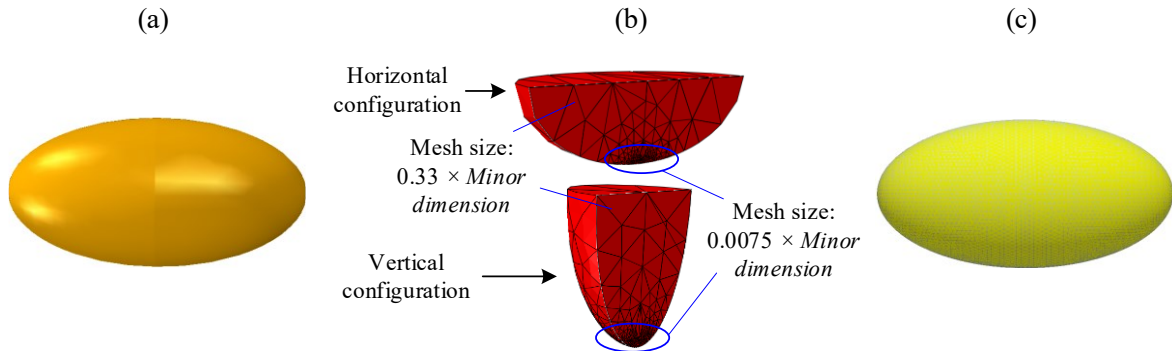

Figure 5.7: Prolate particle: (a) smooth geometry, (b) mesh of smooth geometry for FEM, and (c) multi-sphere shape for DEM with original smooth geometry mesh template.

For FEM, the smooth geometry (Figure 5.7a) was used for meshing process. Two different meshed hemispheroids were obtained. The cut views of these models are shown in Figure 5.7b. These were separately investigated in terms of contact force-deformation to show the effect of contact orientation as hinted in the previous section. In order to show the effect of number of used sub-spheres, two multi-sphere particles were generated for DEM: 21 sub-spheres and 51 sub-spheres. As shown in Figure 5.7c (51 sub-spheres), the analytical multi-sphere representation of prolate particle almost exactly matched with the original geometry mesh template. There were about 0.4% and 0.05% errors in the original particle volume with 21 sub-spheres and 51 sub-spheres, respectively.

Note that the minor dimension axis of particle was the normal deformation direction in the horizontal configuration whereas the normal deformation direction was the major dimension axis for the vertical configuration. The normalisations were done by respectively replacing

the sphere radius in Equation (5.17) and for displacements with the halves of minor and major dimensions of the prolate spheroid for the horizontal and vertical configurations.

The normal contact force-deformation comparisons for the prolate spheroid are presented in Figure 5.8a. For the horizontal case, the both created particles (21 and 51 sub-spheres) provide very consistent contact force-deformation results with the smooth FEM model at relatively small deformations. However, the higher number of sub-spheres leads to a more successful representation of the particle at larger deformations as the smaller number of sub-spheres produces lower stiffness than the smooth particle (the FEM model). When the normalised deformation exceeds 0.45, the 51 sub-spheres particle surprisingly exhibits higher stiffness than the smooth model as can be seen in Figure 5.8a. This is because of the indented structure of the multi-sphere particle surface – it has many ripples on the surface. In the DEM model, when the normal compression increases, more sub-spheres are involved in the contact (due to the deformations of the ripples) which eventually yields a higher stiffness than the smooth particle. For the 21 sub-spheres particle, the similar phenomena would be encountered at a larger deformation as it has wider overlapping segments (therefore higher ripples).
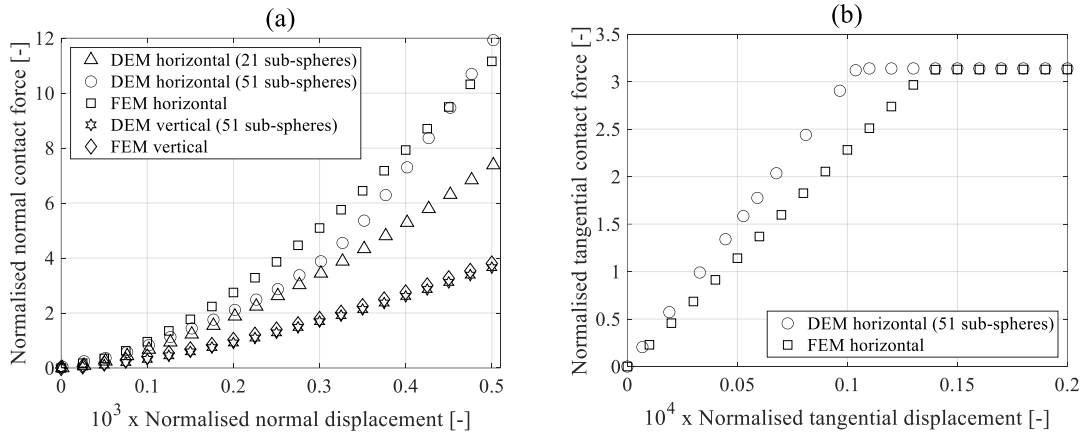
Figure 5.8: Individual contact force-deformation comparisons for a prolate spheroid in (a) normal and (b) tangential directions.
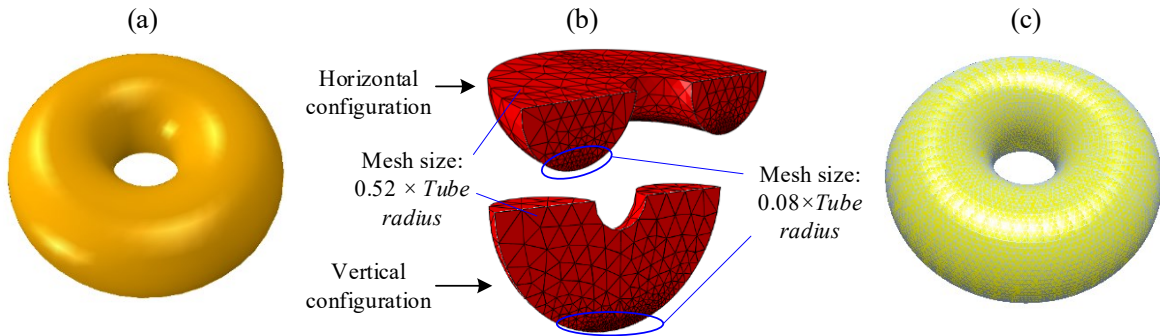
Differently aligned contacts can occur in a granular medium subjected to vibration as also mentioned in the previous section. Thus, one another specific case apart from the horizontal configuration, i.e., the vertical configuration shown in Figure 5.7b, was also investigated for the prolate particle. The results shown in Figure 5.8a indicate that the multi-sphere particle is in a greater agreement with the FEM model than the horizontal case. This finding shows that the particularly investigated interaction configurations, which many sub-sphere surfaces of the approximated particle are involved, might be the worst scenario for the contact-deformation accuracy of multi-sphere particles. As a result, as the interactions may occur in many different orientations in a granular medium – most-likely a single surface point on the particles, the force-deformation would be more accurate in DEM simulations.

The tangential contact force-deformation comparison is presented in Figure 5.8b. Note that they were carried using the horizontal configuration. It is seen that the tangential contact behaviour of smooth particle is represented by the multi-sphere particle with the maximum of 15% relative error. Increase in errors around the transition between sticking and slipping stages can be attributed to the difference between the original and simplified MD models. If one analysed the vertical case, the tangential behaviour would be the same as the spherical particles provided in Figure 5.4b as only one spherical surface would be in tangential contact in this orientation. It implies that the comment made for the normal investigations about the accuracy of differently oriented contacts is also valid for tangential contacts.

5.4.4 Circular toroid particle

Circular toroid is another analytical multi-sphere particle type investigated for granular dampers in this thesis. Individual contact force-deformation behaviours were conducted on the toroid particle demonstrated in Figure 5.9. The radius of circular toroid was 3 mm, and the tube radius was 1.15 mm.

Similar to the prolate particle case, the smooth geometry shown in Figure 5.9a was used to generate two different meshed particles for FEM analyses as shown in Figure 5.9b. These two configurations were investigated to show the effect of contact orientation for circular toroid particles. The multi-sphere circular toroid particle shown in Figure 5.9c was constructed using 50 sub-spheres. The error in the volume was about 0.59%.

(a)   (b)   (c)

Horizontal configuration

Mesh size:
0.52 × *Tube radius*

Vertical configuration

Mesh size:
0.08×*Tube radius*

Figure 5.9: Circular toroid: (a) smooth geometry, (b) mesh of smooth geometry for FEM and (c) multi-sphere shape for DEM with original smooth geometry mesh template.

As the sub-spheres are regularly aligned along the circular axis of the toroid tube, the described contact force-deformation theories (i.e., the Hertz and MD) can be easily adapted for the horizontal interaction investigations. In order to obtain the theoretical contact forces, the Hertzian force determined by Equation (5.7) and the MD forces computed with Equations (5.13) and (5.15) are multiplied by the number of sub-spheres used to construct the circular toroid particle. These theoretical and the numerical force-deformation results are illustrated in Figure 5.10. Normalisations were done by replacing the sphere radius in Equation (5.17) and for displacements with the tube radius for the horizontal configuration and with the radius of whole toroid shape for the vertical configuration.

The horizontal configuration results are shown in Figure 5.10. As the DEM model uses the contact theories, the DEM results exactly replicate the theories as seen in the normal contact investigation of 50 sub-spheres particle in Figure 5.10a. As expected from the theoretical engagement, increasing number of sub-spheres produces stiffer normal contact behaviour.
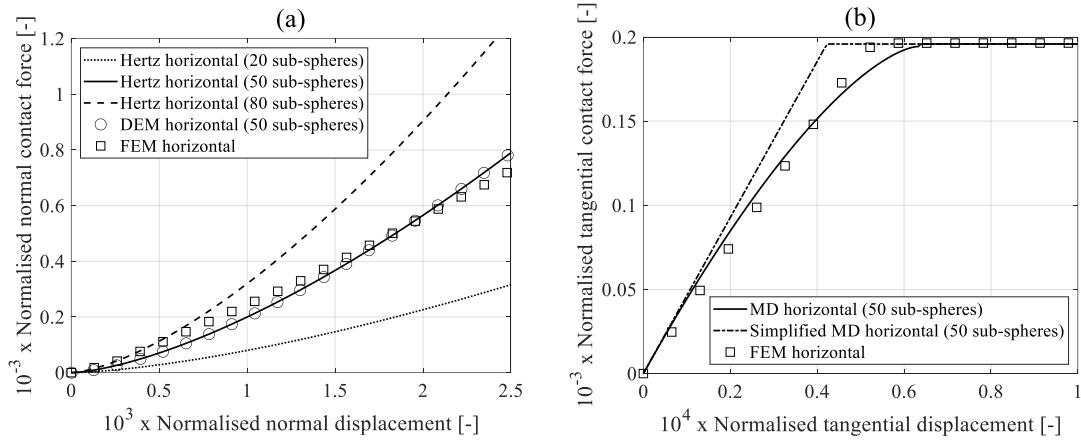
Figure 5.10: Individual contact force-deformation comparisons for a circular toroid in (a) normal and (b) tangential directions for horizontal configuration.

It can be seen from Figure 5.10a, the DEM and Hertz theory results show non-linear characteristics as expected, however, the smooth FEM model exhibits rather linear relationship. This is because the FEM model has a line contact in the horizontal configuration which indicates a linear contact area increasing rate with deformation. Still, it can be said that the multi-sphere particle can still approximate the smooth particle if an adequate number of sub-spheres is employed. For example, using 50 sub-spheres, a sufficient multi-sphere representation can be obtained producing relatively small errors in the normal and tangential directions shown in Figure 5.10a and Figure 5.10b.

When comparing the multi-sphere toroid particle with the smooth one from the FEM model in Figure 5.10a, it can be said that higher number of sub-spheres leads to more accurate representation of the circular toroid at small deformations (for example smaller than 0.5 in Figure 5.10a), but not at large deformations. It increasingly exhibits non-realistic contact force-deformation characteristics at relatively large normal deformations providing much stiffer contact than the smooth particle.

This is related to the height of the ripples on the particle surface emerged from the overlapping sub-spheres. It is because the normal contact theory fails for the multi-sphere toroid particle (in case of the horizontal contact configuration) if the deformation exceeds

the height of the ripples. This limit case can be determined considering the indented structure on the particle surface. The figure which shows two intersecting neighbour sub-spheres in a circular toroid multi-sphere particle is shown in Figure 4.10. It is re-sketched including the limit normal deformation (the height of the ripples) in Figure 5.11.
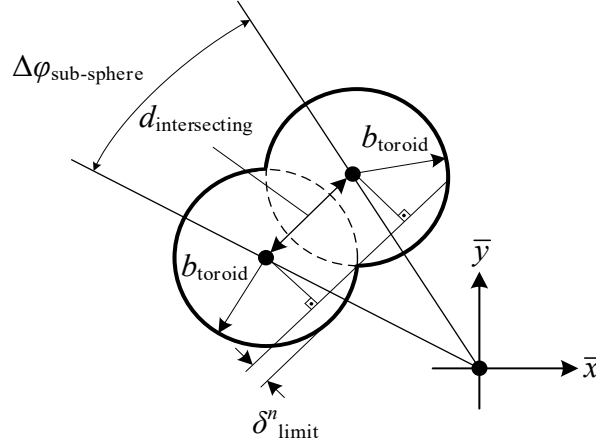
Figure 5.11: Limit normal deformation of a multi-sphere toroid particle.

Assuming small intersecting angle between two sub-spheres ($\Delta\varphi_{\text{sub-sphere}}$) or large number of used sub-spheres (n), the intersecting distance can be simplified as:

$$d_{\text{intersecting}} \approx a_{\text{toroid}}\Delta\varphi_{\text{sub-sphere}} = a_{\text{toroid}}\frac{2\pi}{n} \tag{5.18}$$

where a_{toroid} is the radius of overall toroid shape. The limit of normal deformation for the horizontal contact configuration is therefore obtained as:

$$\delta^{n}_{\text{limit}} \approx b_{\text{toroid}} - \sqrt{b_{\text{toroid}}^{2} - \left(\frac{a_{\text{toroid}}\pi}{n}\right)^{2}} \tag{5.19}$$

If one calculates this limit for the use of 50 sub-spheres toroid case whose normal force-deformation behaviour is demonstrated in Figure 5.10a, the non-dimensional displacement limit is obtained about 2.5×10^{-3} which approximately estimates the deformation at which the multi-sphere particle is no longer valid to represent the smooth particle. It is because its stiffness exceeds the actual stiffness (of the smooth particle) for larger deformations than

this value – see Figure 5.10a for justification. This particular result shows that the proposed multi-sphere approach for generating circular toroid particles in DEM has a maximum deformation threshold in a completely horizontal contact configuration and this limitation can be accurately estimated by Equation (5.19).

Equation (5.19) can be re-arranged and a maximum limit can be found for the number of sub-spheres as:

$$n_{\mathrm{max}} \approx \frac{a_{\mathrm{toroid}}\pi}{\sqrt{b_{\mathrm{toroid}}^{2} - \left(b_{\mathrm{toroid}} - \delta^{n}_{\mathrm{limit}}\right)^{2}}} \tag{5.20}$$

The maximum number of sub-spheres in terms of normalised normal displacement is shown in Figure 5.12 for different dimensional ratios. Since the limit is larger for lower number of sub-spheres, the number of sub-spheres should be accordingly reduced to capture accurate behaviour at the interested deformation range. On the other hand, wider hole indicates more separated sub-sphere alignments and larger ripples and, thus, it is possible to use more sub-spheres without exceeding the maximum normal deformation threshold.
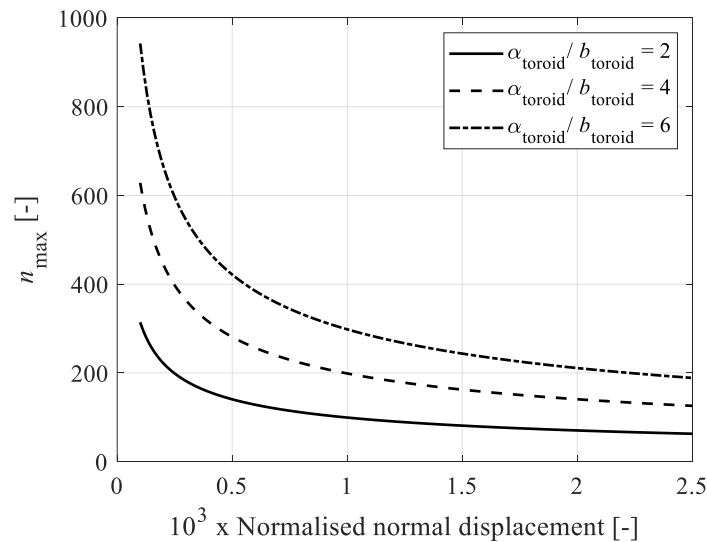
Figure 5.12: Maximum number of sub-spheres in multi-sphere circular toroid particle depending on normal deformation.

As also discussed before, the horizontal contact configuration is a particular interaction type which possibly produces the worst estimation scenario for the force-deformation relationship of multi-sphere particles. Therefore, the vertical configuration shown in Figure 5.9b was proposed for investigation. The FEM and DEM results for the vertical contact configuration are shown in Figure 5.13. Since this interaction produces a circular contact for both models in contrast to the horizontal case, the force-deformation characteristic of DEM is more consistent with the FEM model.
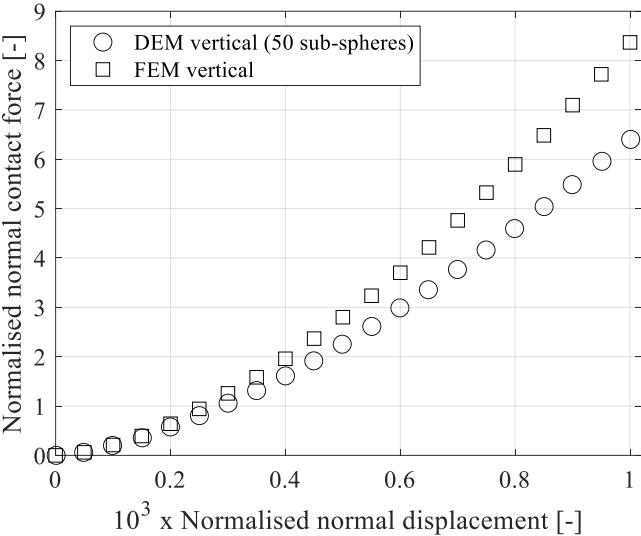
Figure 5.13: Individual contact force-deformation comparison for a circular toroid in normal contact for vertical configuration.

5.5 Inclusion of Impact-Based Dissipative Forces

In the previous sections, the contact models and numerical investigations have considered contact force-deformation behaviour assuming fully elastic impacts. However, impacts are never fully elastic in a realistic physical environment – i.e., an amount of energy is dissipated during an impact because of material inelasticity. Here, these inelastic events are included in the elastic contact models by implementing impact-based dissipative forces. The dissipative components of contact forces are considered for perfect spheres only addressing

that the non-spherical particles are generated via the multi-sphere approach. Note that frictional dissipation is already included in the tangential contact model.

5.5.1 Damped contact forces and DEM contact modelling

In the DEM environment, contact regions are modelled as deformable to represent contact force-deformation behaviour. Therefore, contact regions are simply represented by spring, dashpot and friction elements as illustrated in Figure 5.14.
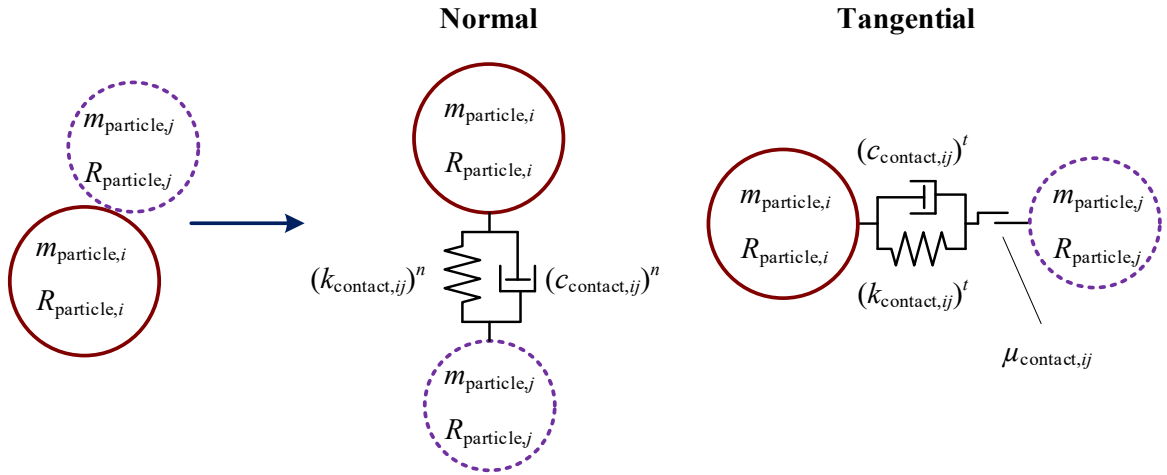
Figure 5.14: Overall contact model for DEM.

Utilising this stiffness-dashpot-friction representation, the normal and tangential contact forces introduced in Equation (5.1) are obtained as damped, respectively:

$$\left(F_{\text{contact},ij}\right)^n = \left(k_{\text{contact},ij}\right)^n \left(\delta_{\text{contact},ij}\right)^n + \left(c_{\text{contact},ij}\right)^n \left(\dot{\delta}_{\text{contact},ij}\right)^n \tag{5.21}$$

$$\begin{aligned}\left(F_{\text{contact},ij}\right)^t &= \left(1 - \gamma_{\text{contact},ij}\right)\left[\left(k_{\text{contact},ij}\right)^t \left(\delta_{\text{contact},ij}\right)^t + \left(c_{\text{contact},ij}\right)^t \left(\dot{\delta}_{\text{contact},ij}\right)^t\right] \\ &+ \gamma_{\text{contact},ij}\mu_{\text{contact},ij}\left(F_{\text{contact},ij}\right)^n\end{aligned} \tag{5.22}$$

where the non-linear normal and tangential stiffness coefficients, $\left(k_{\text{contact},ij}\right)^n$ and $\left(k_{\text{contact},ij}\right)^t$, are respectively derived from the Hertz theory (Equation (5.7)) and the simplified MD theory (Equation (5.15)) as:

$$\left(k_{\text{contact},ij}\right)^n = \frac{4}{3} E_{\text{eq},ij} \sqrt{R_{\text{eq},ij} \left(\delta_{\text{contact},ij}\right)^n} \tag{5.23}$$

$$\left(k_{\text{contact},ij}\right)^{t} = 8G_{\text{eq},ij}\sqrt{R_{\text{eq},ij}\left(\delta_{\text{contact},ij}\right)^{n}} \qquad (5.24)$$

It should be noted that all parameter definitions used in the above relations are already provided in Section 5.1, Section 5.2 and Section 5.3 except the normal and tangential contact damping terms, $\left(c_{\text{contact},ij}\right)^{n}$ and $\left(c_{\text{contact},ij}\right)^{t}$, which result from inelastic impacts. The determination of these terms is discussed in the subsequent sub-sections.

5.5.2 Coefficient of restitution

The inelasticity level of an impact can be associated with the coefficient of restitution (COR) [177,178,192–197]. This is a normalised measure of energy dissipated during an impact. COR is typically defined between two co-axially impacting (e.g., along normal direction) spheres i and j as:

$$e_{\text{contact},ij} = \frac{\left(\dot{\delta}_{\text{contact},ij}\right)^{n}\left(t = t_{\text{final}}\right)}{\left(\dot{\delta}_{\text{contact},ij}\right)^{n}\left(t = t_{\text{initial}}\right)} \qquad (5.25)$$

where $\left(\dot{\delta}_{\text{contact},ij}\right)^{n}\left(t = t_{\text{initial}}\right)$ and $\left(\dot{\delta}_{\text{contact},ij}\right)^{n}\left(t = t_{\text{final}}\right)$ are the normal relative velocities at contact initiation and separation, respectively. For fully elastic impacts, the contact duration (i.e., $t_{\text{final}} - t_{\text{initial}}$) can be approximated by $2t_{\text{max,def}}$ where $t_{\text{max,def}}$ is given by Equation (5.10) and Equation (5.25) produces 1. However, for inelastic impacts, the contact duration is smaller than $2t_{\text{max,def}}$, and COR becomes smaller than 1.

COR depends on both intensity of impact (i.e., impact velocity) and material properties [177,197]. The measurement of COR can be found in the literature for a range of material types using a number of different experimental setups [67,135,158,175,195,196,198].

It has been experimentally demonstrated that COR generally decreases with increasing impact velocity which means more energy dissipation for a contact [174,186,199]. As can

be seen in Figure 5.15, this decreasing relationship is more apparent after a certain velocity whilst COR is nearly constant for the velocities smaller than this threshold. The impact-based dissipation at the relative velocities smaller than this threshold can be considered as viscoelastic dissipation whereas it is mainly plastic dissipation at larger velocities [177,199,200].
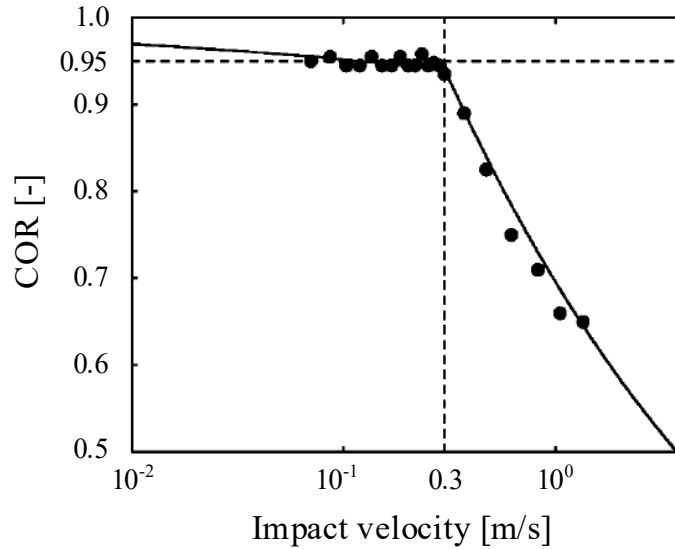
Figure 5.15: COR obtained from the contact between a steel sphere (12.7 mm in diameter) and a thick steel block: measured (discrete points) [186] and velocity-dependent representative function (flat line) [200].

This critical velocity is defined as the yield velocity [166,201], and it mostly depends on the yield strength of impacting bodies [192,193]. For example, it has been measured as approximately 10 m/s for nylon spheres with diameters ranging between 6.35 mm and 25.4 mm [199], while it has been around 0.3 m/s for the 12.7 mm chrome steel spheres as shown in Figure 5.15. The yield velocity can be approximated calculating the maximum pressure on the circular contacting area between two contacting surfaces. Employing the Hertz contact theory, Johnson [166] presents a relation for this:

$$v_{yield,ij} = \sqrt{\frac{107 R_{eq,ij}^{3} \sigma_{yield,ij}^{5}}{E_{eq,ij}^{4} m_{eq,ij}}} \tag{5.26}$$

where $\sigma_{\text{yield},ij}$ is the yield strength of sphere material and the other parameters are described in Section 5.2.

5.5.3 Contact damping in terms of COR

If impact velocity is smaller than the yield velocity, the damping ratio of a contact, ζ_{contact} can be expressed as a function of COR [197] – see Figure 5.15. This can be shown using the SDOF system presented in Figure 5.16 which represents a normal impact between a sphere and a rigid flat surface. Note that the contact stiffness in this model, $k_{\text{contact,eq}}$, is assumed to be a constant for simplicity, and the contact initiates at exactly $t = 0$.
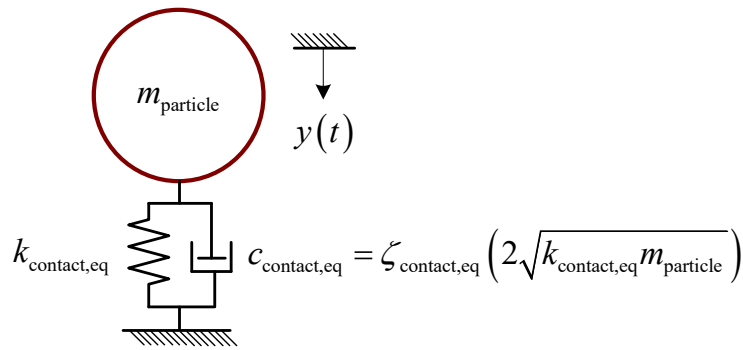
Figure 5.16: SDOF representation of a normal contact.

The equation of motion that governs the impact and the initial conditions are:

$$m_{\text{particle}}\ddot{y} + c_{\text{contact,eq}}\dot{y} + k_{\text{contact,eq}}y = 0; \quad y(0) = 0, \ \dot{y}(0) = v_{\text{impact}} \tag{5.27}$$

where v_{impact} is the impact velocity at which the contact initiates.

There are mainly two different approaches to solve this equation of motion depending on the estimation of contact end time [197]. The most common one assumes that the contact finishes when the contacting bodies are separated from each other [197,202,203], i.e., $y(t_{\text{contact}}) = 0$ where t_{contact} is the contact duration. The solution of this approach is demonstrated in Figure 5.17. In the figure, the contact deformation, velocity and force were provided by normalising them as:

$$\text{Normalised deformation} = y \,/\, \left(v_{\text{impact}} \sqrt{k_{\text{contact,eq}} \,/\, m_{\text{particle}}} \right)$$

$$\text{Normalised velocity} = \dot{y} \,/\, v_{\text{impact}} \tag{5.28}$$

$$\text{Normalised force} = \left(-c_{\text{contact,eq}} \dot{y} - k_{\text{contact,eq}} y \right) \Big/ \left(m_{\text{particle}} v_{\text{impact}} \sqrt{k_{\text{contact,eq}} \,/\, m_{\text{particle}}} \right)$$
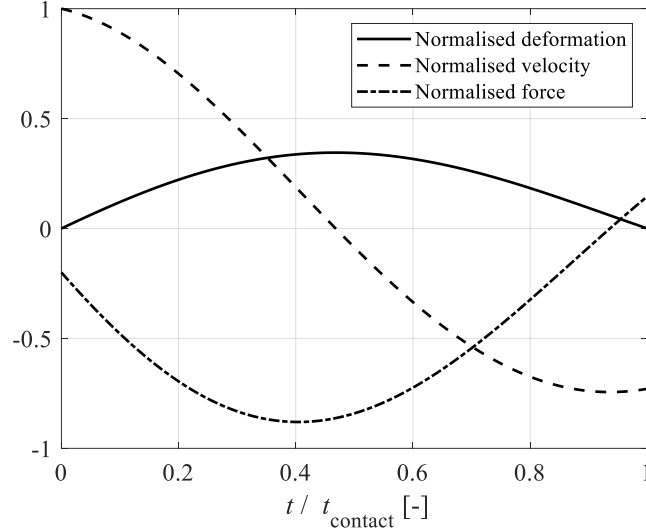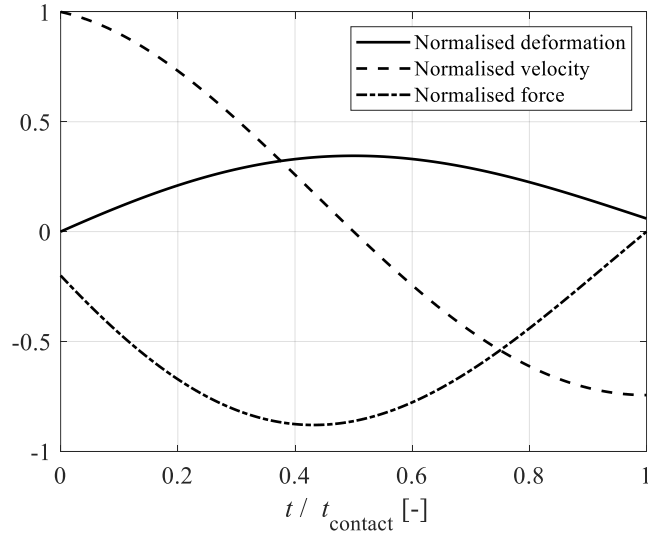

Figure 5.17: Contact deformation, velocity and force for no deformation case at contact end.

Note that this approach yields the following relation for the contact damping ratio:

$$\zeta_{\text{contact}} = -\frac{\ln\left(e_{\text{contact}}\right)}{\sqrt{\left\{ \ln\left(e_{\text{contact}}\right) \right\}^2 + \pi^2}} \tag{5.29}$$

As can be seen in Figure 5.17, this approach produces an attractive force slightly before the end of the contact, i.e., positive contact force. However, it is known that the contact force should always be repulsive during the contact as there is no adhesive forces [197]. This shows that the contact can end before the initiated deformation is completely restored [180]. Therefore, the second solution approach assumes that the contact finishes when the contact force is zero [197,204]. In this case, the contact responses are as in Figure 5.18, and the relation between the contact damping ratio and COR becomes:

$$\ln\left(e_{\text{contact}}\right) = -\frac{2\zeta_{\text{contact}}}{\sqrt{1 - \zeta_{\text{contact}}^2}} \tan^{-1}\left(\frac{\sqrt{1 - \zeta_{\text{contact}}^2}}{\zeta_{\text{contact}}} \right) \tag{5.30}$$

Figure 5.18: Contact deformation, velocity and force for no force case at contact end.

Both approaches produce a linear damping coefficient, $c_{\text{contact,eq}}$, as they are derived by supposing linear contact stiffness in the SDOF model provided in Figure 5.16. As a result, the contact forces shown in Figure 5.17 and Figure 5.18 are non-zero at the beginning of contact. Tsuji et al. [179] used non-linear stiffness as given by Equation (5.23) and proposed a non-linear expression for the viscous damping coefficient which ensures that the contact force is zero at the start of contact. In this case, the damping ratio is obtained as:

$$\zeta_{\text{contact}} = -\frac{\sqrt{5}}{2} \frac{\ln\left(e_{\text{contact}}\right)}{\sqrt{\left\{\ln\left(e_{\text{contact}}\right)\right\}^2 + \pi^2}} \tag{5.31}$$

The contact damping ratio is shown in Figure 5.19 for each approach presented depending on COR. As can be seen in this figure, although the assumptions made in the approaches are different there are slight variations between the different approaches for small damping (i.e., $\zeta_{\text{contact}} < 0.1$).
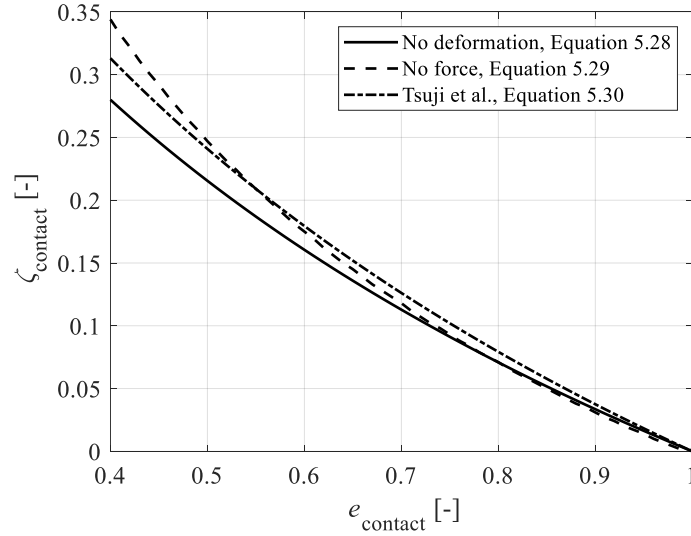
Figure 5.19: COR-dependent contact damping ratio comparisons.

The approach, developed by Tsuji et al. [179], was used in the contact model used for DEM simulations of this thesis. Employing this approach, the normal viscous damping coefficient is determined as:

$$\left(c_{contact,ij}\right)^n = -\sqrt{5}\,\frac{\ln\left(e_{contact}\right)}{\sqrt{\left\{\ln\left(e_{contact}\right)\right\}^2 + \pi^2}}\sqrt{\left(k_{contact,ij}\right)^n m^{eq}} \tag{5.32}$$

and the tangential viscous damping coefficient is similarly obtained as:

$$\left(c_{contact,ij}\right)^t = -\sqrt{\frac{10}{3}}\,\frac{\ln\left(e_{contact}\right)}{\sqrt{\left\{\ln\left(e_{contact}\right)\right\}^2 + \pi^2}}\sqrt{\left(k_{contact,ij}\right)^t m^{eq}} \tag{5.33}$$

It should be noted here that several research studies have modelled the tangential contact as a friction element for granular material simulations [94,95,120,142,143]. However, it has been reported that the existence of other elements (i.e., spring and damping) provides more accurate representation of tangential interactions [83,182].

5.5.4 Case studies

The damped contact model has been extensively compared with experimental results and found to agree by different authors in literature [174,180]. As it offers efficient computations

in DEM while maintaining accuracy, this verified contact model has been successfully used for a variety of numerical granular studies [39,59,68,111,138,170].

In this section, works were carried out to both understand the validity limit of the non-linear impact contact model and provide a general understanding of inelastic impact behaviour of particles. To achieve this, normal impact contacts were considered. The experimental and elastic-plastic FEM analysis observations obtained in the literature were used as a reference. Note that Equation (5.27) with the non-linear contact stiffness (Equation (5.23)) and the non-linear damping (Equation (5.32)) were used to simulate impact behaviour.

First, the model is compared with the experimental case study from Mishra et al. [168] in Figure 5.20. In this experimental investigation, Mishra et al. measured the contact behaviour of a steel particle (the material properties can be found in Table 5.1) dropped on a flat block. In this experiment, the particle was 40 mm in diameter, and the impact velocity of particle was about 2.4 m/s. The ratio of impact velocity to the yield velocity (can be calculated using Equation (5.26) where the yield strength of steel is 1350 MPa) was 8.1. This ratio showed that the impact occurred at a velocity larger than the yield velocity. Note that lower this ratio (or higher COR) indicates more accurate representation of impact contact with the contact model used. Typical COR value of steel balls for this impact velocity is about 0.57 [200].

As can be seen in Figure 5.20, even at such a large impact velocity, the contact model provides a good representation. The contact duration is slightly underestimated, the peak force and maximum deformation are obtained with a slight error. The dissipated energy (during the contact) calculated by the damped contact model agrees with the experiment – 0.47 J by the experiment and 0.50 J by the contact model.
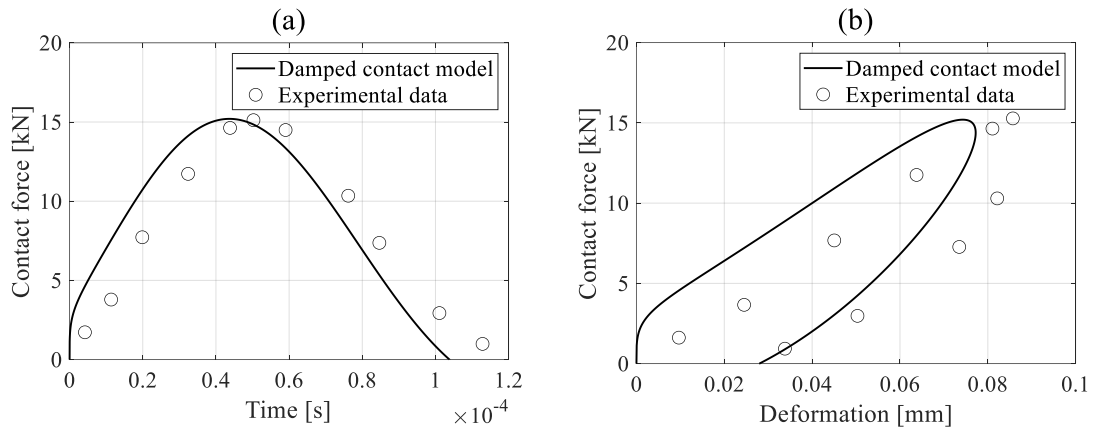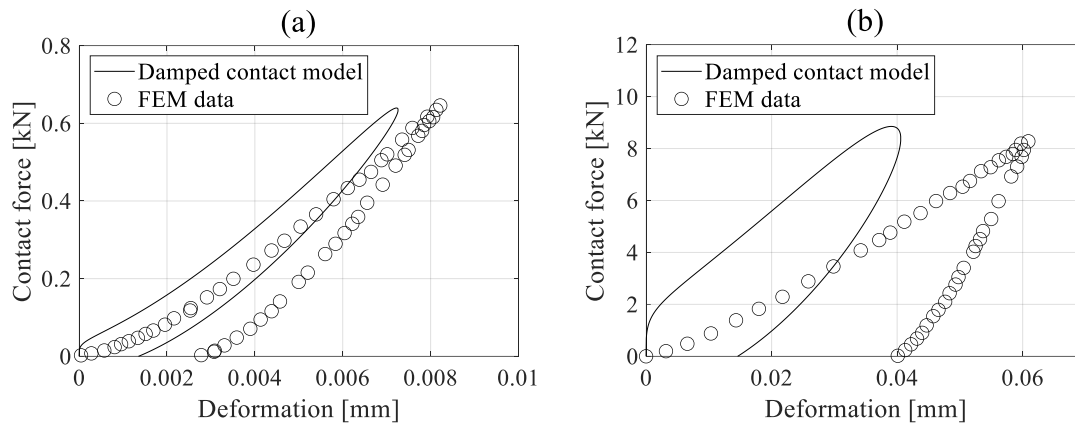
Figure 5.20: Contact behaviour between a steel ball and a flat rigid surface: (a) contact force-duration and (b) contact force-deformation relationships.

To show the effect of the ratio of impact velocity to the yield velocity, a FEM case study conducted by Vu-Quoc's research team [205] was considered. In this study, an aluminium ball impacted on a rigid wall with different velocities. The properties can be found in Table 5.2.

Table 5.2: Properties of impact investigations from the reference [205].

Property	Value
Elastic modulus [GPa]	70
Poisson's ratio [-]	0.3
Density [kg/m^3]	2699
Yield strength [MPa]	100
Particle diameter [mm]	200
Yield velocity [m/s]	0.0016
Tested impact velocities [m/s]	0.02, 0,20
Impact velocity/Yield velocity	12.2, 122
COR values for tested velocities	0.81, 0.56

The damped contact model is compared with the reference FEM results [205] in Figure 5.21. As can be observed, the model significantly differs from the FEM results when the impact velocity increases in terms of contact deformation. However, the dissipated energy and the peak force are very similar. As a result, it can be said that the contact model represents physical contacts successfully if the ratio of the impact velocity to the yield velocity is sufficiently small.

Figure 5.21: Contact force-deformation behaviour between an aluminium ball and a flat rigid surface with impact velocities of: (a) 0.02 m/s and (b) 0.2 m/s.

5.6 Chapter Summary and Conclusions

In this chapter, two well-tested and widely-used contact models (i.e., the Hertz theory for normal contacts and the Mindlin-Deresiewicz theory for tangential contacts) have been investigated as the contact model for granular damper simulations in DEM. The contact model has been verified using the FEM contact analyses for spherical particles. The model has been implemented for the multi-sphere non-spherical particle models. The DEM contact force-deformation behaviours have been compared with the FEM contact analysis results obtained using smooth non-spherical particle surfaces, and the limitations for the contact model have been discussed for non-spherical particles.

In order to apply impact dissipation into the contact model, a computationally efficient method has been addressed with the corresponding detailed explanations. The validity and the limitations of this method have been discussed comparing the damped contact model with the literature results. It has been demonstrated that the contact model can be reliably used as long as the ratio of impact velocity to the particle yield velocity is sufficiently low.

106

6 Granular Energy Dissipation and Dynamic Motional Phase

6.1 Overview

This chapter proposes a general relationship between the energy dissipation effectiveness of granular dampers and granular medium motional state. This allows understanding the dissipative potential of different motional mechanisms, and, as a result, identify efficient and inefficient dynamic particle motion types, which directly affect granular damper designs. The work is conducted performing numerical simulations of granular dampers (constructed using spherical particles) subjected to sinusoidal vibrations over a broad range of frequencies and amplitudes. In this way, measurements in any motional phase can be obtained while allowing greater control of excitation conditions and parameters than experiments.

6.2 Modelling approach

As discussed in Section 2.3, structure-independent modelling of granular dampers was used to investigate the granular dampers. Therefore, only the motion and interaction of discrete bodies (i.e., particles) and surrounding boundaries (i.e., enclosure walls) had to be described in numerical models – see Figure 6.1.

The DEM approach, whose principles and computational properties were discussed for spherical particles in Chapter 3, was utilised to model numerical granular dampers. In this work, the DEM damper models were subjected to vibrational excitations. The displacements

and rotations of each particle were computed at small discretised time points. In the simulations, the deformation of spherical particles was assumed small with respect to the diameter – for example; 0.04 mm maximum deformation was observed for 5 mm diameter particles under the most intense loading case simulated (i.e., $\Gamma = 100$ at 20 Hz). This indicated that particles could be considered as perfect spheres when defining properties used in the equations of motion and identifying contact with other particles or the walls. It should be noted that the theoretical force-deformation model described in Chapter 5 was employed for each sphere-sphere or sphere-enclosure wall contact.

6.2.1 Model

The granular damper model used in this chapter is illustrated in Figure 6.1. The model consisted of a cylindrical enclosure and a number of spherical particles. As the gravity-to-vibration orientation can affect the granular motional phases, two different model configurations were considered in this study: vertical and horizontal.
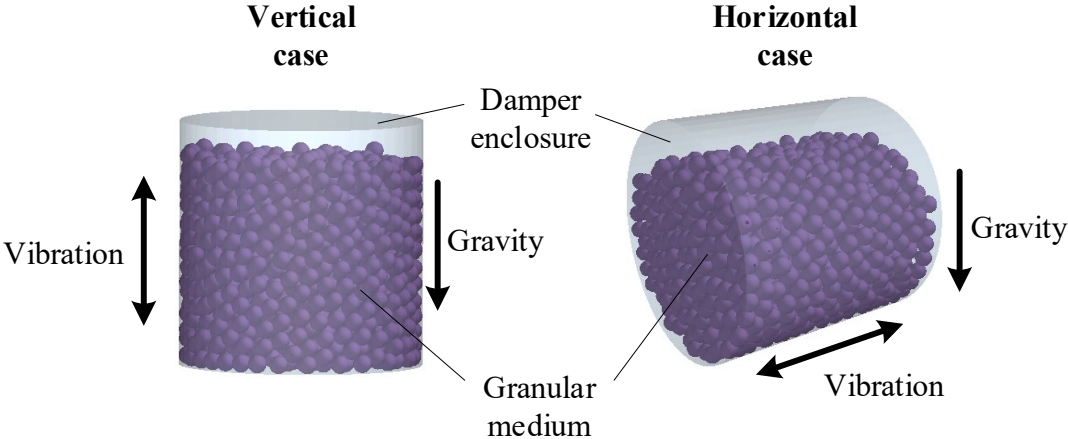
Figure 6.1: A granular damper model in vertical and horizontal gravity-to-vibration orientation cases.

In order to investigate the effect of particle size, four different particle diameters were simulated as shown in Table 6.1. To allow consistent comparisons, the total particle mass (and therefore the total particle volume) was kept constant for each particle diameter. Thus, the number of particles were set accordingly.

The dimensions of the cylindrical enclosure are also shown in Table 6.1. To analyse the effect of volume fill ratio and observe various phases, four different enclosure heights were used. Note that the volume fill ratio was described as:

$$\upsilon = N_{\text{particle}} V_{\text{particle}} / V_{\text{enclosure}}$$
(6.1)

where V_{particle} is the volume of a particle and $V_{\text{enclosure}}$ is the enclosure volume.

Table 6.1: Damper model and simulation properties.

Property	Value
Enclosure diameter [m]	0.040
Enclosure heights, L [m]	0.040, 0.045, 0.050, 0.055
Volume fill ratios, υ [-]	0.466, 0.415, 0.373, 0.339
Particle diameters [mm]	3, 4, 5, 6
Number of particles, N_{particle} [-]	1659, 700, 358, 207
Dimensionless excitation acceleration, Γ [-]	1, 1.5, 2, 3, 4, 5, 6, 7, 8, 10, 12, 15, 20, 30, 40, 50, 60, 80, 100
Excitation frequency [Hz]	20, 40, 80, 125, 160, 200, 320, 625, 1024
Gravitational acceleration, g [m/s^2]	9.81
Rayleigh time step [s]	8.4×10^{-6}
Simulation time step, Δt [s]	1×10^{-6}
Pre-simulation step [s]	0.2

For each configuration, particles were randomly initialised inside the enclosure void and allowed settling under the effect of gravity. Afterwards, to apply vibrational motion, the axial position of enclosure was changed with time prescribing the motion function as:

$$u = \frac{\Gamma g}{\omega^2} \sin(\omega t)$$
(6.2)

where t and ω are the time and the excitation frequency (in rad/s). Wide excitation amplitude and frequency ranges were used as given in Table 6.1.

6.2.2 Material

Although much harder materials are typically used for granular dampers such as steel, a hard polymer material, acrylic polymer produced from polymethyl methacrylate, was deliberately

selected for these studies. The typical properties of this material type can be found in Table 6.2.

Table 6.2: Typical material properties of acrylic polymer.

Property	Value
Elastic modulus [GPa]	3.3
Poisson's ratio [-]	0.37
Density [kg/m^3]	1190
Yield strength [MPa]	125

The most important practical advantages of using the chosen material are summarised below.

i. It increases contact durations, and, therefore allows a larger critical time step in DEM models as a result of relatively low elastic (and shear) modulus – see Equations (3.31) and (5.10) for clarification. This significantly reduces the computational cost of simulations.

ii. Owing to low modulus, the yield velocity becomes larger, see Equation (5.26) for justification. This maintains the validity of the contact model for larger collision velocities, as discussed in Section 5.5. For example; the yield velocity of sphere-sphere collision is 3.5 m/s for acrylic whilst it is 0.15 m/s for steel. To verify that the ratio of impact velocities to the yield velocity is sufficiently low, the maximum particle-particle impact velocity encountered in the simulations was obtained for 5 mm diameter spheres. The maximum impact velocity was found as 4.3 m/s, and the ratio of maximum impact velocity to the yield velocity was therefore 1.2 which can be regarded as adequate considering the discussions in Section 5.5.4.

As discussed in Chapters 3 and 5, contact properties (for example; COR and COF) are needed for DEM to model contacts. Therefore, they were determined from the literature studies which use the same damper material [86,142]. COR and COF were set as 0.86 and 0.52, respectively, for all contact types. Note that a constant value for COR was used because

the ratio of impact velocity to the yield velocity does not exceed 1 much for contacts in simulations – see Figure 5.15 for justification.

6.2.3   Quantification of granular damping

As DEM is a time-discretised approach, the total dissipated energy in a period of time can be cumulatively computed by summing the dissipation over each time step. Supposing that the target is to calculate the total dissipated energy from the start of a simulation (i.e., $t = 0$) to an arbitrary time, t, it is formulated as:

$$E_{\text{dissipated}}\left(t\right) = \sum_{k=1}^{t/\Delta t} \Delta E_{\text{dissipated}}\left(t_k = k\Delta t\right) \tag{6.3}$$

where Δt is the simulation time step and t_k represents the time points at the end of each time step. Assuming that the energy dissipation arises from only the described contact forces, the dissipation at each time step, $\Delta E_{\text{dissipated}}$, can be obtained considering all particles and contacts as:

$$\Delta E_{\text{dissipated}}\left(t_k\right) = \sum_{i=1}^{N_{\text{particle}}} \sum_{j=1}^{N_{\text{contact},i}} \begin{Bmatrix} F_{\text{contact},ij}^{\;nd}\left(t_k\right)\left(\delta_{ij}^{\;n}\left(t_k\right) - \delta_{ij}^{\;n}\left(t_k - \Delta t\right)\right) + \\ F_{\text{contact},ij}^{\;td}\left(t_k\right)\left(\delta_{ij}^{\;t}\left(t_k\right) - \delta_{ij}^{\;t}\left(t_k - \Delta t\right)\right) \end{Bmatrix} \tag{6.4}$$

where $N_{\text{contact},i}$ is the total number of contacts that particle i has, $\delta_{ij}^{\;nd}$ and $\delta_{ij}^{\;td}$ are respectively normal and tangential deformation at the contact between particle i and particle (or enclosure surface) j, and $F_{\text{contact},ij}^{\;nd}$ and $F_{\text{contact},ij}^{\;td}$ are the dissipative components of contact forces at normal and tangential directions, respectively.

As Equation (6.4) requires the deformations at a previous time step, it causes significant computational load in a simulation. Thus, supposing that the time step is sufficiently small, the deformations can be approximated as:

$$\delta_{ij}{}^{n}(t_k) - \delta_{ij}{}^{n}(t_k - \Delta t) \approx \underbrace{\left.\frac{d\delta_{ij}{}^{n}}{dt}\right|_{t_k}}_{v_{\text{rel},ij}{}^{n}(t_k)} \Delta t \tag{6.5}$$

$$\delta_{ij}{}^{t}(t_k) - \delta_{ij}{}^{t}(t_k - \Delta t) \approx \underbrace{\left.\frac{d\delta_{ij}{}^{t}}{dt}\right|_{t_k}}_{v_{\text{rel},ij}{}^{t}(t_k)} \Delta t \tag{6.6}$$

where $v_{\text{rel},ij}{}^{n}$ and $v_{\text{rel},ij}{}^{t}$ are the relative velocities between particles at normal and tangential directions, respectively. By writing Equation (6.5) and Equation (6.6) into Equation (6.4), the energy dissipated over each time step becomes:

$$\Delta E_{\text{dissipated}}(t_k) = \sum_{i=1}^{N_{\text{particle}}} \sum_{j=1}^{N_{\text{contact},i}} \left\{ F_{\text{contact},ij}{}^{nd}(t_k) v_{\text{rel},ij}{}^{n}(t_k) + F_{\text{contact},ij}{}^{td}(t_k) v_{\text{rel},ij}{}^{t}(t_k) \right\} \Delta t \tag{6.7}$$

In order to provide consistent comparisons for different excitation conditions, a normalised damping measure (the damping efficiency) was used to represent the effectiveness of granular energy dissipation in this thesis. The definition of the granular damping efficiency is the ratio of dissipated energy in a vibration cycle, $\tilde{E}_{\text{dissipated}}$, to the maximum energy that can be dissipated in a vibration cycle, $\tilde{E}_{\text{dissipated}}{}^{\max}$.

$$\eta_{\text{granular}} = \tilde{E}_{\text{dissipated}} / \tilde{E}_{\text{dissipated}}{}^{\max} \tag{6.8}$$

As the energy dissipation is complex and non-linear in granular dampers, the dissipated energy differs from one vibration cycle to another even in nominally steady-state conditions. Therefore, the dissipated energy in a vibration cycle was obtained as an average value over a number of nominally steady-state vibration cycles. This can be expressed as:

$$\tilde{E}_{\text{dissipated}} = \frac{E_{\text{dissipated}}(t_{\text{initial}}) - E_{\text{dissipated}}(t_{\text{final}})}{t_{\text{final}} - t_{\text{initial}}} \frac{2\pi}{\omega} \tag{6.9}$$

112

where t_{initial} and t_{final} are respectively the time at which the steady-state vibration begins and the time at which the simulation ends. Note that each excitation condition was simulated 8 complete vibration cycle and the last 5 of those were considered as the steady-state in the simulations of this chapter as it was seen from trial simulations that most of transient effects were eliminated within the first 3 cycles.

For the maximum achievable energy dissipation in Equation (6.8), the definition used by the Humboldt university research team [10,77,91,110] was used, which gives:

$$\tilde{E}_{\text{dissipated}}{}^{\max} = 2\left(\frac{1}{2}\left(2\frac{\Gamma g}{\omega}\right)^2 \sum_{i=1}^{N_{\text{particle}}} m_{\text{particle},i}\right) = 4\left(\frac{\Gamma g}{\omega}\right)^2 \sum_{i=1}^{N_{\text{particle}}} m_{\text{particle},i} \tag{6.10}$$

where $m_{\text{particle},i}$ is the mass of particle i. The physical explanation for this equation is that

    i.   all the particles within the damper move as an agglomerated mass,

    ii.   it collides with the both ends of enclosure in a vibration cycle with a velocity which is twice that of the enclosure maximum velocity,

    iii.   and COR of these collisions is assumed to be 0 which means that the kinetic energy is completely dissipated.

It should be noted that different authors have used alternative expressions for the maximum dissipated energy in Equation (6.8) by providing different perspectives [65,78]. However, these differ from Equation (6.10) by only a constant scaling factor.

6.3   Relationship Between Motional Phase Map and Damping Effectiveness

Granular motional phases were identified through both the visual observation of particle movements from the recorded simulation animations and the instantaneous particle velocity vectors from the stored simulation histories. This was performed for each excitation

condition simulated – see Table 6.1. The aim was to name the motional behaviours observed as consistent with those already discussed in the literature review (see Section 2.5). It should be also mentioned that a phase name assigned for a particular excitation was determined by the type of dynamic motion appeared to dominate the granular medium as particle motion changes were gradual rather than sudden. Note that the illustration and detailed explanation of each particular motional phase observed are provided in Section 6.4.

The observed motional phases were mapped over the investigated frequency-amplitude space. For a particle size, the constructed phase maps are shown in Figure 6.2 and Figure 6.3 for varying volume fill ratio in the vertical and horizontal cases.

As can be seen, seven different phases in the vertical case and four different phases in the horizontal case were identified. As discussed in Section 2.5, they can be classified as five principal phases: solid-like, fluidisation-based, convection-based, gas-like and bouncing bed. However, the gas-like phase was not encountered within the investigated excitation conditions. Therefore, only the onset amplitude boundaries of bouncing bed, $\Gamma_{bouncing\ bed}$, fluidisation, $\Gamma_{fluidisation}$, and convection, $\Gamma_{convection}$, are approximately shown on the phase maps.

There is no fluidisation onset amplitude boundary shown on the horizontal phase maps because of the selection of excitation limits – no solid-like phase was observed at $\Gamma = 1$ in the horizontal case. Apart from that, Figure 6.2 and Figure 6.3 demonstrate the same formation of phase variations on the frequency-amplitude space. In both excitation orientations, the bouncing bed onset amplitude increases and the bouncing bed region becomes narrower as the volume fill ratio decreases.
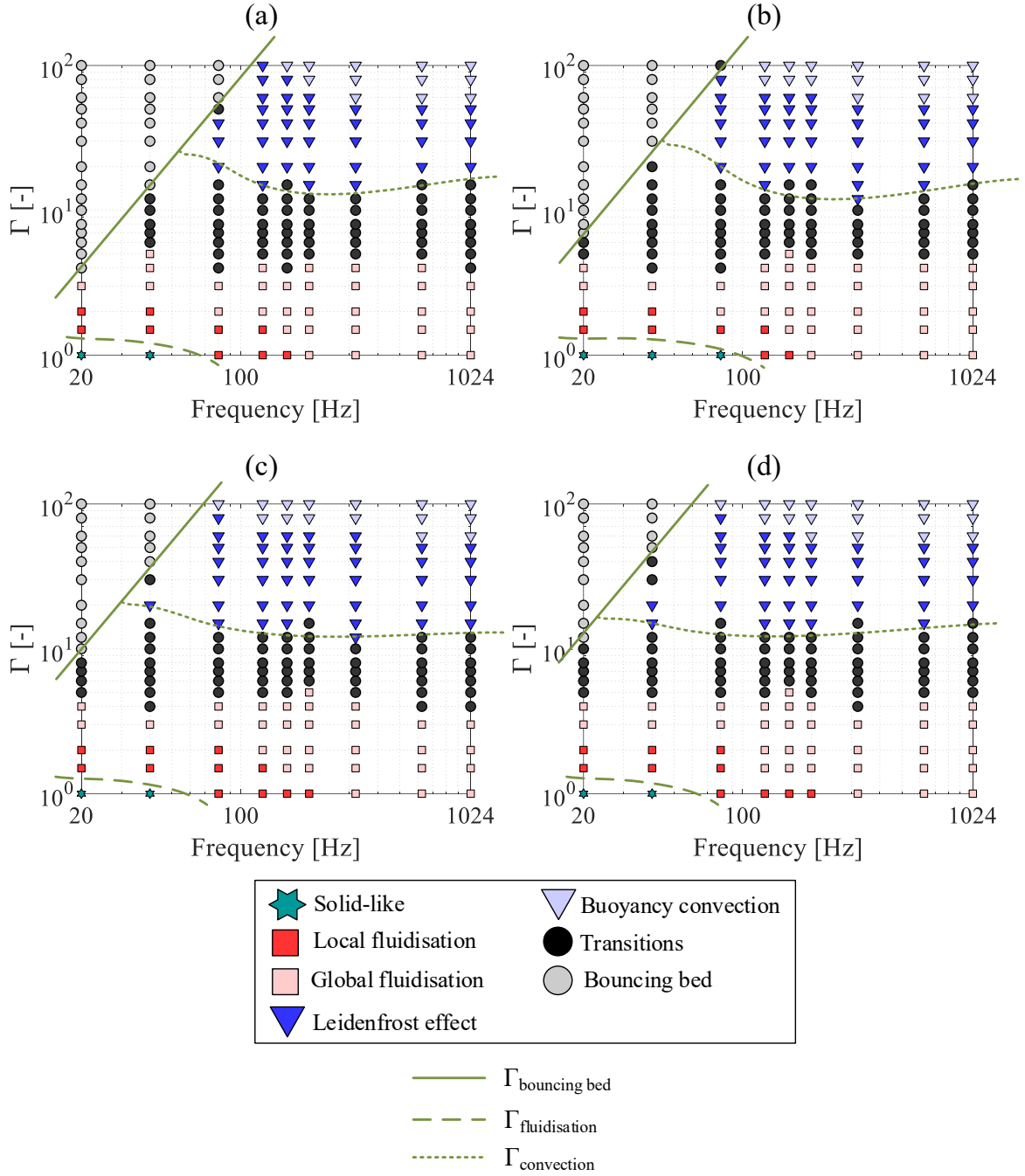
Figure 6.2: Motional phase maps of 5 mm spheres for vertical case: (a) $v = 0.466$, (b) $v = 0.415$, (c) $v = 0.373$, and (d) $v = 0.339$.
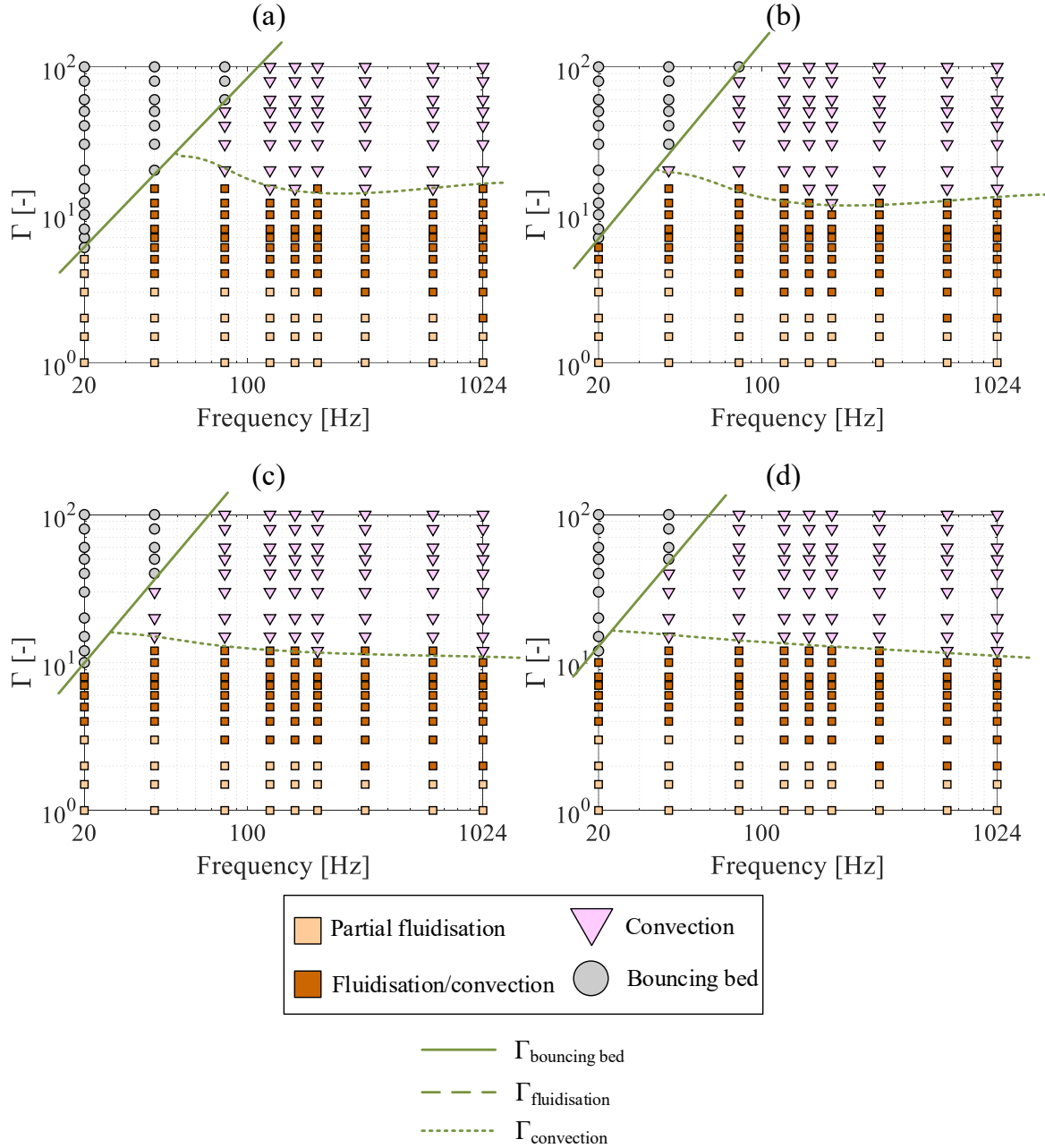
Figure 6.3: Motional phase maps of 5 mm spheres for horizontal case: (a) $v = 0.466$, (b) $v = 0.415$, (c) $v = 0.373$, and (d) $v = 0.339$.

Energy dissipation performance was also evaluated for the same excitation ranges as the phase maps presented by computing the granular damping efficiency as discussed in Section 6.2.3. The contour plots of the damping efficiency are shown in Figure 6.4 and Figure 6.5 for both excitation orientations. It should be noted that only a few damping efficiency levels

were used in these contour plots to clearly highlight the zones from low to high energy dissipation effectiveness.
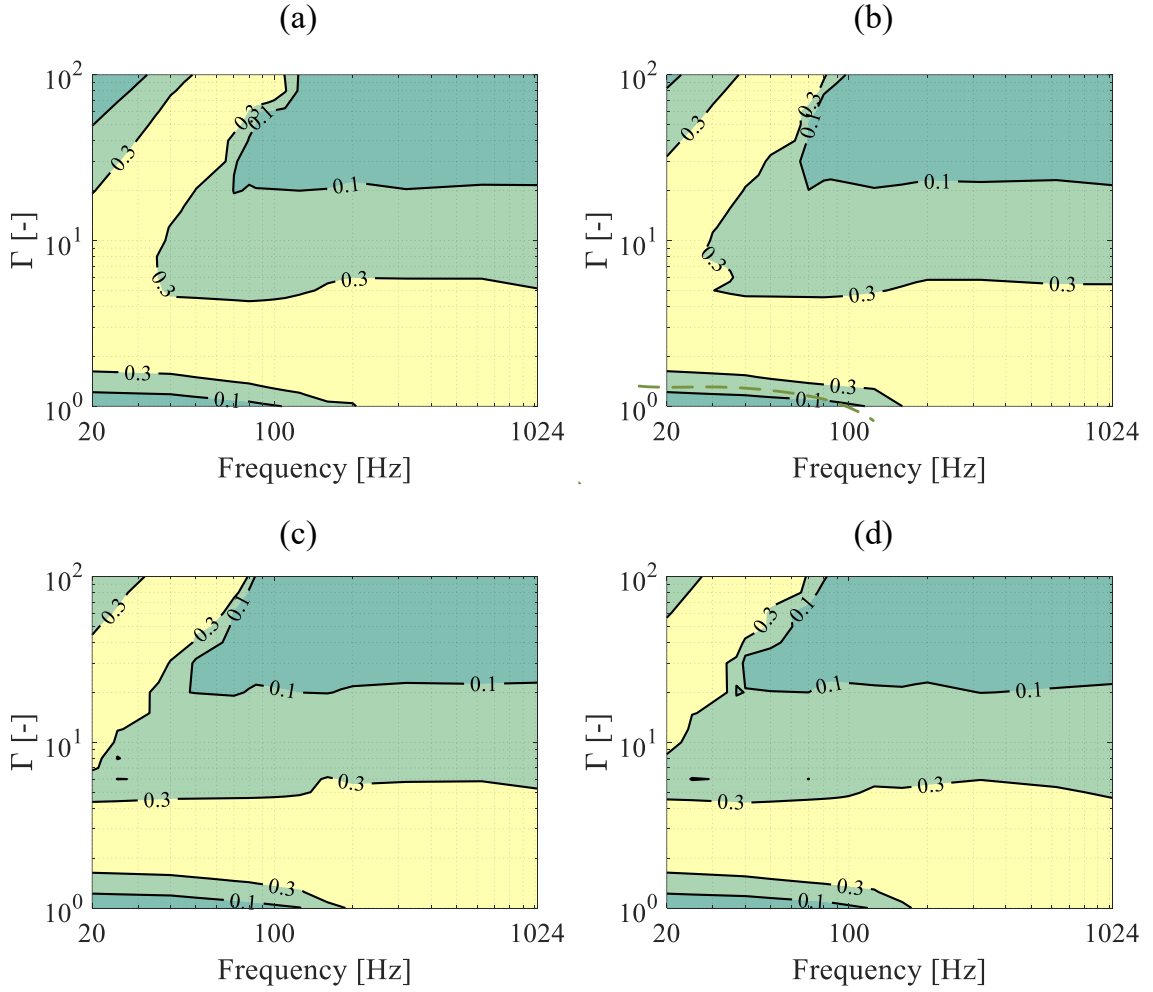
Figure 6.4: Granular damping efficiency contour plots of 5 mm spheres for vertical case: (a) $v = 0.466$, (b) $v = 0.415$, (c) $v = 0.373$, and (d) $v = 0.339$.

By comparing Figure 6.4 and Figure 6.5, it can be seen that the vertical and horizontal orientation cases have the same form despite minor differences. For each volume fill ratio studied, both orientation cases explicitly show two distinguishable areas of high energy dissipation effectiveness. These areas can be identified as ridges in the contour plots – i.e., yellow zones on the plots where $\eta_{granular} > 0.3$. One of those runs diagonally and the other one runs across the whole frequency axis as nearly horizontal.
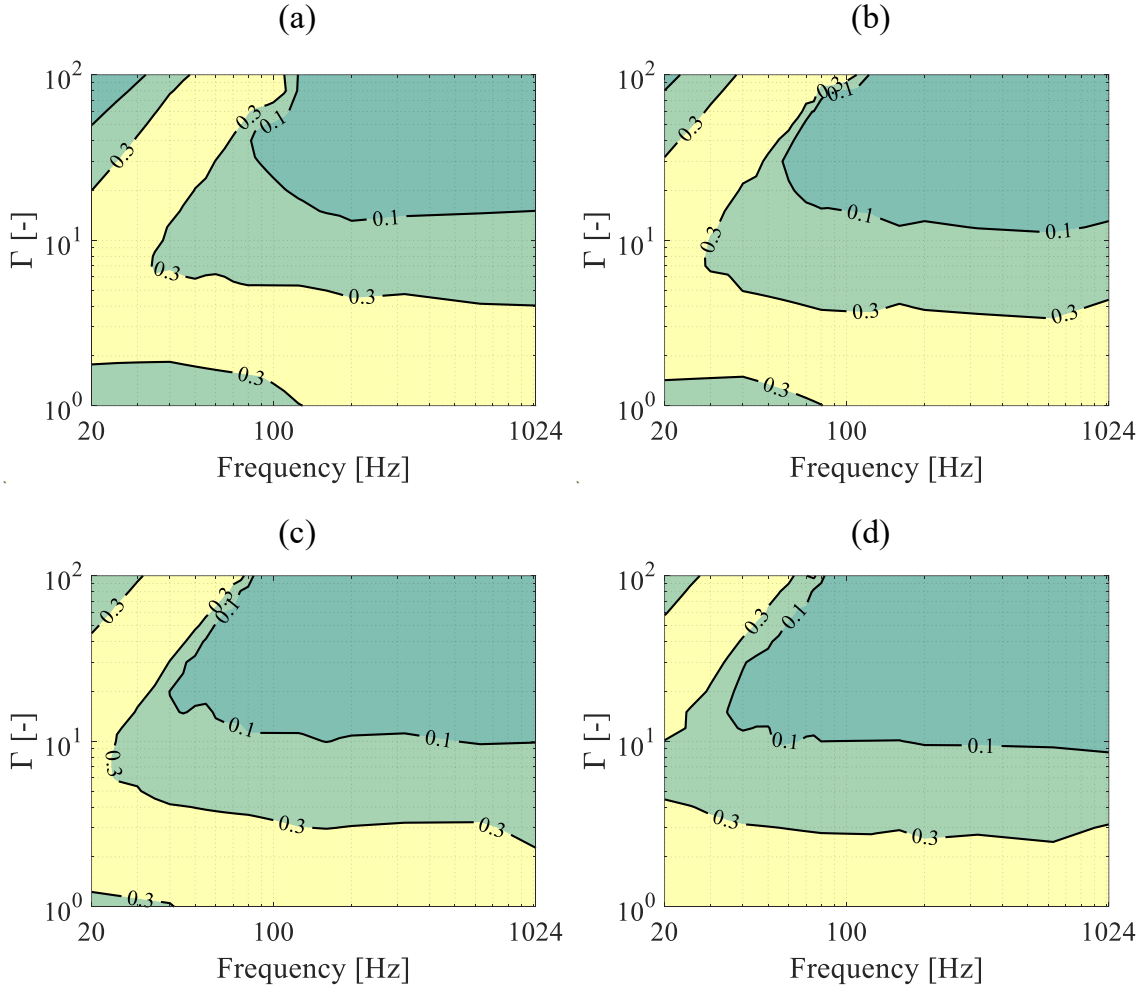
Figure 6.5: Granular damping efficiency contour plots of 5 mm spheres for horizontal case: (a) $v = 0.466$, (b) $v = 0.415$, (c) $v = 0.373$, and (d) $v = 0.339$.

Comparison of the phase maps (Figure 6.2 and Figure 6.3) and the damping efficiency maps (Figure 6.4 and Figure 6.5) clearly indicates that the different damping efficiency zones arise from the different operating motional phases. The diagonal high energy dissipation effectiveness ridge occurs when the bouncing bed phase commences for both excitation orientation cases. The relatively frequency-independent high energy dissipation effectiveness ridge is observed within the global fluidisation for the vertical case and the partial fluidisation for the horizontal case. As a result, it can be said that the factors that affect the occurrences of these two high damping efficiency zones are different from each other.

The detailed discussions on the granular energy dissipation effectiveness of each particular motional type are conducted in the next section. Whilst the presented figures above are obtained for 5 mm spheres, the other particle sizes considered provides similar motional and dissipation behaviour on the frequency-amplitude space. Thus, the effect of particle size is discussed along with the particular motion type investigation in the next section.

6.4   Granular Energy Dissipation Behaviour in Different Phases

The dissipative effectiveness of each particular motional behaviour is studied here in three sub-sections. First, the bouncing bed phase, where the most effective energy dissipation is observed, is investigated. Then, the solid-like phase, which exhibits insignificant energy dissipation, is briefly shown. In the third sub-section, the gradual dissipative and motional changes from the fluidisation-based phases to the convection-based phases are discussed.

6.4.1   Bouncing bed phase

The bouncing bed phase, sometimes referred as "two-sided bouncing bed" and "collect-and-collide" in the literature, was observed in low frequency and high amplitude conditions for the vertical and horizontal excitations in the simulations conducted as shown in Figure 6.2 and Figure 6.3. It is stated in the previous section addressing Figure 6.4 and Figure 6.5 that this phase creates a diagonal high damping efficiency ridge on the frequency-amplitude space.

As illustrated in Figure 6.6, the damping particles moves together in a closely packed arrangement and collectively collide with each end wall of the enclosure in the bouncing bed phase. Note that these collective collisions periodically occur in a vibration cycle – twice per cycle.

Phase	$t = 0$	$t = \pi/\omega$	$t = 2\pi/\omega$	Characteristic motional features

Bouncing bed

Approximated granular medium area

Relative motion in contacting bodies:

- Particles collect in a compact arrangement and collide with the enclosure each time it changes direction
- Primary particle motion is in the same orientation as the enclosure motion
- Significant relative motion between particles only occurs during each collective collision event

From simulation:

1.2$g\Gamma/\omega$

0.6$g\Gamma/\omega$

0

Figure 6.6: Bouncing bed motional phase.

The duration of each collective collision is short in comparison with the period of vibration of the enclosure. A large amount of momentum is transferred between the enclosure and the body of particles over this short duration. This, therefore, induces large contact forces and significant relative motions between the particles during a collective collision. As a result, a high level of energy dissipation is observed. Between these collisions, the particles form a compact particle bed exhibiting negligible relative motions with respect to each other. The cumulative energy dissipation history has a staircase-like shape at which two steps occur in a cycle as can be seen in Figure 6.7. Figure 6.7 also shows that each collective collision is observed earlier in the cycle and vibrational energy is dissipated over a shorter collisional period as the vibration intensity increases in the bouncing bed phase.
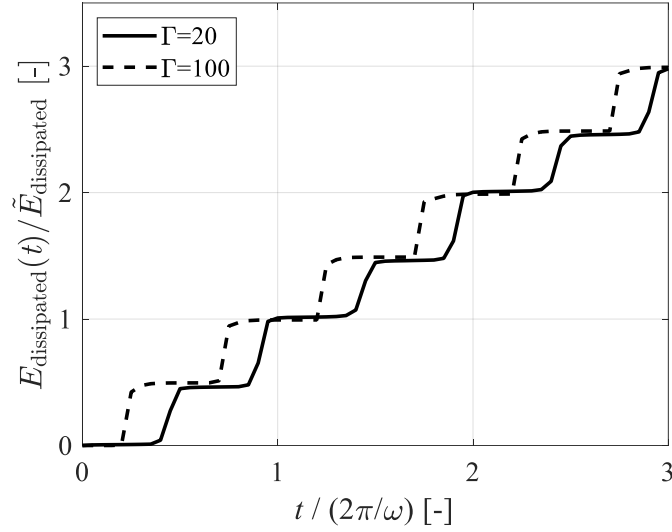
Figure 6.7: Steady-state granular energy dissipation histories with 5 mm spheres under vertical 40 Hz vibration, $v = 0.466$.

The granular damping efficiency results at 20 Hz and 40 Hz, where the bouncing bed phase can be observed, are provided in Figure 6.8 and Figure 6.9. In order to be consistent with Figure 6.4 and Figure 6.5, $\eta_{granular} = 0.3$ level is also shown.

Comparing these graphs (Figure 6.8 and Figure 6.9) with the corresponding phase maps given in Figure 6.2 and Figure 6.3, it is apparent that the damping efficiency reaches a maximum in the bouncing bed phase for each volume fill ratio, excitation orientation and frequency. Once this optimum is achieved, increasing in the amplitude results in gradual decreasing in the damping efficiency. It indicates that the average dissipated energy increases with amplitude at a slower rate than $\tilde{E}_{dissipated}^{max}$ beyond the optimum. However, the rate of this decrease is lower than the rate of the increase in the damping efficiency just before the peak amplitude. This creates a relatively broad excitation amplitude range beyond the optimum for effective damper operation – see the diagonal high damping efficiency ridges in Figure 6.4 and Figure 6.5. Thus, it can be said that a damper design that operates at amplitudes larger than the optimum is more robust to uncertainty.
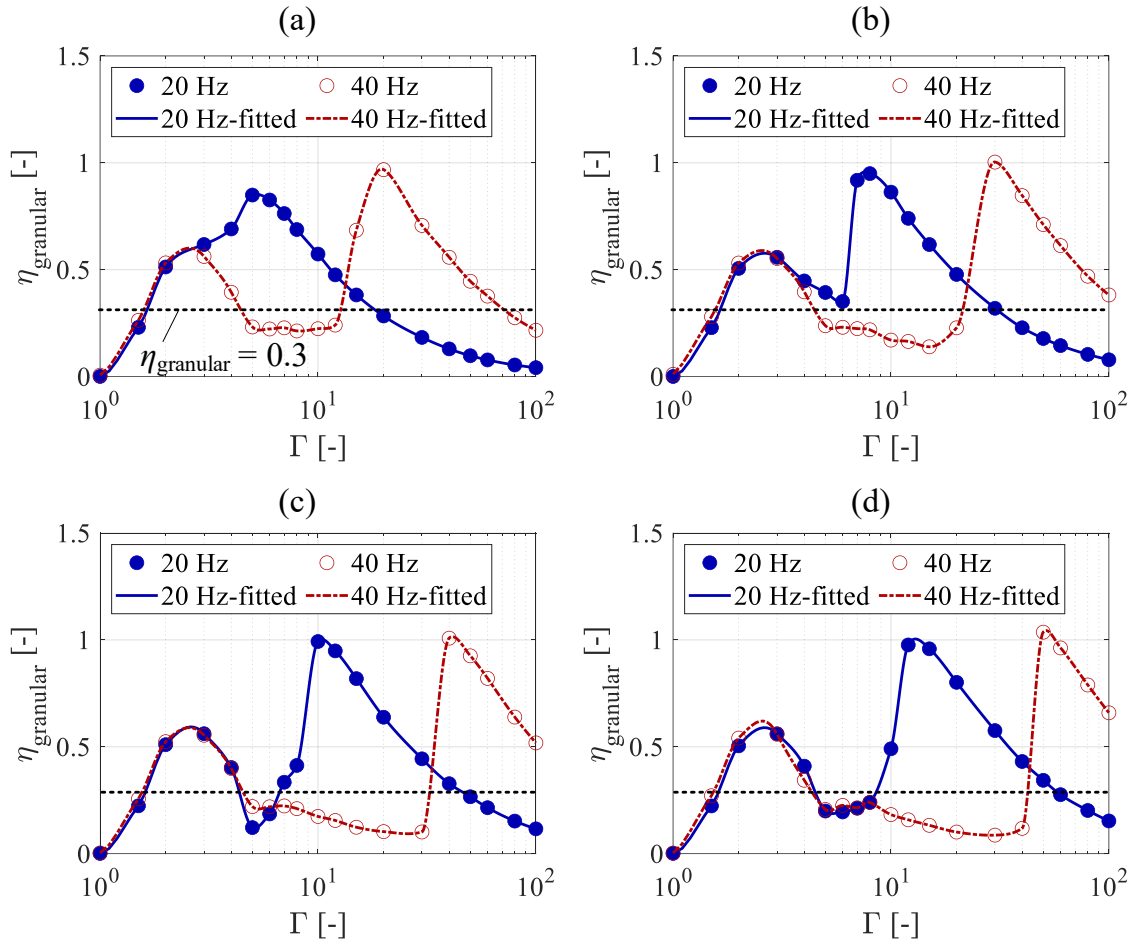
Figure 6.8: Granular damping efficiency at 20 Hz and 40 Hz using 5 mm spheres in vertical case: (a) $v = 0.466$, (b) $v = 0.415$, (c) $v = 0.373$, and (d) $v = 0.339$.
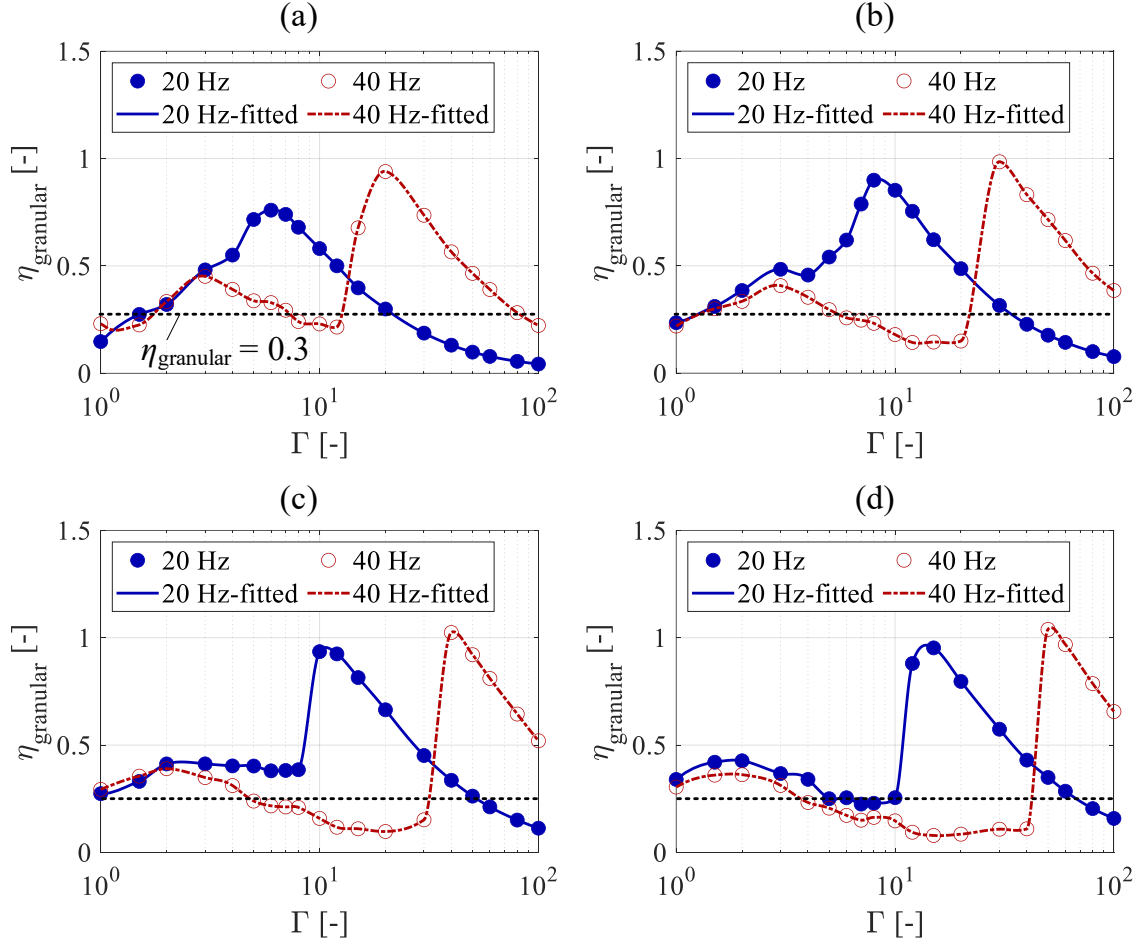
Figure 6.9: Granular damping efficiency at 20 Hz and 40 Hz using 5 mm spheres in horizontal case: (a) $v = 0.466$, (b) $v = 0.415$, (c) $v = 0.373$, and (d) $v = 0.339$.

In the bouncing bed phase, most of the energy dissipated in a cycle comes from the two collective collisions between the granular medium and enclosure as shown in Figure 6.7. Therefore, it is possible to say that the relative velocity between the particle collection and the enclosure just before and during a collective collision directly affects the effectiveness of energy dissipation. In order to examine this, the mean velocity of the granular medium along the excitation direction is compared with the enclosure velocity for vertical 40 Hz excitation in Figure 6.10. One of the presented cases is $\Gamma = 20$ which is close to the bouncing bed onset and the other is $\Gamma = 100$ where the bouncing bed is developed more (i.e., far away from the onset). Note that the change in the granular medium velocity is achieved during a

collision and as a result of the gravitational acceleration as the excitation orientation is vertical.
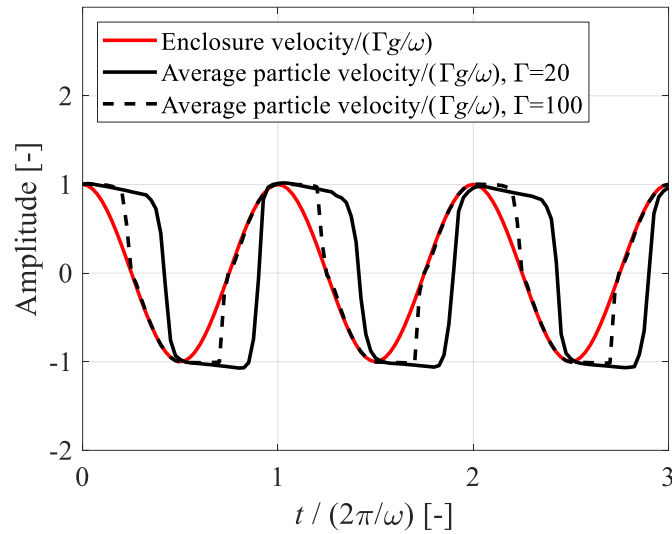
Figure 6.10: Steady-state velocity histories of granular damper with 5 mm spheres exposing vertical 40 Hz vibration, $v = 0.466$.

By looking at both Figure 6.7 and Figure 6.10, it can be noticed that deformation of granular medium, hence energy dissipation, is observed during the collective collisions but only when the body of particles move relative to the enclosure. Figure 6.10 also indicates that these collisions occur when the enclosure velocity is maximum and the granular medium moves in the opposite direction to the enclosure with almost the same velocity amplitude for $\Gamma = 20$ case, where the damping efficiency is optimum (see Figure 6.8a). For $\Gamma = 100$ case when the damping efficiency is much lower, the collisions commence earlier in the cycle at a smaller enclosure velocity, and the granular medium moves with enclosure longer. As Figure 6.10 shows, the initial deceleration of granular medium increases with amplitude before it reaches the velocity of the enclosure. The faster initial deceleration can be attributed to tighter packing of particles which leads an increase in the overall stiffness of the granular medium. It means that a lower amplitude in the bouncing bed phase provides a less stiff granular medium leading a larger deformation of the granular medium. As a result, it can be said that

the most effective granular energy dissipation occurs at the lowest amplitude that the bouncing bed phase can exist for a particular frequency: the onset amplitude of bouncing bed phase, i.e., $\Gamma_{\text{optimum}} = \Gamma_{\text{bouncing bed}}$, where Γ_{optimum} is the optimum amplitude for granular energy dissipation effectiveness. In other words, it can be described that this is the optimum condition for the collective collisions for granular dampers.

Assuming that the granular medium has a constant velocity, which is the maximum enclosure velocity, between the two collective collisions in a cycle, Sack et al. [77,110] have equated the distances travelled by the granular medium and the enclosure – the condition for the bouncing bed onset. This yields the following relationship:

$$\Gamma_{\text{optimum}} = \frac{\omega^2 h_{\text{clearance}}}{g\pi} \tag{6.11}$$

where $h_{\text{clearance}}$ is the clearance in the enclosure as depicted in Figure 6.11.
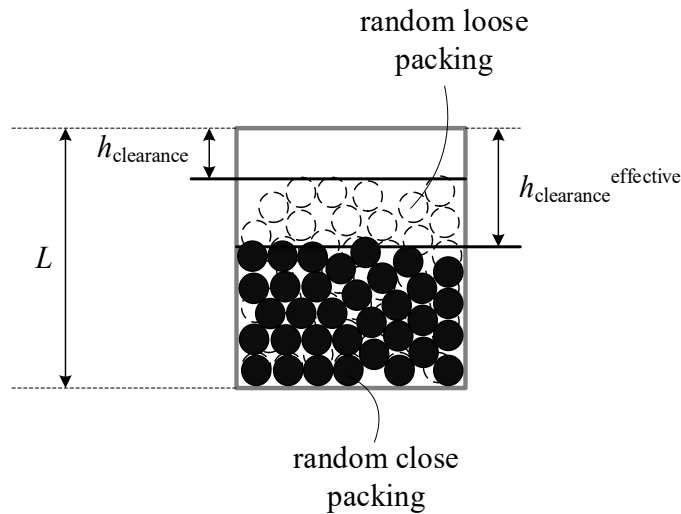
Figure 6.11: Estimation of clearance in a granular damper.

As the volume occupied by particles is not continuous, it is inaccurate to determine the clearance as the distance between the upper layer of particles and the top end of enclosure. Therefore, the relative clearance can be used as a practical measure of clearance [89]:

$$h_{\text{clearance}} = \left(1 - \frac{N_{\text{particle}}}{\left(N_{\text{particle}}\right)_{\text{max}}}\right)L \tag{6.12}$$

where $(N_{\text{particle}})_{\text{max}}$ is the maximum number of particles that can be filled within the enclosure void. However, since $(N_{\text{particle}})_{\text{max}}$ varies with packing arrangement and particle size, this estimation method produces significant errors when predicting Γ_{optimum} [89].

If the damping particles are filled into an empty enclosure under the effect of gravity without any external vibration, the random loose packing arrangement is most likely obtained in the enclosure as shown Figure 6.11. The packing density can increase due to vibrational loading [206,207]. Therefore, it is reasonable to say that the particles form a tighter arrangement than the random loose packing as the granular medium is significantly compressed during the collective collisions – i.e., the random close packing arrangement demonstrated in Figure 6.11. By accounting this effect, a more realistic estimation for the clearance can be made by introducing the effective clearance as:

$$h_{\text{clearance}}{}^{\text{effective}} = \left(1 - \frac{\upsilon}{\upsilon_{\text{max}}}\right)L \tag{6.13}$$

where υ_{max} is the maximum volume fill ratio that can be achieved by the particles in the enclosure volume. This ratio is nominally 0.64 for a random close packing of perfect spheres [208–211] and can change with excitation and particle properties [206,211,212]. It should be noticed that the method described by Equation (6.12) exhibits the random loose packing arrangement. The equivalency of loose packing arrangement condition can be captured using Equation (6.13) by assuming $\upsilon_{\text{max}} = 0.55$. Table 6.3 compares the close packing (CP) and loose packing (LP) estimations with the DEM simulation results for a granular damper.

126

Table 6.3: Optimum vibration amplitude estimations of granular damper using 5 mm spheres.

Volume filling ratio	Approach	20 Hz	40 Hz	80 Hz
0.466	DEM-vertical	5.2	19.6	79.9
	DEM-horizontal	6.1	19.8	80.0
	LP	3.1	12.5	49.9
	CP	5.6	22.3	89.2
0.415	DEM-vertical	7.6	29.9	>100
	DEM-horizontal	8.3	30.0	>100
	LP	5.7	22.6	90.6
	CP	8.1	32.4	130
0.373	DEM-vertical	10.4	41.4	>100
	DEM-horizontal	10.7	40.9	>100
	LP	8.2	33.0	132
	CP	10.7	42.8	171
0.339	DEM-vertical	12.9	51.5	>100
	DEM-horizontal	13.9	51.6	>100
	LP	10.8	43.2	173
	CP	13.3	53.0	212

It can be seen from this table and predicted from Equation (6.11) that the optimum (i.e., the bouncing bed onset) amplitude becomes larger as the frequency and clearance increases whilst the effect of excitation orientation on it stays small for all cases simulated. Table 6.3 shows that the LP approach significantly underestimates the optimum amplitude as it underestimates the clearances. It is apparent that the CP approach results in more accurate predictions. Small differences between the CP predictions and the DEM simulations can be explained by the variations in the actual maximum achievable volume fill ratio (assumed to be 0.64 as default) with vibration. In addition, as the optimum amplitudes are determined using the fitted curves at each frequency, there would be a level of uncertainty in the simulation results due to logarithmic interpolation.

The damping efficiency results of different sized particles are provided in Figure 6.12 for 20 Hz excitation. It shows that there is a small effect of particle size on the optimum amplitude – generally decreasing as the particle size grows. This observation may be related to the

variability in packing with particle size. The accuracies of estimation methods can also be visually compared in Figure 6.12 as the prediction lines are attached on the graphs.
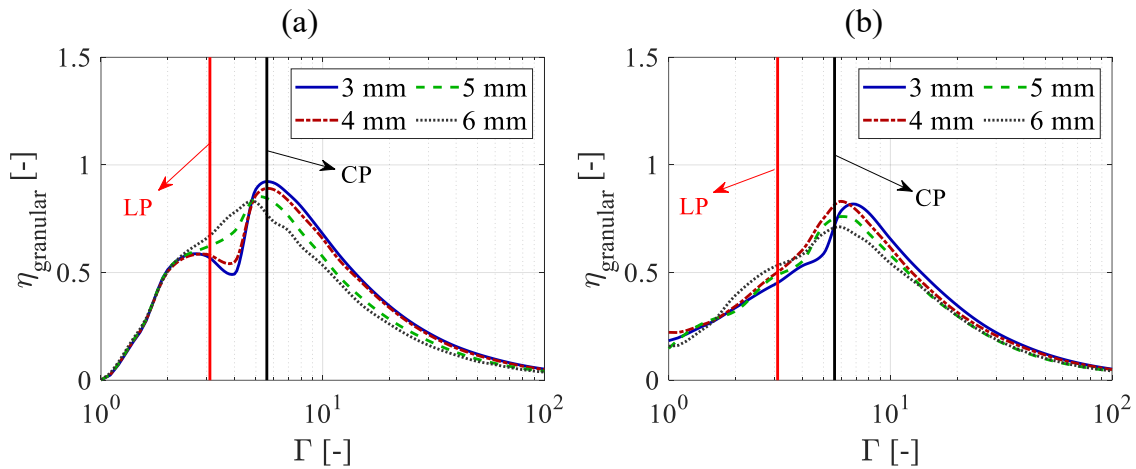
Figure 6.12: Damping efficiency results of different particle sizes at 20 Hz for (a) vertical and (b) horizontal cases where $\upsilon = 0.466$.

The effects of material and contact properties on the optimum amplitude were examined by conducting a sensitivity analysis employing DEM. The simulated damper was based on the volume ratio of $\upsilon = 0.466$ under 20 Hz vertical excitation. The results of this study are set out in Figure 6.13. It can be said that the optimum amplitude is insensitive to material and contact properties of granular damper.

In addition, although the trend of the damping efficiency, which is a result of motional phases, is maintained for each property change investigated, the level of damping efficiency slightly differs as similarly observed in the literature [94,120]. For example; as can be seen in Figure 6.13b, larger elastic modulus provides more effective energy dissipation as it exhibits a less dense particle bed by reducing individual contact durations (see Equation (5.10) for justification) and thus its tendency to collect tightly. As a result, it creates a more deformable granular medium for collective collisions which dissipates more energy for the same vibrational condition.
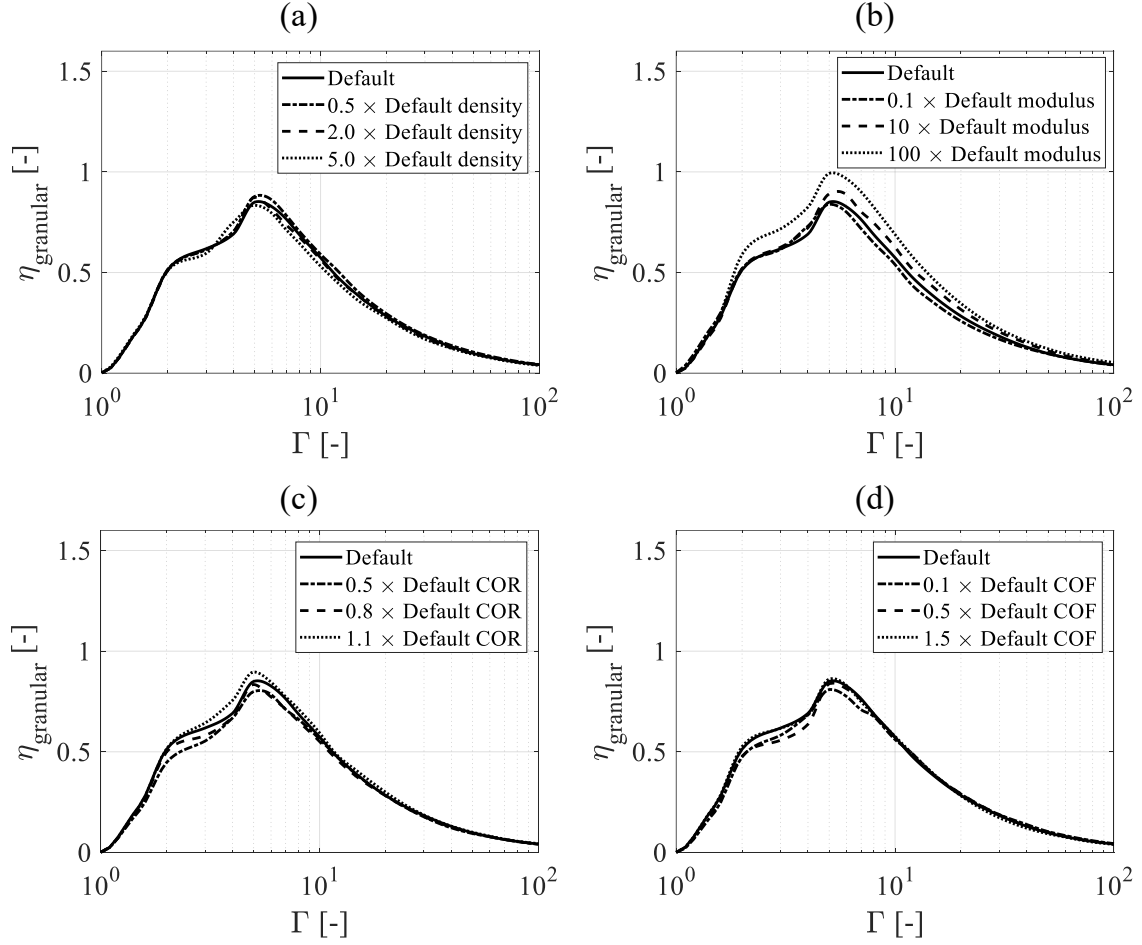
Figure 6.13: Sensitivity of granular damping efficiency to (a) material density, (b) elastic modulus, (c) coefficient of restitution and (d) coefficient of friction for 20 Hz vertical excitation where $v = 0.466$.

6.4.2 Solid-like phase

The solid-like phase was observed only for $\Gamma = 1$ at low frequencies of the vertical case as can be seen in Figure 6.2. It was not noticed in the simulations of horizontal case since it can occur in the case of $\Gamma < 1$ for the horizontal case [100].

In this phase, the particles are like a solid mass fixed onto the enclosure bottom surface and moves with the same velocity as the enclosure. As demonstrated in Figure 6.14, there is no considerable relative motions amongst the loosely packed particles or relative to the enclosure. It is because the inertial forces generated by vibration remain smaller than the restraining forces between the entities (particles and enclosure surfaces) from gravity and

friction. It should be noted that this phase is therefore not observed in zero-gravity environment as there is no restraining force [91].
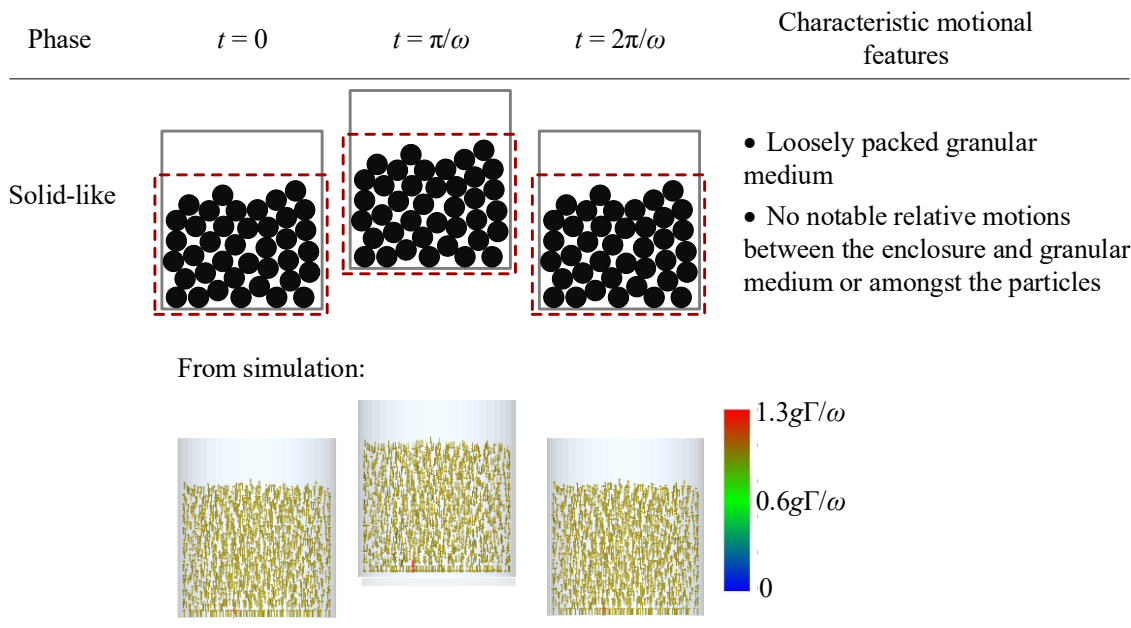
Figure 6.14: Solid-like motional phase.

As a result of this motion, granular energy dissipation is negligible as can be clearly seen by comparing Figure 6.2 and Figure 6.4. Thus, granular dampers are often considered to operate beyond this phase. However, it should also be noted that useful energy dissipation can be achieved in this phase by employing a particular configuration of high-loss, low-modulus particles which maximises strain within particles [66].

6.4.3   Fluidisation-based to convection-based phases

As determined in Section 2.5 while reviewing literature, in this thesis, the "fluidisation" term is used to address the condition where contacting particles temporarily lose contacts and move relative to each other, then, over a vibration period, approximately maintain their average position with respect to the enclosure and existing contacts. On the other hand, the "convection" term stands for indicating significant decompaction of particles in a cycle that allows the particles to be transported to different locations of the enclosure and lose their existing contacts. In addition, the convection motion typically has a noticeable component

perpendicular to the excitation direction. These described motion types are simply illustrated in Figure 6.15.
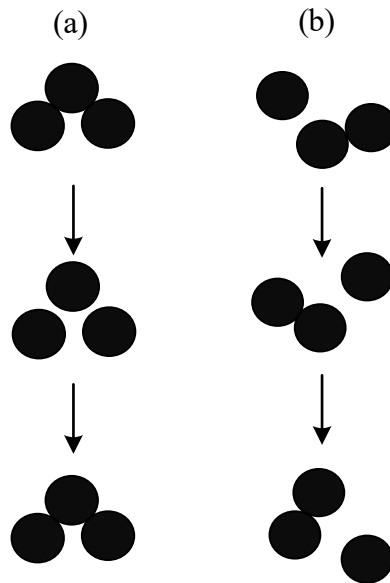
Figure 6.15: Particle relative motion types: (a) fluidisation and (b) convection.

Excluding the bouncing bed phase, developing and disappearing of the described fluidisation and convection motions within the granular medium determine motional phases and control phase maps. When the fluidisation motion appears in the granular medium, the solid-like phase is replaced by the fluidisation-based phases. By increasing the vibration amplitude beyond the solid-like phase, the occurrence of fluidisation motion increases. If the vibration amplitude is increased further, convection motions begin replacing the fluidisation motions, and they can dominate the granular medium at larger amplitudes leading to the convection-based phases. Therefore, it is apparent that the three principal phases (i.e., solid-like, fluidisation-based and convection-based) are in an inter-related relationship. If the bouncing bed phase does not occur, there are gradual changes in the operating phase (Figure 6.2 and Figure 6.3) and the granular damping efficiency (Figure 6.4 and Figure 6.5) depending on vibration amplitude for both excitation orientation cases.

As can be also noticed, the fluidisation motion type has the most capability for energy dissipation throughout the solid-fluidisation-convection inter-related process. This is because there is no relative motion in the solid-like phase, and within the convection zone, the contacts are lost frequently and less severe as a result of the low particle velocity.

6.4.3.1 Collective collision and energy dissipation

In contrast to the bouncing bed and solid-like phases, there are some fundamental differences between different excitation orientations in the fluidisation-based and convection-based phases in terms of both motional behaviour and energy dissipation. This can be seen by simply comparing the energy dissipation histories as shown in Figure 6.16.
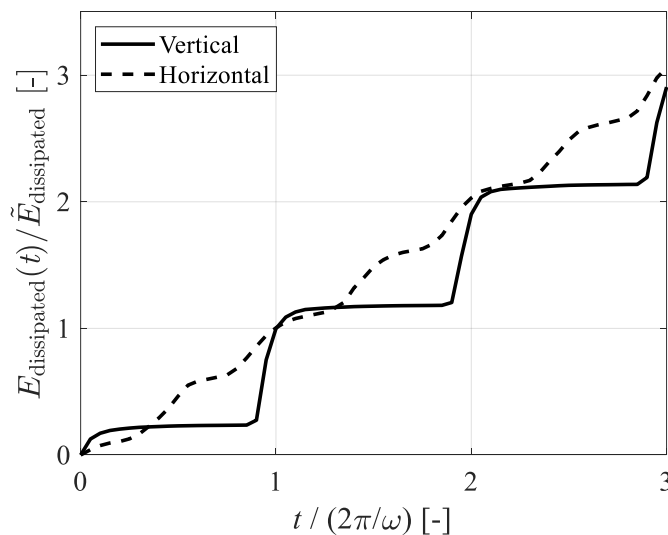
Figure 6.16: Steady-state granular energy dissipation histories with 5 mm spheres at 40 Hz where $\Gamma = 3$ and $\upsilon = 0.466$.

For $\Gamma = 3$ at 40 Hz, both excitation orientation cases exhibit a fluidisation-based phase as can be seen in Figure 6.2 and Figure 6.3. However, the particular phases that they show are different: the global fluidisation in the vertical case and the fluidisation/convection phase in the horizontal case. This is mainly caused by the behaviour of collective collisions observed under different orientations as it affects the way that energy is transferred and therefore the motion types that occur.

132

In the vertical fluidisation-based and convection-based phases, there is only one collective collision (with the enclosure bottom surface) in a vibration cycle. This may look like the bouncing bed collective collisions, but, in fact, its intensity is much lower. Nevertheless, it creates a single step within a vibration cycle in the energy dissipation history as shown in Figure 6.16 as vibrational energy is transferred and dissipated in this relatively short collision duration. In the horizontal case, two collective collisions occur as with the bouncing bed phase, but they are much longer and milder than the bouncing bed collisions as can be seen in Figure 6.16 as a result of the granular medium layout inside the enclosure. The described behaviours can be visually seen in Sections 6.4.3.3 and 6.4.3.4 where the particular phases and their energy dissipation potential are discussed.

6.4.3.2 Optimum energy dissipation in fluidisation

As can be seen from each result set shown in Figure 6.8 and Figure 6.9, there is a second peak around $\Gamma = 3$ which is smaller than the bouncing bed optimum. This peak is clearly shown from the zoom plots of an excitation frequency case for both orientations in Figure 6.17.

The peak efficiency is observed in the fluidisation-based phases for both orientations, and it occurs when the ratio of fluidised particles is maximised in the granular medium – can be called as the fluidisation optimum. The fluidisation optimum condition can occur at each frequency which creates the horizontal high damping efficiency ridge as shown in Figure 6.4 and Figure 6.5. As can be seen in Figure 6.17, this optimum condition provides higher peak damping efficiency for the vertical case whereas the horizontal case has a broader range in which an effective granular energy dissipation is obtained.
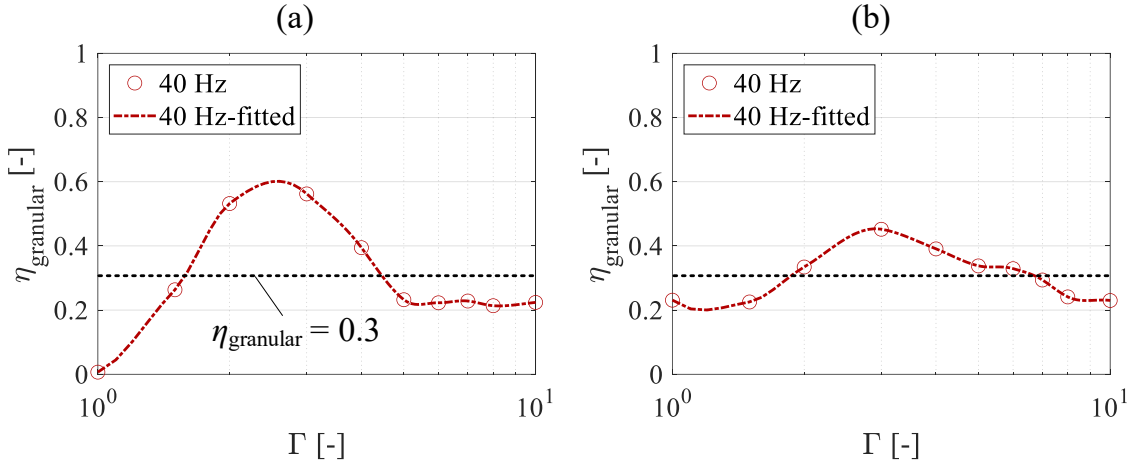
Figure 6.17: Granular damping efficiency results between $\Gamma = 1$ and $\Gamma = 10$ at 40 Hz using 5 mm spheres in (a) vertical and (b) horizontal cases, $\upsilon = 0.466$.

As the dominant motion type (or the ratio of fluidised particles to others) gradually changes depending the level of momentum transferred to the granular medium, the described fluidisation optimum can be noticed by observing the collective collision (or collisions for the horizontal case) in the mean particle velocity history plots. To discuss this, the velocity histories of three excitation cases around the fluidisation optimum are plotted in Figure 6.18 for both excitation orientations.
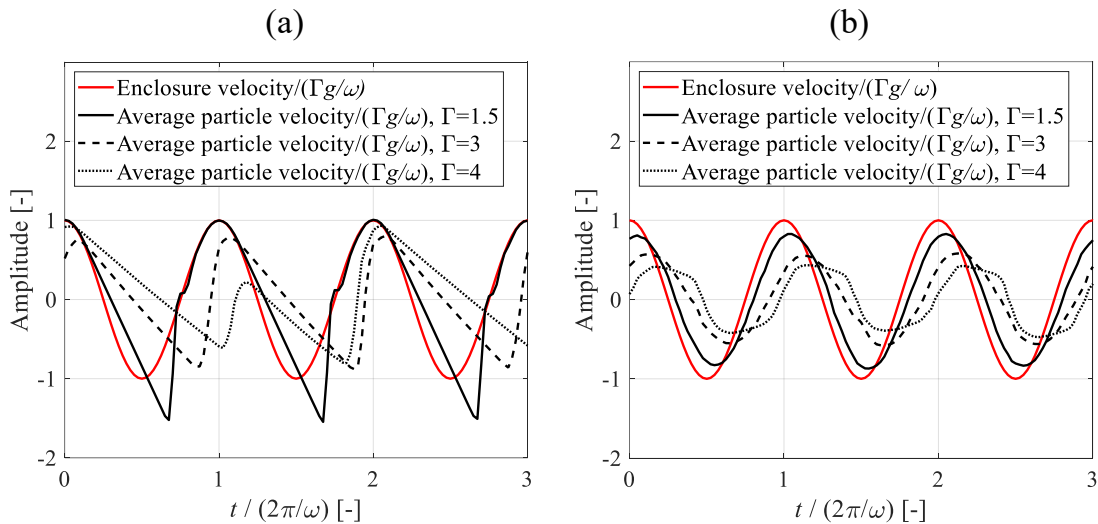
Figure 6.18: Steady-state velocity histories of granular damper with 5 mm spheres exposing vertical (a) and horizontal (b) 40 Hz vibration, $\upsilon = 0.466$.

Below the optimum condition in the vertical excitation (i.e., $\Gamma = 1.5$ in Figure 6.18a), the granular medium collides with the enclosure base when the enclosure velocity is nearly zero, and they move together for approximately half cycle similar to the solid-like phase. This induces an insufficient momentum transfer to be able to reach the maximum ratio for the fluidisation motion. About the optimum (i.e., $\Gamma = 3$ in Figure 6.18a), the granular medium collides with the enclosure base when the enclosure velocity is around its maximum and the granular medium has nearly the same velocity magnitude in the opposite direction. This leads the maximum fluidisation providing an efficient momentum transfer to the particles. Beyond the optimum (i.e., $\Gamma = 4$ in Figure 6.18a), as the particles start convecting the mean velocity of the granular medium (and the intensity of collective collision) decreases and the collective collision occurs at a smaller enclosure velocity. This can initiate as non-periodical motion (one collective collision in two cycles or significant difference in the intensity of collective collisions). It produces an apparent transition phase at some amplitudes in the vertical case (see in the phase map of Figure 6.2) – demonstrated in Figure 6.19. Beyond the transition phase (i.e., the convection-based phases), the described reduction in collision intensity can be seen for each periodic collective collision.
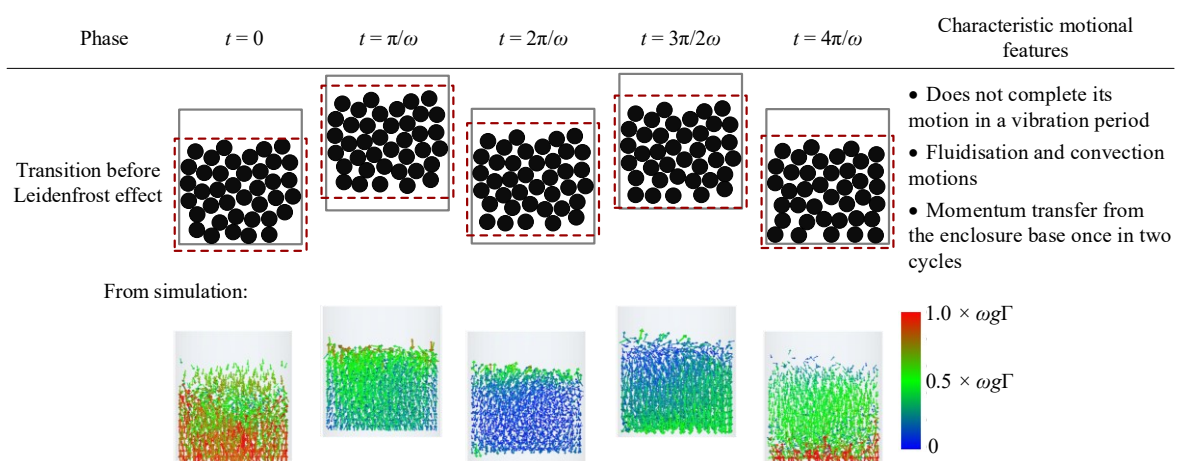
Figure 6.19: Transition motional phase.

As there are two collective collisions in each cycle for any motional phase of the horizontal case, the momentum is transferred from both collisions periodically and the transition phase does not develop. The granular medium velocity reduces with increasing amplitude as it detaches from the enclosure ends at a lower enclosure velocity as shown in Figure 6.18b. However, it does not mean that the relative velocity at the collisions becomes smaller. Therefore, this relative velocity should be estimated observing both the granular medium velocity and the phase angle between the granular medium and enclosure velocities. When the relative velocity reaches its maximum value and provides efficient momentum transfer (i.e., $\Gamma = 3$ in Figure 6.18b), the maximum fluidisation ratio (i.e., the optimum fluidisation condition) is obtained.

6.4.3.3 Vertical case

As can be seen in Figure 6.2, as the vibration intensity grows in the vertical case, the granular phase first turns into the local fluidisation after the solid-like phase. In this phase, the granular medium moves to the opposite direction of gravity as a result of momentum transfer by the collective collision. As the deceleration of enclosure is greater than that of the granular medium (or gravity), the body of particles lifts relative to the enclosure base resulting in decompactions and therefore relative motions – the fluidisation motion, particularly near the uppermost particle layers at which the particles are least restrained. This motional behaviour occurs periodically as illustrated in Figure 6.20. It should be stated that the local fluidisation is regarded as the first vertical motional phase in which considerable granular energy dissipation can be obtained as the momentum exchange is essential for the operation of granular dampers.

When the level of momentum transferred to the particles increases to a sufficient level at the collective collision, the fluidisation motion spreads from the top particle layers to the deep particle layers. This granular motional behaviour is addressed as the global fluidisation

phase, and it is also demonstrated in Figure 6.20. It should be noticed that the maximum

fluidisation ratio in the granular medium is achieved in this phase, and few particles can

begin exhibiting the convection motion as the vibration amplitude increases.
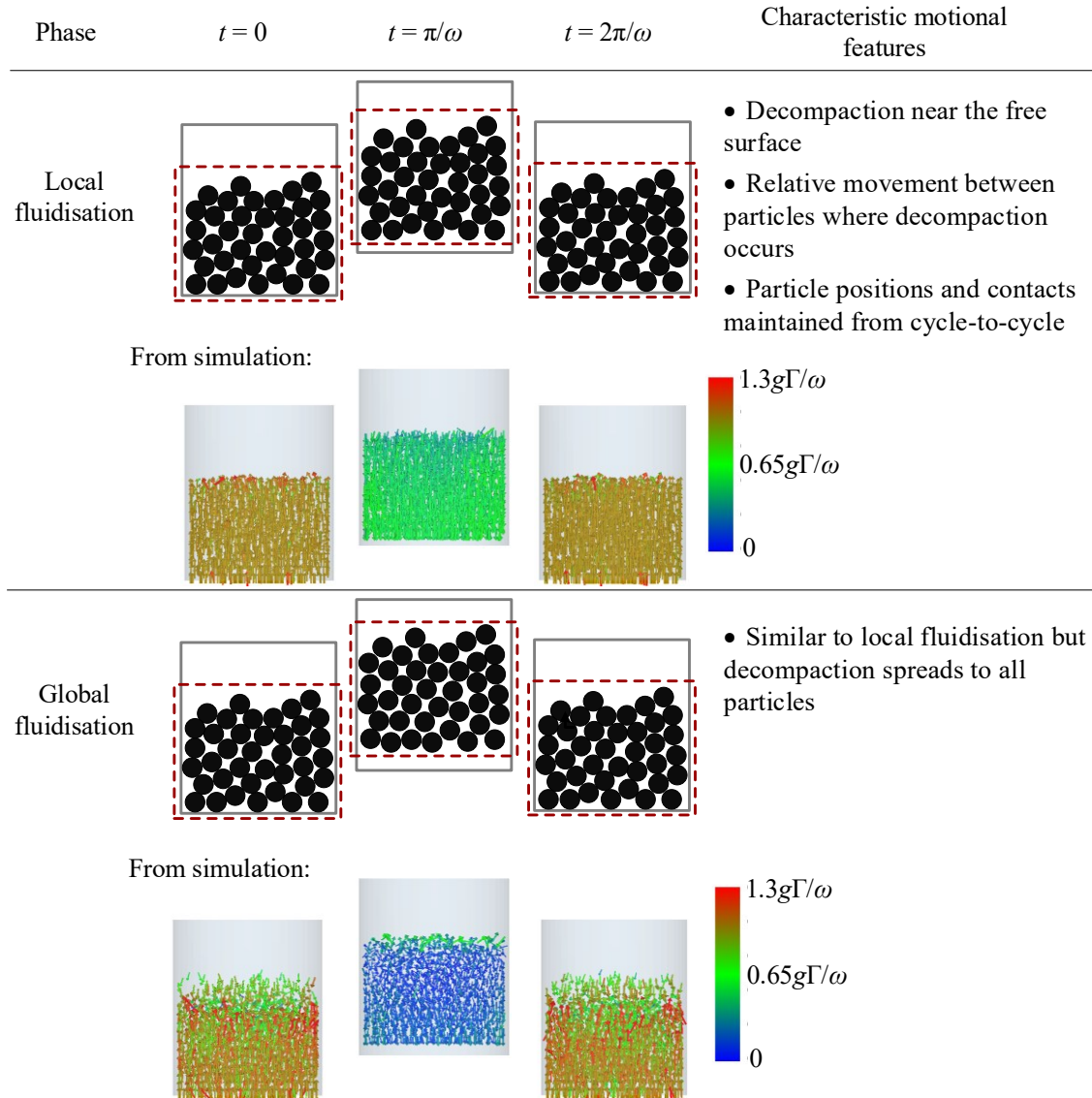
Figure 6.20: Vertical fluidisation-based phases.

As the vibration intensity further increases, the granular medium first demonstrates the

transition phase as a result of non-periodic reduction in the intensity of collective collision

as discussed before. Afterwards, the convection motion replaces the fluidisation motion

more and densifies within the granular medium. Therefore, it dominates the granular

medium at a larger amplitude than $\Gamma_{convection}$, resulting the vertical convection-based phases

referred as the Leidenfrost effect and the buoyancy convection whose motional patterns are demonstrated in Figure 6.21.
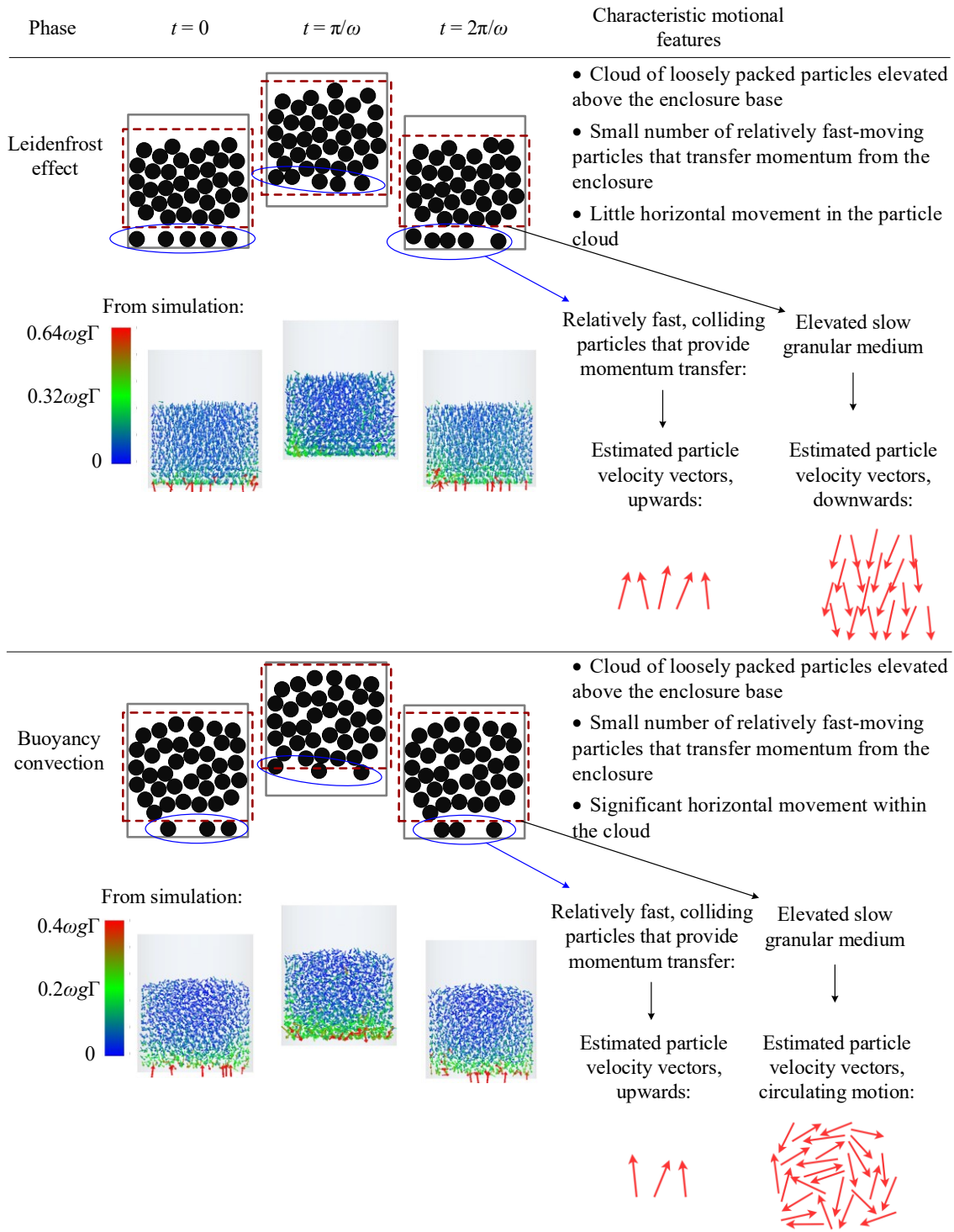
Figure 6.21: Vertical convection-based phases.

The Leidenfrost effect is the most observed convection-based phase in the phase maps of Figure 6.2 over the amplitude range of $12 < \Gamma < 80$ and the frequencies generally above 40

Hz. In this phase, a group of particles forms a loosely packed cloud that is elevated from the enclosure base and remains at a steady height relative to the enclosure base during a cycle. This cloud consists of slow-moving particles, and it is suspended by a small number of fast-moving particles underneath which provides the momentum transfer by colliding with the enclosure base.

As the horizontal component of particle convection motions increases at larger vibration amplitudes, the particles exhibit circulating motions in the granular medium where the Leidenfrost effects gives way to the buoyancy convection. Due to the transverse and rolling particle motions, the granular medium expands, and a curved shape is observed on the upper particle surface rather than an approximate flat surface in this phase.

To show the granular energy dissipation-phase relationship for the fluidisation-based and the convection-based phases, a close inspection of Figure 6.4 with the related phase amplitude ranges is provided in Figure 6.22 for varying volume fill ratio. The sensitivity of the results to particle size are also shown in the graphs. To show the effect of frequency, the results at different frequencies are also presented in Figure 6.23 for a volume fill ratio.

As can be seen from Figure 6.22 and Figure 6.23, the damping efficiency grows with amplitude in the local fluidisation phase as the number of fluidised particles increases in the solid-like body of particles, and this increase continues until a maximum level (i.e., the maximum fluidisation) observed in the global fluidisation. Beyond this peak, in the global fluidisation, as convection gradually develops, the damping efficiency start decreasing. However, it can be said that a significant energy dissipation effectiveness is evident up to the end of transition phase (or the beginning of the convection-based phases, the Leidenfrost effect). It is because the ratio of fluidised particles to the particles exhibiting the convection motion still remains relatively high. It can also be noticed in the transition phase that the

damping efficiency fluctuates more than the other phases. The most-likely reason is that the collective collision differs in intensity from one cycle to another, and therefore, the number of cycles used to evaluate the average energy dissipated is inadequate to eliminate this uncertainty in the transition phase. The damping efficiency is lower in the convection-based phases, i.e., the Leidenfrost effect and the buoyancy convection, as the intensity of particle contacts and the efficiency of momentum transfer decreases with increase in the occurrence of convective motions. This is an inevitable result of the low potential of convection motion for energy dissipation.

LF: Local fluidisation   LE: Leidenfrost effect
GF: Global fluidisation   BC: Buoyancy convection
T: Transition
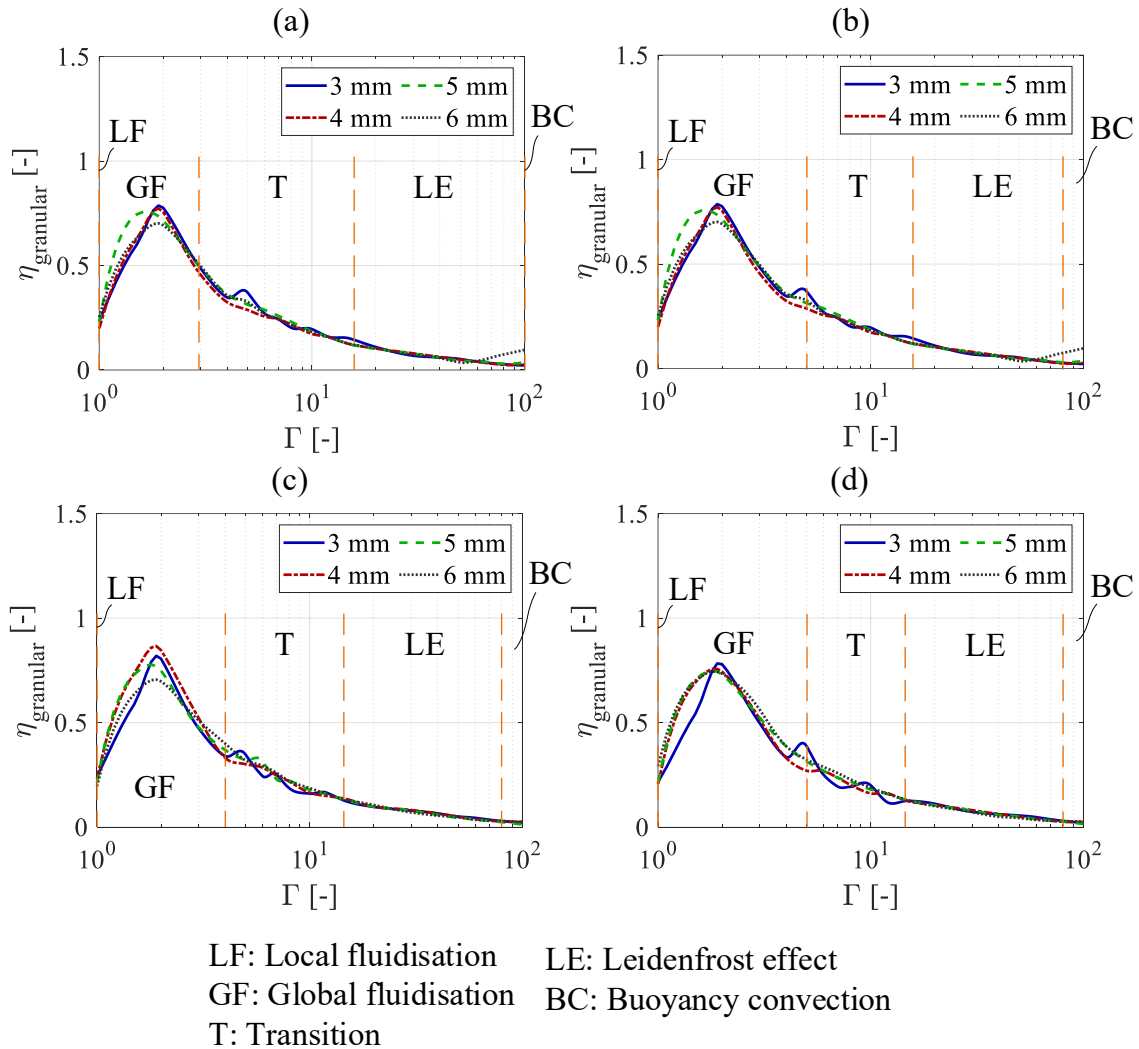
Figure 6.22: Granular damping efficiency results of different particle sizes at vertical 160 Hz excitation for: (a) $\upsilon = 0.466$, (b) $\upsilon = 0.415$, (c) $\upsilon = 0.373$, and (d) $\upsilon = 0.339$.
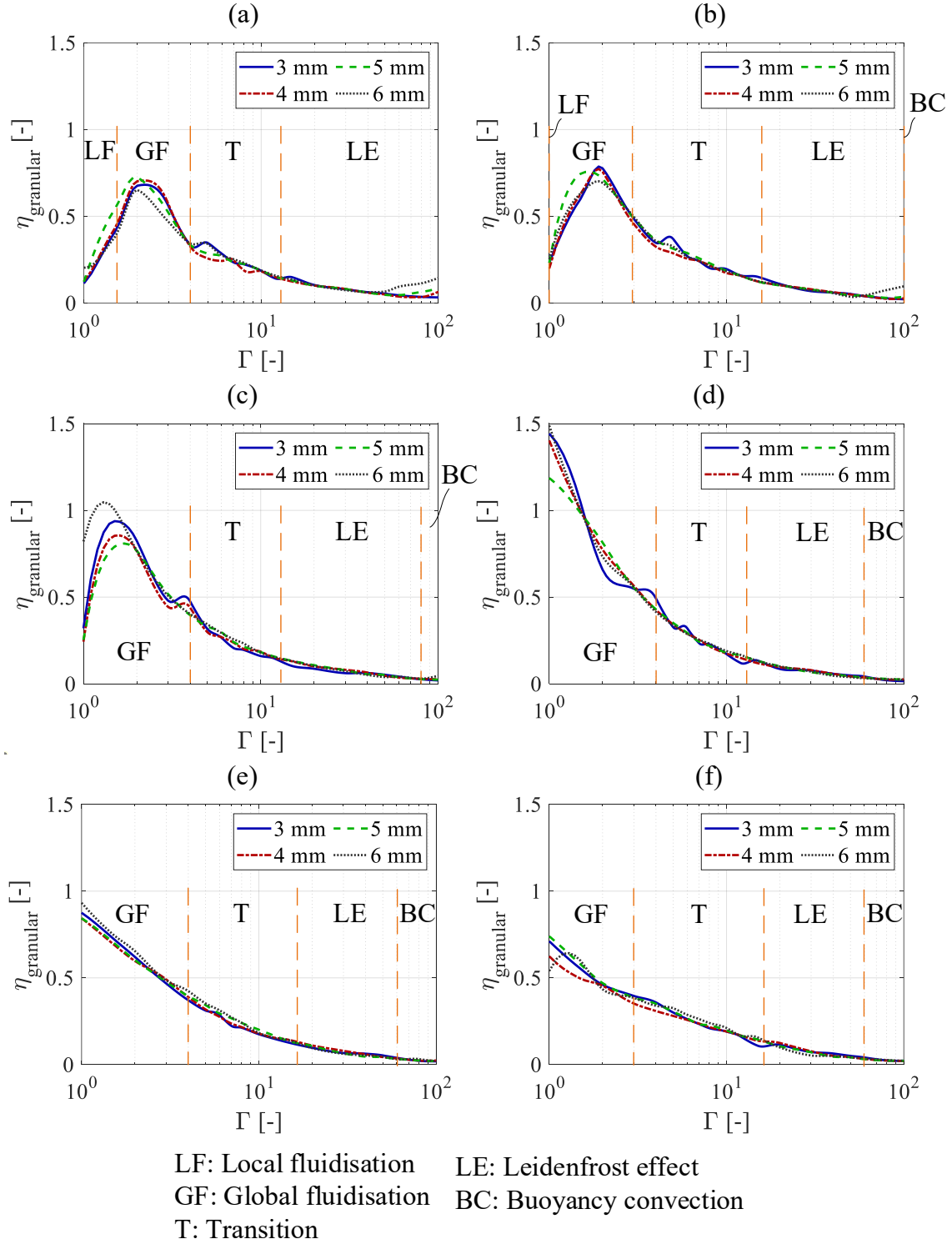
Figure 6.23: Granular damping efficiency results of different particle sizes for $\upsilon = 0.466$ at vertical excitations of: (a) 125 Hz, (b) 160 Hz, (c) 200 Hz, (d) 320 Hz, (e) 625 Hz and (f) 1024 Hz.

It can be noticed from Figure 6.22 and Figure 6.23 that the energy dissipation behaviour is not notably affected by particle size in the vertical fluidisation-based and convection-based

phases. However, this may not be valid if an insufficient number of particle layers is used inside the enclosure void as these phases cannot be obtained. In addition, in contrast to the bouncing bed phase, the damping efficiency level and the optimum fluidisation condition are insensitive to volume fill ratio as shown in Figure 6.22. It is because the momentum transfer is independent from the clearance in these phases as the collective collision occurs only with the enclosure bottom.

Figure 6.2 shows that the global fluidisation lower boundary shifts towards smaller vibration amplitude as the excitation frequency increases. As a result, the fluidisation optimum is obtained at a smaller vibration amplitude for a higher frequency in the vertical case (and the peak damping efficiency becomes higher) as demonstrated in Figure 6.23. This is because the required momentum level to fluidise the majority of particles is lower for higher frequencies. However, as the rate of this frequency-dependent change is slow, effective granular energy dissipation can be achieved over a broad frequency range utilising the vertical fluidisation-based phases, particularly the global fluidisation phase.

6.4.3.4 Horizontal case

The fluidisation and convection motions also occur for the horizontal excitation of granular dampers. However, as the excitation and gravity are perpendicular to each other and the momentum transmission occurs from both ends of the enclosure, the particular motional patterns of particles are somewhat different from those of the observed in the vertical case.

As the fluidisation motion can initiate at a relatively low amplitudes because of the particles restrained less in the horizontal case, the fluidisation-based phases are observed at lower amplitudes than the vertical case. Therefore, the first phase observed for the amplitude of Γ = 1 is one of the horizontal fluidisation-based phases in Figure 6.3: the partial fluidisation. In this phase, the gravity ensures that the body of particles rests on the enclosure side wall

and creates a free surface parallel to the excitation direction. As a result of this relatively large free surface area (compared to the vertical case), the upper particle layers generate the convection motion as well as the fluidisation motion. It is because the free surface accommodates the particles that has less restraining force than the other positions of the granular medium. On the other hand, the deep particle layers (near the contact of granular medium with the enclosure) exhibit a similar motion to that can be seen in the solid-like phase. The described motional phase is illustrated in Figure 6.24.
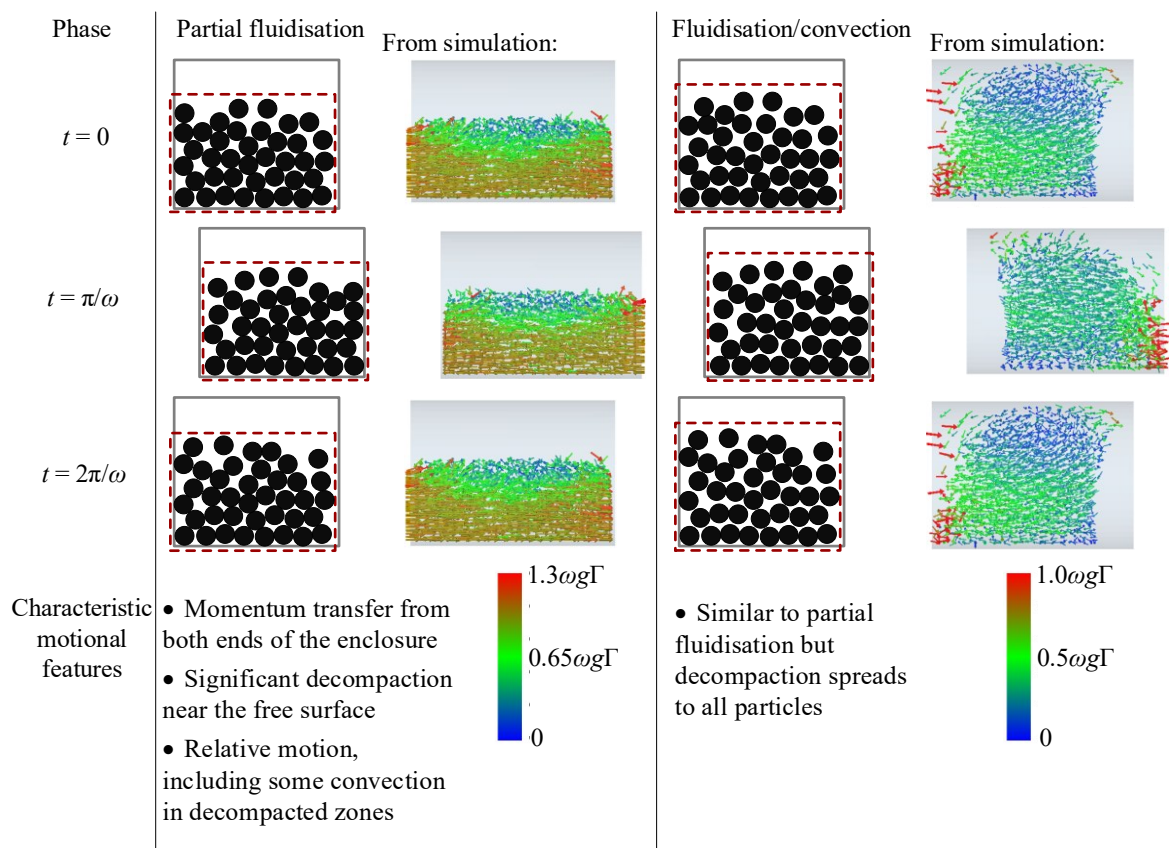
Figure 6.24: Horizontal fluidisation-based phases.

Figure 6.24 also shows the fluidisation/convection phase which is the second horizontal fluidisation-based phase observed at larger amplitudes than the partial fluidisation. In this phase, as the vibration amplitude increases, the number of fluidised particles becomes higher, but the ratio of these in the whole body of particles reduces. Because, the convection motion zones extend deeper into the particle layers more rapidly with amplitude. Therefore,

it can be estimated that the maximum fluidisation ratio in the granular medium is obtained when the operating phase is the partial fluidisation in the horizontal case.

If the vibration amplitude is increased more, most of particles undergo the convection motion and the convection phase occurs in the horizontal case which can be identified for large amplitudes at high frequencies in Figure 6.3. As can be seen in Figure 6.25, significant decompaction is seen throughout the granular medium, and fast-moving particles (which provides the momentum transfer) occur at both boundaries of slow particle cloud.
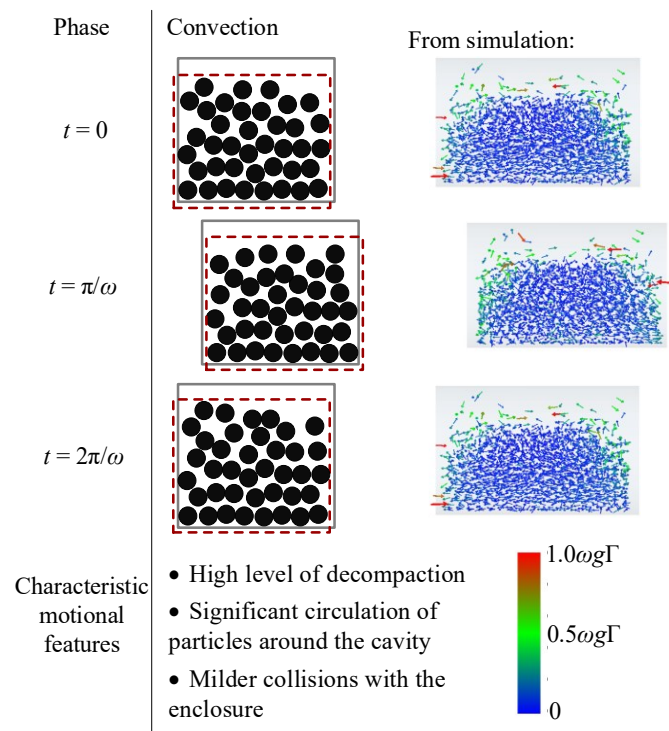
Figure 6.25: Horizontal convection phase.

Similar to the vertical case, the granular energy dissipation-phase relationship for the horizontal fluidisation-based and convection-based phases is discussed using the close inspection of Figure 6.5 with the related phases shown in Figure 6.3. The results are set out in Figure 6.26 and Figure 6.27.

As estimated while defining the motional features of horizontal fluidisation-based phases, the fluidisation optimum is achieved in the partial fluidisation phase. As can be realised by

comparing both orientation cases (e.g., Figure 6.22 and Figure 6.26), the damping efficiency is smaller in the horizontal case around the fluidisation optimum amplitude. It is because the ratio of fluidised particles is smaller in the horizontal case as a result of the initiation of convection motion into the granular medium at relatively lower vibration amplitudes. Beyond the optimum amplitude, the damping efficiency gradually decreases and becomes very low as the convection motion increases within the granular medium.

PF: Partial fluidisation
FC: Fluidisation/convection
C: Convection
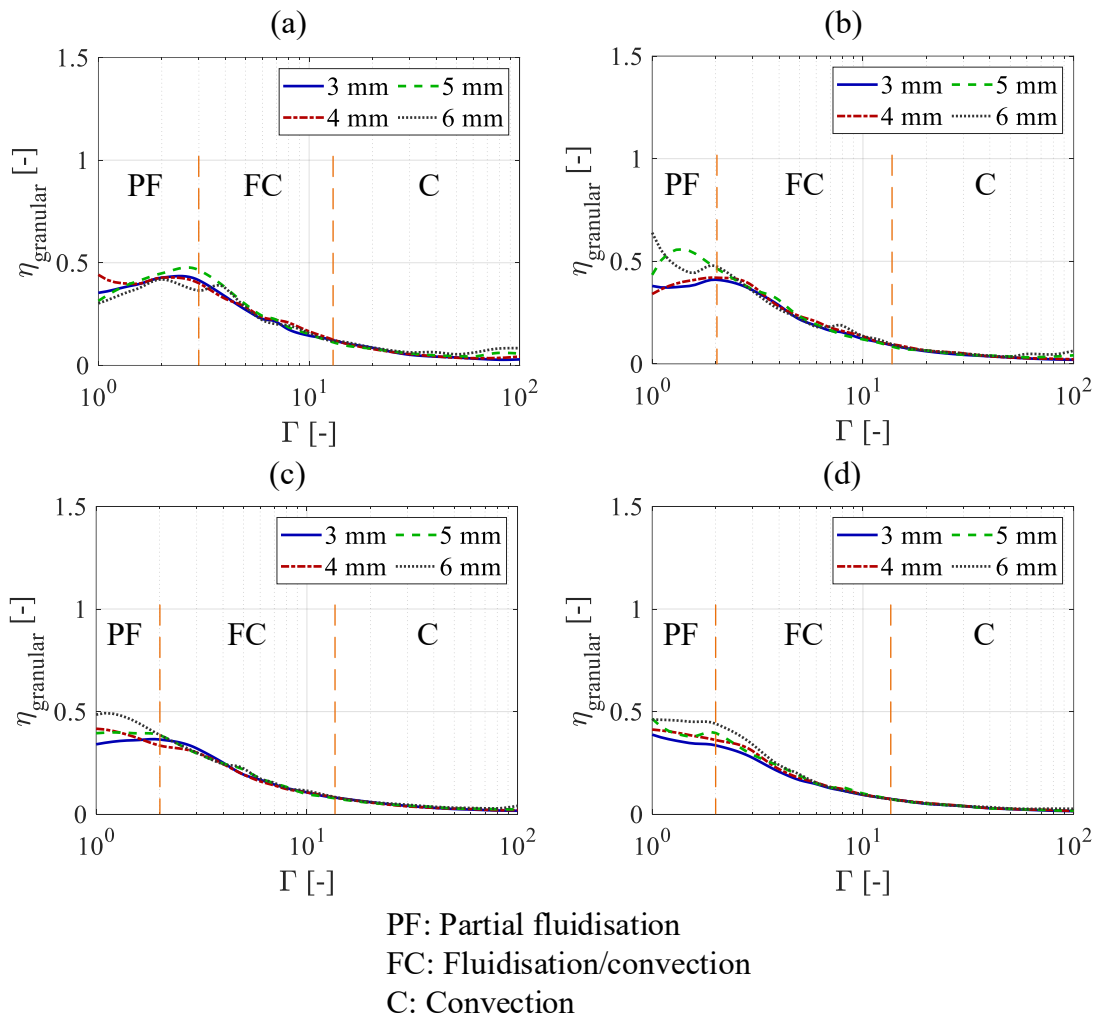
Figure 6.26: Granular damping efficiency results of different particle sizes at horizontal 160 Hz excitation for: (a) $v = 0.466$, (b) $v = 0.415$, (c) $v = 0.373$, and (d) $v = 0.339$.
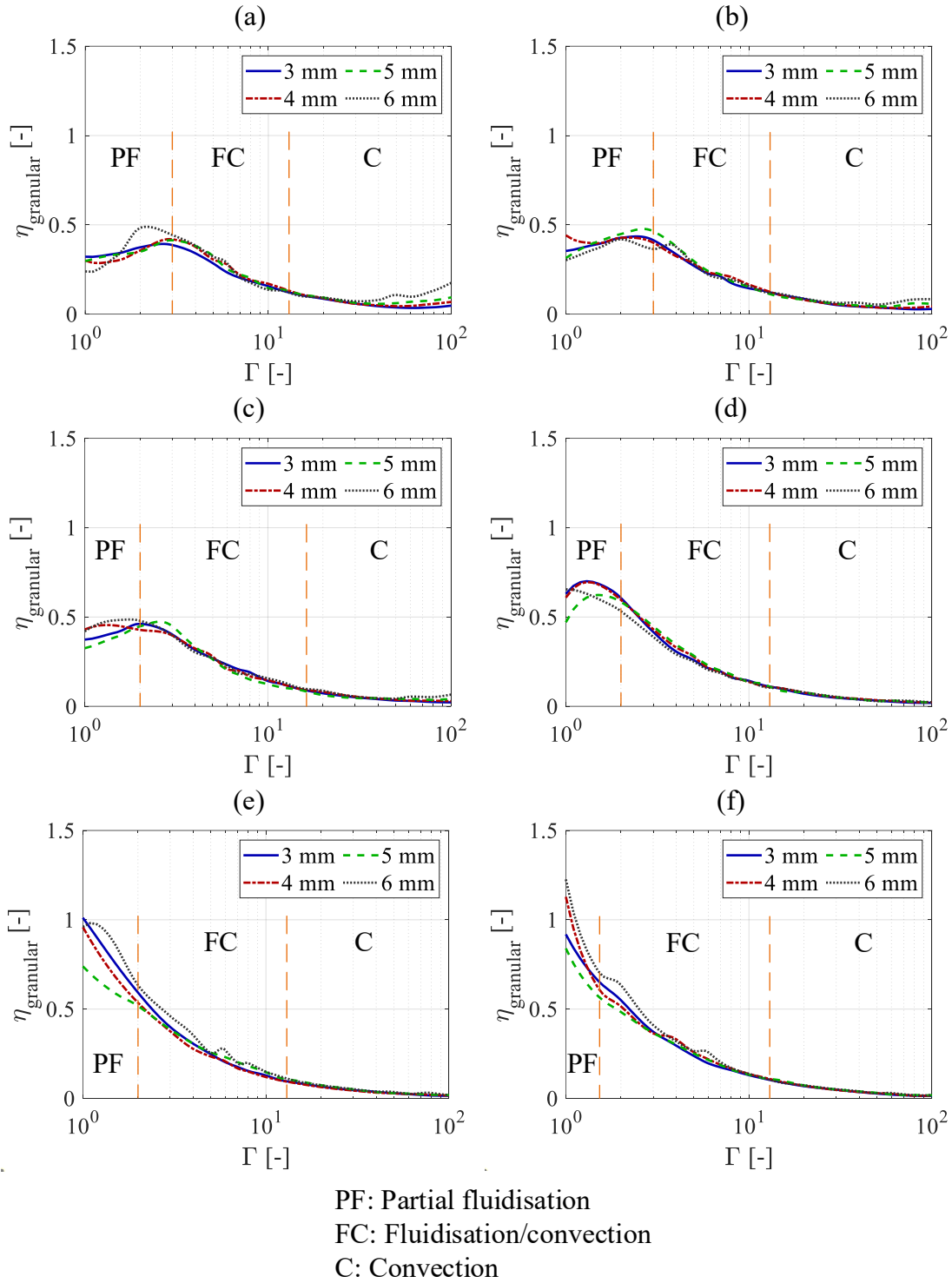
Figure 6.27: Granular damping efficiency results of different particle sizes for $v = 0.466$ at horizontal excitations of: (a) 125 Hz, (b) 160 Hz, (c) 200 Hz, (d) 320 Hz, (e) 625 Hz and (f) 1024 Hz.

As shown in Figure 6.26 and Figure 6.27, although there is no clear effect of particle size on

the granular damping efficiency in the horizontal fluidisation-based and convection phases,

the employment of insufficient number of particle layers can cause change in the damping efficiency levels as mentioned for the vertical case. It can be noticed in Figure 6.26 that the fluidisation optimum amplitude slightly decreases as the volume fill ratio reduces in the horizontal case. Note that this is a different observation from the vertical case. The main reason for this is that larger clearance creates a shallower particle bed and therefore a less restrained particle collection by the gravity-induced pressure, which allows the development of fluidisation and convection motion at smaller amplitudes.

As the excitation frequency increases, the optimum fluidisation shifts to smaller amplitudes and the peak damping efficiency becomes larger (see Figure 6.27) because of the reduction in the required momentum level to stimulate the fluidisation motion as similarly observed in the vertical case.

6.5   Importance of Dissipation Sources

As identified in Section 2.4.1, vibrational energy is dissipated in granular dampers in different ways. The relative importance of these dissipation mechanisms for different motional phases is investigated in this section. It should be noted $v = 0.466$ fill ratio damper configuration under the vertical 40 Hz and 160 Hz vibrations was considered in this work as this included all the significant phases observed (see Figure 6.8 and Figure 6.22). The other configurations showed similar outcomes to those shown here.

The total damping efficiency can be simply de-composed into the dissipation sources involved using the same analogy of Equation (2.2) as given below.

$$\eta_{\text{granular}} \approx \underbrace{\left(\eta_{\text{granular}}\right)_{\text{PS}}^{\text{friction}} + \left(\eta_{\text{granular}}\right)_{\text{PP}}^{\text{friction}}}_{\left(\eta_{\text{granular}}\right)^{\text{friction}}} + \underbrace{\left(\eta_{\text{granular}}\right)_{\text{PS}}^{\text{impact}} + \left(\eta_{\text{granular}}\right)_{\text{PP}}^{\text{impact}}}_{\left(\eta_{\text{granular}}\right)^{\text{impact}}} \qquad (6.14)$$

Note that the sub-script PS represents particle-enclosure surface interaction components, the sub-script PP stands for inter-particle interaction components and the detailed explanations of terms can be found in Section 2.4.1.

At the considered frequencies, the contribution of inter-particle interactions (as opposed to particle-enclosure interactions) to the damping efficiency is shown in Figure 6.28 depending on the vibration amplitude and particle size. The optimum fluidisation and bouncing bed onset amplitudes identified in the figures were determined from Figure 6.8 and Figure 6.22.
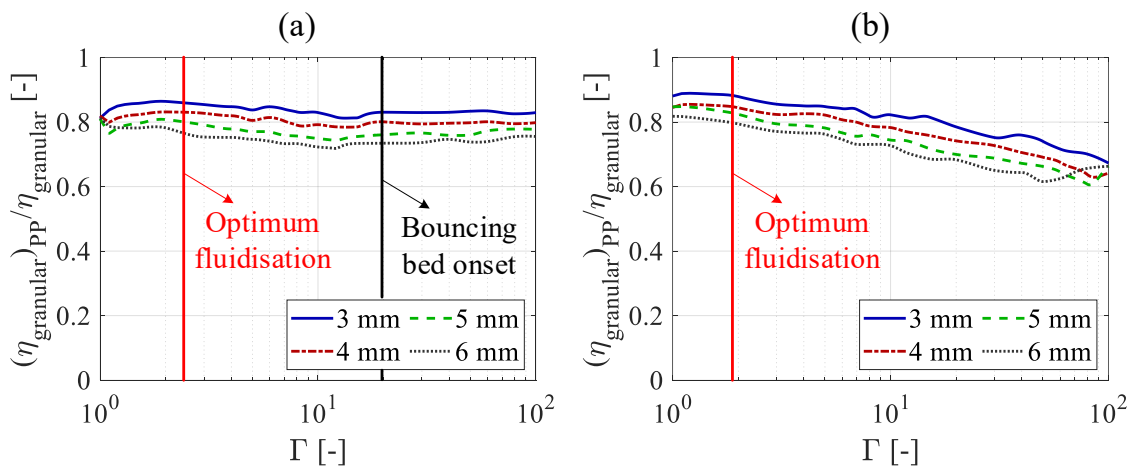
Figure 6.28: Inter-particle dissipation contribution at: (a) 40 Hz and (b) 160 Hz.

The inter-particle contribution consistently decreases with increasing particle size since the ratio of the number of inter-particle contacts to the number of particle-enclosure contacts decreases. It should be also noticed that that the inter-particle contribution would be zero when a single equivalent particle is employed, i.e., the impact damper. Figure 6.28 indicates that the vibrational energy is mostly dissipated between damping particles in granular dampers – exhibiting a contribution level larger than 60% in any motional phase. This contribution is significantly high (above 80%) up to the optimum fluidisation amplitude (from the solid-like phase, $\Gamma \leq 1$). For larger amplitudes than the optimum fluidisation amplitude, it gradually decreases as the prevalence of fluidisation motion decreases (and the convection motion increases) – see the amplitude range between the optimum fluidisation

and bouncing bed onset in Figure 6.28a and the amplitudes larger than the optimum fluidisation Figure 6.28b. As a result of the bouncing bed initiation, the inter-particle contribution increases (as the effect of convection motions is removed) and stays approximately constant about a level generally larger than 80% beyond the bouncing bed onset amplitude as can be seen in Figure 6.28a.

For the same damper configuration and excitation conditions, the frictional contribution and its inter-particle component are provided in Figure 6.29 as a function of vibration amplitude and particle size.
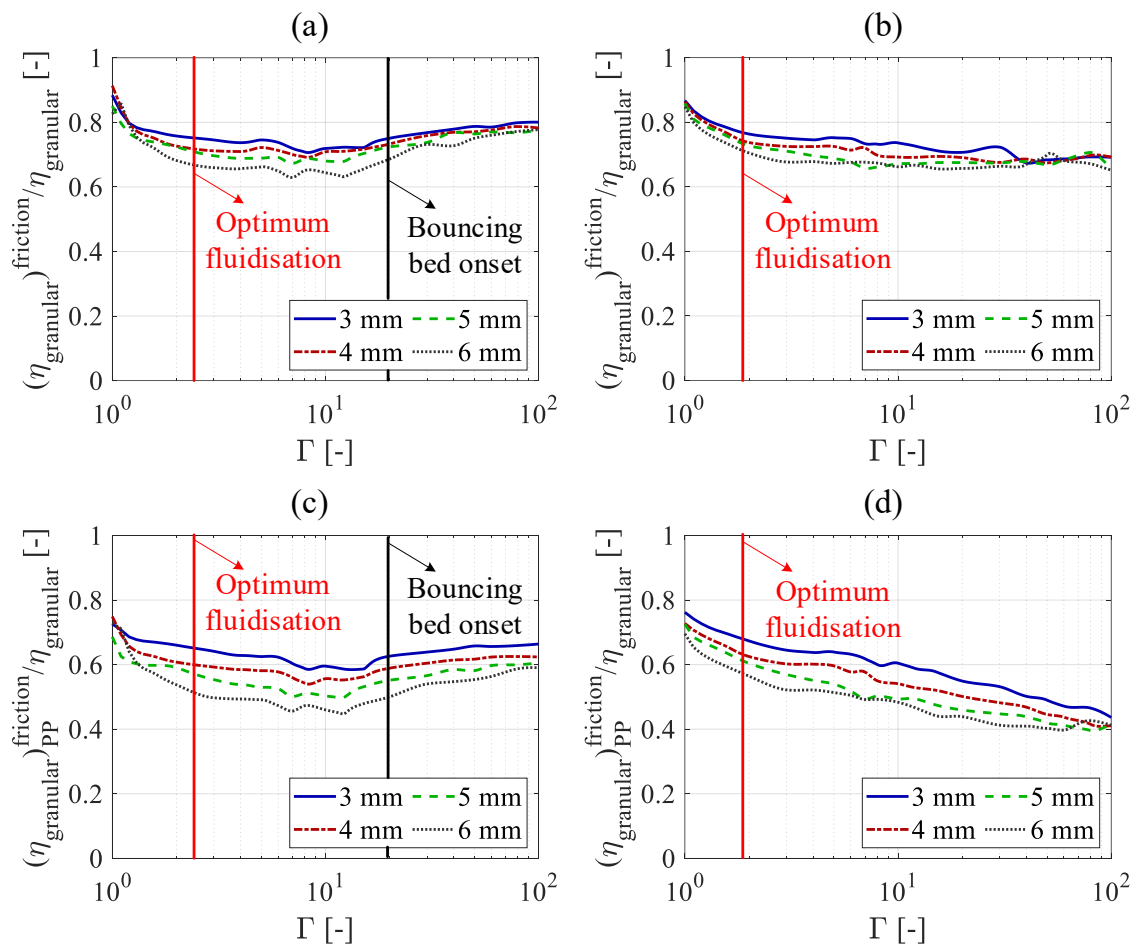
Figure 6.29: Frictional dissipation contribution at: (a) 40 Hz and (b) 160 Hz, and inter-particle frictional contribution at: (a) 40 Hz and (b) 160 Hz.

As shown in Figure 6.29a and b, the frictional contribution generally decreases as the particle size increases, especially when the convection motion appears in the granular medium. It is

because the tangential contact activities (i.e., slipping-sliding) are much less within the convective zones of the granular medium, and, therefore a decrease in the number of particles causes decreases in the frictional contribution. Figure 6.29a and Figure 6.29b demonstrate that the dominant dissipation source is friction for granular dampers regardless of operating motional phase, and this mainly arises from inter-particle frictions as can be seen in Figure 6.29c and Figure 6.29d. The frictional contribution rapidly reduces as the fluidisation motion increases within the granular medium from lower amplitudes to the optimum fluidisation. It is because the relative motion in the fluidisation has more impact dissipation than the solid-like behaviour (see Figure 6.15 for the motional definition). As a result of decrease in the tangential contact activities (i.e., slipping-sliding) in the convection zones, the frictional contribution continues to decrease beyond the optimum fluidisation as the vibration amplitude increases. Although the bouncing bed phase generates two intensive collective collisions with the enclosure ends, the frictional dissipation significantly dominates the energy dissipation in this phase reaching about 80%.

6.6   Chapter Summary and Conclusions

In this chapter, a link between the granular motional phase map and energy dissipation effectiveness has been demonstrated by employing simulations using the DEM approach. This relationship has been explained by showing how different granular motional behaviours affect dissipation characteristics. It has been shown that the developed understanding is consistent regardless of excitation orientation, particle size, material and contact properties.

The dissipative performance of granular dampers is controlled by two principal motional mechanisms: collective collision and particle fluidisation. Optimum performance can be achieved for each mechanism, but optimum conditions are different for each mechanism because the motional behaviour differs.

The most effective performance occurs when there are two collisions per vibration cycle, between the granular medium and the alternate enclosure ends. It is referred to the bouncing bed phase, and the optimum is found about the onset of this phase. This phase provides the most efficient granular energy dissipation for a broad amplitude range, which is a significant advantage for the deployment of amplitude-dependent granular dampers. However, efficient granular energy dissipation is obtained over a narrow excitation frequency range as the optimum condition depends on the flight time during which the clearance is travelled by the granular medium. As the clearance changes depending on the arrangement of the particle group within the enclosure void, it has been shown that the accurate estimation of the effective clearance is important to accurately predict the optimum condition in this phase.

It has been shown that the solid-fluid-convection behaviours of granular medium form an inter-related phase transition process, and they are independent from the bouncing bed phase. Amongst them, fluidisation is the most effective motion for dissipating energy. Therefore, it has been shown that the key factor is the ratio of the fluidised particles to the other particles (which exhibit solid-like or convection motion) for the optimum condition. This is primarily controlled by the activation level of particles which depends on the relative level of dynamic and static forces. The optimum is achieved when the maximum ratio of the fluidised particles to the other particles is obtained. It has been shown by comparing different excitation orientation cases that the quality of the fluidisation optimum depends on the level of this maximum ratio. The optimum is relatively insensitive to frequency compared to the bouncing bed phase and provides efficient energy dissipation for a broad frequency range. This significant design feature of the fluidisation optimum condition can be utilised for low-amplitude vibrations.

7 Experimental Measurement of Granular Energy Dissipation

7.1 Overview

To demonstrate the validity of the simulation model used to evaluate the general relationship between granular energy dissipation and dynamic motional behaviour in Chapter 6, this chapter presents equivalent physical measurements. Since 3D printed particles (which have relatively high level of surface roughness) are used for non-spherical particle investigations in the next chapter, it is also aimed to explore the effect of particle surface roughness in this chapter.

7.2 Spherical Particles

For experimental measurements of granular energy dissipation, 5 mm diameter spherical acrylic particles with properties matching with those used in the simulations were used. Note that this diameter was selected from one of particle sizes used in the simulations in Chapter 6. Two particle types (namely smooth and non-smooth) were used to understand the energy dissipation performance of different particle surface types and recognise any significant change depending on particle surface. These particles are shown in Figure 7.1a and Figure 7.1b. The smooth particles were moulded whilst the non-smooth ones were manufactured using 3D printing.
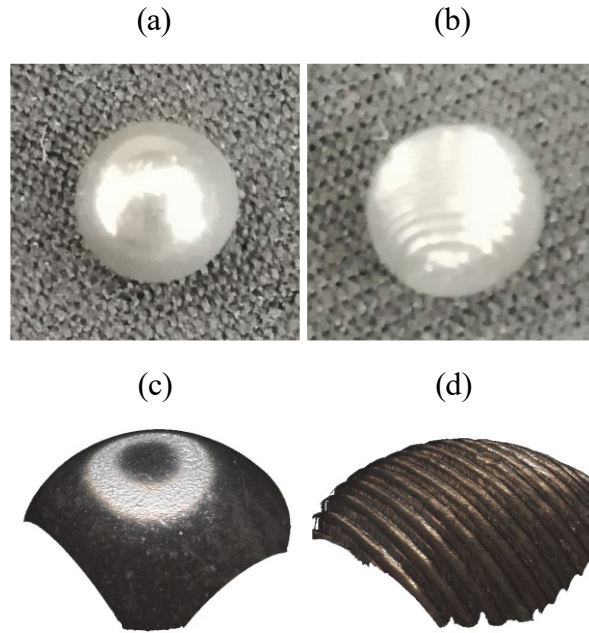
Figure 7.1: Spherical particles: (a) smooth and (b) non-smooth, and surface textures: (c) smooth and (d) non-smooth.

In order to quantify the surface characteristics of particle types, a set of surface roughness measurements was carried out using an Alicona InfiniteFocus optical surface roughness measurement machine. The particle images scanned by the machine are illustrated in Figure 7.1c and Figure 7.1d. As can be seen from the figures, there are periodic parallel (printing) ridges and small defects on these ridges on the non-smooth particle surface whereas the smooth particle surface has slight roughness. The average mean roughness parameter (Ra) is calculated to compare the particle surface types using the equation:

$$\mathrm{Ra} = \frac{1}{L_{\mathrm{path}}} \int_{0}^{L_{\mathrm{path}}} \left| z_{\mathrm{path}}(x) \right| dx \tag{7.1}$$

where $z_{\mathrm{path}}(x)$ is the depth profile function of a selected path line on surface and L_{path} is the total length of this selected path line. As the curvature of particles could affect $z_{\mathrm{path}}(x)$, L_{path} was selected sufficiently small for each measurement to minimise the effect of curvature on results.

154

The directional orientation of path selections with respect to the alignment direction of the printing ridges significantly changes results for the non-smooth particle. Therefore, two principal path orientations were separately measured for the non-smooth particle as described in Figure 7.2.
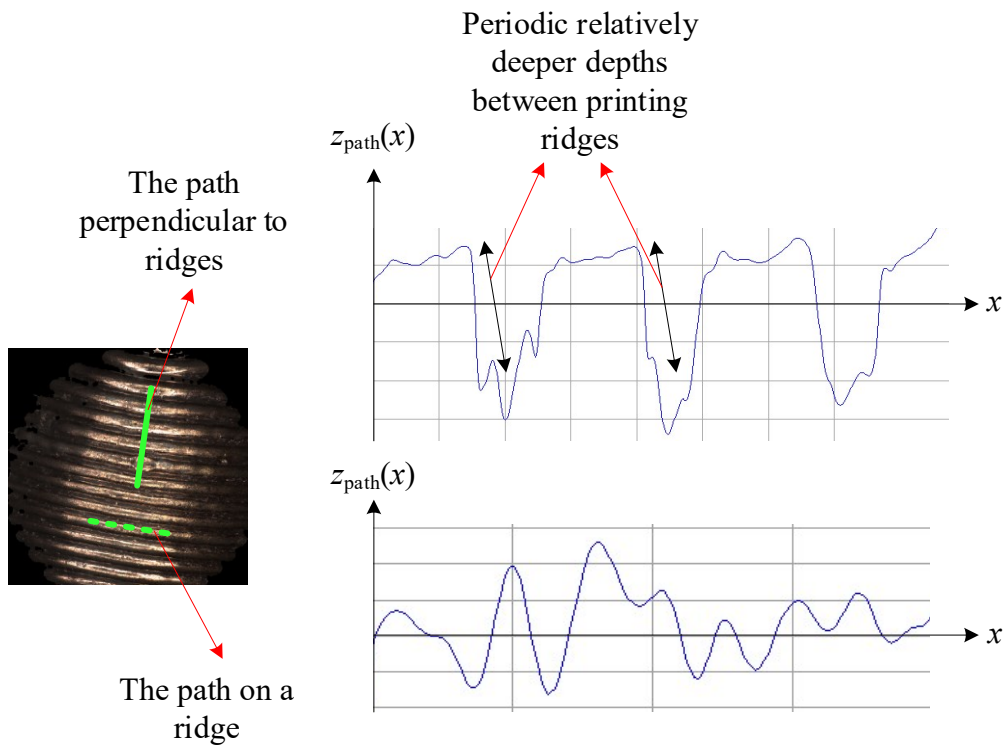
Figure 7.2: Path orientations on non-smooth printed particle surface.

In measurements, 5 different specimens were used for each particle type to measure the average surface roughness. To show the variation in the surface roughness depending on the selected path position, 4 different lines were constructed on each specimen surface and an average surface roughness value was obtained from these paths for each specimen.

The measurement results are provided in Table 7.1. The smooth particle surface roughness level is notably lower than the non-smooth particle. The surface roughness of non-smooth particle is significant when the perpendicular path orientation is considered. However, it should be also noted that the ratio of the maximum non-smooth particle surface roughness to the nominal sphere diameter (i.e., 5 mm) is about 0.2%. This indicates that the overall

particle sphericity level is not significantly affected by the printing ridges of the non-smooth particle.

Table 7.1: Surface roughness measurement results of spherical particles.

Particle no	Smooth particle, Ra [μm]	Non-smooth particle – perpendicular to ridges, Ra [μm]	Non-smooth particle – on ridge, Ra [μm]
1	0.15 ± 0.02	11.22 ± 0.58	0.34 ± 0.04
2	0.16 ± 0.02	12.47 ± 0.24	0.34 ± 0.03
3	0.17 ± 0.04	11.66 ± 1.04	0.38 ± 0.02
4	0.15 ± 0.02	11.56 ± 0.80	0.35 ± 0.05
5	0.17 ± 0.01	12.96 ± 0.69	0.33 ± 0.04
Average	0.16	11.97	0.35

7.3   Simple Measurement of Coefficient of Restitution

To reveal the difference between the individual contact damping levels of the smooth and non-smooth particles, a simple drop test rig was proposed as shown in Figure 7.3. This test aimed to measure the coefficient of restitution (COR) between a particle specimen and a flat surface.

(1) Personal Computer (PC)
(2) Signal conditioner
(3) Oscilloscope analyser
(4) Force transducer
(5) Acrylic cylindrical base plate
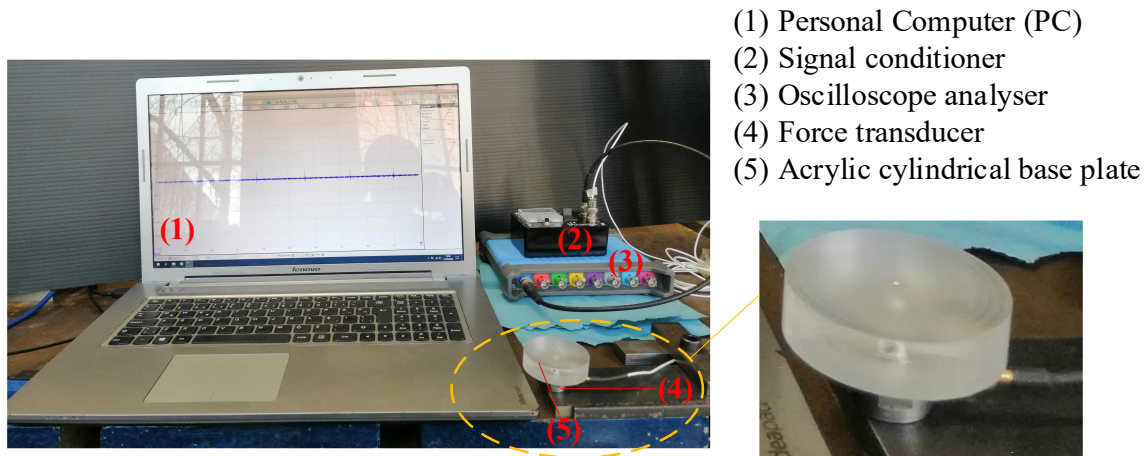
Figure 7.3: Individual particle drop test rig.

The measurement was performed by releasing a particle onto the cylindrical base plate from an arbitrary height. Afterwards, the particle was allowed to generate several successive impacts (at least 3) with the plate in a measurement sequence. The force signal was captured by the force transducer mounted between the plate and the fixed ground. The force history

of each measurement was then stored in PC by the ways of the signal conditioner and the oscilloscope analyser.

A measurement example is presented in Figure 7.4. It shows 3 successive impacts of the smooth particle at which the force magnitudes are significant compared the non-impact times. A simple algorithm was used in Matlab to automatically identify impacts. In this way, the time gaps between subsequent impacts, i.e., T_{1-2} and T_{2-3}, were also captured for each measurement. It should be noted that the sampling rate of the force signal was 200 kHz for all drop tests in order to capture impacts accurately.
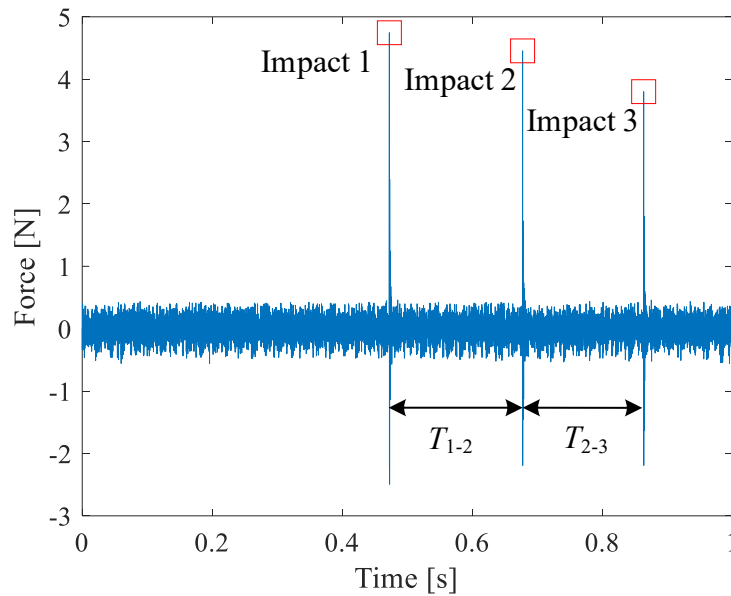
Figure 7.4: A sample force measurement showing 3 successive impacts.

Considering Impact 2 of the three successive impacts shown in Figure 7.4, COR can be defined as:

$$e_{contact} = v_{impact-2^-} / v_{impact-2^+} \qquad (7.2)$$

where $v_{impact-2^+}$ and $v_{impact-2^-}$ are the impact velocity at the beginning of Impact 2 and the leaving velocity at the end of Impact 2, respectively. Supposing that the energy of particle is

only dissipated by inelasticity during contact, the impact velocity of Impact 2 is determined

as:

$$v_{impact\text{-}2^+} = T_{1-2}\,g\,/\,2 \qquad\qquad (7.3)$$

As $v_{impact\text{-}2^-}$ is equal to the impact velocity of Impact 3, it is similarly expressed as:

$$v_{impact\text{-}2^-} = T_{2-3}\,g\,/\,2 \qquad\qquad (7.4)$$

Thus, COR is re-written in terms of the time gaps between the impacts as:

$$e_{contact} = T_{2-3}\,/\,T_{1-2} \qquad\qquad (7.5)$$

In this experimental method, the sampling rate and the base plate vibration after the

separation with the particle are the most significant factors that can affect accuracy by

changing the duration of a contact. However, as the time gaps are much larger than the

contact durations, it is reasonable to assume that this method is relatively insensitive to these

issues. It should be also noted that different models and measurement techniques can be

found in the literature [135,178,195,196,198,202–205,213,214].

Measurements were performed by releasing the particles from various heights, and COR was

calculated applying Equation (7.5) for each test. The results are set out depending on the

impact velocity of Impact 2 in Figure 7.5. The results indicate that COR values are

independent of the impact velocity – approximately a horizontal distribution. This is because

the impact velocities are smaller than the yield velocity of particles. The mean COR value is

0.91 for the smooth particle and 0.83 for the non-smooth particle. This shows that rougher

surfaces indicate lower COR (i.e., higher impact dissipation) as similarly reported the in

literature [215,216]. It should be also noticed that the COR value used in the DEM

simulations (i.e., 0.86) is consistent with the physical measurement results shown in Figure

7.5.
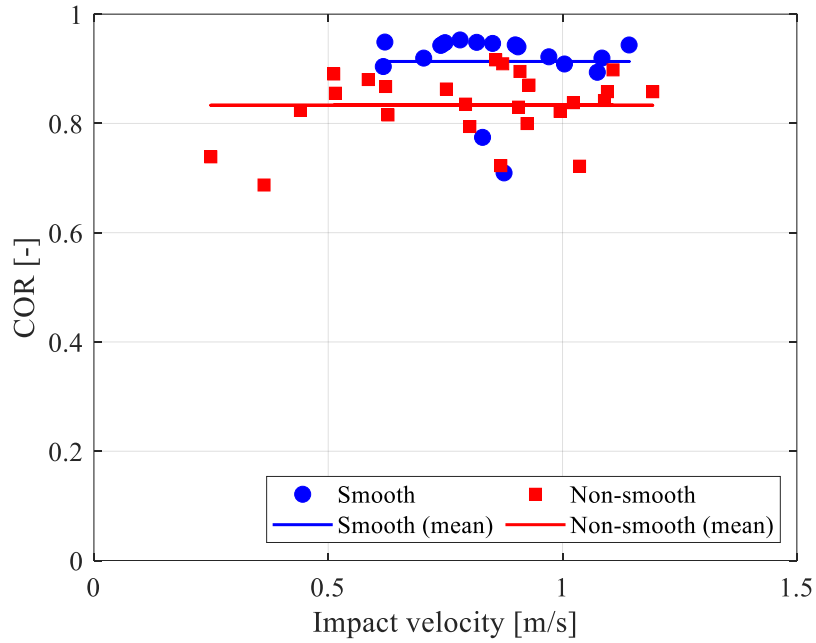
Figure 7.5: Measured COR depending on impact velocity.

7.4 Energy Dissipation Measurement: Model and Method

7.4.1 Damper model

A granular damper model was proposed for experimental investigations as illustrated in Figure 7.6. The vertical case, where the excitation direction is parallel to the gravity direction, was considered in this experimental model. It should be noted that the horizontal case was not attempted as this work aimed to validate the numerical damper model used in Chapter 6. In addition, Chapter 6 shows that there is the main characteristics of granular energy dissipation are independent from the vibration-to-gravity directional orientation.

(1) Enclosure lid
(2) Securing ring
(3) Main damper enclosure
(4a) Granular medium having smooth particles
(4b) Granular medium having non-smooth particles
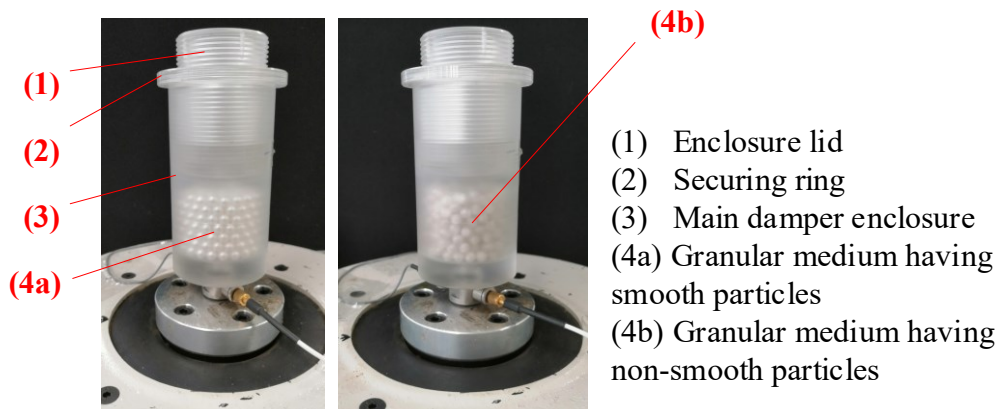
Figure 7.6: Experimental granular damper model.

To be able to use experimental results for the validation of the DEM simulations conducted, the enclosure was manufactured as consistent with the DEM model presented in Chapter 6. The enclosure inner diameter was therefore set to 40 mm, and the height of enclosure void was designed to be adjustable to achieve any volume fill ratio. In experiments, one of the simulated volume fill ratios in Chapter 6, $v = 0.466$ was considered. This was obtained by filling the enclosure inner void with 358 particles and arranging the enclosure height as 40 mm.

Experiments were carried out for all the excitation frequencies previously shown for the DEM model in Table 6.1. However, the acceleration amplitude had to be smaller than 12 g at 20 Hz and smaller than 40 g for the other frequencies because of the peak-to-peak displacement limit on the shaker. Note that g is the gravitational acceleration.

To match the rigid enclosure assumed for the DEM model, the enclosure was designed to keep any of its vibration modes at frequencies beyond the expecting range for testing. The detailed sketches of manufactured damper enclosure showing all dimensions and eigen-frequency analysis results (i.e., natural frequencies) can be found in Appendix-B.

7.4.2   Experimental setup and testing method

In order to measure the energy dissipated by the granular damper model presented in Figure 7.6, an experimental test rig was prepared as shown in Figure 7.7. This testing rig follows the approach used by Yang [64], and the dissipated energy measurement depends on simultaneous acquisition of acceleration and force signals while the damper undergoes harmonic excitations.
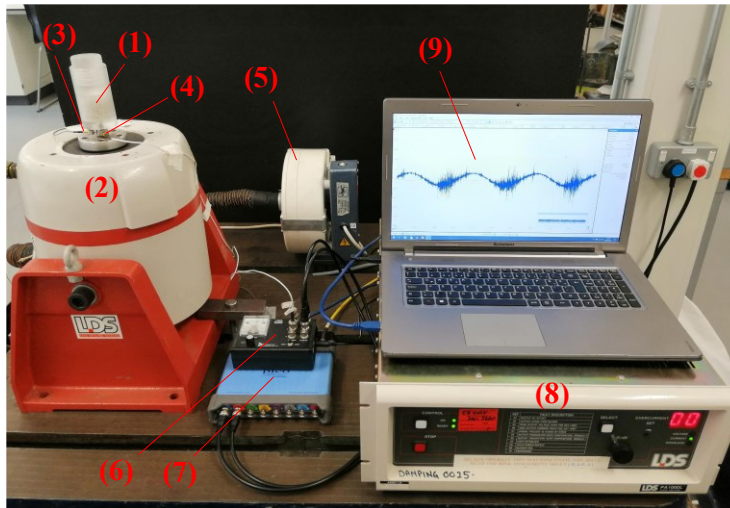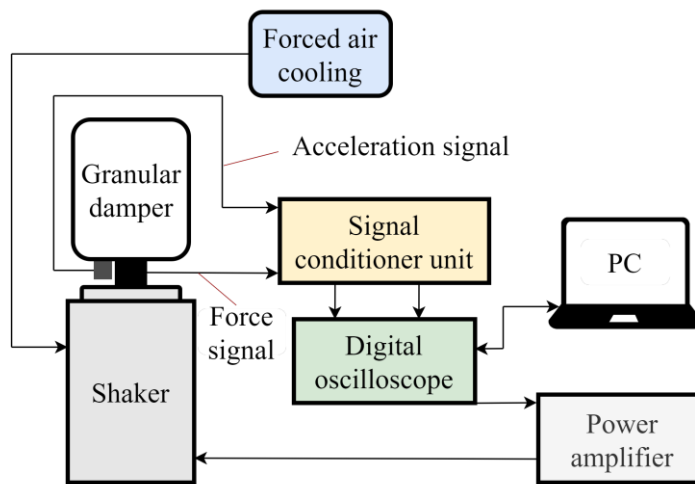
Figure 7.7: Granular energy dissipation measurement test rig.

In this test rig, first, the excitation signal was generated by PC setting the excitation conditions (i.e., amplitude and frequency):

$$u = \frac{\Gamma g}{\omega^2} \sin(\omega t) \tag{7.6}$$

where ω is the excitation frequency, Γ is the non-dimensional acceleration amplitude, and t is the time. This was sent to the electro-magnetic shaker by the way of the digital-analogue converter of the oscilloscope analyser and the power amplifier. As the damper was mounted to the shaker, it underwent the pre-described vibrational excitation. When the granular medium reached a steady-state condition (i.e., periodically generating a specific motional phase), the accelerometer and force transducer captured analogue data during a time period,

i.e., from $t = 0$ to $t = T_{\text{measurement}}$. These data sets were conditioned by the signal conditioner and digitised by the analyser. These were then converted to the acceleration, a(t), and force, f(t), signals using the associated transducer sensitivities, and a(t) and f(t) were stored in PC. Note that each steady-state measurement was carried out for 5 seconds using 40 kHz sampling rate (f_{sampling}). This eased data processing at different frequencies and provided to eliminate possible uncertainties that can occur in a single vibration period as many cycles were considered.

To be consistent with the DEM simulations in Chapter 6 and therefore allow comparisons, the damping efficiency described by Equation (6.8) is similarly used for the experimental damper model as:

$$\eta_{\text{granular}}^{\text{experimental}} = \tilde{E}_{\text{dissipated}}^{\text{experimental}} / \tilde{E}_{\text{dissipated}}^{\text{max}} \tag{7.7}$$

where the maximum dissipated energy that can be achieved in a vibration cycle, $\tilde{E}_{\text{dissipated}}^{\text{max}}$, is determined using Equation (6.10) as in the simulations.

The main difference between Equation (7.7) and Equation (6.8) is the calculation of average energy dissipated in a vibration cycle, i.e., $\tilde{E}_{\text{dissipated}}^{\text{experimental}}$. It can be expressed using the power dissipated by the granular damper in experiments, $P_{\text{dissipated}}^{\text{experimental}}$:

$$\tilde{E}_{\text{dissipated}}^{\text{experimental}} = 2\pi P_{\text{dissipated}}^{\text{experimental}} / \omega \tag{7.8}$$

The dissipated power is obtained by calculating the real part of average transmitted power to the damper enclosure in a measurement as:

$$P_{\text{dissipated}}^{\text{experimental}} = \text{real}\left(\sum_{k=0}^{T_{\text{measurement}} f_{\text{sampling}} - 1} \mathbf{F}_k \mathbf{V}_k^* / 2 \right) \tag{7.9}$$

where $\mathbf{F}_k$ is the complex force at the frequency point k, $\mathbf{V}_k$ is the complex velocity at the same frequency point, and the superscript star represents complex conjugate manipulation. The complex force and velocity are respectively determined by applying the discrete Fourier transform for the measured time-domain signals as:

$$\mathbf{F}_k = \sum_{i=0}^{T_{\text{measurement}} f_{\text{sampling}}} \mathrm{f}\left(t_i\right) e^{-\mathrm{j}2\pi ki/\left(T_{\text{measurement}} f_{\text{sampling}} - 1\right)} \tag{7.10}$$

$$\mathbf{V}_k = \sum_{i=0}^{T_{\text{measurement}} f_{\text{sampling}}} \mathrm{a}\left(t_i\right) e^{-\mathrm{j}2\pi ki/\left(T_{\text{measurement}} f_{\text{sampling}} - 1\right)} / \mathrm{j}\omega_k \tag{7.11}$$

where t_i is the discrete time points, ω_k is the kth discretised frequency, and j is the imaginary number.

Alternatively, Equation (7.9) can be explicitly expressed by introducing the phase angles of the kth complex force ($\varphi_{\mathbf{F}_k}$) and the velocity ($\varphi_{\mathbf{V}_k}$) as:

$$P_{\text{dissipated}}^{\text{experimental}} = \frac{1}{2} \sum_{k=0}^{T_{\text{measurement}} f_{\text{sampling}} - 1} \left|\mathbf{F}_k\right|\left|\mathbf{V}_k\right| \cos\left(\varphi_{\mathbf{F}_k} - \varphi_{\mathbf{V}_k}\right) \tag{7.12}$$

Equation (7.12) should indicate that there is no dissipative source other than damping particles in experiments. This means that the phase angle between the acceleration and force signals should be exactly π ($\pi/2$ if the velocity is considered) if the empty enclosure is tested. A sample measurement of the empty enclosure is shown in Figure 7.8, where $m_{\text{enclosure}}$ is the mass of the enclosure.
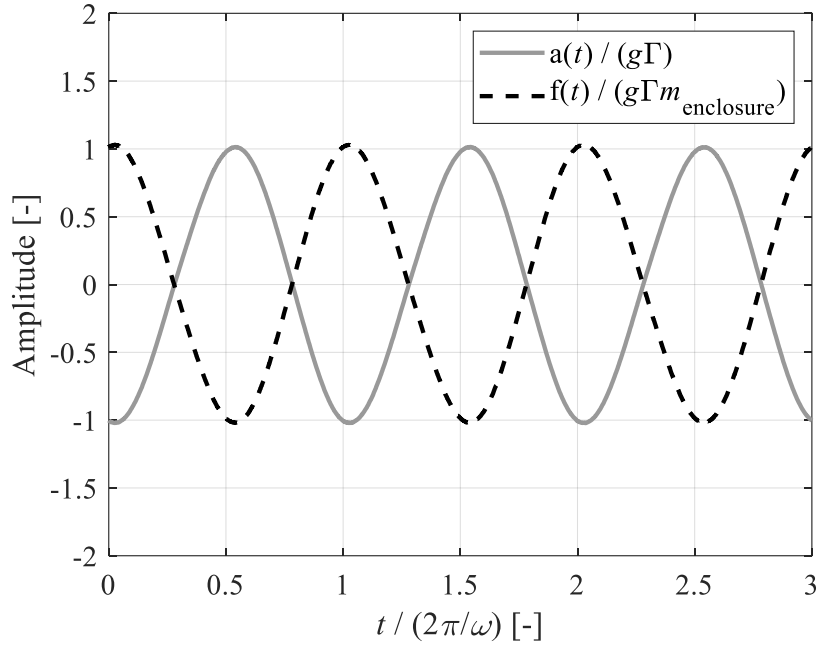
Figure 7.8: Acceleration and force histories of empty enclosure measurement for $\Gamma = 20$ excitation at 40 Hz.

Although it may not be apparent in Figure 7.8, the phase angle between these signals was not exactly π, i.e., there was an initial phase angle error. This can come from several uncertainties in experiments:

i. flexibility in the connections between different parts such as force transducer-shaker, enclosure-shaker, enclosure-accelerometer, enclosure-enclosure lid,

ii. other dissipative sources such as air viscosity,

iii. high frequency noise arisen from the forced cooling of the shaker,

iv. ground vibrations,

v. electrical current issues.

In order to keep the initial error small and consistent for each measurement case, the testing assembly was constructed using sufficiently large torque levels at connections, and was the unchanged until all measurements were completed. In the testing assembly, the enclosure lid

was the only assembly part of granular damper that was removed during experiments to replace particles inside the enclosure void. In order to reduce the possible effect of this particle empty-fill process on measurements, the accelerometer was fixed onto the outer bottom surface of the enclosure.

Any remaining phase angle error between the velocity and force was determined for various vibration amplitudes at each frequency investigated as shown in Figure 7.9 to subtract it from Equation (7.12) for each measurement case. As can be seen from this figure, the initial phase angle error is very small and similar for different excitation conditions as targeted. It should be noted that the initial phase angle error was frequently measured before and after a damper test with particles to verify that it stayed at similar levels.
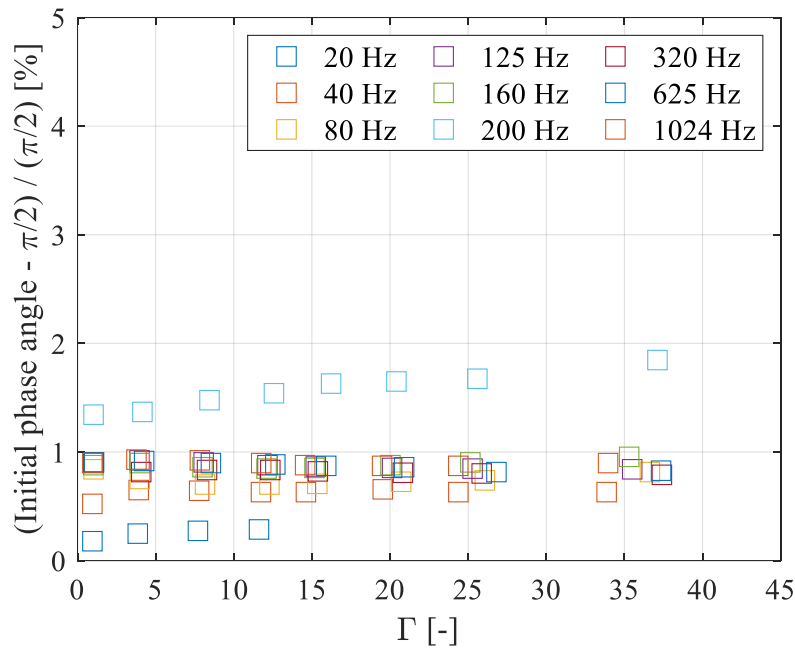
Figure 7.9: Initial phase angle error between velocity and force.

7.5   Energy Dissipation Measurement: Results

The granular damping efficiencies of smooth and non-smooth particle types measured using the experimental model are shown Figure 7.10 and Figure 7.11 for various vibration amplitudes at each frequency considered. The DEM results related to these sets of

experiments (having the same volume fill ratio and particle size) are included in these figures for comparisons.
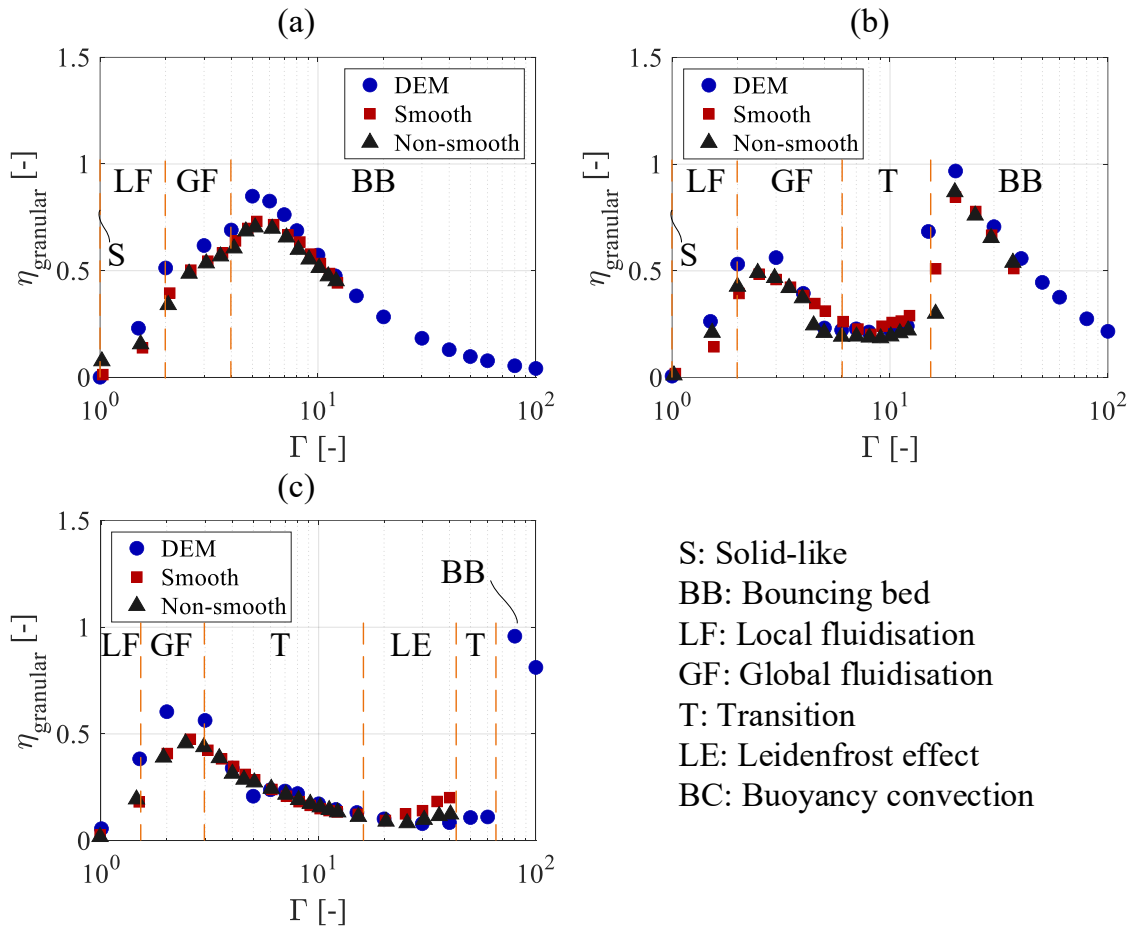
Figure 7.10: Granular damping efficiency comparisons using $\upsilon = 0.466$ for excitation frequencies of: (a) 20 Hz, (b) 40 Hz and (c) 80 Hz.

The presented results show that the smooth and non-smooth particles provide very similar granular damping efficiency levels for all excitation conditions tested despite the measured difference in their surface characteristics. Slightly higher damping efficiency levels were achieved by the smooth particle in most of the excitation conditions. This results from a higher COR value of the smooth particle (see Figure 7.5). Note that this explanation can be supported by the sensitivity analysis results demonstrated in Figure 6.13.
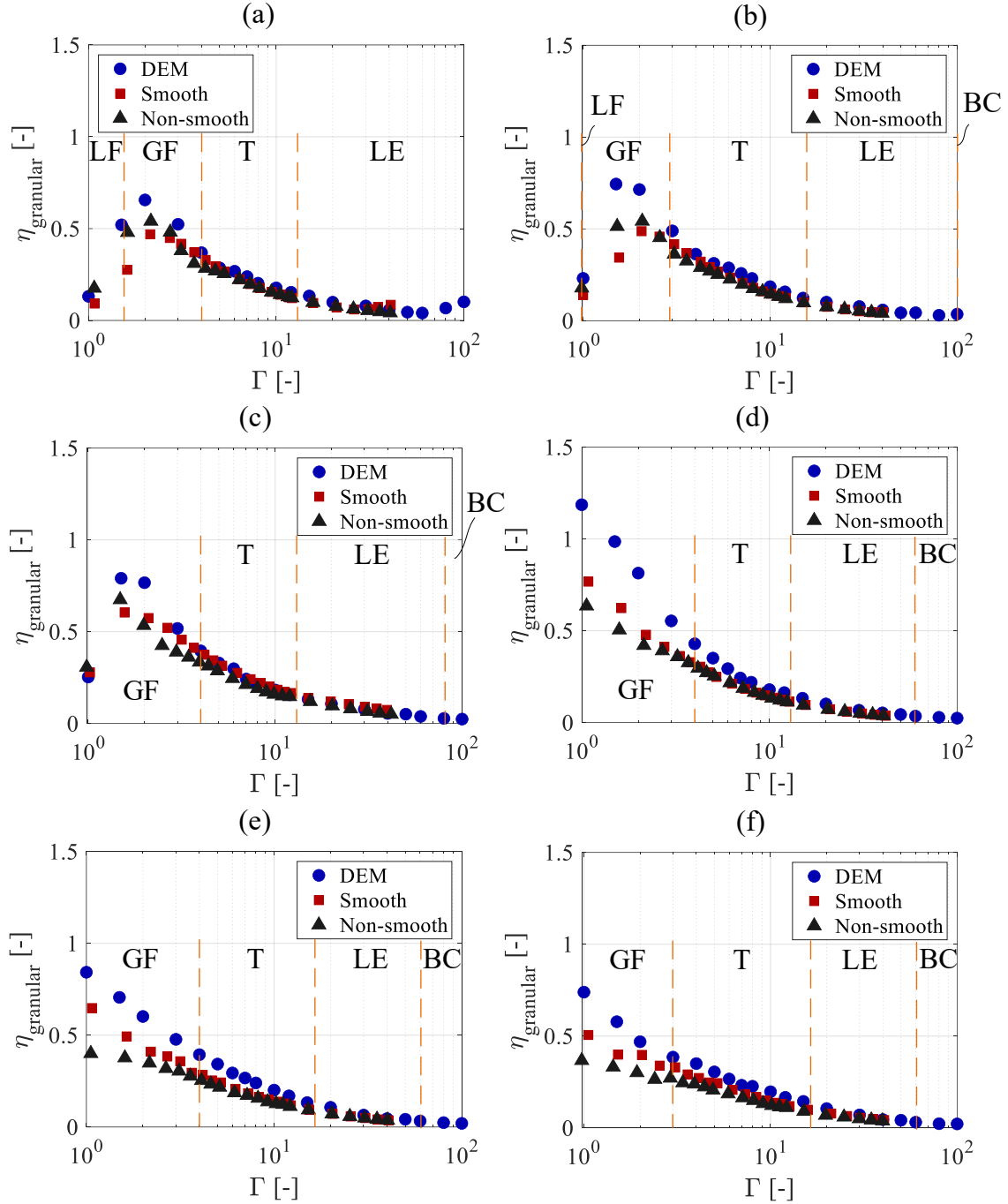
Figure 7.11: Granular damping efficiency comparisons using $v = 0.466$ for excitation frequencies of: (a) 125 Hz, (b) 160 Hz, (c) 200 Hz, (d) 320 Hz, (e) 625 Hz and (f) 1024 Hz. The motional phase amplitude ranges determined in Chapter 6 employing the DEM simulations are also illustrated in Figure 7.10 and Figure 7.11. These ranges were same in the experiments since the same volume fill ratio was used in both simulation and experiment. As a result, the most important amplitude and frequency dependent granular energy

dissipation characteristics (e.g., locations of collective collision and fluidisation optimums) captured by the DEM model greatly matches with the experimental observations by both particle types. In addition, the damping efficiency levels of DEM are in a consistent agreement with the experiments even though the DEM generally overestimates the experiments. These small overestimations change with excitation conditions and can be attributed to the approximations made in the DEM model (e.g., contact model and dissipated energy calculation), relatively small number of cycles computed in the DEM simulations to reach steady-state conditions, discrepancy in material properties and typical uncertainties in experiments.

7.6 Signs of Granular Motional Phases in Measured Signals

Indications of collective collisions can be seen in the acceleration and force signals measured using the experimental granular damper model. Therefore, to both briefly re-emphasise the effect of collective collisions on the granular energy dissipation effectiveness using the experimental data and broaden the understanding on collective collisions for enabling future research, the time-dependent signals recorded around the bouncing bed and fluidisation optimum amplitudes are investigated in this section. In this investigation, an excitation frequency of 40 Hz is considered as it exhibits both optimum conditions – see Figure 7.10b.

Figure 7.12 shows the measured signals for $\Gamma \approx 20$ which is close to the bouncing bed optimum amplitude. Note that m_{total} is the total mass of the enclosure and the particles. As can be seen from this figure, the collective collisions are observed twice in a cycle – i.e., with the enclosure base and top. Similar to the observation noticed in the simulation study, these collisions occur when the acceleration signal is almost zero – i.e., maximum enclosure velocity. As discussed before, this creates most effective energy transmission mechanism to the damping particles and stimulates intensive particle relativity within the body of particles.
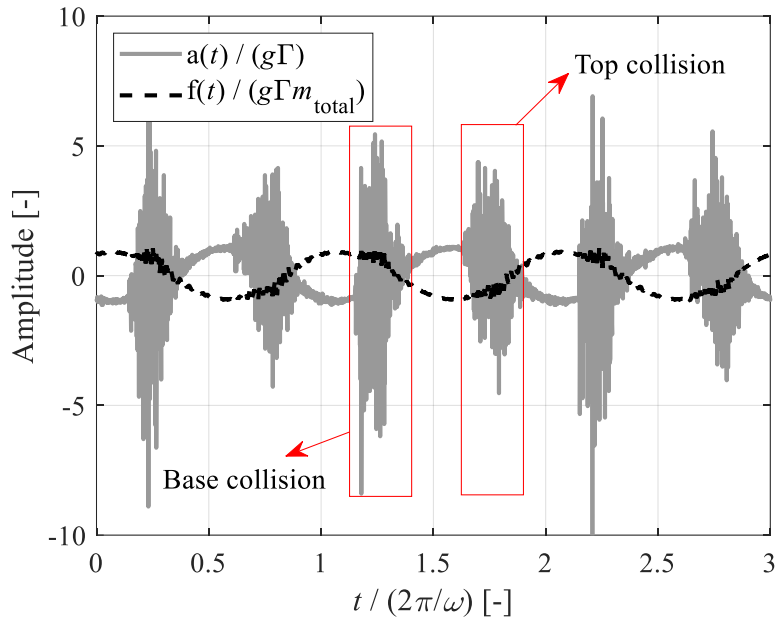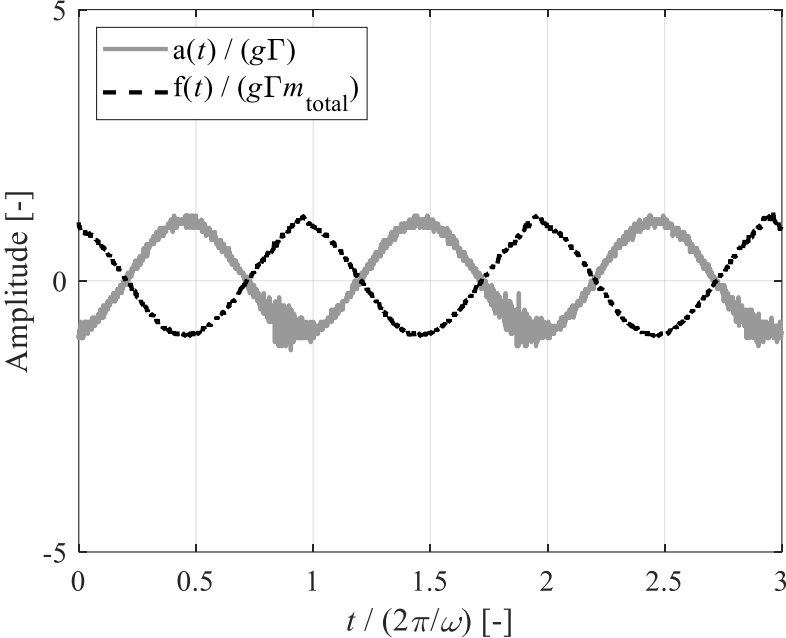
Figure 7.12: Measured acceleration and force signals at 40 Hz for $\Gamma \approx 20$.

At larger amplitudes than the bouncing bed optimum, the enclosure acceleration at which the collisions occur is away from zero as shown in Figure 7.13. This means that the collision velocities are smaller than the enclosure maximum velocity in the cycle. It therefore reduces the relative intensity of collisions – see comparing the acceleration signal amplitude of collisions in Figure 7.12 and Figure 7.13.
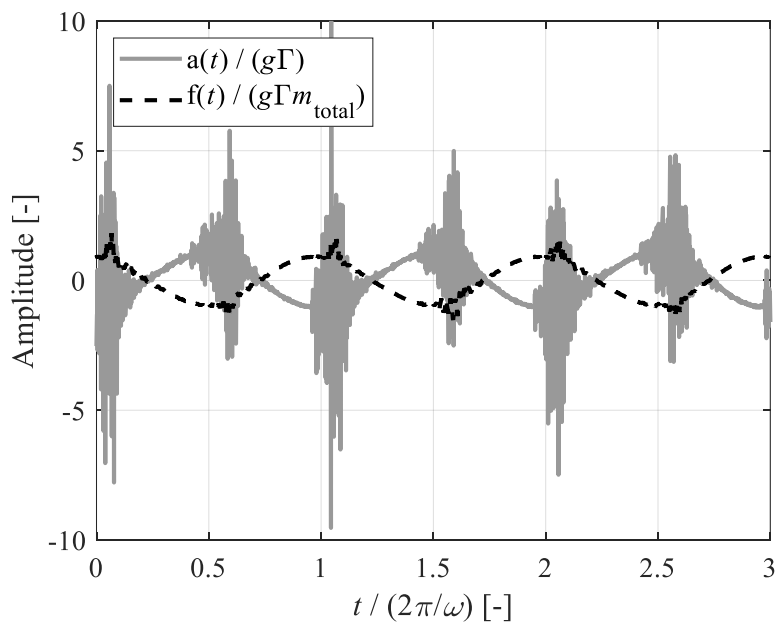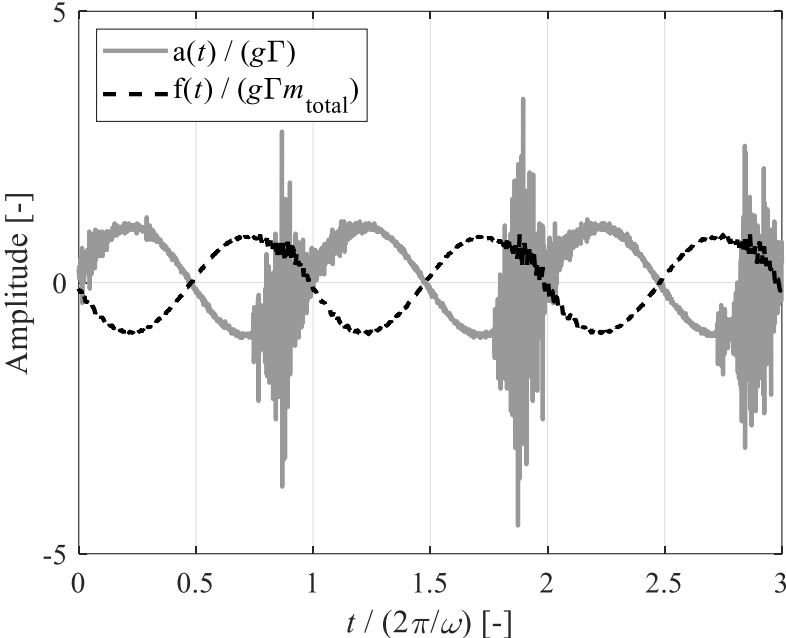

Figure 7.13: Measured acceleration and force signals at 40 Hz for $\Gamma \approx 37$.

The signals measured for three different amplitude cases around the fluidisation optimum condition are respectively shown in Figure 7.14, Figure 7.15 and Figure 7.16.

Figure 7.14: Measured acceleration and force signals at 40 Hz for $\Gamma \approx 1.5$.

Figure 7.15: Measured acceleration and force signals at 40 Hz for $\Gamma \approx 3$.
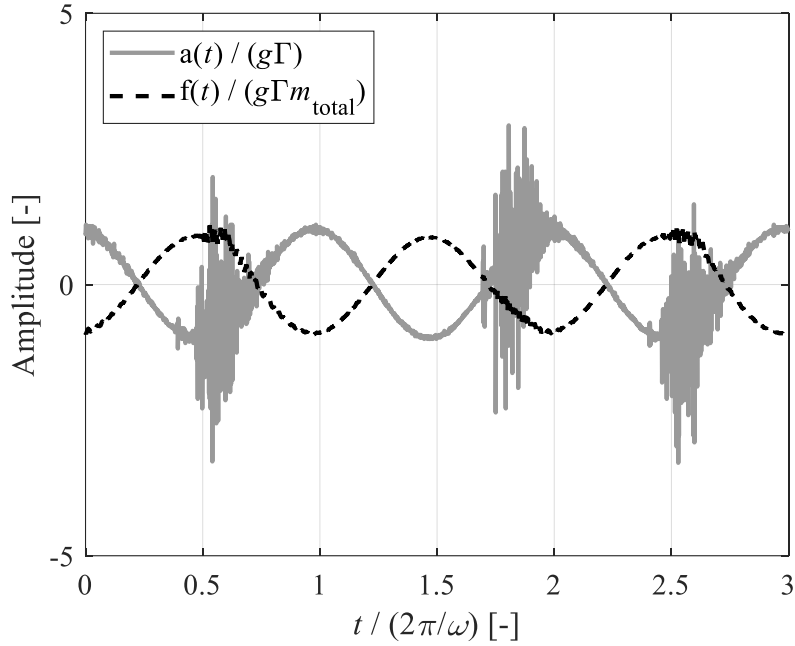
Figure 7.16: Measured acceleration and force signals at 40 Hz for $\Gamma \approx 4.5$.

Before the fluidisation optimum condition (Figure 7.14), the collective collision with the enclosure base is relatively weak as the granular medium collides with the enclosure at large enclosure acceleration amplitudes (i.e., small enclosure velocity amplitudes). Near the optimum (Figure 7.15), the collision occurs at smaller enclosure accelerations (i.e., larger enclosure velocities) – yielding stronger collective collision which increases fluidised particles and therefore granular energy dissipation performance. As the vibration amplitude increases above the optimum (Figure 7.16), the flight time of granular medium increases much introducing convective motions in a vibration cycle. This induces the collective collision of subsequent cycle at a larger acceleration amplitude. Therefore, this results in non-periodic collective collisions cycle-to-cycle and reduces the intensity of one collision in two cycles. As a result, the granular energy dissipation effectiveness decreases.

7.7   Chapter Summary and Conclusions

This chapter has presented physical experimental results to validate the findings of Chapter 6. It has been shown that the dissipated energies and dynamic motional behaviours predicted

using the numerical damper model of Chapter 6 match with the experimental measurements. Investigating the experimental time data obtained about the optimum damper amplitudes, it has been shown that the explanations related to the operating conditions of different optimums are valid.

In the experiments, the effect of particle surface roughness has been also examined by measuring the surface conditions of two different spheres whose surface characteristics are different from each other. The granular damping efficiency and motional differences between the particle types have been found small although the deviation in the individual collisional properties has been apparent because of surface roughness. Therefore, it has been concluded that there is negligible effect of surface roughness on the energy dissipation effectiveness and the amplitude-frequency dependent characteristics of granular dampers if particle surface roughness does not create a distinct particle shape. This result points the second main objective of this thesis, "What would it be observed if the particle shape deviates from being a perfect sphere?".

8 Influence of Non-Spherical Particle Shapes on Granular Energy Dissipation

8.1 Overview

The relationship between operating motional phase and non-linear energy dissipation behaviour of granular dampers have been described in Chapter 6 employing perfectly spherical particles. This chapter extends the understanding of this relationship by investigating non-spherical particles in granular dampers. The aim is to discover the effect of particle shape on the energy dissipation behaviour of granular dampers for particular motional phases and detect any change in the conditions that stimulate motional phases. This investigation is carried out using both controlled experimental and validated simulation models for a wide range of excitation conditions to comprise as many as possible motional phases identified in Chapter 6. Two distinct particle geometries are considered for this study: spheroids and circular toroids. A broad collection of principal dimensions is used for both geometry types to provide a systematic investigation.

8.2 Particle Shapes

8.2.1 Spheroids

The first particle shape change follows the spheroid path to observe dissipative and motional changes in granular dampers depending on the deviation level from a perfect sphere. This group of particles consists of sphere, oblate and prolate shapes. A spheroid shape is obtained

by revolving an ellipse around one of its principal axes as shown in Figure 8.1. These spheroid shapes can be defined by the aspect ratio described as $\alpha_{spheroid} = a_{spheroid}/b_{spheroid}$. When $\alpha_{spheroid} < 1$, a flattened spheroid (i.e., oblate) is obtained whilst $\alpha_{spheroid} > 1$ provides an elongated spheroid (i.e., prolate). Note that $\alpha_{spheroid} = 1$ represents a perfect spherical shape.
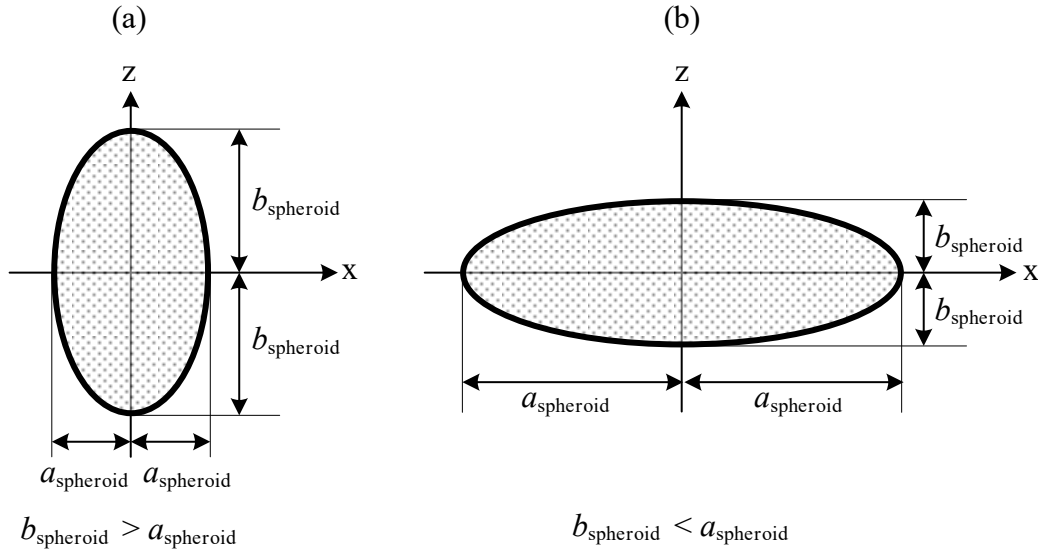
Figure 8.1: Ellipse geometries of (a) oblate and (b) prolate spheroids created by rotation around the x-axis.

For a comprehensive analysis, a collection of spheroid particles providing an aspect ratio range of 0.70 to 3.00 was used. To allow consistent comparisons, it was aimed to generate identical particles in terms of volume. This required the definition of the principal spheroid dimensions of generated particles depending on the aspect ratio as:

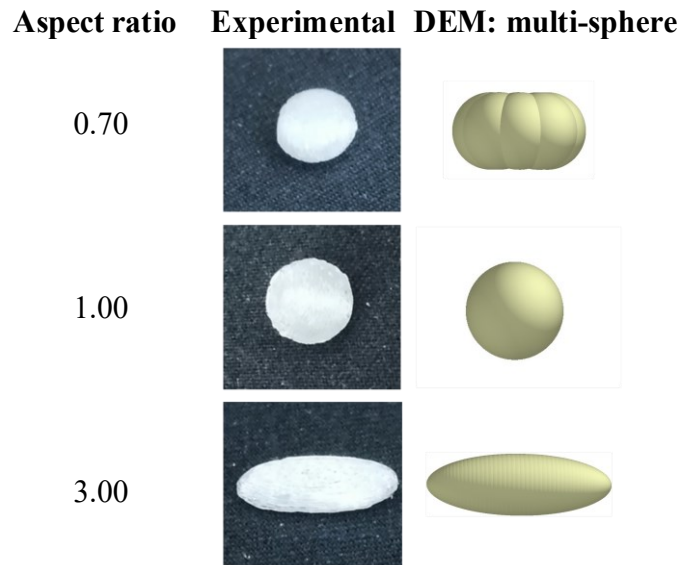$$a_{spheroid} = \alpha_{spheroid} b_{spheroid} \tag{8.1}$$

$$b_{spheroid} = \alpha_{spheroid}^{-1/3} r_{spheroid} \tag{8.2}$$

where $r_{spheroid}$ is the radius of perfect sphere whose volume is the reference for all generated spheroid particles.

The aspect ratios of the generated spheroid particles are shown Table 8.1 and illustrations of 3 different particles are provided in Figure 8.2. The particle material and its properties are equivalent to those provided in Chapter 6 and Chapter 7. It should be noted that $r_{spheroid}$ was set to approximately 3.8 mm for the spheroid particles generated.

Table 8.1: Spheroid particles for experimental and simulation study.

Aspect ratio	Sphericity	Experimental	DEM: multi-sphere
0.70	0.977	+	+
0.75	0.985	-	+
0.80	0.991	-	+
0.85	0.995	+	+
0.90	0.998	-	+
1.00	1.000	+	+
1.25	0.992	-	+
1.50	0.973	+	+
2.00	0.929	+	+
2.50	0.885	-	+
3.00	0.846	+	+

| Aspect ratio	Experimental	DEM: multi-sphere

Figure 8.2: Example pictures of spheroid particles.

Note that the sphericity values of spheroids are also included in Table 8.1 using the true sphericity parameter [217,218]:

$$\Psi = \sqrt[3]{36\pi \left(4\pi r_{sphere}^{3}/3\right)^{2}} / S_{particle} \tag{8.3}$$

where r_{sphere} is the radius of a sphere which has the same volume as the considered particle (note that $r_{\text{sphere}} = r_{\text{spheroid}}$ in this case) and S_{particle} is the surface area of this particle.

As shown in Table 8.1, 6 of the aspect ratios presented were considered for experimental studies. The production process resulted in some surface defects on particle surfaces as can be seen in Figure 8.2. The average surface roughness due to these defects was about 11.3 μm which was 0.2% of the reference particle diameter. It has been discussed in Chapter 7 that such a surface roughness level does not affect overall particle shapes. In addition, Figure 8.3 shows that these defects did not change the default volume of particles significantly exhibiting an error level being below 2% for each experimental particle.
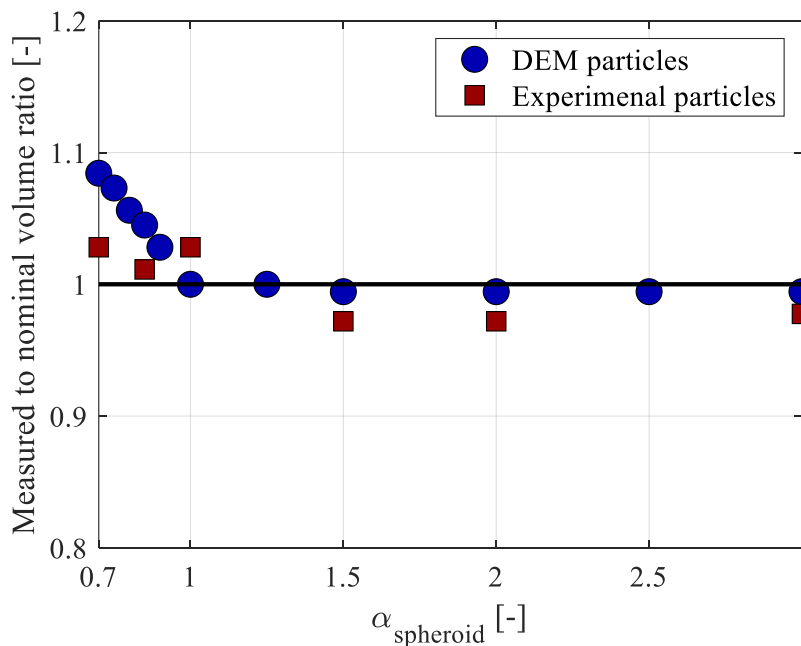
Figure 8.3: Volume inconsistencies in generated spheroid particles with respect to the exact volume of reference sphere.

All of the aspect ratios in Table 8.1 were numerically constructed for simulation studies. As broadly discussed in Chapter 4, the multi-sphere method was employed to generate non-spherical particles for numerical granular damper models in order to exploit the advantages of spherical DEM computations.

The prolate particles in Table 8.1, i.e., where $\alpha_{spheroid} > 1$, were generated implementing the analytical multi-sphere approach described in Section 4.4.1. In Figure 4.7, it has been shown that the use of 51 sub-spheres provides a high level of accuracy in the volume of represented non-spherical particle for aspect ratios smaller than 6. Thus, it was decided to use 51 sub-spheres for all numerical prolate particles as this case delivered a reasonable compromise between the accuracy and computational effort. As can be seen in Figure 8.3, the generated prolate particles represented the exact volume very accurately by producing small errors.

However, as there was no such analytical approach for oblate shapes, the aspect ratios which yielded oblate spheroids, i.e., $\alpha_{spheroid} < 1$, were obtained using the built-in multi-sphere optimisation tool of EDEM commercial software (explained in Section 4.3). It was determined by trial in this algorithm that 9 sub-spheres provided the most-satisfactory volume consistency and computational load. The most flatted oblate particle (i.e., $\alpha_{spheroid} = 0.7$) was obtained first, and the other oblates were generated scaling it according to the related dimensions. This non-analytical method produced large volume inconsistencies in the form of surface ridges and troughs and over-flattened oblate particles as can be seen in Figure 8.2. The volume differences between the generated oblates and the exact value were therefore relatively large producing volume errors reaching up to 10% as shown in Figure 8.3. This error was considered large enough to alter results in the numerical investigation of oblate particles. Nevertheless, they were tested to show both the limitation of multi-sphere method and notice this limitation in granular energy dissipation analyses when compared with experiments.

8.2.2 Circular toroids

The second particle change path is circular toroids. This aims to investigate the effect of hole level in a particle on granular energy dissipation behaviours. A circular toroid shape is

formed by sweeping a circle (whose radius is b_{toroid}) through a circular trajectory (whose radius is a_{toroid}). A two-dimensional view of toroid geometry is given in Figure 8.4. A circular toroid can be described by its hole ratio as $h_{toroid} = (a_{toroid} - b_{toroid})/(a_{toroid} + b_{toroid})$. When $0 < h_{toroid} < 1$, a circular toroid is obtained.
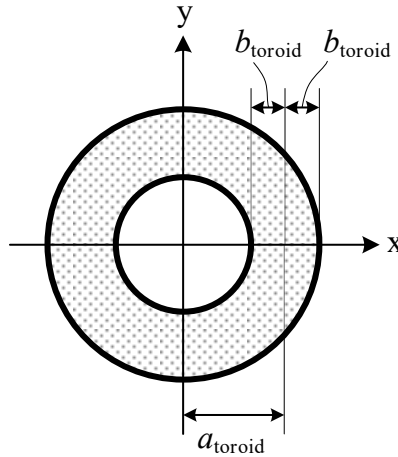
Figure 8.4: Two-dimensional view of circular toroid geometry.

A range of circular toroid particles whose hole ratios are between 0 and 0.33 was considered for investigations. For consistent comparisons, each was generated having identical volume. This created a relationship between the principal circular toroid dimensions as:

$$b_{toroid} = \left(3\pi a_{toroid} / 2b_{toroid}\right)^{-1/3} r_{toroid} \tag{8.4}$$

where r_{toroid} is the radius of equivalent perfect sphere volume for circular toroid particles.

The generated circular toroid particles are listed in Table 8.2, and some of those generated are demonstrated in Figure 8.5. Note that r_{toroid} was about 3.5 mm for dimensioning, and the same material and its properties (mentioned for the spheroid particles) were used.

In experiments, 4 of the hole ratios shown in Table 8.2 were manufactured. As they are visible in Figure 8.5, there were a level surface roughness on the particle surfaces (about 13.15 μm), and the produced circular toroid particles seemed more flatted on the top and

bottom surfaces than the original geometries targeted. These created an amount of volume error between the produced particles and the reference sphere reaching up to about 5% as demonstrated in Figure 8.6.

Table 8.2: Circular toroid particles for experimental and simulation study.

Hole ratio	Sphericity	Experimental	DEM: multi-sphere
0	1.000	+	+
0.05	0.867	+	+
0.11	0.831	-	+
0.20	0.782	+	+
0.27	0.743	-	+
0.33	0.710	+	+

Hole ratio	Experimental	DEM: multi-sphere
1.00		
0.20		
0.33		
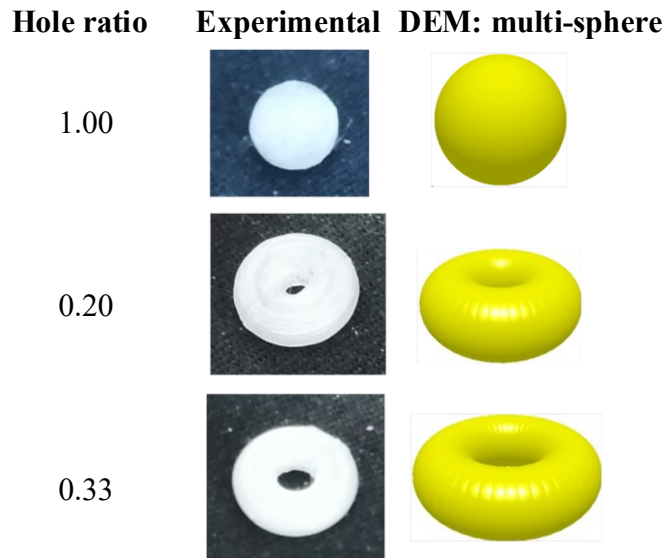
Figure 8.5: Example pictures of circular toroid particles.

The circular toroid particles in Table 8.2 were numerically generated applying the analytical multi-sphere approach presented in Section 4.4.2. Using the curves shown in Figure 4.11, it was found sufficient to employ 50 sub-spheres for all numerical circular toroid particles considering the trade-off between the accuracy of representative non-spherical particle shape and computational load. As can be seen in Figure 8.6, the constructed numerical particles had reasonable agreement with the reference exact volume.
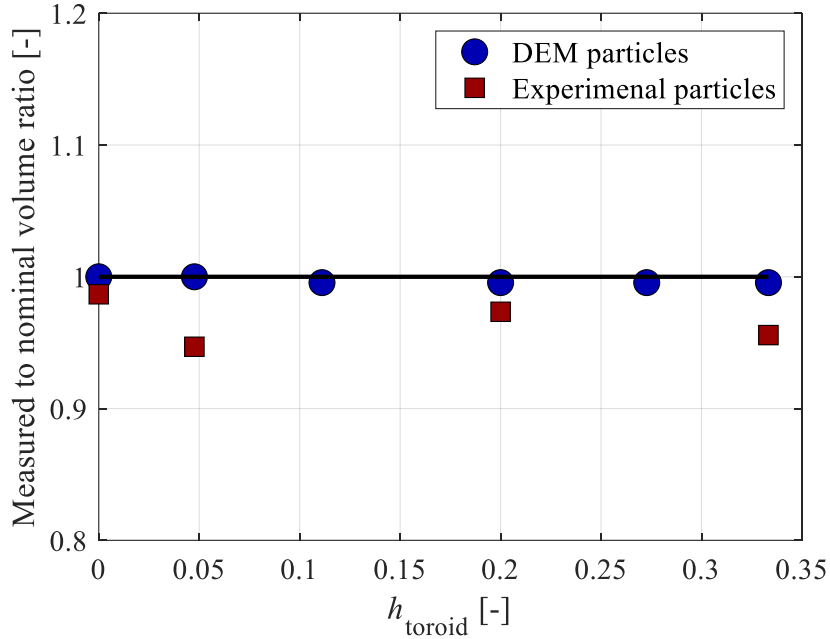
Figure 8.6: Volume inconsistencies in generated circular toroid particles with respect to the exact volume of reference sphere.

8.3 Approach and Model Properties

In this chapter, the effect of particle shape on granular damping behaviours were examined using a parallel investigation. This meant that both experimental and numerical studies were carried out together for each particle shape change path to obtain reliable results, detect any discrepancy and discover possible reasons behind quantative observations. In addition, the simulation study provided a better observation of particle motions at any excitation condition and allowed to conduct a sensitivity analysis by altering a single material property at a time. It was also possible to test more particle shapes in the simulation study as demonstrated in Section 8.2.

As in Chapter 6 and Chapter 7, the structure-independent damper model was employed to allow consistent particle shape comparisons to be made over different excitation conditions without involving the dynamics of host structures. The model is illustrated in Figure 8.7 for a particular particle shape.
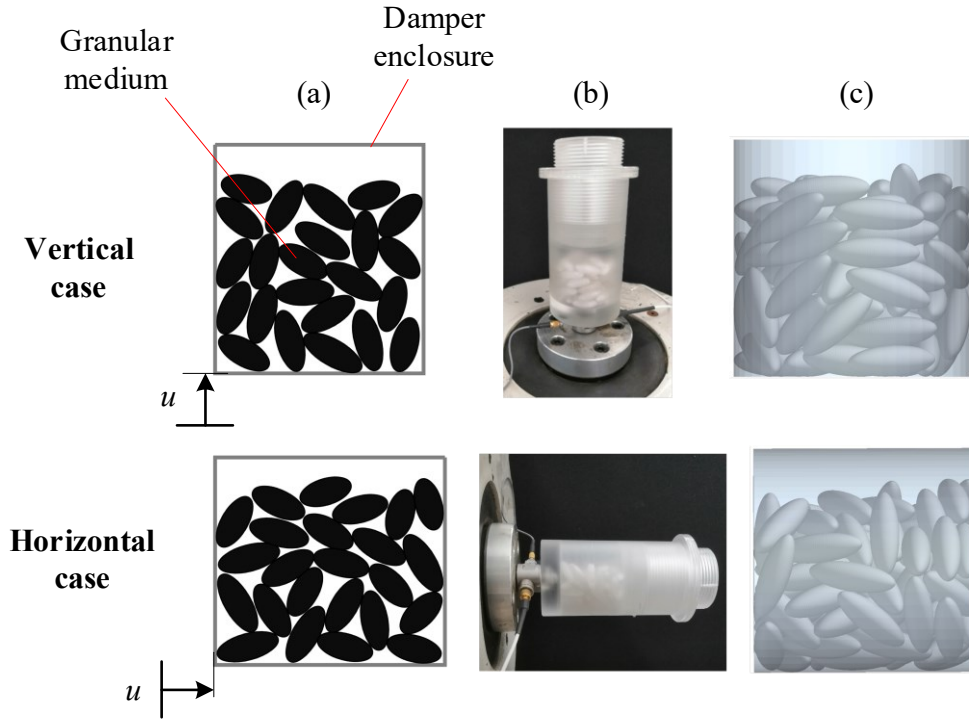
Figure 8.7: Granular damper involving prolate spheroid particles for different vibration-to-gravity orientations: (a) conceptual, (b) experimental and (c) simulation models.

To understand the effect of vibration orientation with respect to gravity, the vertical and horizontal cases were considered as shown in Figure 8.7 similar to Chapter 6 and 7. For both loading directions, the enclosure motion is described as:

$$u = \frac{\Gamma g}{\omega^2} \sin(\omega t) \tag{8.5}$$

where g is the gravitational acceleration, ω is the excitation frequency, and t stands for the time. As also mentioned before, Γ is the non-dimensional acceleration amplitude, defined as the amplitude of acceleration experienced by the damper enclosure divided by the acceleration due to gravity.

The cylindrical enclosure, whose material and geometric properties was provided in Chapter 6 and Chapter 7, was used as the damper enclosure. As the effect of volume fill ratio was determined in Chapter 6, only one enclosure height, i.e., 40 mm, was considered in the presented models. For the spheroidal particle investigation, the number of particles

employed was 90 for each spheroid particle (Table 8.1) which provided approximately the volume fill ratio of 0.41. It was about 0.38 for the circular toroid particle investigation by using 110 particles for each toroid presented in Table 8.2.

## 8.4 Experimental and Simulation Methodologies

For experimental and simulation studies, the energy dissipation effectiveness of granular dampers was determined by computing the damping efficiency, defined by Equation (6.8) and re-written in Equation (8.6).

$$\eta_{\text{granular}} = \tilde{E}_{\text{dissipated}} / \tilde{E}_{\text{dissipated}}^{\text{max}} \tag{8.6}$$

where $\tilde{E}_{\text{dissipated}}$ is the dissipated energy in a vibration cycle; $\tilde{E}_{\text{dissipated}}^{\text{max}}$ is the maximum energy that can be dissipated in the cycle that can be calculated using Equation (6.10). This damping measure allowed consistent comparisons for different particle shapes at various excitation conditions.

For the experimental investigations of all particle arrangements, the dissipated energy per cycle was measured by applying the same methodology described in Section 7.4.2. Note that the used experimental configurations (e.g., sampling frequency, excitation ranges) were also same as the provided ones in Section 7.4.2.

As sub-spheres were used to model numerical non-spherical particles as shown in Figure 8.8, the numerical DEM damper models comprising non-spherical particles were simulated applying the same computational procedures (e.g., contact model, excitation ranges) used in Chapter 6. However, the method to calculate the dissipated energy per cycle in simulations of non-spherical particles slightly differed from those of presented in Section 6.2.3 as a number of sub-spheres were used to construct a non-spherical particle.
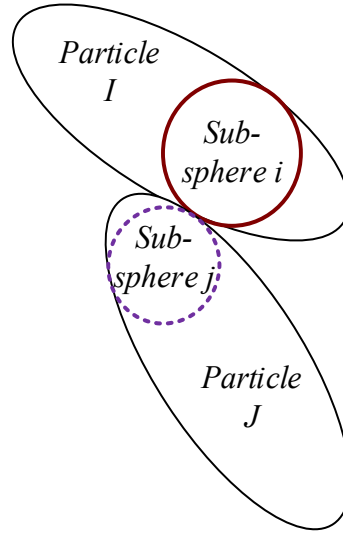
Figure 8.8: Two contacting sub-spheres.

The total dissipated energy in a numerical granular assembly was cumulatively calculated using the same equation (Equation (6.3)):

$$E_{\text{dissipated}}(t) = \sum_{k=1}^{t/\Delta t} \Delta E_{\text{dissipated}}(t_k = k\Delta t) \tag{8.7}$$

where Δt was the simulation time step and t_k was the time points at the end of each time step. Considering the simple illustration shown in Figure 8.8, the energy dissipation at each time step, $\Delta E_{\text{dissipated}}$, can be written accounting all the sub-spheres used in the simulation and initiated contacts as:

$$\Delta E_{\text{dissipated}}(t_k) = \sum_{I=1}^{N_{\text{particle}}} \sum_{i=1}^{N_{\text{sub-sphere},I}} \sum_{J=1}^{N_{\text{contact},Ii}} \sum_{j=1}^{N_{\text{contact},IiJ}} \left(\begin{array}{l} F_{\text{contact},IiJj}{}^{nd}(t_k) v_{\text{rel},IiJj}{}^{n}(t_k) + \\ F_{\text{contact},IiJj}{}^{td}(t_k) v_{\text{rel},IiJj}{}^{t}(t_k) \end{array} \right) \Delta t \tag{8.8}$$

where $N_{\text{contact},IiJ}$ is the number of contacts that the sub-sphere i of the particle I has with the sub-spheres of particle J, $N_{\text{contact},Ii}$ is the number of contacts of the particle I has with the other particles, $N_{\text{sub-sphere},I}$ is the number of sub-spheres that constructs the particle I, N_{particle} is the number of particles used in the simulation, $F_{\text{contact},IiJj}{}^{nd}$ and $F_{\text{contact},IiJj}{}^{td}$ are the

dissipative components of contact forces between the corresponding sub-spheres at normal and tangential directions, respectively, $v_{\text{rel},IiJj}{}^{n}$ and $v_{\text{rel},iJj}{}^{t}$ are the relative velocities between corresponding sub-spheres at normal and tangential directions, respectively.

To obtain the dissipated energy per cycle, the average of total dissipated energy (Equation (8.7)) was evaluated as:

$$\tilde{E}_{\text{dissipated}} = \frac{E_{\text{dissipated}}\left(t_{\text{initial}}\right) - E_{\text{dissipated}}\left(t_{\text{final}}\right)}{t_{\text{final}} - t_{\text{initial}}}\frac{2\pi}{\omega} \qquad (8.9)$$

where t_{initial} and t_{final} are respectively the times at which the steady-state vibration begins and the simulation ends. It should be noted that each excitation condition was simulated 18 complete vibration cycles, and the last 15 of those were considered as the steady-state in the simulations of this chapter.

## 8.5   Results and Discussions

As presented in Chapter 6, there are two principal motional mechanisms that control the effectiveness of granular dampers: collective collision and fluidisation. It has been shown that each has an optimum condition for granular energy dissipation. Therefore, in this chapter, the effect of particle shape is investigated by focusing on two main granular phase regions which the operation of granular dampers is efficient and practical: the bouncing bed phase where the collective collisions can be optimised and the inter-related fluid-convection based phased where the fluidisation motion can be optimised.

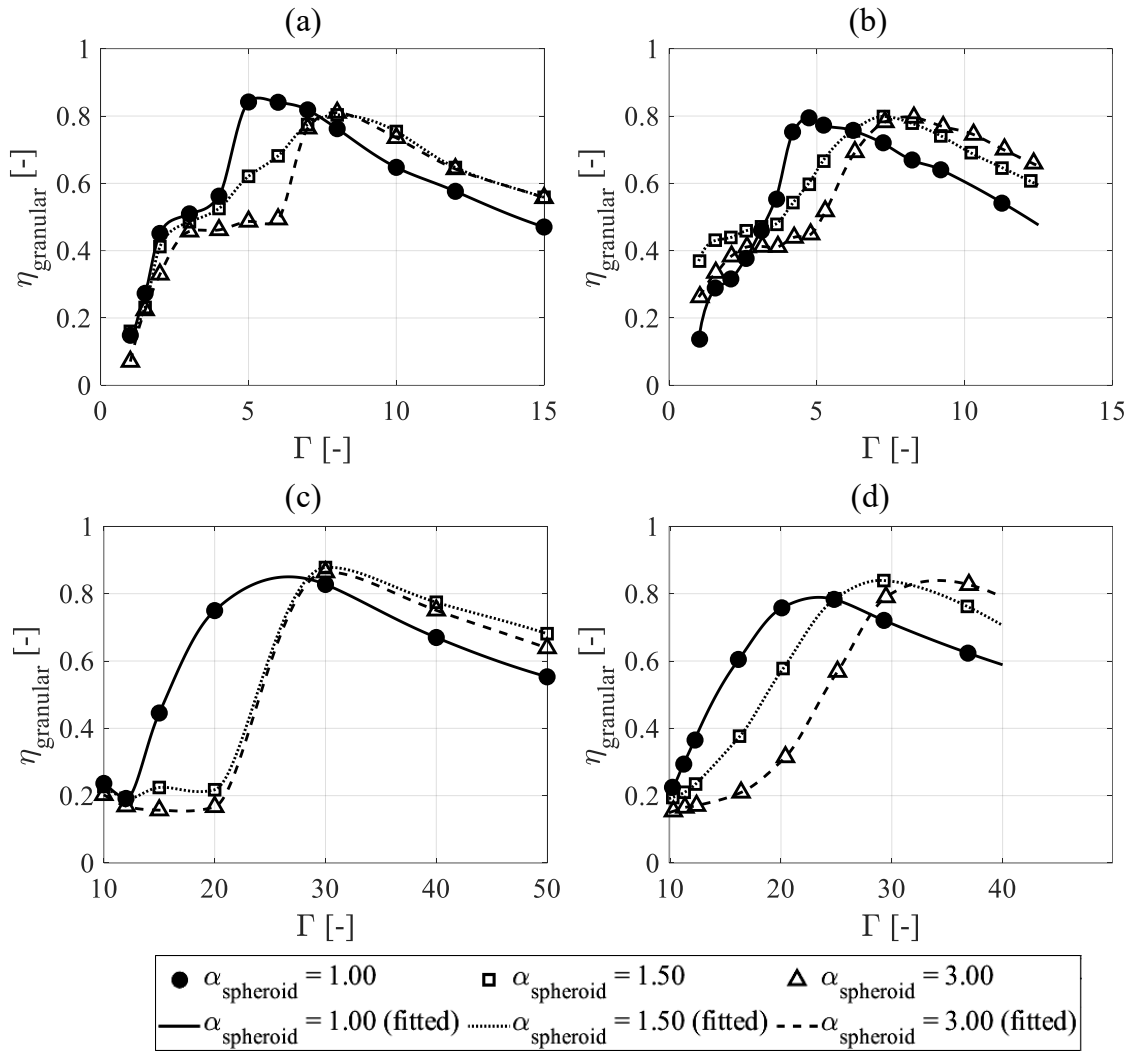### 8.5.1   Particle shape effect in the bouncing bed phase

As described in Section 6.4.1, the initiation of bouncing bed phase, in which two collective collisions are observed in a vibration cycle, depends on the distance that the granular medium can travel between two boundaries of the enclosure. As a result, to develop, it needs larger excitation displacement amplitudes than the other phases. Depending on packing achieved,

this condition is generally met at low frequencies. In this work, the bouncing bed phase was only observed at two lowest frequencies considered:20 Hz and 40 Hz.

Figure 8.9 and Figure 8.10 show the simulated and measured damping efficiency curves at these frequencies for the spheroid particle types $\alpha_{\text{spheroid}} = 1.00$, $\alpha_{\text{spheroid}} = 1.50$ and $\alpha_{\text{spheroid}} = 3.00$ in the vertical and horizontal excitation cases, respectively. As discussed before, the highest peak amplitude of each curve is the onset amplitude of the bouncing bed motional phase, i.e., the optimum energy dissipation condition.
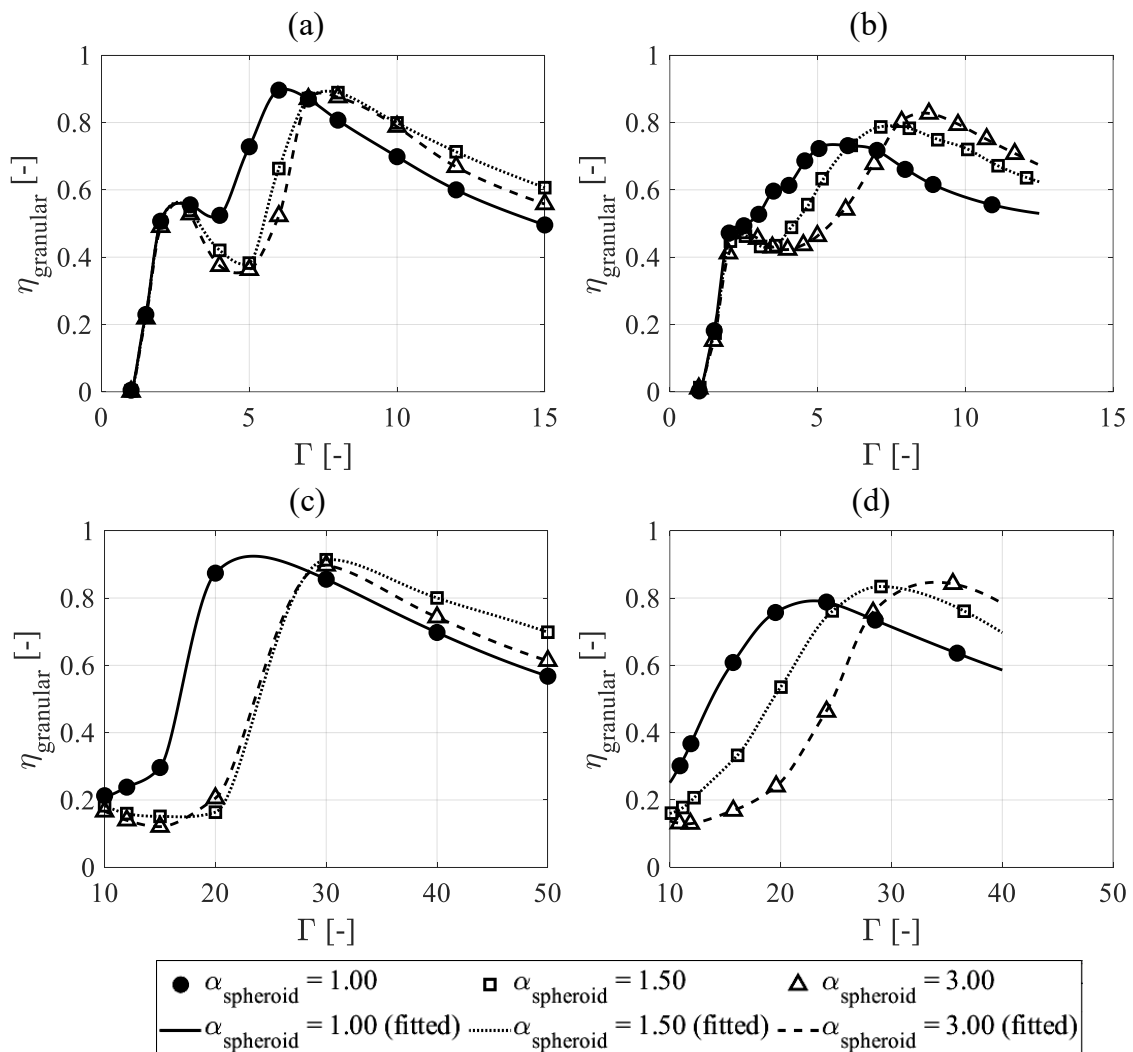
Figure 8.9: Effect of particle shape on damping efficiency in the vertical bouncing bed phase: (a) 20 Hz – simulation, (b) 20 Hz – experiment, (c) 40 Hz – simulation and (d) 40 Hz – experiment.

Figure 8.10: Effect of particle shape on damping efficiency in the horizontal bouncing bed phase: (a) 20 Hz – simulation, (b) 20 Hz – experiment, (c) 40 Hz – simulation and (d) 40 Hz – experiment.

As can be noticed in Figure 8.9 and Figure 8.10, the maximum damping efficiency observed seems relatively insensitive to particle shape, vibration frequency and excitation orientation. However, it is apparent that the bouncing bed onset amplitude changes considerably depending on particle shape regardless of vibration frequency and excitation orientation.

When the presented prolate particles (i.e., $\alpha_{\text{spheroid}} = 1.50$ and $\alpha_{\text{spheroid}} = 3.00$) are compared with the perfect sphere shape (i.e., $\alpha_{\text{spheroid}} = 1.00$), it can be seen that they increase the bouncing bed onset amplitude in granular dampers. As a related outcome, the presented

prolate particles provides higher granular damping efficiency at any operating amplitudes larger than their bouncing bed onset amplitudes, e.g., $\Gamma > 8$ at 20 Hz and $\Gamma > 35$ at 40 Hz.

The resulting bouncing bed amplitude shift indicates two important observations that are directly related to the practical design of a granular damper. First, if a granular damper is developed to operate at its optimum amplitude (i.e., the bouncing bed onset amplitude) supposing perfect spheres as the damping particles, its energy dissipation effectiveness can dramatically decrease in case of particle shape deviation from a perfect sphere. For an example, the damping efficiency drop as a result of non-spherical particles can be seen for $\Gamma \approx 20$ in Figure 8.9c. Secondly, if there is a length restriction in the designed granular damper void such that the bouncing bed phase onset cannot be achieved under the anticipated operating conditions, the problem can be overcome by using non-spherical particles. This can be clearly seen from the damping efficiency results of $\Gamma > 8$ at 20 Hz and $\Gamma > 30$ at 40 Hz in Figure 8.9 and Figure 8.10.

As a brief conclusion, it is clear that the particle shape has an important role in granular dampers operating in the bouncing bed phase. Thus, the extent of this effect should be determined by characterising the bouncing bed onset amplitude shift depending on particle shape parameter, and the reasons that stimulate this shift should be addressed to provide a deep understanding on the use of non-spherical particles in granular dampers.

8.5.1.1 Characterisation of the onset amplitude shift

The characteristic change of bouncing bed onset amplitude (i.e., $\Gamma_{optimum}$) depending on the spheroid particle aspect ratio is presented in Figure 8.11. It should be noted that the precise onset amplitude values were determined from the damping efficiency curves fitted to the measured and simulated damping efficiency datapoints.
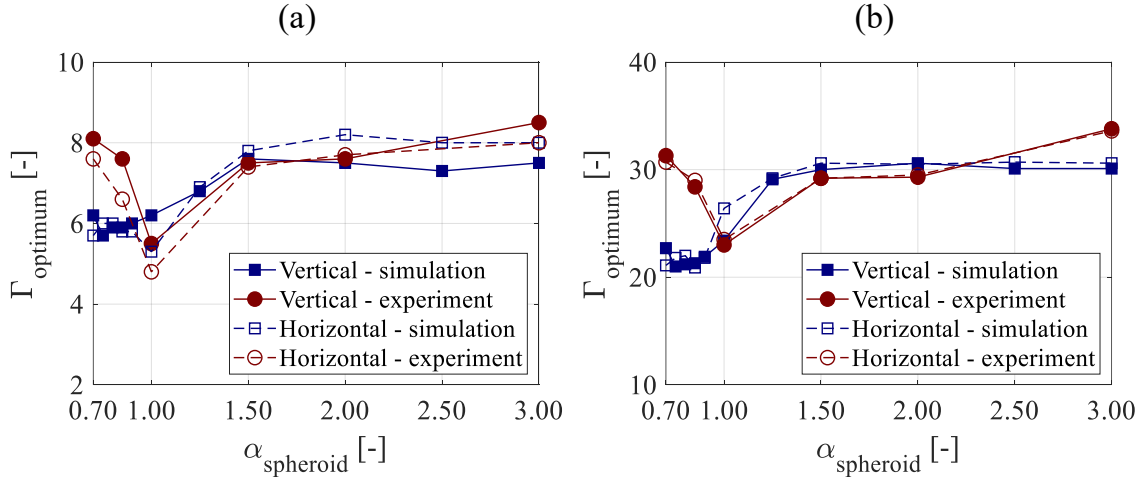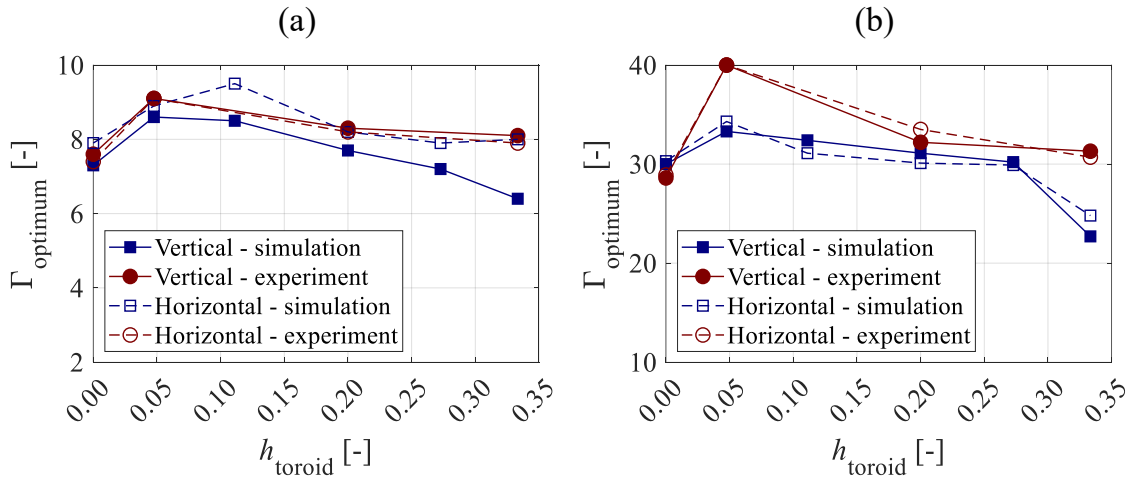
Figure 8.11: Variation of bouncing bed onset amplitude depending on spheroid particle aspect ratio: (a) 20 Hz and (b) 40 Hz.

As can be seen from Figure 8.11, the experimental study of the spheroid particles shows a consistent trend with respect to the aspect ratio regardless of excitation frequency or orientation. This particle shape-dependent Γ_{optimum} behaviour has two apparent zones: *i*) a v-shaped trough between $\alpha_{\text{spheroid}} = 0.70$ and $\alpha_{\text{spheroid}} = 1.50$ having a minimum at $\alpha_{\text{spheroid}} = 1.00$, and *ii*) an almost constant level between $\alpha_{\text{spheroid}} = 1.50$ and $\alpha_{\text{spheroid}} = 3.00$. It can be noticed that the left edge of v-shaped trough (i.e., $\alpha_{\text{spheroid}} = 0.70$) has a similar Γ_{optimum} value to that of the constant zone. The nearly identical rises from $\alpha_{\text{spheroid}} = 1.00$ to $\alpha_{\text{spheroid}} = 0.70$ and $\alpha_{\text{spheroid}} = 1.50$ can be attributed having the same sphericity levels in the left side of v-shaped trough (i.e., $0.70 < \alpha_{\text{spheroid}} < 1.00$) and the right side of v-shaped trough (i.e., $1.00 < \alpha_{\text{spheroid}} < 1.50$) as given in Table 8.1. As briefly stated before, this characteristic clearly shows that Γ_{optimum} of a granular damper is shifted to larger vibration amplitudes by introducing non-spherical spheroid particles. However, it can be noticed that the level of this shift becomes insensitive to the aspect ratio for $1.50 < \alpha_{\text{spheroid}}$ 3.00.

Figure 8.11 shows that the simulation results mostly agree with the observation of physical measurements. With the additional aspect ratios (i.e., $\alpha_{\text{spheroid}} = 1.25$ – an intermediate aspect

ratio at the right side of v-shaped trough and $\alpha_{\text{spheroid}} = 2.50$ – an aspect ratio in the constant level region), the simulation verifies the described characteristic. However, the left side of v-shaped trough is not clearly visible in the simulation results as can be seen in Figure 8.11. The likely explanation for this is that the numerically generated oblate spheroids are not able to represent the actual oblate geometries, i.e., the generated oblate spheroid particles do not indicate a perfect oblate geometry because of relatively large surface ridges, troughs and over-flattened structure in the overall geometry as demonstrated in Figure 8.2. Therefore, it can be deduced that the employed multi-sphere-based optimisation algorithm (see Section 4.3) may not be reliable to create some particle shapes for granular-based simulations.

Using the same methodology, the particle shape-dependent Γ_{optimum} was also determined for the circular toroids from the experiments and simulations as shown in Figure 8.12, with respect to the circular toroid particle hole ratio. As in the v-shaped trough of the spheroid particle characteristic, similar increase in Γ_{optimum} can be seen from the perfect sphere (i.e., $h_{\text{toroid}} = 0$) to $h_{\text{toroid}} = 0.05$ in the experimental result sets regardless of excitation frequency or orientation. However, rather than a constant region, they present a consistent decrease in Γ_{optimum} between $h_{\text{toroid}} = 0.05$ and $h_{\text{toroid}} = 0.33$, nearly reaching the level obtained by the perfect sphere. The simulation results follow the experimental trend. The relatively large difference between the experiments and simulations at some hole ratios (see $h_{\text{toroid}} = 0.35$ results in Figure 8.12) may result from the slight over-flattened structure on the bottom and top surfaces of manufactured experimental circular toroids.
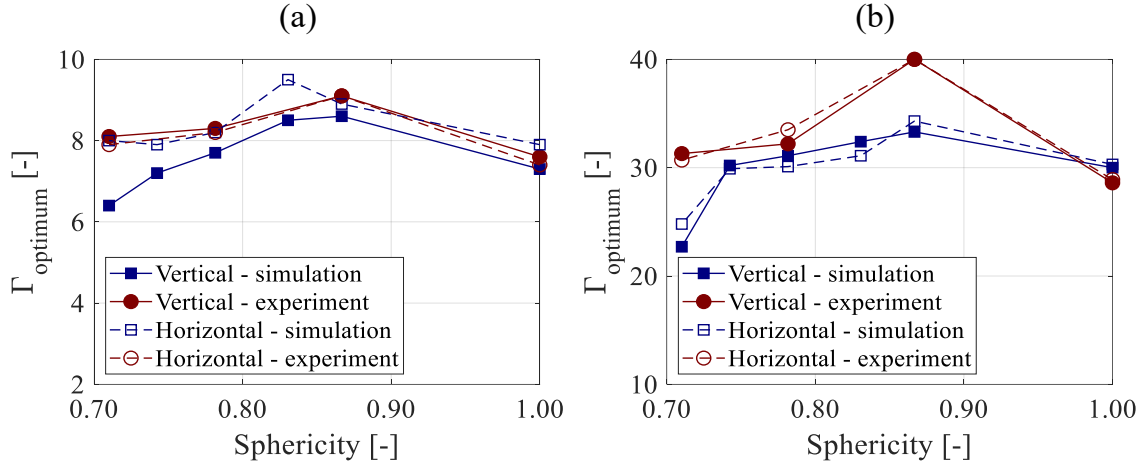
Figure 8.12: Variation of bouncing bed onset amplitude depending on circular toroid particle hole ratio: (a) 20 Hz and (b) 40 Hz – note that data points at $h_{\text{toroid}} = 0$ are instead those for perfect spheres.

In order to generalise the observed shift in the bouncing bed onset due to particle shape, the results presented in Figure 8.11 and Figure 8.12 are re-plotted in Figure 8.13 and Figure 8.14 depending on the sphericity of particles which represents how close a geometric shape is to a perfect sphere. Note that the oblate particle results are not included as they have the same sphericity levels as the prolate particles of $1.50 < \alpha_{\text{spheroid}}\ 3.00$, and the numerically generated oblates are not able to represent actual oblate geometries as mentioned before.
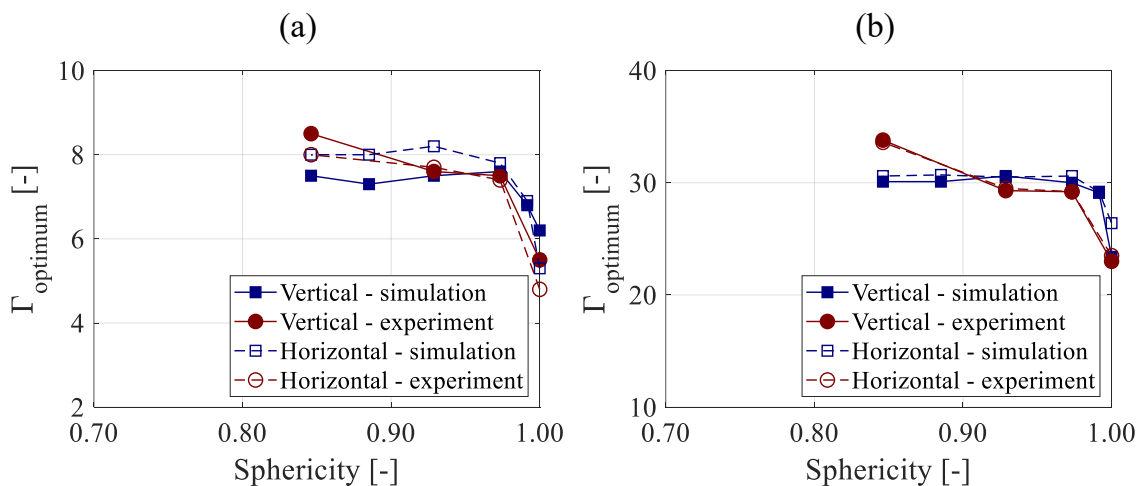
Figure 8.13: Variation of bouncing bed onset amplitude depending on particle sphericity for spheroids: (a) 20 Hz and (b) 40 Hz.

Figure 8.14: Variation of bouncing bed onset amplitude depending on particle sphericity for circular toroids: (a) 20 Hz and (b) 40 Hz.

By considering the results shown in Figure 8.13 and Figure 8.14 together, it can be concluded that $\Gamma_{optimum}$ first increases when the particle shape deviates from a perfect sphere, and, afterwards it approximately reaches a maximum level between the sphericity levels of 0.97 and 0.95. Then, it stays nearly constant between the sphericity levels of 0.95 and 0.85. From about the sphericity level of 0.85 to 0.70, $\Gamma_{optimum}$ has a decreasing trend reaching a level smaller than the perfect sphere around 0.70.

8.5.1.2 Explanation for the onset shift characteristic

The observed characteristic of $\Gamma_{optimum}$ shift presented in Section 8.5.1.1 is associated with the combination of two physical reasons:

I.   Particle geometry affects the (volume) packing ratio of particles in a void (or the porosity of granular medium). Non-spherical particle shapes may have the ability to pack more closely than perfect spheres exhibiting less porosity. This creates a larger apparent clearance in a damper enclosure, which causes a higher $\Gamma_{optimum}$ as also indicated by the bouncing bed onset amplitude estimation relation for perfect spheres, i.e., Equation (6.12).

For example; $\alpha_{spheroid}$ = 1.50 produces the maximum random packing ratio of 0.71 [219], whilst it is 0.64 for $\alpha_{spheroid}$ = 1.00. According to Equation (6.12), this means that $\Gamma_{optimum}$ of $\alpha_{spheroid}$ = 1.50 should be approximately 18% higher. However, as shown in Figure 8.11, the increase in $\Gamma_{optimum}$ is over 50% for this condition. This indicates that there is at least one additional physical cause for the particle shape-dependent characteristic of $\Gamma_{optimum}$.

II.   Significant local shear deformations occur in a granular medium during collective collisions with enclosure walls. Thus, in order to initiate the bouncing bed phase, it is needed to provide a vibration amplitude at which sufficient shear deformations are achieved to create approximately same collision intensity at both ends of enclosure. As rotational degrees-of-freedom of a non-spherical particle are generally restricted more in a granular medium than an equivalent perfect sphere, the use of non-spherical particles is likely to create a granular medium that is more resistant to shear deformations. This means that the vibration amplitude required to achieve the perfect bouncing bed phase onset needs to be higher.

In order to test these explanations, the normal and shear force-displacement behaviours of prolate spheroid and circular toroid particle collections were analysed conducting quasi-static DEM simulations. The simulation model used for this investigation is illustrated in Figure 8.15. The simulation model involved two identical cylindrical containers whose diameters and heights were 40 mm and 20 mm (half of the used damper enclosure), respectively. As can be seen in Figure 8.15, the bottom container was fixed onto the motionless ground along the gravity direction (i.e., vertical or normal) as its opening looked upward, and the top container was placed along the same axis as its opening looked against the fixed container. Particles (100 pcs for each particle shape investigated) were randomly

generated within the void between the containers. There was a relatively small gap (0.5 mm) between the containers to allow the motion of top container perpendicular to the vertical direction (i.e., horizontal or shear) whereas its vertical motion was suspended. Thus, to be able to apply compressive normal displacements to the body of particles, a disc shaped table, whose diameter was 19.9 mm, was assembled to the top container.
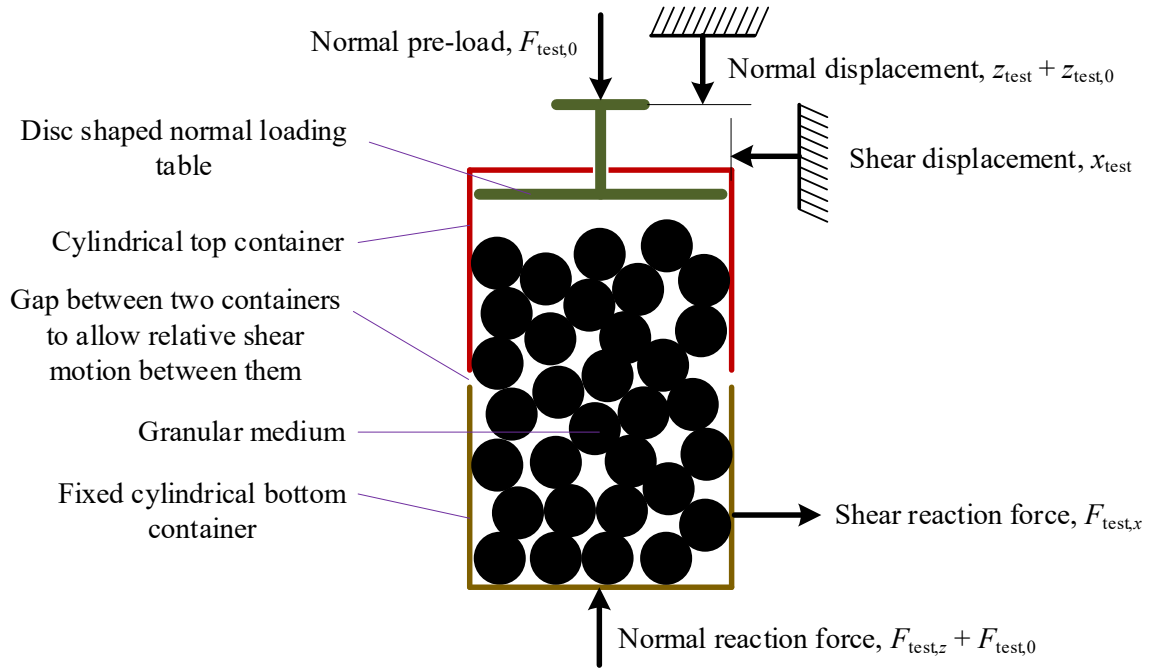

Figure 8.15: Force-displacement simulation model.

In the normal force-displacement simulations, first, a constant normal pre-load, $F_{test,0}$ (10 N) was applied by the loading table to avoid excessive and sudden particle movements (e.g., slips because of initial contacts with the loading plate) during tests. The initial normal displacement exerted by the loading table due to the pre-load, $z_{test,0}$ was recorded for each particle shape. After the steady-state was achieved for the loading plate, the testing normal displacement, z_{test} was applied to the granular medium by providing a constant vertical velocity to the loading plate, and the resulting reaction force on the fixed container base due to the compression test, $F_{test,z}$ was determined.

For the shear force-displacement simulations, the normal pre-load of 50 N was applied in the first step. When the steady-state condition was met for the loading table, the testing shear displacement, x_{test} was applied by giving a constant horizontal velocity to the top container. The resulting shear force, $F_{test,x}$ was obtained by measuring the experienced horizontal reaction force on the fixed container walls by the granular medium.

The force-displacement results for the normal and shear testing are provided in Figure 8.16, Figure 8.17, Figure 8.18 and Figure 8.19 for prolate spheroid and circular toroid particle sets. These results could be affected by initial placements of particles inside the void as a result of random packing. Thus, it was determined that the uncertainty level did not significantly affect the presented stiffness order of particle types by running the simulation several times for a particle type– see Appendix-D.

As shown in Figure 8.16 and Figure 8.17, regardless of particle type, significant stiffening occurs with increasing in the normal load as particles pack together more tightly (i.e., porosity decreases and granular medium approaches to a continuum formation). The prolate spheroid aspect ratio or the circular toroid hole ratio apparently affects the normal stiffness of granular medium (or effective elastic modulus). It is lowest for perfect spheres, rises to a maximum and then reduces again as the prolate spheroid aspect ratio or the circular toroid hole ratio increases. Note that the observed particle shape effect on the modulus of a granular medium is consistent with literature [133,134,156]. The normal stiffness of a granular medium is in a direct correlation with its porosity level [156]. This means that better packing produces higher normal stiffness. Therefore, if the explanation I was the only factor that yields the particle-shape dependent $\Gamma_{optimum}$ shift, the particle order seen in Figure 8.16 and Figure 8.17 would have exactly represented the $\Gamma_{optimum}$ characteristics presented by Figure 8.11 and Figure 8.12, but they do not.
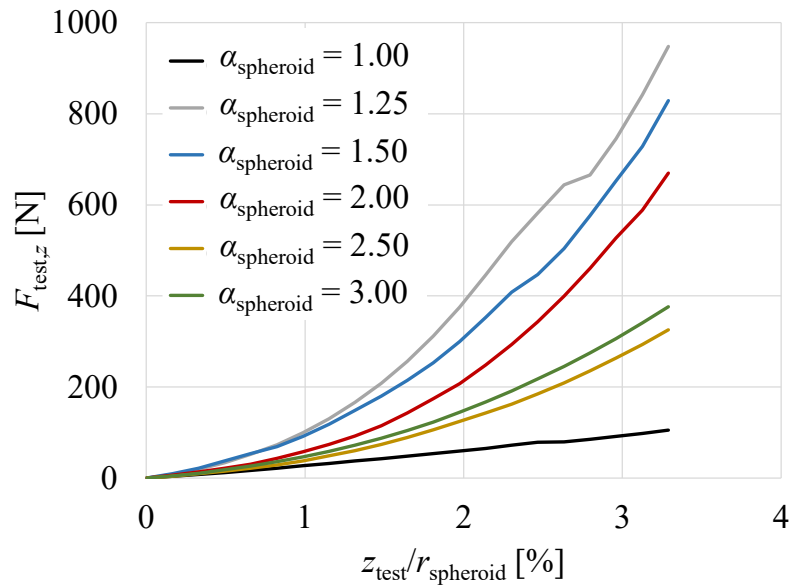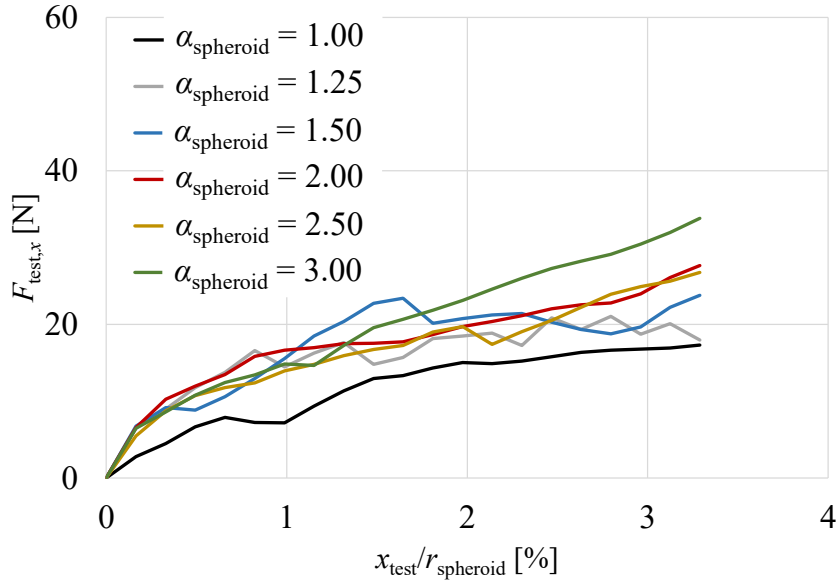
Figure 8.16: Normal force-displacement curves of prolate spheroid particle sets.
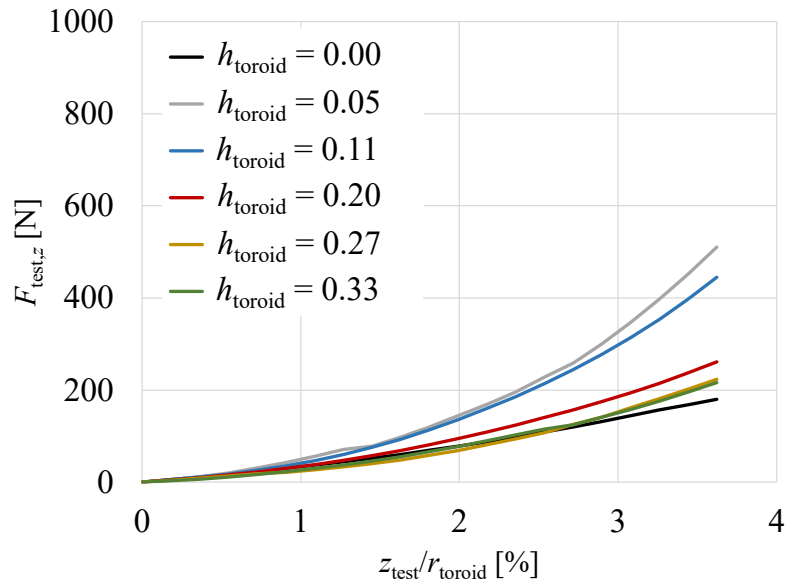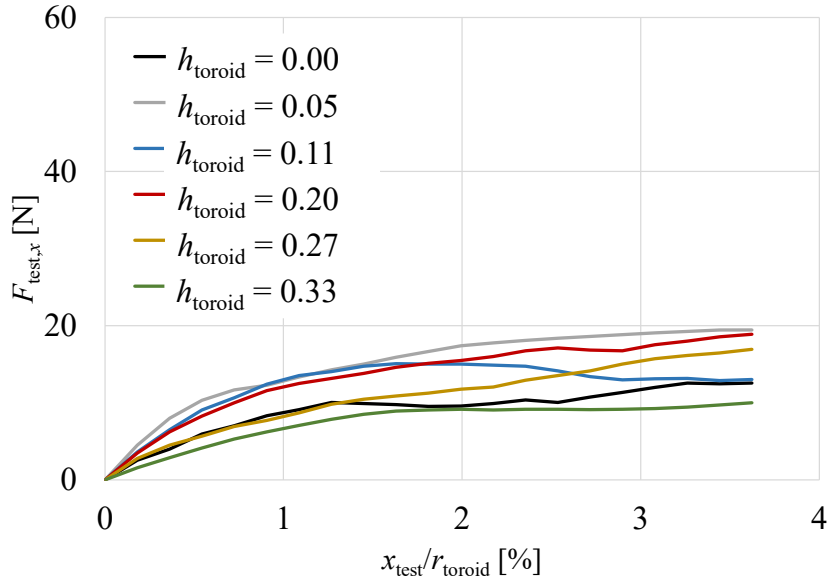

Figure 8.17: Normal force-displacement curves of circular toroid particle sets.

Figure 8.18 and Figure 8.19 show that the shear behaviour of a granular medium is different from the normal behaviour. As the shear displacement increases, the shear stiffness decreases as a result of macro slip behaviour in the granular medium. Note that individual particle slips are also visible and can be identified from the zig-zag force-displacement formations in the presented curves. More details can be found in the literature on the fundamental shear behaviour of granular materials [134,156,220,221].

Figure 8.18: Shear force-displacement curves of prolate spheroid particle sets.

**Figure 8.19:** Shear force-displacement curves of circular toroid particle sets.

As can be seen in Figure 8.18, the non-spherical spheroid particles create a stiffer granular medium than perfect spheres against shear deformations. The results show that the force-displacement curves for $\alpha_{\text{spheroid}} > 1.00$ are approximately the same. This observation has the same trend as the particle shape-dependent Γ_{optimum} characteristics demonstrated by Figure 8.11. Similarly, the shear stiffness is higher for the circular toroids than perfect spheres for $h_{\text{toroid}} \leq 0.20$ and nearly the same as can be seen in Figure 8.19. However, for $h_{\text{toroid}} > 0.20$,

it decreases and drops to a level which is similar to perfect spheres (or even smaller, $h_{\text{toroid}} = 0.33$). This was not noticed for the investigated prolate spheroids as discussed for Figure 8.18. Thus, this can be attributed to smaller sphericity levels of $h_{\text{toroid}} > 0.20$ circular toroid particles than the investigated prolate spheroids. Nevertheless, it should be noted that the observed particle shape-dependent shear stiffness order of circular toroids represents Γ_{optimum} characteristics shown in Figure 8.12. As a result, it is justified that the explanation II is a major factor that controls the condition of bouncing bed phase initiation in a granular medium.

8.5.1.3 Sensitivity of the onset shift to contact and material properties

As reviewed in Section 2.6 and investigated in Section 6.4.1 using perfect spheres that the bouncing bed onset amplitude and amplitude-frequency-dependent energy dissipation characteristic of a granular damper is independent from contact and material properties whilst the level of damping efficiency curves can slightly change – see Figure 6.13 for more detail. In this section, the sensitivity of the observed particle shape-dependent Γ_{optimum} characteristic to material and contact properties was examined by using the prolate particles.

For this study, the same changes in density, elastic modulus, coefficient of restitution (COR) and coefficient of friction (COF) as in Section 6.4.1 were considered. It should be noted here that the rate of damping efficiency reduction with the increase in vibration amplitude beyond the bouncing bed onset amplitude (i.e., $\Gamma > \Gamma_{\text{optimum}}$) is not significantly affected by particle shape as demonstrated in Figure 8.9 and Figure 8.10. Thus, it is possible to say that the highness of damping efficiency level at a specific amplitude in the zone of bouncing bed phase is an indicator of Γ_{optimum}. This can be clearly seen by comparing the curve of default case in Figure 8.20 and the $\alpha_{\text{spheroid}} \geq 1.00$ part of curves in Figure 8.11b. As a result, to reduce computational efforts, a single excitation condition (i.e., horizontal vibrations at 40

Hz having vibration amplitude of $\Gamma = 35$) was simulated for each property change as this excitation results in the bouncing bed phase for all particle types – see Figure 8.11b. The results of sensitivity analysis simulations are provided in Figure 8.20.
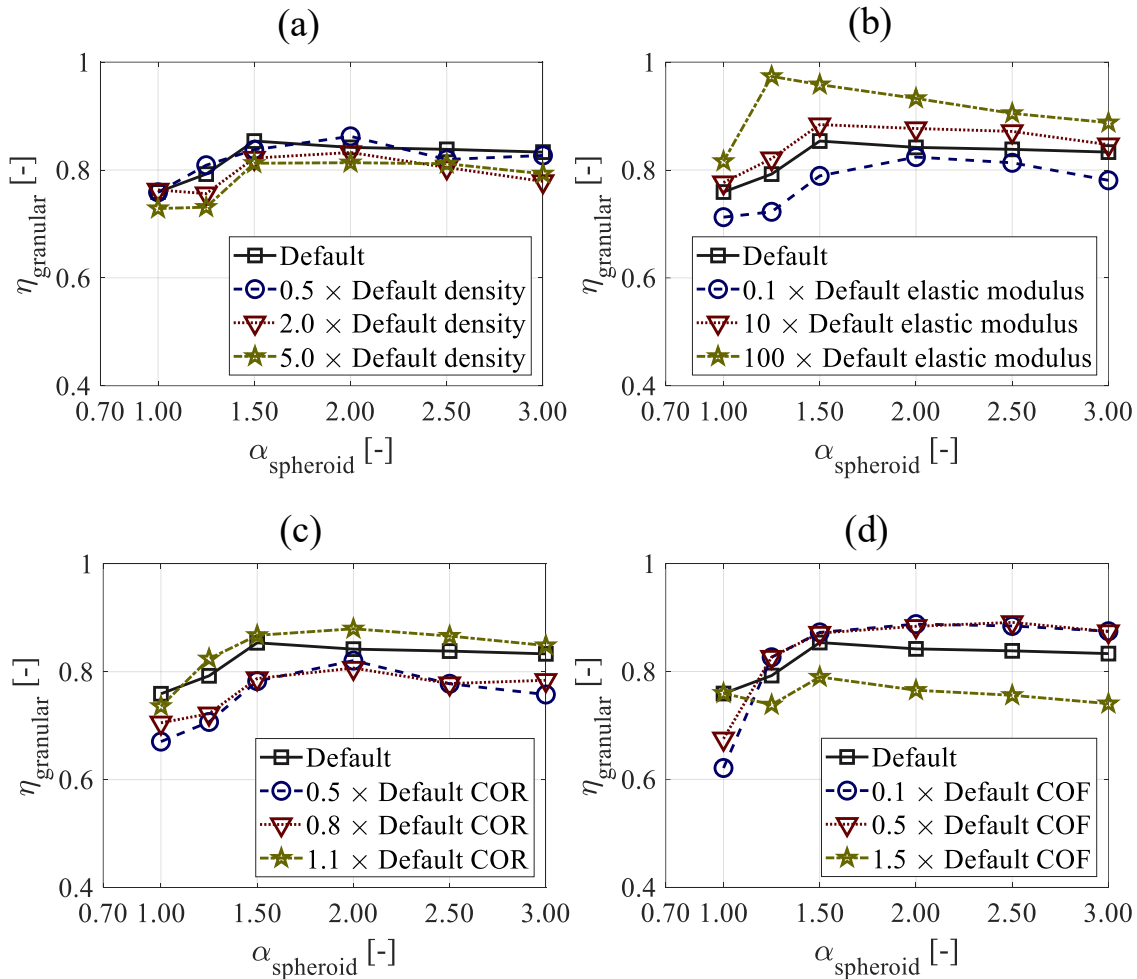
Figure 8.20: Sensitivity of particle-shape dependent granular damping efficiency to: (a) density, (b) elastic modulus, (c) COR and (d) COF using DEM simulations of $\Gamma = 35$ horizontal excitations at 40 Hz.

As also observed in Figure 6.13b, in the bouncing bed phase, Figure 8.20a shows that the granular damping efficiency slightly decreases as the density increases. This slight effect may be related to changes in the deformation of whole particle bed during each collective collision. As can be seen in Equation (5.10), an increase in the density increases individual contact durations and yields more compact granular medium during collective collisions (i.e., lower bed deformation is observed as individual particles translate less) which reduces

particle relative motions and energy dissipation. This effect is observed for each particle type, thus, does not change the particle shape-dependent $\Gamma_{optimum}$ characteristic.

As opposite to the influence of density, Figure 8.20b and c show that higher elastic modulus or higher COR provides higher damping efficiency for each particle type in the bouncing bed phase. Because, particles with higher modulus (or higher COR) exhibits a less compact particle bed as a higher modulus means shorter individual contact duration (as also discussed in Section 6.4.1 by addressing Equation (5.10)) and a higher COR also results in larger post-impact velocities for individual particles by reducing energy lost in individual inter-particle impacts. As these effects are valid for each particle type, the particle shape-dependent $\Gamma_{optimum}$ characteristic is not affected by elastic modulus of COR changes.

As mentioned above, the changes in density, elastic modulus and COR affect overall stiffness of granular medium, and this can be observed for any particle shape. However, COF significantly alters the ratio of shear stiffness to normal stiffness of granular medium [156]. This is basically similar to what the particle shape does as shown in Section 8.5.1.2. Thus, as shown in Figure 8.20d, a reduction in COF increases the sensitivity of $\Gamma_{optimum}$ to particle shape – particularly it can be seen by a larger increase between $\alpha_{spheroid} = 1.00$ and $\alpha_{spheroid} = 1.50$. It can be also noticed that an increase in COF causes a decrease in this sensitivity.

8.5.2   Particle shape effect in the fluidisation-based and convection-based phases

For the vertical case, the simulation and experimental damping efficiency results at the high frequencies, at which the fluidisation-based and convection-based phases are observed but the bouncing bed phase is not apparent, are given in Figure 8.21-Figure 8.26. Figure 8.21 and Figure 8.22 show the results of prolate spheroid particles; Figure 8.23 and Figure 8.24 show the results of circular toroid particles; and Figure 8.25 and Figure 8.26 show the results of oblate spheroid particles. Note that the results of the horizontal case are not presented here

for clarity as they indicate the same conclusions as the vertical case, but they are provided in Appendix-E.

As discussed in detail in Section 6.4.3, the peak in these result sets corresponds to the fluidisation optimum in which the number of fluidised particles (Figure 6.15a) reaches its maximum in the granular medium. As the excitation frequency increases, the damping efficiency level of this peak increases and its location in the amplitude axis shifts towards lower values. From the smaller amplitudes to the peak amplitude, the damping efficiency increases as the particle fluidisation densifies by replacing the solid-like motions. Beyond the peak amplitude, the damping efficiency decreases as a result of the increase in the occurrence of particle convection motion. If the bouncing bed phase develops at an amplitude larger than the fluidisation peak, the decrease in the damping efficiency stops and a significant increase is observed in the damping efficiency plot – see the second peaks in Figure 6.8 and Figure 6.9 for examples.

As similarly noticed in Section 7.5, it can be realised by comparing the simulations (Figure 8.21, 8.23 and 8.25) and the experiments (Figure 8.22, 8.24 and Figure 8.26) that the simulations overestimate the damping efficiency in the fluidisation-based and the convection-based phases for all particle types, especially at low amplitudes and high frequencies. However, the main amplitude and frequency dependent damping efficiency characteristics observed in the simulations and the experiments match with each other.
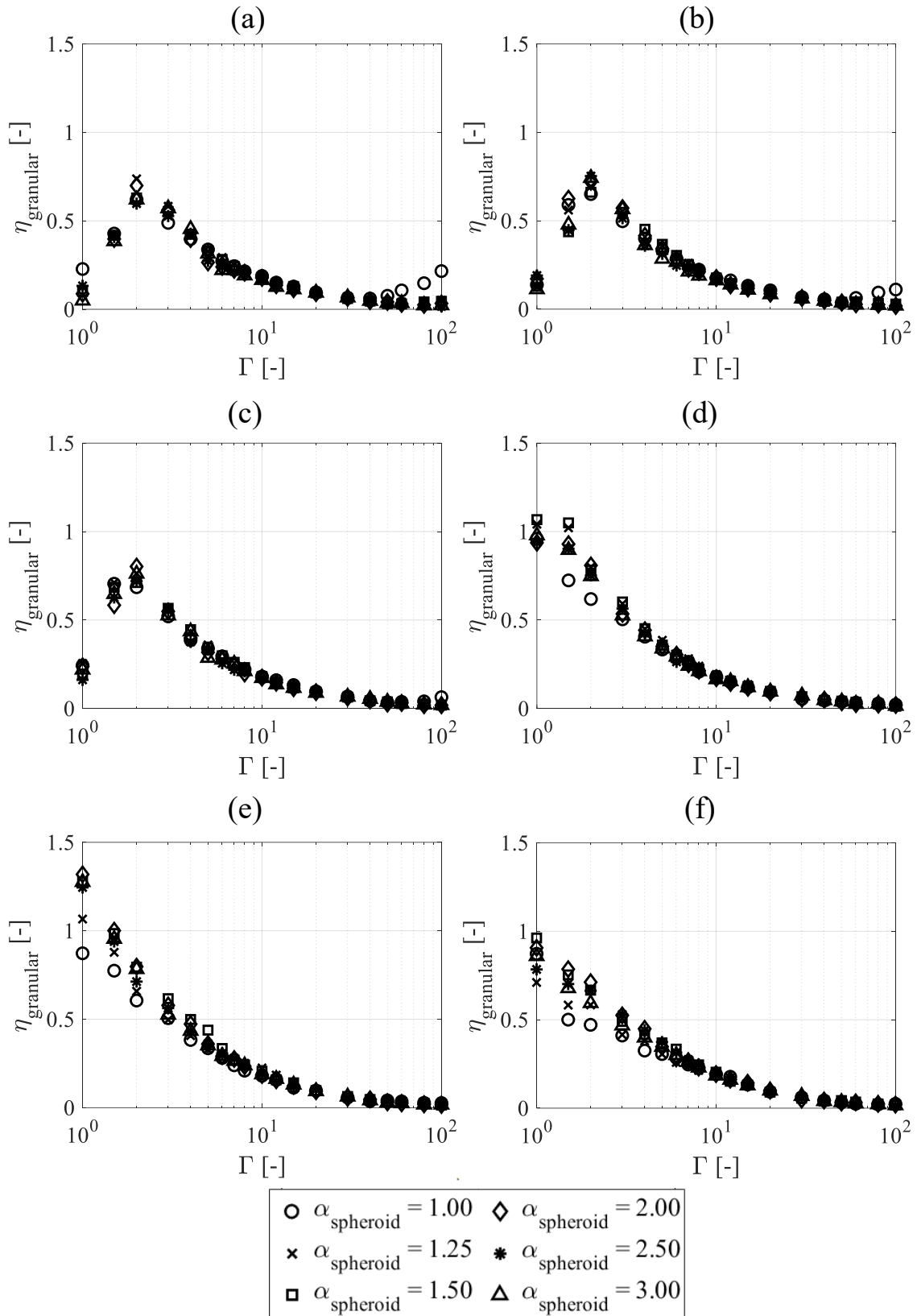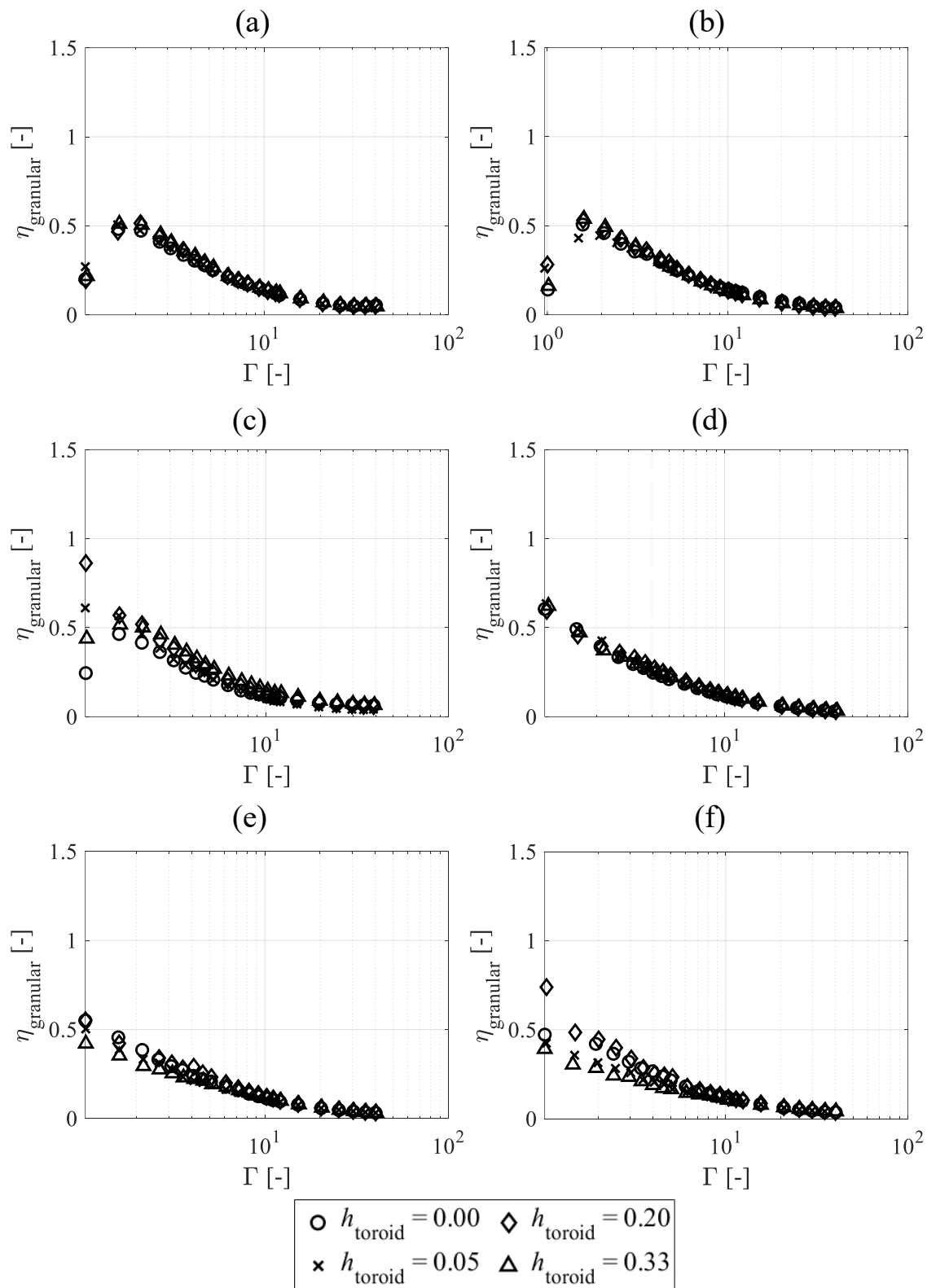
Figure 8.21: Granular damping efficiency results of different prolate spheroids at vertical excitations of: (a) 125 Hz, (b) 160 Hz, (c) 200 Hz, (d) 320 Hz, (e) 625 Hz and (f) 1024 Hz – simulation.
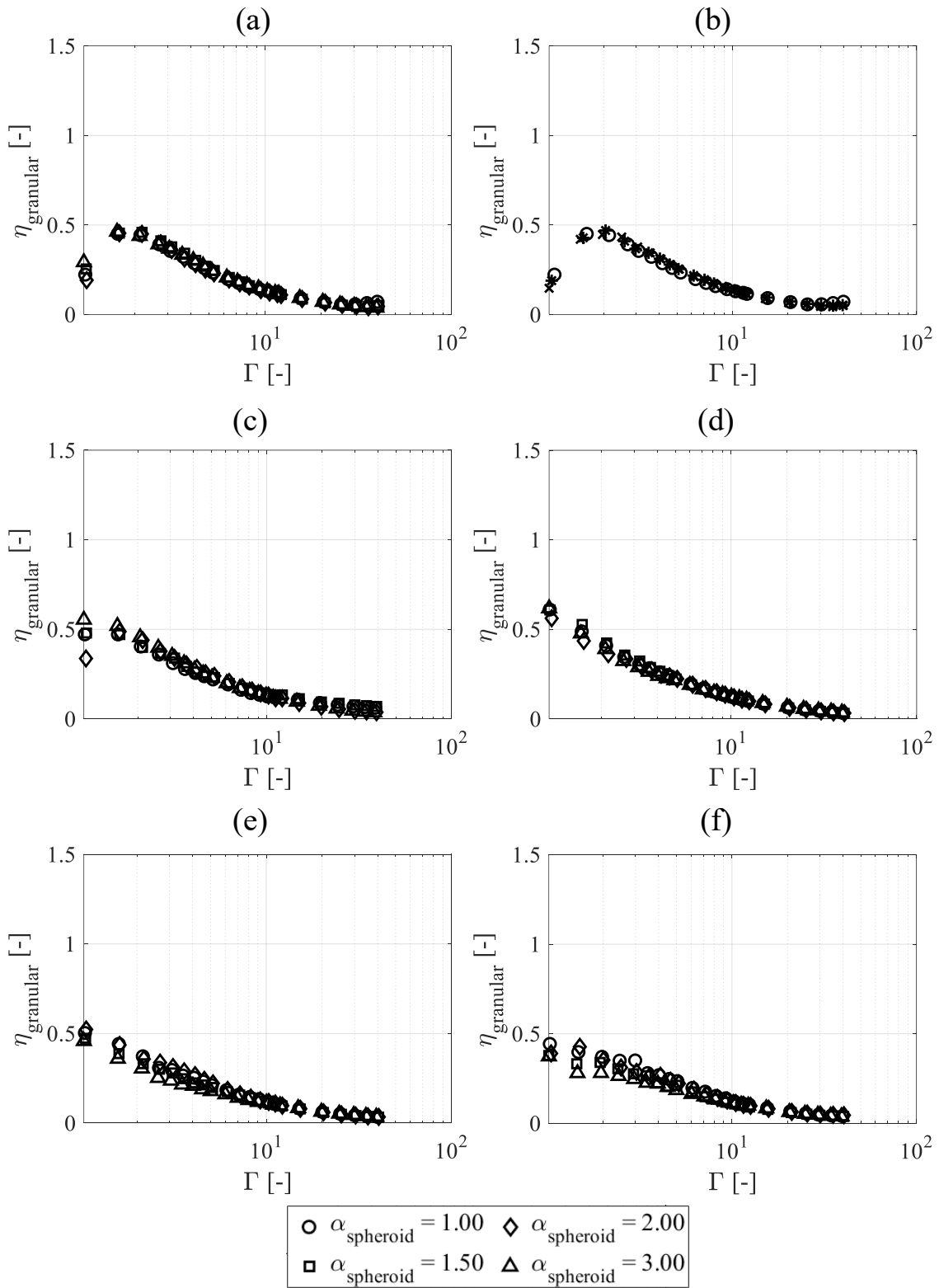
Figure 8.22: Granular damping efficiency results of different prolate spheroids at vertical excitations of: (a) 125 Hz, (b) 160 Hz, (c) 200 Hz, (d) 320 Hz, (e) 625 Hz and (f) 1024 Hz – experiment.
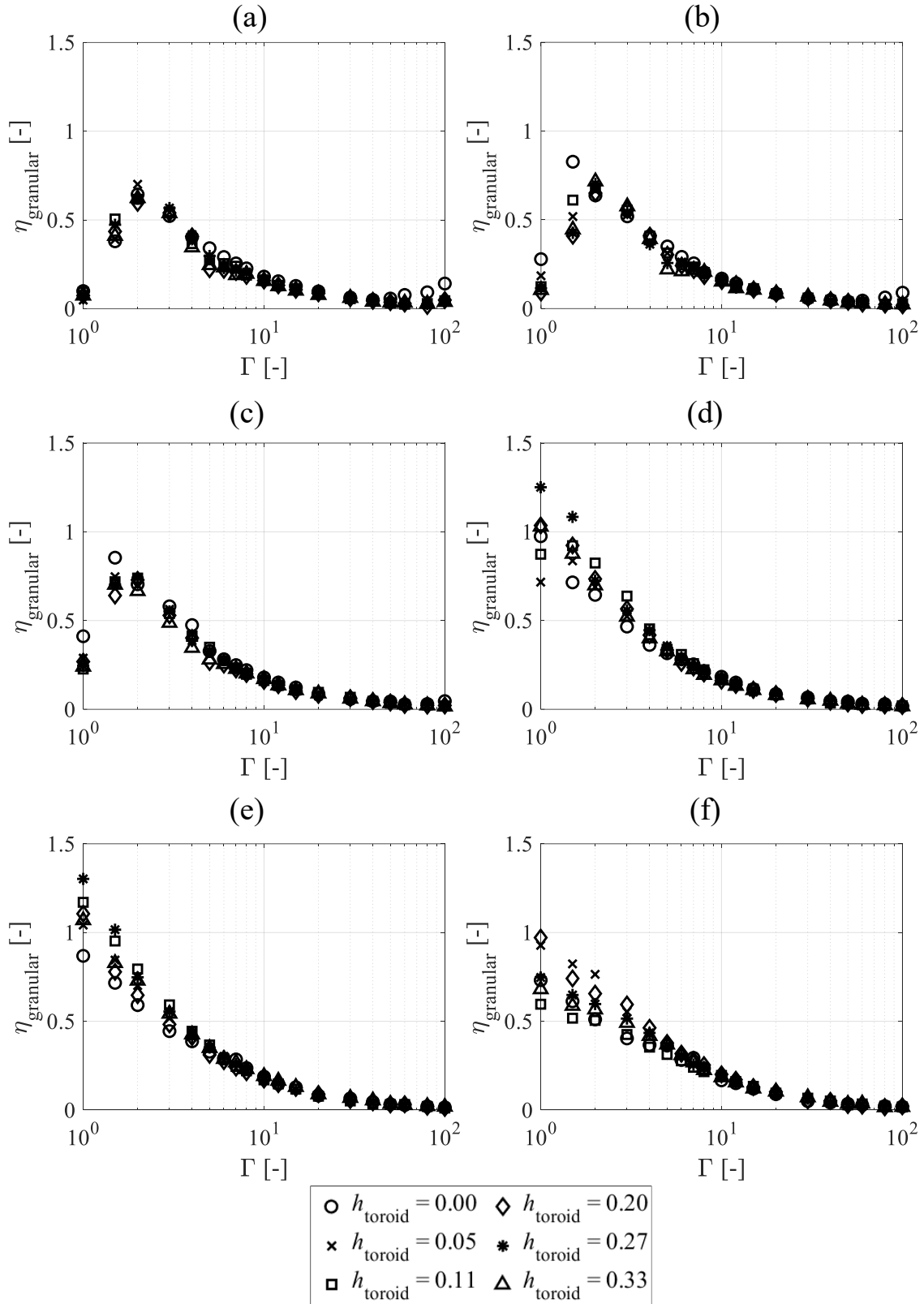
Figure 8.23: Granular damping efficiency results of different toroids at vertical excitations of: (a) 125 Hz, (b) 160 Hz, (c) 200 Hz, (d) 320 Hz, (e) 625 Hz and (f) 1024 Hz – simulation.

Figure 8.24: Granular damping efficiency results of different toroids at vertical excitations of: (a) 125 Hz, (b) 160 Hz, (c) 200 Hz, (d) 320 Hz, (e) 625 Hz and (f) 1024 Hz – experiment.

Figure 8.25: Granular damping efficiency results of different oblate spheroids at vertical excitations of: (a) 125 Hz, (b) 160 Hz, (c) 200 Hz, (d) 320 Hz, (e) 625 Hz and (f) 1024 Hz – simulation.
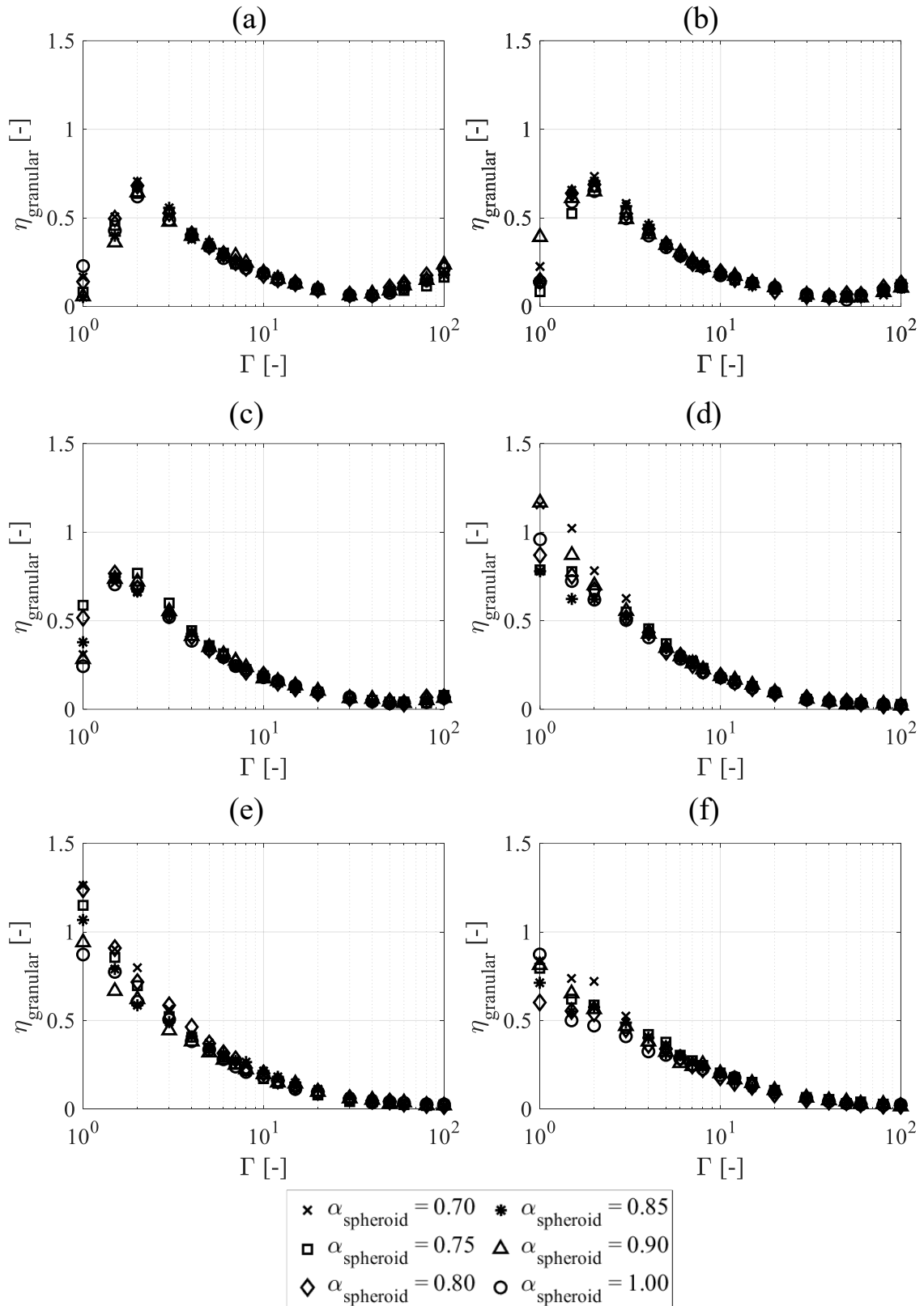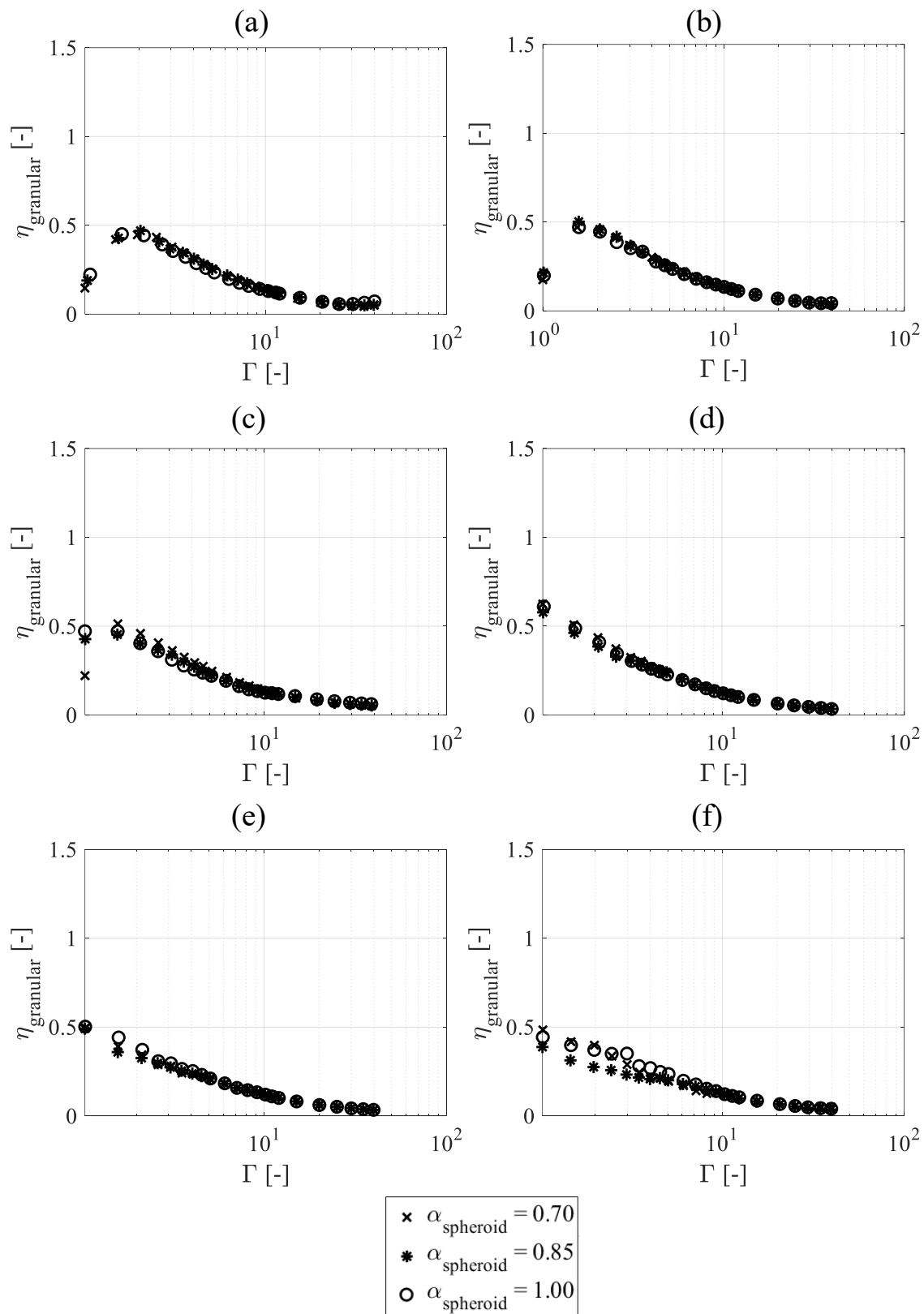
Figure 8.26: Granular damping efficiency results of different oblate spheroids at vertical excitations of: (a) 125 Hz, (b) 160 Hz, (c) 200 Hz, (d) 320 Hz, (e) 625 Hz and (f) 1024 Hz – experiment.

As shown in Figure 8.21-Figure 8.26, the particle shape does not shift the optimum fluidisation amplitude. This is different from what has been observed for the bouncing bed optimum amplitude where the particle shape affects the condition of bouncing bed phase onset. The amplitude and frequency dependent energy dissipation behaviour is maintained regardless of the particle shape used. The small variations observed in the damping efficiency level depending on the particle shape do not follow a consistent trend, and this can be attributed to the uncertainty due to the random packing of particles within the enclosure void.

It can be surprising that the numerical oblate particles (Figure 8.25) also show the same observations even though it has been shown in Section 8.5.1 that they do not represent the actual intended oblate geometries. This indicates an important conclusion: the fluidisation-based and the convection-based phases are independent from the particle shape. It should be noted here that this verifies the hypothesis proposed by Sanchez et. al [11] using only the two-dimensional numerical simulations of a few particle types where the granular medium does not produce the bouncing bed phase.

The main explanation of the particle shape independency in those phases mentioned is that the fluidisation-based and the convection-based phases are dominated by the individual particle decompaction from the body of particles and decompacted free transportation within the enclosure void as discussed in Section 6.4.3. It indicates that the resistance level of a particle to rotate within the granular medium, which is found to be sensitive to the particle shape, is unimportant in these phases. As shown elsewhere [58], the major factor that controls the decompaction and therefore changes the energy dissipation behaviour in these phases is the ratio of dynamic pressure to static pressure which the particles of a granular damper experience. Therefore, as an overall result, it can be said that the change in particle shape does not alter the conditions of fluidisation and convection motion initiations.

8.6   Chapter Summary and Conclusions

This chapter has investigated the influence of particle shape on the energy dissipation of granular dampers using both numerical simulations and physical experiments. This study has been conducted using a broad range of oblate spheroids, prolate spheroids and circular toroids to provide a systematic analysis and therefore obtain general conclusions. It has been shown that the effect of particle shape on the dissipative behaviour of granular dampers differs depending on the operating motional behaviour of granular medium. It has been demonstrated that the particle shape effects observed in this chapter are not affected by the changes in material and contact properties or the vibration-to-gravity orientation.

It has been found that the bouncing bed onset amplitude at which the granular energy dissipation performance is maximised changes depending on particle shape whereas the peak energy dissipation effectiveness at the optimum condition and the damping efficiency behaviour beyond the optimum amplitude are approximately maintained. It has been determined that the particle shape-dependent shift of the bouncing bed onset amplitude has an apparent trend related to the sphericity level of particles. This shifting behaviour is clearly in a correlation with the variation in the overall resistance of granular medium against shear deformations (or rotational resistance of a single particle within the granular medium) depending on the sphericity level of particles used: higher shear stiffness, larger bouncing bed phase onset amplitude.

For the inter-related fluidisation and convection phases, the dissipative behaviour and performance of granular dampers have been found to be insensitive to the particle shape. This is explained by the motional characteristics of particle fluidisation and convection described in Chapter 6. As these motions are basically described by the decompaction of a particle from the whole body of particles and the translational motion of a decompacted

particle, the shear stiffness of granular medium and therefore the particle shape have no influence on the granular relative motions and particle dissipations.

The practical importance of this chapter is that it demonstrates the sensitivity of the two different optimum operating conditions of granular dampers (i.e., the optimum bouncing bed and the optimum fluidisation) to the shape of damping particles. As a result, it extends the understanding on the proposed motional phase-energy dissipation relationship and therefore provides a reliable guide to the designer to exploit the efficient energy dissipation behaviours of these two operating conditions.

9 Conclusions and Future Research

This thesis has focused on explaining the fundamental dissipative phases and mechanisms that generate the amplitude and frequency-dependent non-linear energy dissipation behaviour in granular dampers. The work has considered harmonically vibrated granular dampers whose loading directions are both parallel and perpendicular to gravity. The investigation of dampers has been carried out using validated numerical models (utilising the Discrete Element Method) and physical experiments. This study has not only considered the employment of spherical particles in granular dampers but also involved a systematic investigation of non-spherical particles.

Towards the thesis objectives provided in Section 1.3, the major conclusions determined are provided in this chapter. The explanation of how the first objective of the thesis has been met is shown in Section 9.1. The practical applicability of the findings of the first objective is discussed in Section 9.2. Lastly, the primary conclusions obtained when achieving the second objective of the thesis are presented in Section 9.3.

9.1 Motional Phase Dependent Granular Damping

The link between the motional phase map and energy dissipation effectiveness for granular dampers has been investigated over a wide range of vibrational excitation conditions. As this relationship has been fragmented (and little known) in the literature until now, it has caused various inconsistent even conflicting results in granular dampers. Thus, addressing this

problem in this thesis has been a significant contribution for both granular-based practical damper designs and scientific studies on dissipative properties of granular materials.

The main conclusions from this activity are listed below.

- There are two distinct motional mechanisms that control the effectiveness of energy dissipation in granular dampers:

    i. Collective collision, in which particles collect together and collide with the enclosure end walls.

    ii. Particle fluidisation, in which particles in contact have relative motion with respect to each other during a vibration cycle but return back to their initial position and maintain their existing contacts at the end of cycle.

- Each motional mechanism can be optimised for energy dissipation, but the factors and design parameters involved are different.

- The most efficient collective collision regime is the bouncing bed phase where collisions occur with alternate end walls of the enclosure resulting in two collisions per vibration cycle. This operating motional phase provides the highest energy dissipation effectiveness. However, the optimum condition occurs for a narrow excitation range as it is obtained around the onset of the bouncing bed phase, and the effectiveness of granular energy dissipation gradually reduces as the vibrational intensity increases. This produces a diagonal ridge on a frequency-amplitude damping efficiency map.

- The optimum (or onset) condition of the bouncing bed phase can be accurately predicted by determining the effective clearance in the damper void as it depends on the link between flight time of the particles within the enclosure void and the motion

of enclosure. The random close packing is the most accurate way to represent the packing at the collective collision times and thus provides the best estimation for the effective clearance, therefore the optimum condition.

- Solid-fluidisation-convection motions produce inter-related motional phases whose presence depends on the level of particle activation. The optimum condition is achieved when the majority of particles exhibit fluidisation motion but have not started to convect. This occurs at relatively small vibration amplitudes and changes depending on the relative level of dynamic and static forces that the particles experience. The sensitivity of fluidisation optimum to the excitation frequency is low which produces a relatively broad frequency range for efficient energy dissipation, resulting in a horizontal ridge on a frequency-amplitude damping efficiency map. Moving away from the optimal fluidisation condition either towards the solid-like phase or towards the convection-based phases the effectiveness of the granular energy dissipation reduces.

- Particle size does not significantly affect the energy dissipation effectiveness and behaviour of granular dampers in any motional phase. However, this observation only holds where there are enough particles to allow their distribution to be described in averaged terms and parameters such as bed depth and packing ratio are meaningful.

- The orientation of excitation with respect to gravity is found to be insignificant in terms of the relationship between motional phase and energy dissipation. (This is not to be confused with the fact that gravity usually provides the static loading that controls the phase changes in the solid-fluidisation-convection mechanism.).

9.2 Practical Application Design Guides

One significance of this thesis work which has resulted in the above conclusions is that it simplifies the design procedure of granular dampers for practical applications. The designer is presented with the choice of two different optimum conditions for an application. A phase map of the designed granular damper can be used to assess the outcomes of potential changes without the need for further investigations which greatly reduces the effort spent.

To design an efficient damper for a practical application, it is needed to consider host structure dynamics and external loading conditions. Thus, it can be said that a damper which is highly efficient in attenuating the vibrations of one structure is not necessarily be efficient when implemented to a different structure as the success of design depends not only on having an adequate damper mass but on ensuring that the design maintains to function efficiently. The effective functioning of a granular damper is assessed by the motional phase of damping particles when subjected to vibrations. Therefore, achieving a suitable motional phase (optimal motional condition if possible) is critically significant in the design of granular dampers. To provide a simple but powerful guidance to overcome the difficulties related to the non-linear energy dissipation behaviours of granular dampers, the following general design rules are defined for the practical implementation of granular dampers based on the results of thesis work:

I. If the expected operating excitation conditions of the application location on the considered structure are well-defined and the excitation frequency range is relatively narrow, the bouncing bed phase would present the highest damping level for the structure over a relatively broad amplitude range. As explained in Section 6.4.1, the key design consideration is to predict the optimum operating amplitude based on the effective clearance employed. To set the optimum operating amplitude somewhere within the range of excitation, the effective

clearance can be arranged by changing either the enclosure size or the maximum packing ratio of particles. It should be also noted that this is the most (and only) effective phase for no gravity conditions [77,110].

II.   For a wide frequency range application at relatively low (and narrow) excitation amplitudes, the fluidisation-based phases (global fluidisation for the vertical case and partial fluidisation in the horizontal case) would provide the best damping performance in the structure. As shown in Section 6.4.3, the optimum amplitude decreases slightly with increasing frequency – nearly frequency-independent granular damping operation. The amplitude for the optimum performance can be adjusted within a relatively narrow range by altering the static pressure field for example, by making the particle bed deeper and narrower [8,9,89].

III.   If the excitation amplitudes are beyond the highest-amplitude optimum zone that can be achieved for the fluidisation-based phases, the transition phase (in the vertical case) and fluidisation/convection (in the horizontal case) can be utilised, although the damping achieved for the structure would be somewhat relatively lower.

9.3   Observations on Particle Shape Effect in Granular Damping

The influence of particle shape on the energy dissipation of granular dampers has been determined for both collective collision and particle fluidisation. The work has provided two major contributions to the existing literature. The first is the determination of the influence of particle shape on the granular energy dissipation performance which is an important aspect in practical applications as particles can deviate from being true spheres. Secondly, the understanding on the granular phase-energy dissipation relationship (Section 9.1) has been extended as a result of the systematic investigation of one of the factors that can affect this relationship.

The main conclusions of this study are listed below.

- A reduction in the particle sphericity shifts the bouncing bed onset amplitude, i.e., the conditions for optimal energy dissipation, whilst retaining the shape of the curve. The shift depends on particle sphericity. This is associated with two parameters that depend on the particle shape: *i*) maximum packing ratio that can be achieved and *ii*) overall shear resistance of granular medium. It has been shown that the shear resistance is the major factor that causes this shift.

- Particle shape does not significantly affect the solid-fluidisation-convection process.

- The particle shape effects observed have slight sensitivity to the changes in material and contact properties.

9.4 Future Work

The work presented in this thesis has helped to identify several interesting lines for research for future study. These are identified below.

i. This thesis has not addressed the numerical prediction of vibration response for an engineering structure with attached granular dampers. This is an important capability that an engineer needs when employing granular dampers to address practical vibrational problems. As the dynamics of the host structure should be included, the analysis is generally required to employ a computationally expensive coupled DEM-FEM simulation approach. To reduce this cost and to allow efficient structural design, a simple analytical dissipative force model which represents the main characteristics of granular dampers should be developed considering the motional phase analogy presented in this thesis.

ii. This thesis indicates that the estimation of onset excitation conditions (i.e., amplitude and frequency) for some particular granular motional events (such as the onset of the

216

bouncing bed phase) is an important task for the design of granular dampers. The analytical estimations of these can significantly ease the design effort by allowing the construction of phase maps without DEM simulations. Thus, another study can provide analytical estimations for both: where the particle activation starts (i.e., end of the solid-like phase) and where the maximum ratio of fluidised particles is achieved.

iii. The amplitudes, at which the fluidisation optimum and the bouncing bed optimum are achieved, are distinct and thus this creates an amplitude spacing between two damping efficiency peaks – can be seen in Figure 6.8 and Figure 6.9. As shown in the thesis, this spacing can be altered by adjusting the damper properties, but it also changes the damping efficiency levels of peaks. To provide both a sufficiently broad operating amplitude range and efficient energy dissipation, an optimisation study can be carried out for determining the most effective amplitude locations of peaks for specific applications.

iv. When a granular medium is shaken, an amount of acoustic energy is radiated to surrounding areas as a result of collisional and frictional interactions. This could be a significant concern for some practical applications. Thus, it could be needed to evaluate the noise level variation in granular dampers depending on the operating motional phase, and some designs can be proposed to reduce noises for the optimal operating phases without losing the damping efficiency.

v. One issue that needs to be addressed is that the dissipative performance and optimisation of granular dampers have generally been studied under steady-state single harmonic excitations. More complex loadings (such as multi-harmonic, random and arbitrary-transient) may produce different characteristic behaviours. It is

believed that the best performance under these conditions can be obtained by achieving the fluidisation optimum as a wide range of excitation frequency is involved. However, it is necessary to justify this hypothesis and identify the parameters that can change the conditions of fluidisation optimum for these loading cases.

vi. The granular motional phase-energy dissipation relationship proposed in this thesis is specific to single-directional translational vibrations of granular dampers. Thus, this relationship can be modified for torsional and bi-directional vibrational excitations to both broaden the understanding of the motional phase-granular energy dissipation relationship and show the effectiveness of granular dampers for such an excitation condition.

vii. As identified in Section 2.7, changes to the damper enclosure (such as non-parallel enclosure walls, multiple voids in the enclosure) may fundamentally alter the motional phases. Therefore, this can be explored in another future work.

References

[1]   J.W. Strutt, The theory of sound, Macmillan & Co., New York, 1896.

[2]   Ahid D. Nashif, D.I.G. Jones, J.P. Henderson, Vibration damping, John Wiley & Sons, Ltd., New York, 1985.

[3]   D.J. Inman, Engineering vibration, Pearson, New Jersey, 2014.

[4]   H. V Panossian, Structural damping enhancement via non-obstructive particle damping technique, J. Vib. Acoust. 114 (1992) 101–105. https://doi.org/10.1115/1.2930221.

[5]   K. Mao, M.Y. Wang, Z. Xu, T. Chen, DEM simulation of particle damping, Powder Technol. 142 (2004) 154–165. https://doi.org/10.1016/j.powtec.2004.04.031.

[6]   L. Cremer, M. Heckl, E.E. Ungar, Structure-borne sound, Springer-Verlag, Berlin, 1973.

[7]   Babak Darabi, Dissipation of vibration energy using viscoelastic granular materials, The University of Sheffield, 2013.

[8]   W. Liu, G.R. Tomlinson, J.A. Rongong, The dynamic characterisation of disk geometry particle dampers, J. Sound Vib. 280 (2005) 849–861. https://doi.org/10.1016/j.jsv.2003.12.047.

[9]   C. Salueña, T. Pöschel, S.E. Esipov, Dissipative properties of vibrated granular materials, Phys. Rev. E. 59 (1999) 4422–4425. https://doi.org/10.1103/PhysRevE.59.4422.

[10]   H. Pourtavakoli, E.J.R. Parteli, T. Pöschel, Granular dampers: Does particle shape matter?, New J. Phys. 18 (2016). https://doi.org/10.1088/1367-2630/18/7/073049.

[11]   M. Sánchez, C.M. Carlevaro, L.A. Pugnaloni, Effect of particle shape and fragmentation on the response of particle dampers, J. Vib. Control. 20 (2014) 1846–1854. https://doi.org/10.1177/1077546313480544.

[12]   J.M. Bajkowski, B. Dyniewicz, M. Gębik-Wrona, J. Bajkowski, C.I. Bajer, Reduction of the vibration amplitudes of a harmonically excited sandwich beam with controllable core, Mech. Syst. Signal Process. 129 (2019) 54–69. https://doi.org/10.1016/j.ymssp.2019.04.024.

[13]   S.F. Masri, General motion of impact dampers, J. Acoust. Soc. Am. 47 (1970) 229–237. https://doi.org/10.1121/1.1911470.

[14] C.N. Bapat, S. Sankar, Single unit impact damper in free and forced vibration, J. Sound Vib. 99 (1985) 85–94. https://doi.org/10.1016/0022-460X(85)90446-8.

[15] S.F. Masri, Motion and stability of two-particle, single-container impact dampers, J. Appl. Mech. 34 (1964) 506–507. https://doi.org/10.1115/1.3607718.

[16] N. Popplewell, M. Liao, A simple design procedure for optimum impact dampers, J. Sound Vib. 146 (1991) 519–526. https://doi.org/10.1016/0022-460X(91)90707-Q.

[17] J.J. Moore, A.B. Palazzolo, R. Gadangi, T.A. Nale, S.A. Klusman, G. V. Brown, A.F. Kascak, A forced response analysis and applicationof impact dampers to rotordynamic vibration suppression in a cryogenic environment, J. Vib. Acoust. 117 (1995) 300–310. https://doi.org/10.1115/1.2874452.

[18] D.J. Ewins, Modal testing : theory, practice, and application, Research Studies Press, Hertfordshire, 2000.

[19] M.M. Sadek, The behaviour of the impact damper, Proc. Inst. Mech. Eng. 180 (1965) 895–906. https://doi.org/10.1243/pime_proc_1965_180_058_02.

[20] S.E. Semercigil, N. Popplewell, R. Tyc, Impact damping of random vibrations, J. Sound Vib. 122 (1988) 178–184. https://doi.org/10.1016/S0022-460X(88)80015-4.

[21] A. Olędzki, A new kind of impact damper-from simulation to real design, Mech. Mach. Theory. 16 (1981) 247–253. https://doi.org/10.1016/0094-114X(81)90039-2.

[22] S.F. Masri, Steady-state response of a multidegree system with an impact damper, J. Appl. Mech. Trans. ASME. 40 (1973) 127–132. https://doi.org/10.1115/1.3422910.

[23] K. Li, A.P. Darby, Experiments on the effect of an impact damper on a multiple-degree-of- freedom system, J. Vib. Control. 12 (2006) 445–464. https://doi.org/10.1177/1077546306063504.

[24] K. Li, A.P. Darby, A buffered impact damper for multi-degree-of-freedom structural control, Earthq. Eng. Struct. Dyn. 37 (2008) 1491–1510. https://doi.org/10.1002/eqe.823.

[25] S.F. Masri, Analytical and Experimental Studies of Multiple-Unit Impact Dampers, J. Acoust. Soc. Am. 45 (1969) 1111–1117. https://doi.org/10.1121/1.1911581.

[26] C. Cempel, The multi-unit impact damper: equivalent continuous force approach, J. Sound Vib. 34 (1974) 199–209. https://doi.org/10.1016/S0022-460X(74)80304-4.

[27] C. Cempel, G. Lotz, Efficiency of vibrational energy dissipation by moving shot, J. Struct. Eng. 119 (1993) 2642–2652. https://doi.org/10.1061/(ASCE)0733-9445(1993)119:9(2642).

[28] N. Popplewell, S.E. Semercigil, Performance of the bean bag impact damper for a sinusoidal external force, J. Sound Vib. 133 (1989) 193–223. https://doi.org/10.1016/0022-460X(89)90922-X.

[29] Y. Araki, I. Yokomichi, J. Inoue, Impact damper with granular materials, Bull. JSME. 28 (1985) 1466–1472. https://doi.org/10.1299/jsme1958.28.1466.

[30] H. V Panossian, Non-obstructive particle damping: New experiences and capabilities, in: 49th AIAA/ASME/ASCE/AHS/ASC Struct. Struct. Dyn. Mater. Conf., Schaumburg, Illinois, 2008. https://doi.org/10.2514/6.2008-2102.

[31] Z. Lu, Z. Wang, S.F. Masri, X. Lu, Particle impact dampers: Past, present, and future,

Struct. Control Heal. Monit. 25 (2018) 1–25. https://doi.org/10.1002/stc.2058.

[32]   L. Gagnon, M. Morandini, G.L. Ghiringhelli, A review of particle damping modeling and testing, J. Sound Vib. 459 (2019) 114865. https://doi.org/10.1016/j.jsv.2019.114865.

[33]   S.S. Simonian, Particle beam damper, in: Proc. SPIE 2445, Smart Struct. Mater. 1995 Passiv. Damping, San Diego, California, 1995: pp. 149–160. https://doi.org/10.1117/12.208884.

[34]   R. Ehrgott, H. V. Panossian, G. Davis, Modeling techniques for evaluating the effectiveness of particle damping in turbomachinery, in: AIAA/ASME/ASCE/AHS/ASC Struct. Struct. Dyn. Mater. Conf., Palm springs, California, 2009. https://doi.org/10.2514/6.2009-2690.

[35]   P. Veeramuthuvel, K.K. Sairajan, K. Shankar, Vibration suppression of printed circuit boards using an external particle damper, J. Sound Vib. 366 (2016) 98–116. https://doi.org/10.1016/j.jsv.2015.12.034.

[36]   P. Veeramuthuvel, K. Shankar, K.K. Sairajan, Application of particle damper on electronic packages for spacecraft, Acta Astronaut. 127 (2016) 260–270. https://doi.org/10.1016/j.actaastro.2016.06.003.

[37]   F. Duvigneau, S. Koch, E. Woschke, U. Gabbert, An effective vibration reduction concept for automotive applications based on granular-filled cavities, J. Vib. Control. 24 (2018) 73–82. https://doi.org/10.1177/1077546316632932.

[38]   S. Koch, F. Duvigneau, R. Orszulik, U. Gabbert, E. Woschke, Partial filling of a honeycomb structure by granular materials for vibration and noise reduction, J. Sound Vib. 393 (2017) 30–40. https://doi.org/10.1016/j.jsv.2016.11.024.

[39]   Y.C. Chung, Y.R. Wu, Dynamic modeling of a gear transmission system containing damping particles using coupled multi-body dynamics and discrete element method, Nonlinear Dyn. 98 (2019) 129–149. https://doi.org/10.1007/s11071-019-05177-1.

[40]   W. Xiao, Y. Huang, H. Jiang, H. Lin, J. Li, Energy dissipation mechanism and experiment of particle dampers for gear transmission under centrifugal loads, Particuology. 27 (2016) 40–50. https://doi.org/10.1016/j.partic.2015.10.007.

[41]   S. Ashley, New racket shakes up tennis, Mech. Eng. 117 (1995) 80–81.

[42]   T. Ehlers, S. Tatzko, J. Wallaschek, R. Lachmayer, Design of particle dampers for additive manufacturing, Addit. Manuf. 38 (2021). https://doi.org/10.1016/j.addma.2020.101752.

[43]   N.D. Sims, A. Amarasinghe, K. Ridgway, Particle dampers for workpiece chatter mitigation, in: ASME Int. Mech. Eng. Congr. Expo., Orlando, Florida, 2005. https://doi.org/10.1115/IMECE2005-82687.

[44]   Z. Lu, X. Chen, D. Zhang, K. Dai, Experimental and analytical study on the performance of particle tuned mass dampers under seismic excitation, Earthq. Eng. Struct. Dyn. 46 (2017) 697–714. https://doi.org/10.1002/eqe.2826.

[45]   B. Knight, D. Parsons, A. Smith, Evaluating attenuation of vibration response using particle impact damping for a range of equipment assemblies, in: AIAA Aerosp. Des. Struct. Event, Boston, Massachusetts, 2013: pp. 1–9.

[46]   S.S. Simonian, Particle damping applications, in: 45th

AIAA/ASME/ASCE/AHS/ASC Struct. Struct. Dyn. Mater. Conf., Palm springs, California, 2004: pp. 4145–4161. https://doi.org/10.2514/6.2004-1906.

[47] Z. Xu, M. Yu Wang, T. Chen, A particle damper for vibration and noise reduction, J. Sound Vib. 270 (2004) 1033–1040. https://doi.org/10.1016/S0022-460X(03)00503-0.

[48] L. Hu, Y. Shi, Q. Yang, G. Song, Sound reduction at a target point inside an enclosed cavity using particle dampers, J. Sound Vib. 384 (2016) 45–55. https://doi.org/10.1016/j.jsv.2016.08.016.

[49] B. Wang, M. Yang, Damping of honeycomb sandwich beams, J. Mater. Process. Technol. 105 (2000) 67–72. https://doi.org/10.1016/S0924-0136(00)00564-1.

[50] N. Ahmad, R. Ranganath, A. Ghosal, Modeling and experimental study of a honeycomb beam filled with damping particles, J. Sound Vib. 391 (2017) 20–34. https://doi.org/10.1016/j.jsv.2016.11.011.

[51] B.L. Fowler, E.M. Flint, S.E. Olson, Design methodology for particle damping, in: Proc. SPIE 4331, Smart Struct. Mater. 2001 Damping Isol., Newport Beach, California, 2001: pp. 186–197. https://doi.org/10.1117/12.432703.

[52] B.M. Shah, D. Pillet, X.M. Bai, L.M. Keer, Q. Jane Wang, R.Q. Snurr, Construction and characterization of a particle-based thrust damping system, J. Sound Vib. 326 (2009) 489–502. https://doi.org/10.1016/j.jsv.2009.06.007.

[53] K. Zhang, Y. Xi, T. Chen, Z. Ma, Experimental studies of tuned particle damper: Design and characterization, Mech. Syst. Signal Process. 99 (2018) 219–228. https://doi.org/10.1016/j.ymssp.2017.06.007.

[54] K. Zhang, H. Zhong, F. Kou, Y. Chen, Y. Gao, Dissipation behaviors of suspended granular balls in a vibrated closed container, Powder Technol. 399 (2022) 117158. https://doi.org/10.1016/j.powtec.2022.117158.

[55] J.A. Rongong, G.R. Tomlinson, Amplitude dependent behaviour in the application of particle dampers to vibrating structures, in: 46th AIAA/ASME/ASCE/AHS/ASC Struct. Struct. Dyn. Mater. Conf., Austin, Texas, 2005: pp. 6433–6441. https://doi.org/10.2514/6.2005-2327.

[56] C. Wong, J. Rongong, Control of particle damper nonlinearity, AIAA J. 47 (2009) 953–960. https://doi.org/10.2514/1.38795.

[57] B. Yao, Q. Chen, Investigation on zero-gravity behavior of particle dampers, J. Vib. Control. 21 (2015) 124–133. https://doi.org/10.1177/1077546313488157.

[58] J.M. Bajkowski, B. Dyniewicz, C.I. Bajer, Damping properties of a beam with vacuum-packed granular damper, J. Sound Vib. 341 (2015) 74–85. https://doi.org/10.1016/j.jsv.2014.12.036.

[59] Y. Wang, B. Liu, A. Tian, W. Tang, Experimental and numerical investigations on the performance of particle dampers attached to a primary structure undergoing free vibration in the horizontal and vertical directions, J. Sound Vib. 371 (2016) 35–55. https://doi.org/10.1016/j.jsv.2016.01.056.

[60] A. Papalou, S.F. Masri, An experimental investigation of particle dampers under harmonic excitation, J. Vib. Control. 4 (1998) 361–379. https://doi.org/10.1177/107754639800400402.

[61] A. Papalou, S.F. Masri, Performance of particle dampers under random excitation, J. Vib. Acoust. 118 (1996) 614–621. https://doi.org/10.1115/1.2888343.

[62] G. Michon, A. Almajid, G. Aridon, Soft hollow particle damping identification in honeycomb structures, J. Sound Vib. 332 (2013) 536–544. https://doi.org/10.1016/j.jsv.2012.09.024.

[63] W. Liu, M.S. Ewing, Particle damping of composite honeycomb beams by the power input method, in: AIAA/ASME/ASCE/AHS/ASC Struct. Struct. Dyn. Mater. Conf., Honolulu, Hawaii, 2007: pp. 4183–4191. https://doi.org/10.2514/6.2007-2044.

[64] M.Y. Yang, Development of master design curves for particle impact dampers, The Pennsylvania State University, 2003.

[65] M.Y. Yang, G.A. Lesieutre, S.A. Hambric, G.H. Koopmann, Development of a design curve for particle impact dampers, in: Smart Struct. Mater. 2004 Damping Isol., Bellingham, WA, 2004: p. 450. https://doi.org/10.1117/12.540019.

[66] B. Darabi, J.A. Rongong, Polymeric particle dampers under steady-state vertical vibrations, J. Sound Vib. 331 (2012) 3304–3316. https://doi.org/10.1016/j.jsv.2012.03.005.

[67] C.X. Wong, M.C. Daniel, J.A. Rongong, Energy dissipation prediction of particle dampers, J. Sound Vib. 319 (2009) 91–118. https://doi.org/10.1016/j.jsv.2008.06.027.

[68] Y. Duan, Q. Chen, Simulation and experimental investigation on dissipative properties of particle dampers, J. Vib. Control. 17 (2011) 777–788. https://doi.org/10.1177/1077546309356183.

[69] K. Zhang, T. Chen, L. He, Damping behaviors of granular particles in a vertically vibrated closed container, Powder Technol. 321 (2017) 173–179. https://doi.org/10.1016/j.powtec.2017.08.020.

[70] M. Ben Romdhane, N. Bouhaddi, M. Trigui, E. Foltête, M. Haddar, The loss factor experimental characterisation of the non-obstructive particles damping approach, Mech. Syst. Signal Process. 38 (2013) 585–600. https://doi.org/10.1016/j.ymssp.2013.02.006.

[71] A. Papalou, S.F. Masri, Response of impact dampers with granular materials under random excitation, Earthq. Eng. Struct. Dyn. 25 (1996) 253–267. https://doi.org/10.1002/(SICI)1096-9845(199603)25:3<253::AID-EQE553>3.0.CO;2-4.

[72] R.D. Friend, V.K. Kinra, Particle impact damping, J. Sound Vib. 233 (2000) 93–118. https://doi.org/10.1006/jsvi.1999.2795.

[73] K.S. Marhadi, V.K. Kinra, Particle impact damping: Effect of mass ratio, material, and shape, J. Sound Vib. 283 (2005) 433–448. https://doi.org/10.1016/j.jsv.2004.04.013.

[74] C.J. Wu, W.H. Liao, M.Y. Wang, Modeling of granular particle damping using multiphase flow theory of gas-particle, J. Vib. Acoust. 126 (2004) 196–201. https://doi.org/10.1115/1.1688763.

[75] X. Fang, J. Tang, Granular damping in forced vibration: Qualitative and quantitative analyses, J. Vib. Acoust. 128 (2006) 489–500. https://doi.org/10.1115/1.2203339.

[76] B. Darabi, J.A. Rongong, T. Zhang, Viscoelastic granular dampers under low-amplitude vibration, J. Vib. Control. 24 (2018) 708–721. https://doi.org/10.1177/1077546316650098.

[77] A. Sack, M. Heckel, J.E. Kollmer, F. Zimber, T. Pöschel, Energy dissipation in driven granular matter in the absence of gravity, Phys. Rev. Lett. 111 (2013) 1–5. https://doi.org/10.1103/PhysRevLett.111.018001.

[78] M. Masmoudi, S. Job, M.S. Abbes, I. Tawfiq, M. Haddar, Experimental and numerical investigations of dissipation mechanisms in particle dampers, Granul. Matter. 18 (2016) 1–11. https://doi.org/10.1007/s10035-016-0667-4.

[79] M.V. Ferreyra, M. Baldini, L.A. Pugnaloni, S. Job, Effect of lateral confinement on the apparent mass of granular dampers, Granul. Matter. 23 (2021). https://doi.org/10.1007/s10035-021-01090-w.

[80] N. Meyer, C. Schwartz, M. Morlock, R. Seifried, Systematic design of particle dampers for horizontal vibrations with application to a lightweight manipulator, J. Sound Vib. 510 (2021) 116319. https://doi.org/10.1016/j.jsv.2021.116319.

[81] N. Meyer, R. Seifried, Systematic design of particle dampers for transient vertical vibrations, Granul. Matter. 25 (2023). https://doi.org/10.1007/s10035-022-01290-y.

[82] M. Sánchez, L.A. Pugnaloni, Effective mass overshoot in single degree of freedom mechanical systems with a particle damper, J. Sound Vib. 330 (2011) 5812–5819. https://doi.org/10.1016/j.jsv.2011.07.016.

[83] T. Poschel, T. Schwager, Computational granular dynamics: models and algorithms, Springer-Verlag, Berlin, 2004.

[84] J. Duran, Sands, Powders, and Grains, 2000. http://link.aip.org/link/PHTOAD/v54/i4/p63/s2&Agg=doi%0Ahttp://physicstoday.s citation.org/doi/10.1063/1.1383168%0Ahttp://link.springer.com/10.1007/978-1-4612-0499-2.

[85] H.-G. Matuttis, J. Chen, Understanding the discrete element method, John Wiley & Sons, Incorporated, Singapore, 2014. https://doi.org/10.1002/9781118567210.

[86] M. Saeki, Impact damping with granular materials in a horizontally vibrating system, J. Sound Vib. 251 (2002) 153–161. https://doi.org/10.1006/jsvi.2001.3985.

[87] S.E. Olson, An analytical particle damping model, J. Sound Vib. 264 (2003) 1155–1166. https://doi.org/10.1016/S0022-460X(02)01388-3.

[88] Z. Xu, M.Y. Wang, T. Chen, Particle damping for passive vibration suppression: Numerical modelling and experimental investigation, J. Sound Vib. 279 (2005) 1097–1120. https://doi.org/10.1016/j.jsv.2003.11.023.

[89] N. Meyer, R. Seifried, Toward a design methodology for particle dampers by analyzing their energy dissipation, Comput. Part. Mech. (2020). https://doi.org/10.1007/s40571-020-00363-0.

[90] T. Chen, K. Mao, X. Huang, M.Y. Wang, Dissipation mechanisms of nonobstructive particle damping using discrete element method, in: Proc. SPIE 4331, Smart Struct. Mater. 2001 Damping Isol., Newport Beach, California, 2001: pp. 294–301. https://doi.org/10.1117/12.432713.

[91] M.N. Bannerman, J.E. Kollmer, A. Sack, M. Heckel, P. Mueller, T. Pöschel, Movers

and shakers: Granular damping in microgravity, Phys. Rev. E. 84 (2011) 1–9. https://doi.org/10.1103/PhysRevE.84.011301.

[92] K. Mao, M.Y. Wang, Z.Z. Xu, T. Chen, Simulation and characterization of particle damping in transient vibrations, J. Vib. Acoust. 126 (2004) 202–211. https://doi.org/10.1115/1.1687401.

[93] Z. Xu, M.Y. Wang, T. Chen, An experimental study of particle damping for beams and plates, J. Vib. Acoust. 126 (2004) 141–148. https://doi.org/10.1115/1.1640354.

[94] Z. Lu, X. Lu, S.F. Masri, Studies of the performance of particle dampers under dynamic loads, J. Sound Vib. 329 (2010) 5415–5433. https://doi.org/10.1016/j.jsv.2010.06.027.

[95] Z. Lu, S.F. Masri, X. Lu, Studies of the performance of particle dampers attached to a two-degrees-of-freedom system under random excitation, J. Vib. Control. 17 (2011) 1454–1471. https://doi.org/10.1177/1077546310370687.

[96] S. Fauve, S. Douady, C. Laroche, Collective behaviours of granular masses under vertical vibrations, Le J. Phys. Colloq. 50 (1989) C3-187-C3-191. https://doi.org/10.1051/jphyscol:1989328.

[97] H.K. Pak, R.P. Behringer, Surface waves in vertically vibrated granular materials, Phys. Rev. Lett. 71 (1993) 1832–1835. https://doi.org/10.1103/PhysRevLett.71.1832.

[98] C.R. Wassgren, C.E. Brennen, M.L. Hunt, Vertical vibration of a deep bed of granular material in a container, J. Appl. Mech. 63 (1996) 712–719. https://doi.org/10.1115/1.2823354.

[99] K. Zhang, H. Zhong, T. Chen, F. Kou, Y. Chen, C. Bai, Dissipation behaviors of granular balls in a shaken closed container, Mech. Syst. Signal Process. 172 (2022) 108986. https://doi.org/10.1016/j.ymssp.2022.108986.

[100] G.H. Ristow, Critical exponents for granular phase transitions, Europhys. Lett. 40 (1997) 625–630. https://doi.org/10.1209/epl/i1997-00514-3.

[101] C. Salueña, T. Pöschel, Convection in horizontally shaken granular material, Eur. Phys. J. E. 1 (2000) 55–59. https://doi.org/10.1007/s101890050006.

[102] C. Laroche, S. Douady, S. Fauve, Convective flow of granular masses under vertical vibrations, J. Phys. 50 (1989) 699–706. https://doi.org/10.1051/jphys:01989005007069900.

[103] P. Eshuis, K. van der Weele, D. van der Meer, R. Bos, D. Lohse, Phase diagram of vertically shaken granular matter, Phys. Fluids. 19 (2007). https://doi.org/10.1063/1.2815745.

[104] T. Pöschel, T. Schwager, C. Salueña, Onset of fluidization in vertically shaken granular material, Phys. Rev. E. 62 (2000) 1361–1367. https://doi.org/10.1103/PhysRevE.62.1361.

[105] S. Renard, T. Schwager, T. Pöschel, C. Salueña, Vertically shaken column of spheres. Onset of fluidization, Eur. Phys. J. E. 4 (2001) 233–239. https://doi.org/10.1007/s101890170133.

[106] H.K. Pak, E. Van Doorn, R.P. Behringer, Effects of ambient gases on granular materials under vertical vibration, Phys. Rev. Lett. 74 (1995) 4643–4646. https://doi.org/10.1103/PhysRevLett.74.4643.

[107] P. Eshuis, K. Van Der Weele, D. Van Der Meer, D. Lohse, Granular leidenfrost effect: Experiment and theory of floating particle clusters, Phys. Rev. Lett. 95 (2005) 1–4. https://doi.org/10.1103/PhysRevLett.95.258001.

[108] N. Rivas, A.R. Thornton, S. Luding, D. Van Der Meer, From the granular Leidenfrost state to buoyancy-driven convection, Phys. Rev. E. 91 (2015) 1–10. https://doi.org/10.1103/PhysRevE.91.042202.

[109] J.G. Leidenfrost, On the fixation of water in diverse fire, Int. J. Heat Mass Transf. 9 (1966) 1153–1166. https://doi.org/10.1016/0017-9310(66)90111-6.

[110] A. Sack, K. Windows-Yule, M. Heckel, D. Werner, T. Pöschel, Granular dampers in microgravity: sharp transition between modes of operation, Granul. Matter. 22 (2020) 1–6. https://doi.org/10.1007/s10035-020-01017-x.

[111] Z. Yin, F. Su, H. Zhang, Investigation of the energy dissipation of different rheology behaviors in a non-obstructive particle damper, Powder Technol. 321 (2017) 270–275. https://doi.org/10.1016/j.powtec.2017.07.090.

[112] K. Zhang, T. Chen, X. Wang, J. Fang, Motion mode of the optimal damping particle in particle dampers, J. Mech. Sci. Technol. 30 (2016) 1527–1531. https://doi.org/10.1007/s12206-016-0305-4.

[113] K.M. Aoki, A. Tetsuo, Spontaneous wave pattern formation in vibrated granular materials, Phys. Rev. Lett. 77 (1996) 4166–4169. https://doi.org/10.1103/PhysRevLett.77.4166.

[114] S. Liu, P.Y. Lai, Heaping of granular materials in a cylindrical vibrating bed, J. Phys. A. Math. Gen. 33 (2000) 8241–8249. https://doi.org/10.1088/0305-4470/33/46/307.

[115] O. Sano, Dilatancy, buckling, and undulations on a vertically vibrating granular layer, Phys. Rev. E. 72 (2005) 1–7. https://doi.org/10.1103/PhysRevE.72.051302.

[116] S.G.K. Tennakoon, R.P. Behringer, Vertical and horizontal vibration of granular materials: Coulomb friction and a novel switching State, Phys. Rev. Lett. 81 (1998) 794–797. https://doi.org/10.1103/PhysRevLett.81.794.

[117] N. Meyer, R. Seifried, Energy dissipation in horizontally driven particle dampers of low acceleration intensities, Nonlinear Dyn. 108 (2022) 3009–3024. https://doi.org/10.1007/s11071-022-07348-z.

[118] K. Zhang, T. Chen, X. Wang, J. Fang, Rheology behavior and optimal damping effect of granular particles in a non-obstructive particle damper, J. Sound Vib. 364 (2016) 30–43. https://doi.org/10.1016/j.jsv.2015.11.006.

[119] M. Bustamante, S.N.Y. Gerges, J. Cordioli, O.P. Martin, J. Weisbeck, M. Ott, Experimental study on some parameters that affect the performance of an elastomer particle damper, in: Proc. Meet. Acoust., Montreal, 2013. https://doi.org/10.1121/1.4801066.

[120] Z. Lu, S.F. Masri, X. Lu, Parametric studies of the performance of particle dampers under harmonic excitation, Struct. Control Heal. Monit. 18 (2011) 79–98. https://doi.org/10.1002/stc.359.

[121] X. Lei, C. Wu, P. Chen, Optimizing parameter of particle damping based on Leidenfrost effect of particle flows, Mech. Syst. Signal Process. 104 (2018) 60–71. https://doi.org/10.1016/j.ymssp.2017.10.037.

[122] X. Ye, Y. Ni, M. Sajjadi, Y. Wang, C. Lin, Physics-guided , data-refined modeling of granular material-filled particle dampers by deep transfer learning, Mech. Syst. Signal Process. 180 (2022) 109437. https://doi.org/10.1016/j.ymssp.2022.109437.

[123] B.L. Witt, V.K. Kinra, Particle impact damping in the horizontal plane, in: 47th AIAA/ASME/ASCE/AHS/ASC Struct. Struct. Dyn. Mater. Conf., Newport, Rhode Island, 2006: pp. 7345–7352. https://doi.org/10.2514/6.2006-2209.

[124] J.J. Hollkamp, R.W. Gordon, Experiments with particle damping, in: Proc. SPIE 3327, Smart Struct. Mater. 1998 Passiv. Damping Isol., San Diego, California, 1998: pp. 2–12. https://doi.org/10.1117/12.310675.

[125] M. Sánchez, G. Rosenthal, L.A. Pugnaloni, Universal response of optimal granular damping devices, J. Sound Vib. 331 (2012) 4389–4394. https://doi.org/10.1016/j.jsv.2012.05.001.

[126] B. Darabi, J.A. Rongong, Amplitude dependent damping from granular viscoelastics, J. Phys. Conf. Ser. 382 (2012). https://doi.org/10.1088/1742-6596/382/1/012026.

[127] K.K. Varanasi, S.A. Nayfeh, Damping of flexural vibration using low-density, low-wave-speed media, J. Sound Vib. 292 (2006) 402–414. https://doi.org/10.1016/j.jsv.2005.10.014.

[128] J.R. Fricke, Lodengraf damping-an advanced vibration damping technology, Sound Vib. 34 (2000) 22–27.

[129] M. Bustamante, S.N.Y. Gerges, E.F. Vergara, J.P. Arenas, High damping characteristics of an elastomer particle damper, Int. J. Acoust. Vib. 21 (2016) 112–121. https://doi.org/10.20855/ijav.2016.21.1401.

[130] S.O. Oyadiji, Damping of vibrations of hollow beams using viscoelastic spheres, in: Smart Struct. Mater. 1996 Passiv. Damping Isol., San Diego, California, 1996: pp. 89–98. https://doi.org/10.1117/12.239078.

[131] R.J. Pamley, J.R. House, M.J. Brennan, Comparison of passive damping treatments for hollow structures, in: Proc. SPIE 4331, Smart Struct. Mater. 2001 Damping Isol., Newport Beach, California, 2001: pp. 455–467. https://doi.org/10.1117/12.432729.

[132] C. Wong, A. Spencer, J. Rongong, Effects of enclosure geometry on particle damping performance, in: 50th AIAA/ASME/ASCE/AHS/ASC Struct. Struct. Dyn. Mater. Conf., American Institute of Aeronautics and Astronautics, Reston, Virigina, 2009. https://doi.org/10.2514/6.2009-2689.

[133] A.G. Athanassiadis, M.Z. Miskin, P. Kaplan, N. Rodenberg, S.H. Lee, J. Merritt, E. Brown, J. Amend, H. Lipson, H.M. Jaeger, Particle shape effects on the stress response of granular packings, Soft Matter. 10 (2014) 48–59. https://doi.org/10.1039/c3sm52047a.

[134] P. Parafiniuk, M. Molenda, J. Horabik, Influence of particle shape and sample width on uniaxial compression of assembly of prolate spheroids examined by discrete element method, Phys. A Stat. Mech. Its Appl. 416 (2014) 279–289. https://doi.org/10.1016/j.physa.2014.08.063.

[135] J. Horabik, M. Molenda, Parameters and contact models for DEM simulations of agricultural granular materials: A review, Biosyst. Eng. 147 (2016) 206–225. https://doi.org/10.1016/j.biosystemseng.2016.02.017.

[136] Altair Engineering Inc., EDEM 2021.1, (2021).

[137] P.A. Cundall, O.D.L. Strack, A discrete numerical model for granular assemblies, Geotechnique. 29 (1979) 47–65. https://doi.org/10.1680/geot.1979.29.1.47.

[138] J.M. Boac, R.P.K. Ambrose, M.E. Casada, R.G. Maghirang, D.E. Maier, Applications of Discrete Element Method in Modeling of Grain Postharvest Operations, Food Eng. Rev. 6 (2014) 128–149. https://doi.org/10.1007/s12393-014-9090-y.

[139] S. Bin Yeom, E. Ha, M. Kim, S.H. Jeong, S.J. Hwang, D.H. Choi, Application of the discrete element method for manufacturing process simulation in the pharmaceutical industry, Pharmaceutics. 11 (2019). https://doi.org/10.3390/pharmaceutics11080414.

[140] M. Marigo, E.H. Stitt, Discrete element method (DEM) for industrial applications: Comments on calibration and validation for the modelling of cylindrical pellets, KONA Powder Part. J. 32 (2015) 236–252. https://doi.org/10.14356/kona.2015016.

[141] B.L. Fowler, E.M. Flint, S.E. Olson, Effectiveness and predictability of particle damping, in: Proc. SPIE 3989, Smart Struct. Mater. 2000 Damping Isol., Newport Beach, California, 2000: pp. 356–367. https://doi.org/10.1117/12.384576.

[142] M. Saeki, Analytical study of multi-particle damping, J. Sound Vib. 281 (2005) 1133–1144. https://doi.org/10.1016/j.jsv.2004.02.034.

[143] X. Fang, J. Tang, H. Luo, Granular damping analysis using an improved discrete element approach, J. Sound Vib. 308 (2007) 112–131. https://doi.org/10.1016/j.jsv.2007.07.034.

[144] C.X. Wong, M.C. Daniel, J.A. Rongong, Prediction of the amplitude dependent behaviour of particle dampers, in: AIAA/ASME/ASCE/AHS/ASC Struct. Struct. Dyn. Mater. Conf., Honolulu, Hawaiii, 2007: pp. 4167–4182. https://doi.org/10.2514/6.2007-2043.

[145] Z. Lu, X. Lu, H. Jiang, S.F. Masri, Discrete element method simulation and experimental validation of particle damper system, Eng. Comput. (Swansea, Wales). 31 (2014) 810–823. https://doi.org/10.1108/EC-08-2012-0191.

[146] J. Chen, Discrete element method for 3D simulations of mechanical systems of non-spherical granular materials, The University of Electro-Communacations, 2012.

[147] B.C. Vemuri, L. Chen, L. Vu-Quoc, X. Zhang, O. Walton, Efficient and accurate collision detection for granular flow simulation, Graph. Model. Image Process. 60 (1998) 403–422. https://doi.org/10.1006/gmip.1998.0479.

[148] H. Mio, A. Shimosaka, Y. Shirakawa, J. Hidaka, Optimum cell size for contact detection in the algorithm of the discrete element method, J. Chem. Eng. Japan. 38 (2005) 969–975. https://doi.org/10.1252/jcej.38.969.

[149] H. Baruh, Analytical Dynamics, First, McGraw-Hill, Singapore, 1999.

[150] D.T. Greenwood, Advanced Dynamics, First, Cambridge University Press, New York, 2003. https://doi.org/10.1017/cbo9780511800207.

[151] M.D. Ardema, Newton-Euler dynamics, 2005. https://doi.org/10.1007/b101082.

[152] A. Di Renzo, F.P. Di Maio, Comparison of contact-force models for the simulation of collisions in DEM-based granular flow codes, Chem. Eng. Sci. 59 (2004) 525–541. https://doi.org/10.1016/j.ces.2003.09.037.

[153] S. Lommen, D. Schott, G. Lodewijks, DEM speedup: Stiffness effects on behavior of bulk material, Particuology. 12 (2014) 107–112. https://doi.org/10.1016/j.partic.2013.03.006.

[154] H. Chen, Y.G. Xiao, Y.L. Liu, Y.S. Shi, Effect of Young's modulus on DEM results regarding transverse mixing of particles within a rotating drum, Powder Technol. 318 (2017) 507–517. https://doi.org/10.1016/j.powtec.2017.05.047.

[155] F. Biondani, M. Morandini, G.L. Ghiringhelli, M. Terraneo, P. Cordisco, Efficient Discrete Element Modeling of Particle Dampers, Processes. 10 (2022). https://doi.org/10.3390/pr10071247.

[156] J. Wiacek, M. Molenda, J. Horabik, J.Y. Ooi, Influence of grain shape and intergranular friction on material behavior in uniaxial compression: Experimental and DEM modeling, Powder Technol. 217 (2012) 435–442. https://doi.org/10.1016/j.powtec.2011.10.060.

[157] T. Li, J. Zhang, W. Ge, Simple measurement of restitution coefficient of irregular particles, China Particuology. 2 (2004) 274–275. https://doi.org/10.1016/s1672-2515(07)60074-8.

[158] D.B. Hastie, Experimental measurement of the coefficient of restitution of irregular shaped particles impacting on horizontal surfaces, Chem. Eng. Sci. 101 (2013) 828–836. https://doi.org/10.1016/j.ces.2013.07.010.

[159] M. Pasha, C. Hare, M. Ghadiri, A. Gunadi, P.M. Piccione, Effect of particle shape on flow in discrete element method simulation of a rotary batch seed coater, Powder Technol. 296 (2016) 29–36. https://doi.org/10.1016/j.powtec.2015.10.055.

[160] M. Alizadeh, A. Hassanpour, M. Pasha, M. Ghadiri, A. Bayly, The effect of particle shape on predicted segregation in binary powder mixtures, Powder Technol. 319 (2017) 313–322. https://doi.org/10.1016/j.powtec.2017.06.059.

[161] W. Nan, M. Pasha, T. Bonakdar, A. Lopez, U. Zafar, S. Nadimi, M. Ghadiri, Jamming during particle spreading in additive manufacturing, Powder Technol. 338 (2018) 253–262. https://doi.org/10.1016/j.powtec.2018.07.030.

[162] V. Angelidakis, S. Nadimi, M. Otsubo, S. Utili, CLUMP: A code library to generate universal multi-sphere particles, SoftwareX. 15 (2021) 100735. https://doi.org/10.1016/j.softx.2021.100735.

[163] L. Vu-Quoc, X. Zhang, O.R. Walton, A 3-D discrete-element method for dry granular flows of ellipsoidal particles, Comput. Methods Appl. Mech. Eng. 187 (2000) 483–528. https://doi.org/10.1016/S0045-7825(99)00337-0.

[164] D. Markauskas, R. Kačianauskas, A. Džiugys, R. Navakas, Investigation of adequacy of multi-sphere approximation of elliptical particles for DEM simulations, Granul. Matter. 12 (2010) 107–123. https://doi.org/10.1007/s10035-009-0158-y.

[165] W.J. Stronge, Impact Mechanics, Second, Cambridge University Press, New York, 2018.

[166] K.L. Johnson, Contact Mechanics, First, Cambridge University Press, New York, 1985.

[167] L. Vu-Quoc, X. Zhang, L. Lesburg, Normal and tangential force-displacement relations for frictional elasto-plastic contact of spheres, Int. J. Solids Struct. 38 (2001)

6455–6489. https://doi.org/10.1016/S0020-7683(01)00065-8.

[168] B.K. Mishra, C.V.R. Murty, On the determination of contact parameters for realistic DEM simulations of ball mills, Powder Technol. 115 (2001) 290–297. https://doi.org/10.1016/S0032-5910(00)00347-8.

[169] M. Iwashita K., Oda, Rolling resistance at contacts in simulation of shear band, Asce. 124 (1998) 285–292.

[170] T. Iwasaki, M. Satoh, T. Koga, Analysis of collision energy of bead media in a high-speed elliptical-rotor-type powder mixer using the discrete element method, Powder Technol. 121 (2001) 239–248. https://doi.org/10.1016/S0032-5910(01)00384-9.

[171] Y. Tatemoto, Y. Mawatari, T. Yasukawa, K. Noda, Numerical simulation of particle motion in vibrated fluidized bed, Chem. Eng. Sci. 59 (2004) 437–447. https://doi.org/10.1016/j.ces.2003.10.005.

[172] L. Vu-Quoc, L. Lesburg, X. Zhang, An accurate tangential force-displacement model for granular-flow simulations: Contacting spheres with plastic deformation, force-driven formulation, J. Comput. Phys. 196 (2004) 298–326. https://doi.org/10.1016/j.jcp.2003.10.025.

[173] X. Zhang, L. Vu-Quoc, An accurate elasto-plastic frictional tangential force-displacement model for granular-flow simulations: Displacement-driven formulation, J. Comput. Phys. 225 (2007) 730–752. https://doi.org/10.1016/j.jcp.2006.12.028.

[174] H. Kruggel-Emden, E. Simsek, S. Rickelt, S. Wirtz, V. Scherer, Review and extension of normal force models for the Discrete Element Method, Powder Technol. 171 (2007) 157–173. https://doi.org/10.1016/j.powtec.2006.10.004.

[175] P. Mueller, S. Antonyuk, M. Stasiak, J. Tomas, S. Heinrich, The normal and oblique impact of three types of wet granules, Granul. Matter. 13 (2011) 455–463. https://doi.org/10.1007/s10035-011-0256-5.

[176] J. Ai, J.F. Chen, J.M. Rotter, J.Y. Ooi, Assessment of rolling resistance models in discrete element simulations, Powder Technol. 206 (2011) 269–282. https://doi.org/10.1016/j.powtec.2010.09.030.

[177] G. Kuwabara, K. Kono, Restitution coefficient in a collision between two spheres, Jpn. J. Appl. Phys. 26 (1987) 1219–1223. https://doi.org/10.1143/JJAP.26.1230.

[178] J. Coaplen, W.J. Stronge, B. Ravani, Work equivalent composite coefficient of restitution, Int. J. Impact Eng. 30 (2004) 581–591. https://doi.org/10.1016/j.ijimpeng.2003.10.038.

[179] Y. Tsuji, T. Tanaka, T. Ishida, Lagrangian numerical simulation of plug flow of cohesionless particles in a horizontal pipe, Powder Technol. 71 (1992) 239–250. https://doi.org/10.1016/0032-5910(92)88030-L.

[180] D. Zhang, W.J. Whiten, The calculation of contact forces between particles using spring and damping models, Powder Technol. 88 (1996) 59–64. https://doi.org/10.1016/0032-5910(96)03104-X.

[181] T. Elperin, E. Golshtein, Comparison of different models for tangential forces using the particle dynamics method, Physica A. 242 (1997) 332–340. https://doi.org/10.1016/S0378-4371(97)00218-5.

[182] J. Shäfer, S. Dippel, D.E. Wolf, Force schemes in simulations of granular materials,

J. Phys. I. 6 (1996) 5–20. https://doi.org/10.1051/jp1:1996129.

[183] L. Vu-Quoc, X. Zhang, Accurate and efficient tangential force-displacement model for elastic frictional contact in particle-flow simulations, Mech. Mater. 31 (1999) 235–269. https://doi.org/10.1016/S0167-6636(98)00064-7.

[184] L. Vu-Quoc, X. Zhang, L. Laesburg, A normal force-displacement model for contacting spheres accounting for plastic deformation: Force-Driven formulation, J. Appl. Mech. Trans. ASME. 67 (2000) 363–371. https://doi.org/10.1115/1.1305334.

[185] H. Hertz, On the contact of elastic solids, J. Reine Und Angew. Math. 92 (1882) 156–171.

[186] J.M. Lifshitz, H. Kolsky, Some experiments on anelastic rebound, J. Mech. Phys. Solids. 12 (1964) 35–43. https://doi.org/10.1016/0022-5096(64)90005-5.

[187] R.D. Mindlin, H. Deresiewicz, Elastic spheres in contact under varying oblique forces, Trans. ASME, Ser. E. J. Appl. Mech. 20 (1953) 327–344. https://doi.org/10.1007/978-1-4613-8865-4_35.

[188] J.N. Reddy, An Introduction to the Finite Element Method, Second, McGraw-Hill, Inc., The United States of America, 1993.

[189] T. Belytschko, W.K. Liu, B. Moran, K.I. Elkhodaru, Nonlinear finite elements for continua and structures, Second, John Wiley & Sons, Ltd., West Sussex, 2014.

[190] R.D. Cook, D.S. Malkus, M.E. Plesha, R.J. Witt, Concepts and applications of finite element analysis, Fourth, John Wiley & Sons, Incorporated, New Jersey, 2002. https://doi.org/10.1115/1.3264300.

[191] Dassault Systmes Simulia Corp., Abaqus 6.14 User Guide, (2014).

[192] D. Tabor, A simple theory of static and dynamic hardness, in: Proc. R. Soc. London. Ser. A. Math. Phys. Sci., 1948: pp. 247–274. https://doi.org/10.1098/rspa.1948.0008.

[193] R.M. Davies, The determination of static and dynamic yield stresses using a steel ball, Proc. R. Soc. London. Ser. A. Math. Phys. Sci. 197 (1949) 416–432. https://doi.org/10.1098/rspa.1949.0073.

[194] E. Lee, J. Radok, The contact problem for viscoelastic bodies, J. Appl. Mech. Phys. 27 (1960) 438–444.

[195] H. Tang, R. Song, Y. Dong, X. Song, Measurement of restitution and friction coefficients for granular particles and discrete element simulation for the tests of glass beads, Materials (Basel). 12 (2019). https://doi.org/10.3390/ma12193170.

[196] M.C. Marinack, R.E. Musgrave, C.F. Higgs, Experimental investigations on the coefficient of restitution of single particles, Tribol. Trans. 56 (2013) 572–580. https://doi.org/10.1080/10402004.2012.748233.

[197] T. Schwager, T. Pöschel, Coefficient of restitution for viscoelastic spheres: The effect of delayed recovery, Phys. Rev. E - Stat. Nonlinear, Soft Matter Phys. 78 (2008) 1–12. https://doi.org/10.1103/PhysRevE.78.051304.

[198] C.M. Sorace, M.Y. Louge, M.D. Crozier, V.H.C. Law, High apparent adhesion energy in the breakdown of normal restitution for binary impacts of small spheres at low speed, Mech. Res. Commun. 36 (2009) 364–368. https://doi.org/10.1016/j.mechrescom.2008.10.009.

[199] L. Labous, A.D. Rosato, R.N. Dave, Measurements of collisional properties of spheres using high-speed video analysis, Phys. Rev. E - Stat. Physics, Plasmas, Fluids, Relat. Interdiscip. Top. 56 (1997) 5717–5725. https://doi.org/10.1103/PhysRevE.56.5717.

[200] S. McNamara, E. Falcon, Simulations of vibrated granular medium with impact-velocity-dependent restitution coefficient, Phys. Rev. E. 71 (2005) 1–6. https://doi.org/10.1103/PhysRevE.71.031302.

[201] C. Thornton, Coefficient of restitution for collinear collisions of elastic- perfectly plastic spheres, J. Appl. Mech. Trans. ASME. 64 (1997) 383–386. https://doi.org/10.1115/1.2787319.

[202] M. Nagurka, S. Huang, A mass-spring-damper model of a bouncing ball, in: Proc. Am. Control Conf., Boston, Massachusetts, 2004: pp. 499–504. https://doi.org/10.23919/acc.2004.1383652.

[203] H.A. Sherif, F.A. Almufadi, Models for materials damping, loss factor, and coefficient of restitution, J. Eng. Mater. Technol. Trans. ASME. 142 (2020) 1–12. https://doi.org/10.1115/1.4044281.

[204] I.I. Argatov, Mathematical modeling of linear viscoelastic impact: Application to drop impact testing of articular cartilage, Tribol. Int. 63 (2013) 213–225. https://doi.org/10.1016/j.triboint.2012.09.015.

[205] X. Zhang, L. Vu-Quoc, Modeling the dependence of the coefficient of restitution on the impact velocity in elasto-plastic collisions, Int. J. Impact Eng. 27 (2002) 317–341. https://doi.org/10.1016/S0734-743X(01)00052-5.

[206] X.Z. An, R.Y. Yang, R.P. Zou, A.B. Yu, Effect of vibration condition and inter-particle frictions on the packing of uniform spheres, Powder Technol. 188 (2008) 102–109. https://doi.org/10.1016/j.powtec.2008.04.001.

[207] C. Song, P. Wang, H.A. Makse, A phase diagram for jammed matter, Nature. 453 (2008) 629–632. https://doi.org/10.1038/nature06981.

[208] F. Zamponi, Mathematical physics: Packings close and loose, Nature. 453 (2008) 606–607. https://doi.org/10.1038/453606a.

[209] J.G. Berryman, Random close packing of hard spheres and disks, Phys. Rev. A. 27 (1983) 1053–1061. https://doi.org/10.1103/PhysRevA.27.1053.

[210] G.Y. Onoda, E.G. Liniger, Random loose packings of uniform spheres and the dilatancy onset, Phys. Rev. Lett. 64 (1990).

[211] G.T. Nolan, Computer simulation of random packings of hard spheres, Powder Technol. 62 (1990) 189–196.

[212] L.E. Silbert, D. Ertaş, G.S. Grest, T.C. Halsey, D. Levine, Geometry of frictionless and frictional sphere packings, Phys. Rev. E - Stat. Physics, Plasmas, Fluids, Relat. Interdiscip. Top. 65 (2002) 1–6. https://doi.org/10.1103/PhysRevE.65.031304.

[213] T. Asakura, T. Ishizuka, T. Miyajima, M. Toyoda, S. Sakamoto, Finite-difference time-domain analysis of structure-borne sound using a plate model based on the Kirchhoff-Love plate theory, Acoust. Sci. Technol. 35 (2014) 127–138. https://doi.org/10.1250/ast.35.127.

[214] C.M. Pooley, D. Tabor, Friction and molecular structure: the behaviour of some

thermoplastics, Proc. R. Soc. London. A. Math. Phys. Sci. 329 (1972) 251–274. https://doi.org/10.1098/rspa.1972.0112.

[215] C.S. Sandeep, L. Luo, K. Senetakis, Effect of grain size and surface roughness on the normal coefficient of restitution of single grains, Materials (Basel). 13 (2020). https://doi.org/10.3390/ma13040814.

[216] X. Li, M. Dong, D. Jiang, S. Li, Y. Shang, The effect of surface roughness on normal restitution coefficient, adhesion force and friction coefficient of the particle-wall collision, Powder Technol. 362 (2020) 17–25. https://doi.org/10.1016/j.powtec.2019.11.120.

[217] I. Cruz-Matías, D. Ayala, D. Hiller, S. Gutsch, M. Zacharias, S. Estradé, F. Peiró, Sphericity and roundness computation for particles using the extreme vertices model, J. Comput. Sci. 30 (2019) 28–40. https://doi.org/10.1016/j.jocs.2018.11.005.

[218] H. Wadell, Volume, shape, and roundness of quartz particles, 43 (1935) 250–280.

[219] A. Donev, I. Cisse, D. Sachs, E.A. Variano, F.H. Stillinger, R. Connelly, S. Torquato, P.M. Chaikin, Improving the density of jammed disordered packings using ellipsoids, Science (80-.). 303 (2004) 990–993. https://doi.org/10.1126/science.1093010.

[220] E. Azéma, F. Radjai, F. Dubois, Packings of irregular polyhedral particles: Strength, structure, and effects of angularity, Phys. Rev. E - Stat. Nonlinear, Soft Matter Phys. 87 (2013) 1–14. https://doi.org/10.1103/PhysRevE.87.062203.

[221] J. Härtl, J.Y. Ooi, Numerical investigation of particle shape and particle friction on limiting bulk friction in direct shear tests and comparison with experiments, Powder Technol. 212 (2011) 231–239. https://doi.org/10.1016/j.powtec.2011.05.022.

Appendices

Appendix-A

Dynamic Mechanical Analysis measurements of the acrylic rectangular prism specimen (produced from the particles used in the experiments of the thesis – related to Chapters 7).

The dimensions of specimen: 12.8 mm × 3.0 mm × 3.7 mm

The loading type: axial compressive sinusoidal (after the application of the pre-load)
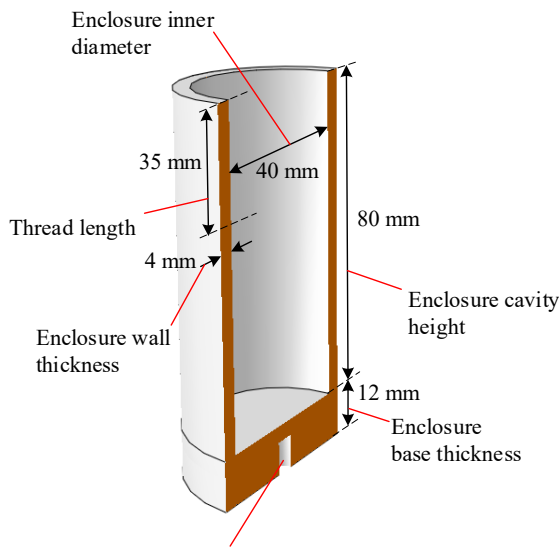
The nominal static strain applied: 0.05

The nominal dynamic strain amplitude applied: 0.001
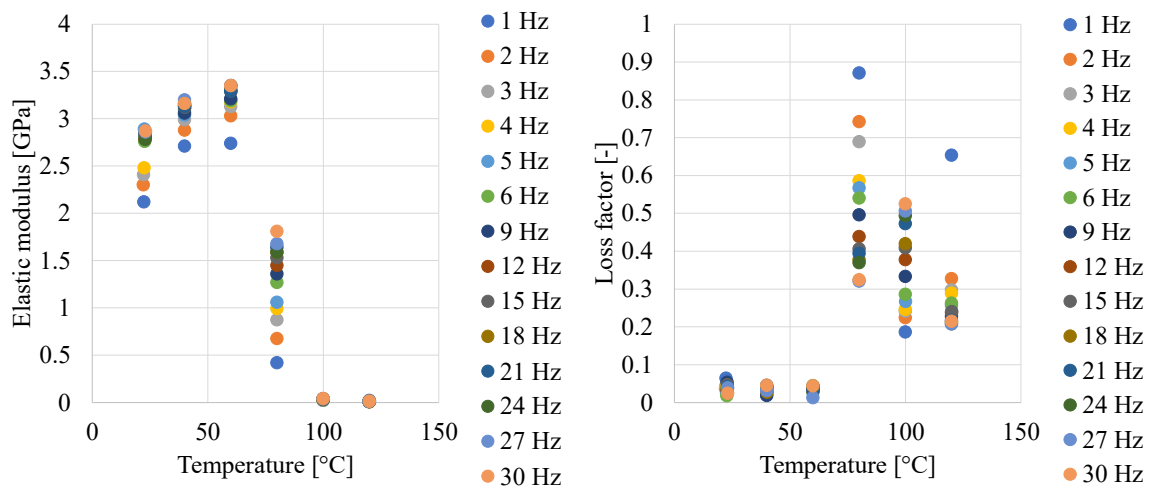
Figure A.1: Elastic modulus and loss factor of acrylic rectangular prism specimen as a function of temperature and frequency.

Appendix-B

Enclosure main body design:

Enclosure inner diameter

35 mm

40 mm

Thread length

4 mm

Enclosure wall thickness

80 mm

Enclosure cavity height

12 mm

Enclosure base thickness

*Screw thread for the threaded steel stud which connects the enclosure base to the force transducer: diameter, length (up to 8 mm leaving 4 mm wall thickness) and pitch should be consistent with force transducer – 10-32 UNF mounting screw thread connection

Adjustable lid design:

5 mm

45 mm

Thread length

5 mm

15 mm

40 mm

Securing ring design:

Ring depth: 5 mm

Inner diameter: 48 mm which is consistent with the enclosure body

Ring thickness: 4 mm
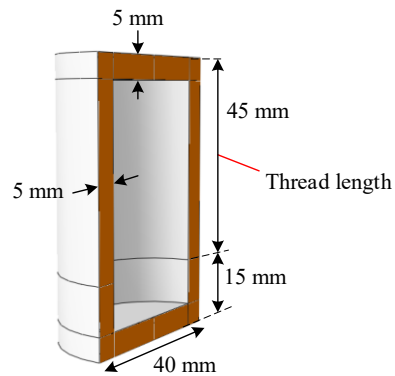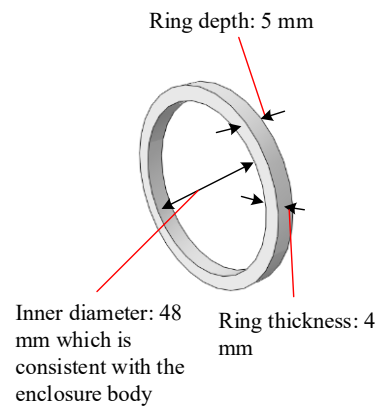
Assembled enclosure design:

Adjustable lid

Securing ring

Enclosure main body

40 mm

Force transducer

Adjustable clearance that can be arranged by the lid: **40 mm was used in this thesis experiments**

Threaded steel stud which connects the enclosure and the force transducer
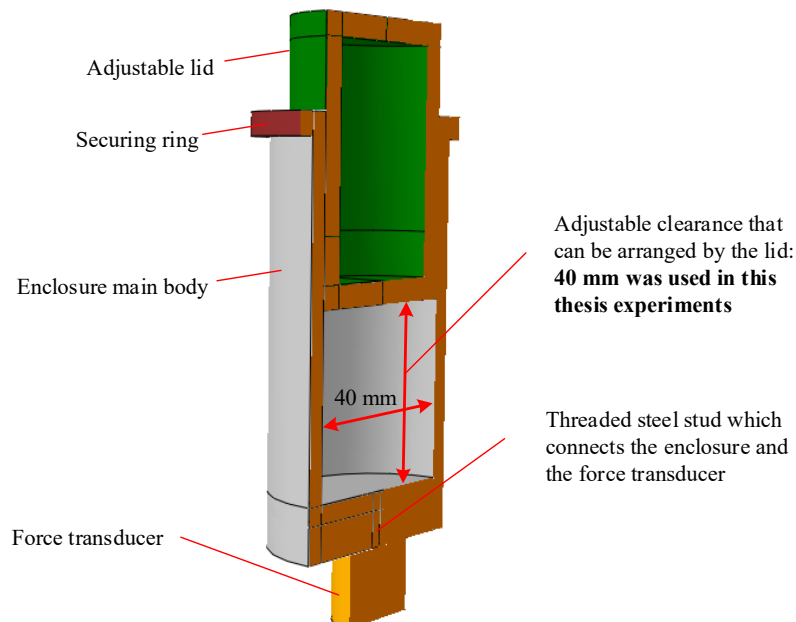
Figure B.1: Geometric details of the damper enclosure used in experiments – related to
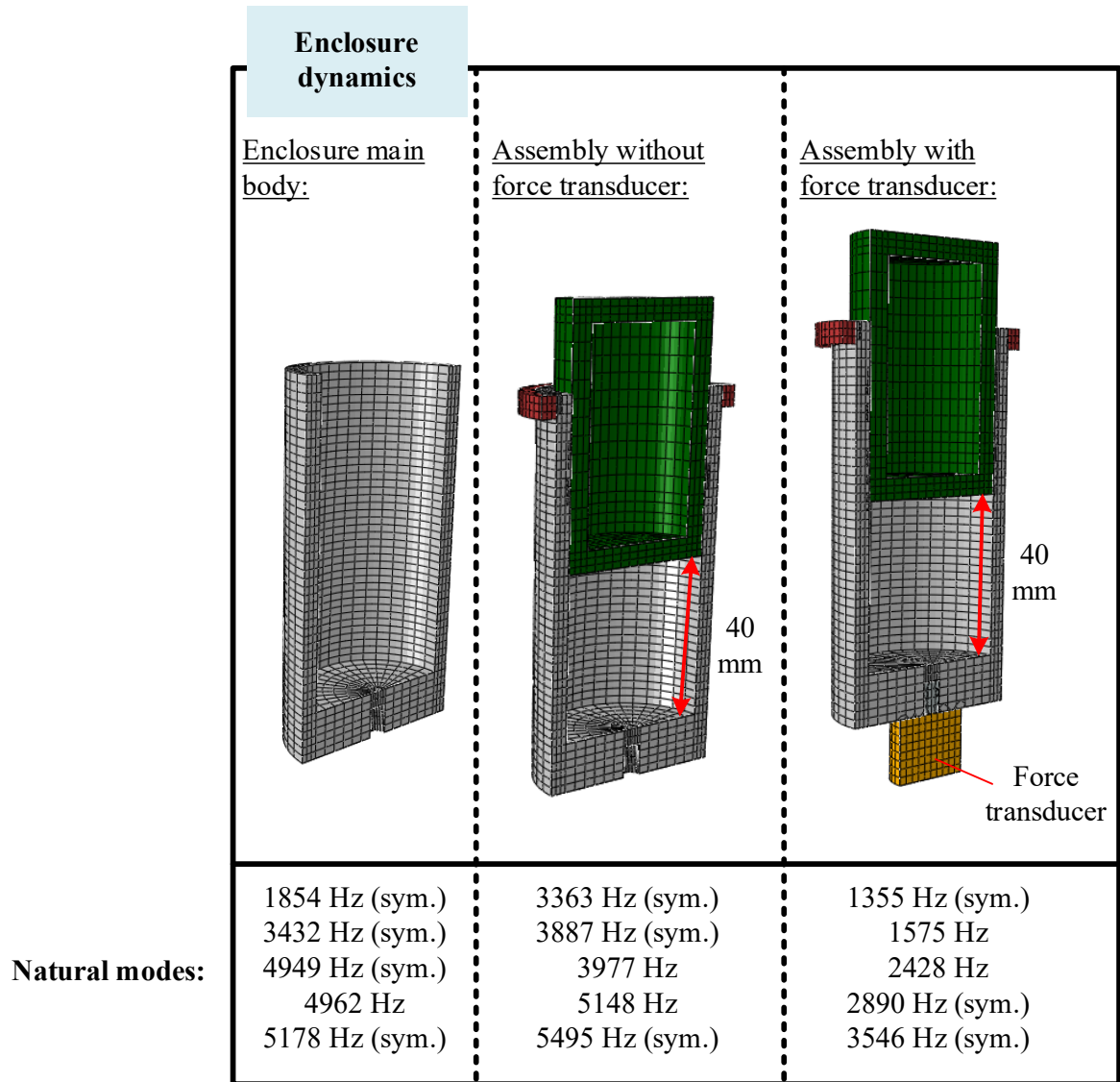
Chapter 7.

Figure B.2: Vibration mode frequencies of the damper enclosure used in experiments –
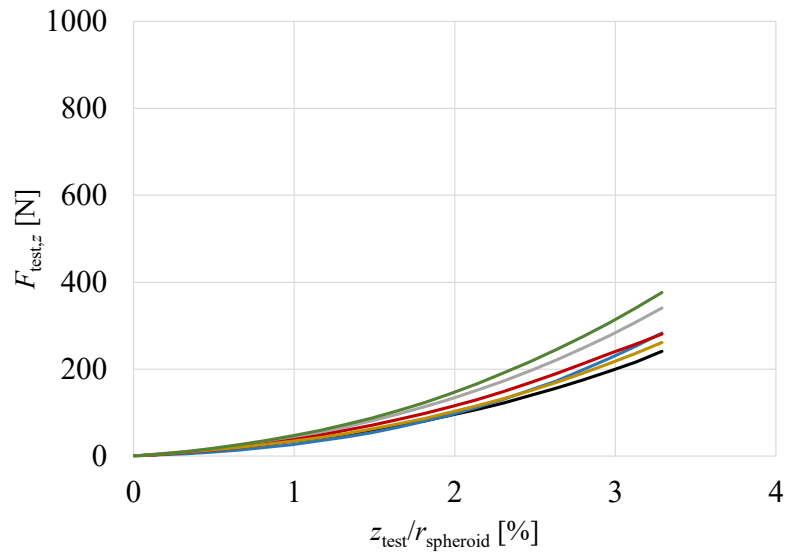
related to Chapter 7.

Appendix-C

Hand calibrator:
generates sine signal at 159.15 Hz having 10 m/s^2 acceleration amplitude for a typical accelerometer
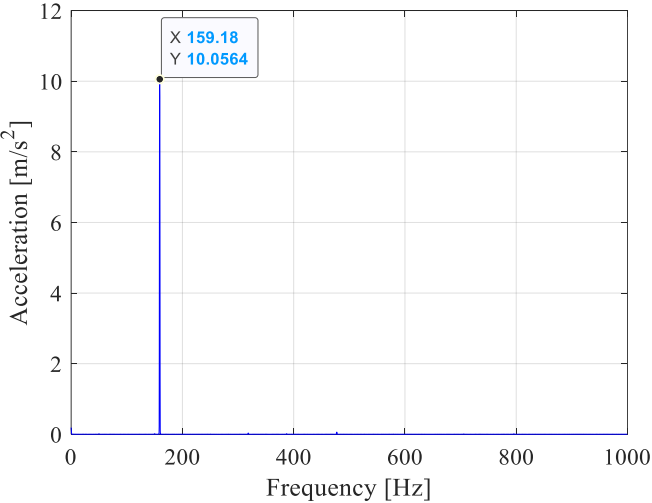

Figure C.1: Calibration of the accelerometer used in experiments – related to Chapter 7.

The resulting graph shows that there is no need to change the specified sensitivity of the used accelerometer.

Appendix-D

Figure D.1: Normal force-displacement results of the body of $\alpha_{\text{spheroid}} = 3.00$ particles via DEM simulations, each colour represents a different test obtained using a different particle settlement in the enclosure void – related to Chapter 8.
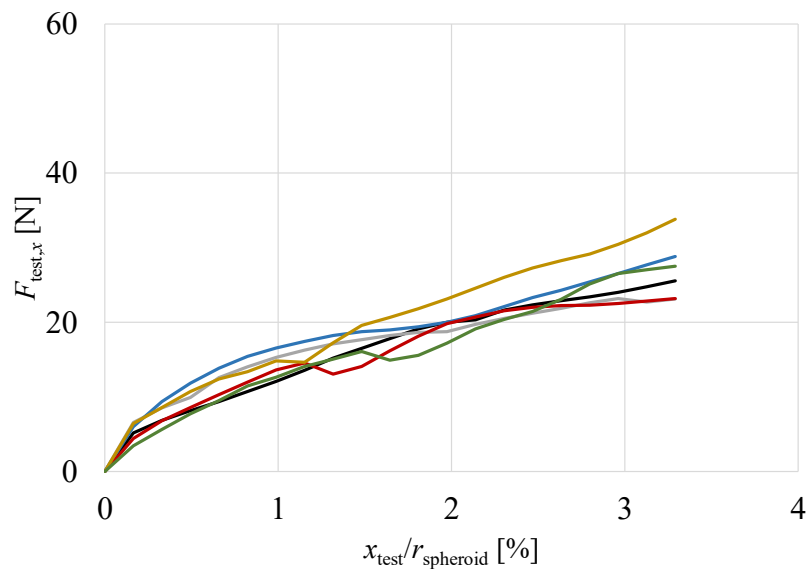

Figure D.2: Shear force-displacement results of the body of $\alpha_{\text{spheroid}} = 3.00$ particles via DEM simulations, each colour represents a different test obtained using a different particle settlement in the enclosure void – related to Chapter 8.
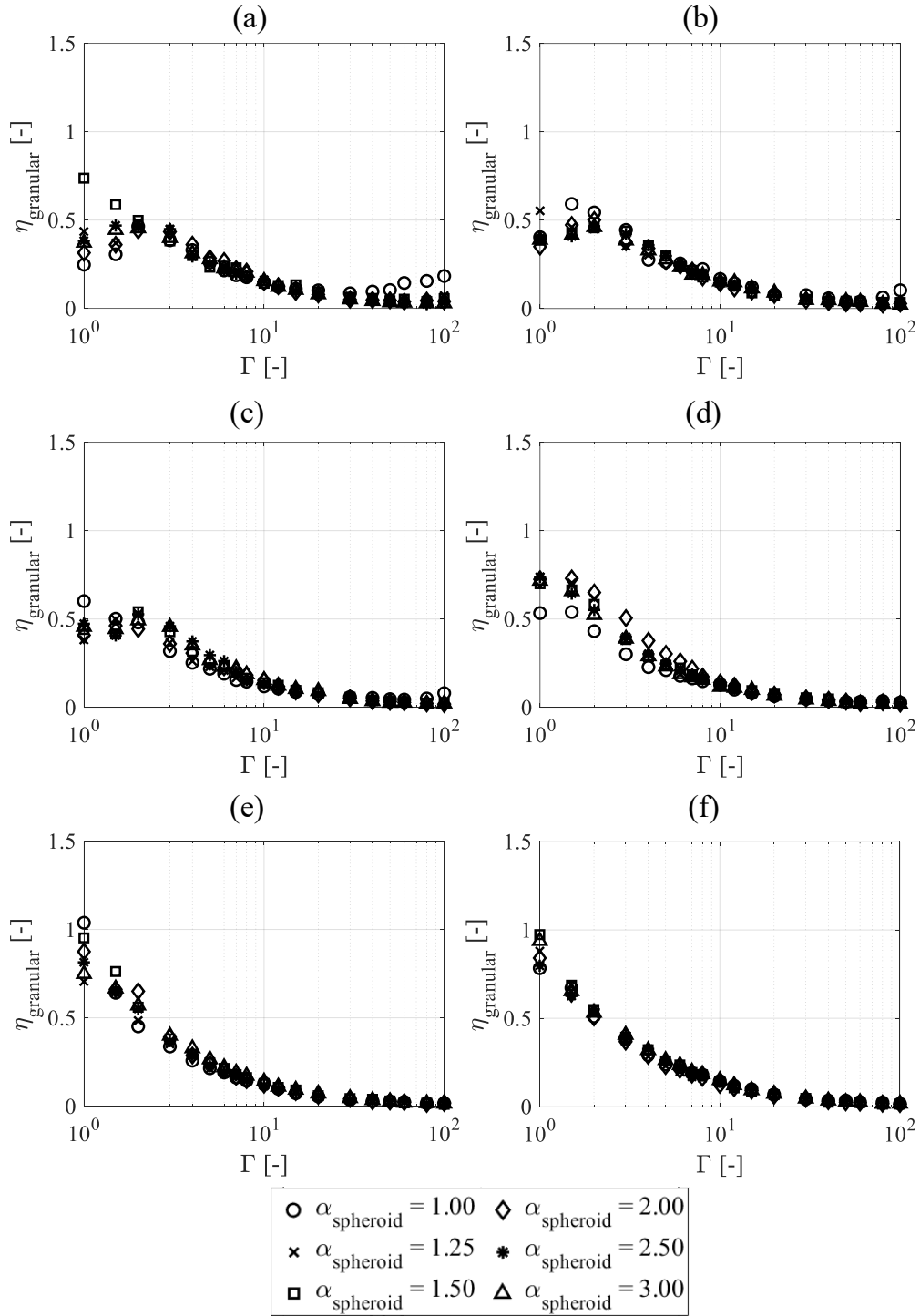
Figure E.1: Granular damping efficiency results of different prolate spheroids at horizontal excitations of: (a) 125 Hz, (b) 160 Hz, (c) 200 Hz, (d) 320 Hz, (e) 625 Hz and (f) 1024 Hz (simulation) – related to Chapter 8.
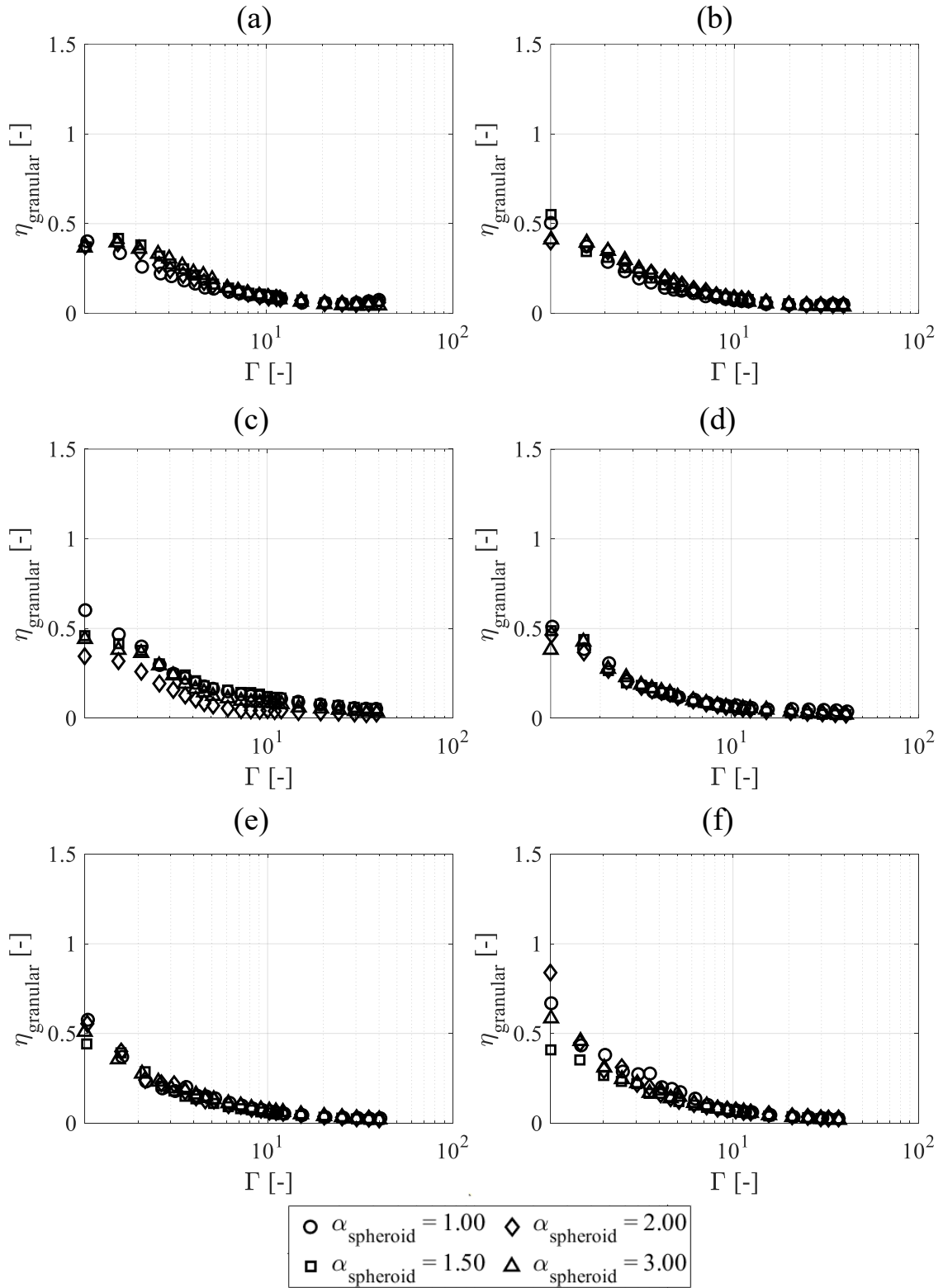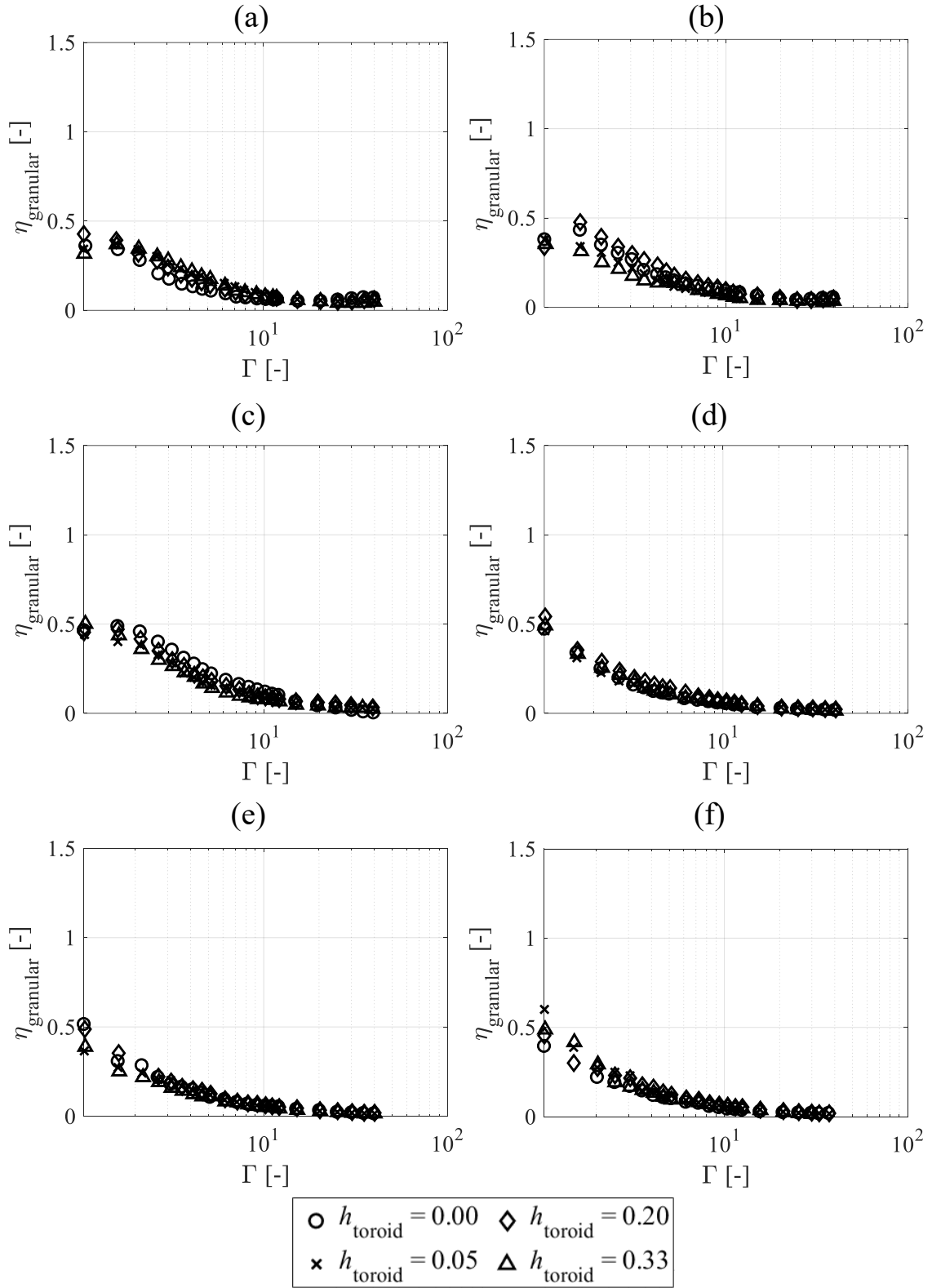
Figure E.2: Granular damping efficiency results of different prolate spheroids at horizontal

excitations of: (a) 125 Hz, (b) 160 Hz, (c) 200 Hz, (d) 320 Hz, (e) 625 Hz and (f) 1024 Hz
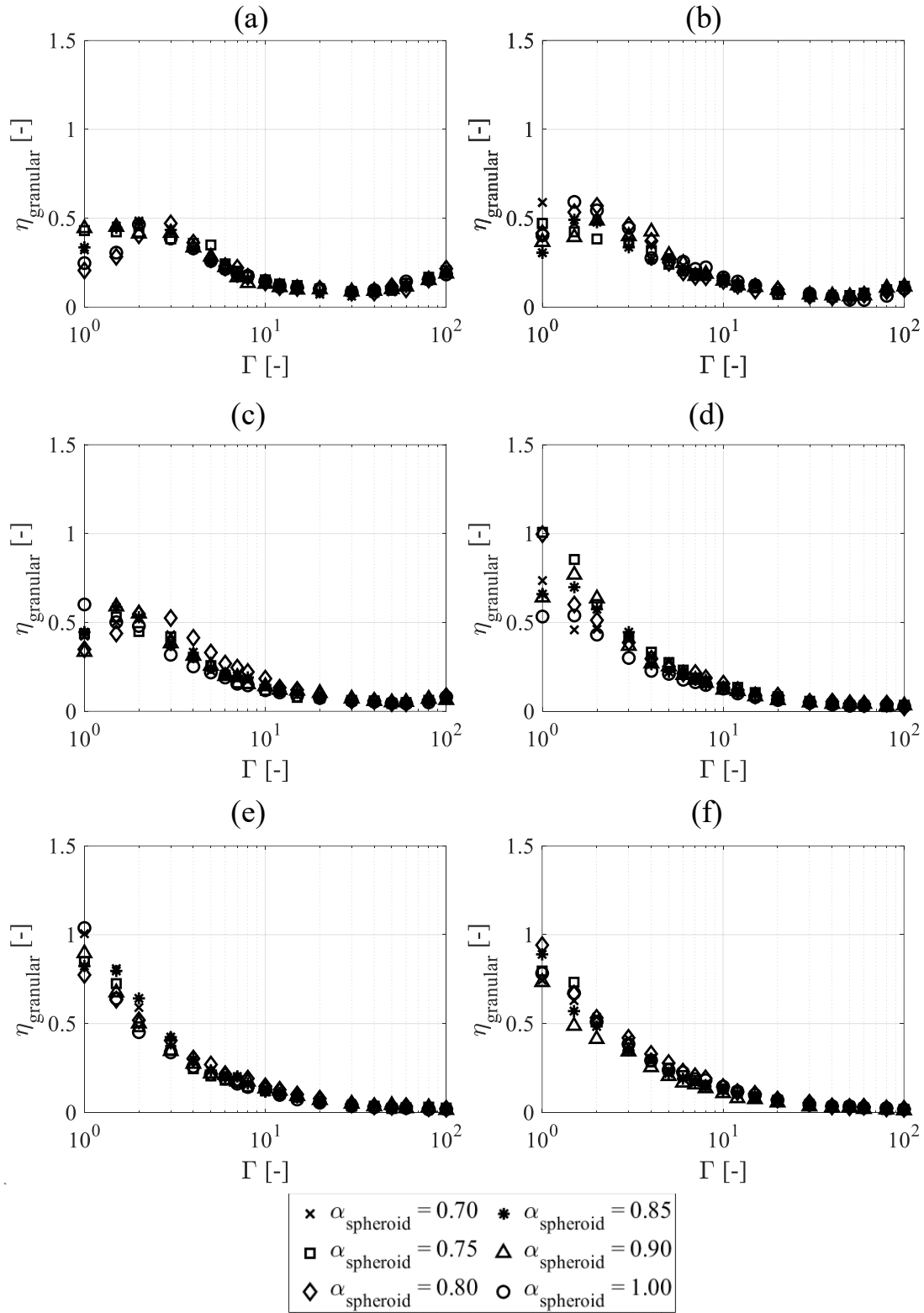
(experiment) – related to Chapter 8.
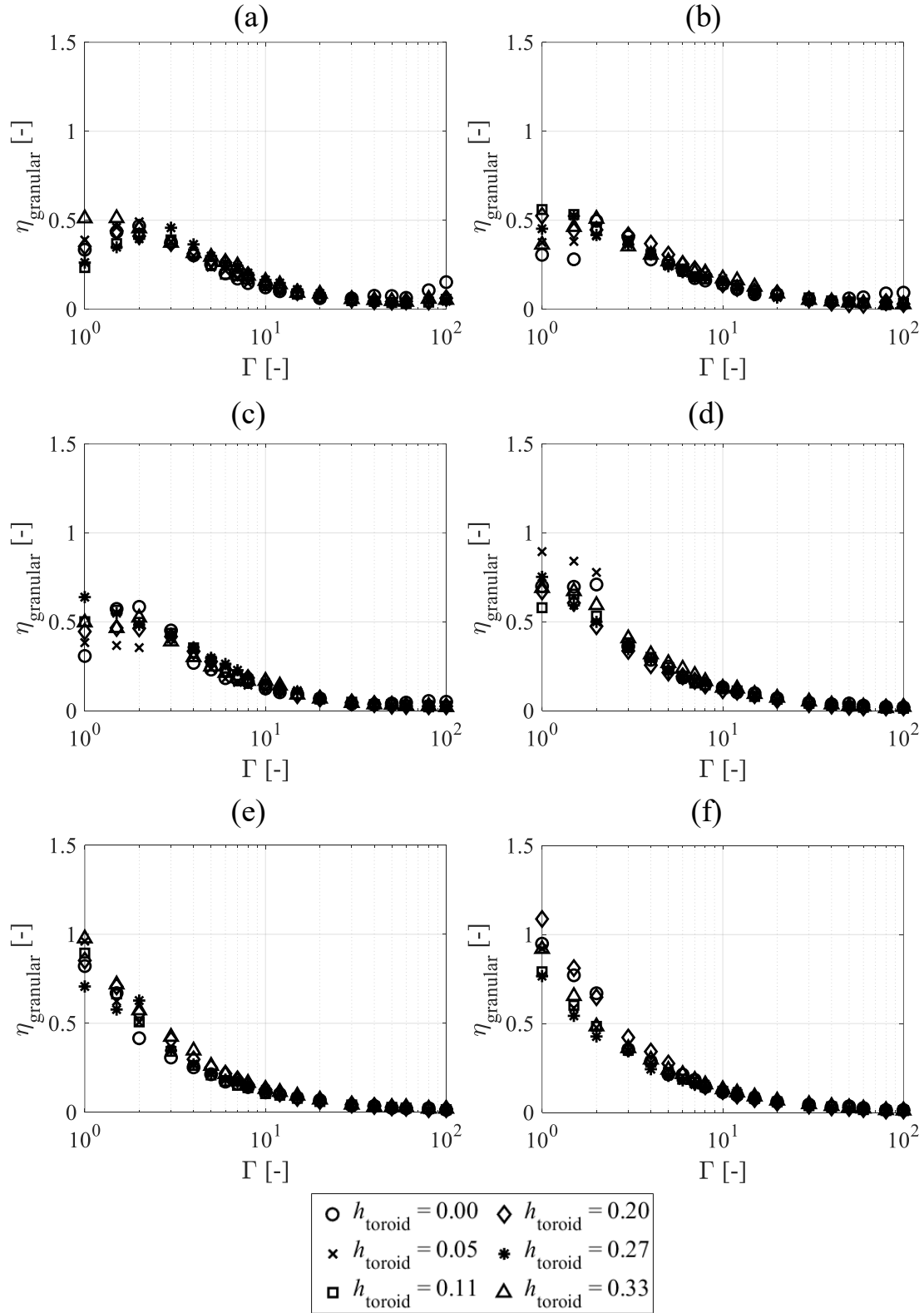
Figure E.3: Granular damping efficiency results of different toroids at horizontal excitations of: (a) 125 Hz, (b) 160 Hz, (c) 200 Hz, (d) 320 Hz, (e) 625 Hz and (f) 1024 Hz (simulation) – related to Chapter 8.
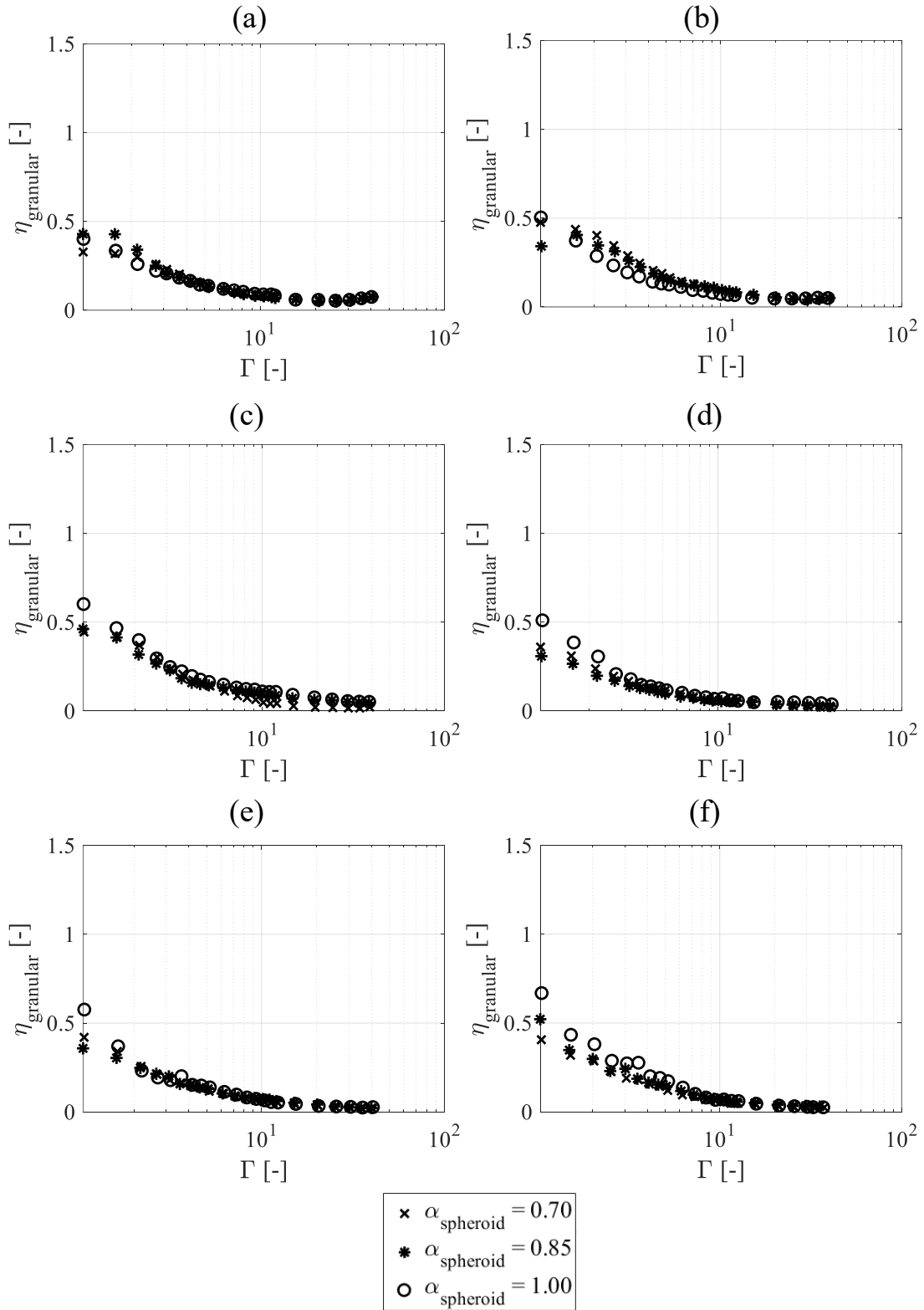
Figure E.4: Granular damping efficiency results of different toroids at horizontal

excitations of: (a) 125 Hz, (b) 160 Hz, (c) 200 Hz, (d) 320 Hz, (e) 625 Hz and (f) 1024 Hz

(experiment) – related to Chapter 8.

Figure E.5: Granular damping efficiency results of different oblate spheroids at horizontal excitations of: (a) 125 Hz, (b) 160 Hz, (c) 200 Hz, (d) 320 Hz, (e) 625 Hz and (f) 1024 Hz (simulation) – related to Chapter 8.

Figure E.6: Granular damping efficiency results of different oblate spheroids at horizontal

excitations of: (a) 125 Hz, (b) 160 Hz, (c) 200 Hz, (d) 320 Hz, (e) 625 Hz and (f) 1024 Hz

(experiment) – related to Chapter 8.

Publications From Thesis

Journal Papers:

Terzioglu F, Rongong J.A, Lord C.E, Motional phase maps for estimating the effectiveness of granular dampers, **Mechanical Systems and Signal Processing**, 188 (2023), pp. 110038. doi: 10.1016/j.ymssp.2022.110038.

Terzioglu F, Rongong J.A, Lord C.E, Influence of particle sphericity on granular dampers operating in the bouncing bed motional phase, **Journal of Sound and Vibration**, 554 (2023), pp. 117690, doi: 10.1016/j.jsv.2023.117690.

Conference Papers:

Terzioglu F, Rongong J.A, Lord C.E, The dissipative characteristics of oblate particles in granular dampers, **Proceedings of International Conference on Structural Dynamic –** *EURODYN*, 2020, vol. 2, pp. 4851-4866, Athens, Greece, doi: 10.47964/1120.9393.20452.

Terzioglu F, Rongong J.A, Lord C.E, Construction of motional phase maps for granular dampers, **INTER-NOISE and NOISE-CON Congress and Conference Proceedings –** *INTER-NOISE*, 2022, vol. 265(7), pp. 128-139, Glasgow, United Kingdom, doi: 10.3397/in_2022_0025.

Terzioglu F, Rongong J.A, Lord C.E, The effect of particle surface roughness on granular energy dissipation performance, **Proceedings of International Congress on Acoustics –** *ICA*, 2022, Gyeongju, South Korea.

Data Sets:

Terzioglu F, Rongong J.A, Lord C.E, Experimental and simulation damping efficiency results of a granular damper, for various particle aspect ratios, 2023, doi: 10.15131/shef.data.21931647.

Terzioglu F, Rongong J.A, Lord C.E, Experimental data sets of a granular damper, 2022, doi: 10.15131/shef.data.21273282.v2.

Collaboration Publication:

Lord C.E, Rongong J.A, Kiley, A, Terzioglu F, Retro-fit particle dampers for panels in space structures, **Proceedings of European Conference on Spacecraft Structures Materials and Environmental Testing –** *ECSSMET*, 2023, Toulouse, France.